Supervised Machine Learning Methods for Complex Data

by

Alessio Petrozziello

School of Computing

University of Portsmouth, UK

The thesis is submitted in partial fulfilment of the requirements for the award of the degree of Doctor of Philosophy of the University of Portsmouth

August, 2019

Copyright

Declaration

The work presented in this thesis has been carried out in the School of Computing at the University of Portsmouth under the supervision of Dr. Ivan Jordanov. Whilst registered as a candidate for the above degree, I have not been registered for any other research award. The results and conclusions embodied in this thesis are the work of the named candidate and have not been submitted for any other academic award.

Wednesday 7th August, 2019,

Portsmouth,

Alessio Petrozziello

Abstract

This dissertation investigates state-of-the-art machine learning methods (both shallow and deep) and their application for knowledge extraction, prediction, recognition, and classification of large-scale real-world problems in different areas (healthcare, online recommender systems, pattern recognition and security, prediction in finance, etc.).

The first part of this work focuses on the missing data problem and its impact on a variety of machine learning tasks (i.e., classification, regression and learn to rank), introducing new methods to tackle this problem for medium, large and big datasets. After an initial overview of the literature on missing data imputation, a classification task for the identification of radar signal emitters with a high percentage of missing values in its features is investigated. Successively, the impact of missing data on Recommender Systems is examined, focussing on Online Travel Agencies and the ranking of their properties. In relation to the missing data imputation problem, two novel approaches have been introduced, the first one is an aggregation model of the most suitable imputation techniques based on their performance for each individual feature of the dataset. The second one aims to impute missing values at scale (large datasets) through a distributed neural network implemented in Apache Spark.

The second part of this dissertation investigates the use of Deep Learning techniques to tackle three real-world problems. In the first one, both Convolutional Neural Networks and Long Short Term Memory Networks are used for the detection of hypoxia during childbirth. Next, the profitability of Multivariate Long Short Term Memory Networks for the forecast of stock market volatility is explored. Lastly, Convolutional Neural Networks and Stacked Autoencoders are used to detect threats from hand-luggage and courier parcel x-ray images.

Contents

List of Tables

List of Figures

Glossary

Abbreviation	Meaning
MAR	Missing at random
MCAR	Missing completely at random
MNAR	Missing not at random
MI	Multiple Imputation
MICE	Multiple Imputation Chained Equations
BTI	Bagged Tree Imputation
KNNI	K-Nearest Neighbours Imputation
SVDI	Single Value Decomposition Imputation
bPCA	Bayesian Principal Component Analysis
EM	Expectation Maximization
RFI	Random Forests Imputation
BGTI	Gradient Boosted Trees Imputation
LRI	Linear Regression Imputation
RS	Recommender Systems
CF	Collaborative Filtering
CBF	Content-Based Filtering
HDFS	Hadoop Distributed File System
RDD	Resilient Distributed Datasets
ML	Machine Learning
ELM	Extreme Learning Machine
DLA	Deep Learning Approach
NN	Neural Networks
RBM	Restricted Boltzmann Machines
CNN	Convolutional Neural Networks
LSTM	Long Short Term Memory Networks
RNN	Recurrent Neural Network
ROC	Receiver Operating Characteristic
TPR	True Positive Rate
TPR	False Positive Rate
AUC	Area Under the Curve
MAE	Mean Absolute Error

Abbreviation	Meaning
MSE	Mean Squared Error
RMSE	Root Mean Squared Error
NRMSE	Normalized Root Mean Squared Error
SA	Standard Accuracy
RE*	Variance Relative Error
MAP@X	Mean Average precision at X
DM	Diebold-Mariano
SOM	Self-Organized Map
EOF	Empirical Orthogonal Functions
SVM	Support Vector Machines
ESM	Electronic Support Measures
RBF	Radial Basis Function
OCA	Overall Classifier Accuracy
OE	Outer Error
IE	Inner Error
IA	Inner Accuracy
OA	Outer Accuracy
sFGDI	Scattered Feature Guided Data Imputation
VR	Vacation Rentals
SGD	Stochastic Gradient Descent
D-NNI	Distributed Neural Network Imputation
CTG	Cardiotocogram
DC	Decelerative Capacity
PRSA	Phase Rectified Signal Averaging
MCNN	Multimodal Convolutional Neural Networks
SPaM	Signal Processing and Monitoring Workshop
CTU-UHB	Czech Technical University / University Hospital Brno
GARCH	Generalized Autoregressive Conditionally Heteroskedastic
MEM	Multiplicative Error Models
R-GARCH	Realized GARCH
DJI 500	Dow Jones Industrial Average index

1 Introduction

1.1 Motivation

The term machine learning was coined in 1959 (Kohavi and Provost, 1998) and refers to the ability of machines to learn from data. The machine learning field slowly progressed through the years with contributions from a variety of disciplines such as statistics, optimization and data mining. However, the last 10 years have seen an extensive and quick growth in interest for the discipline, being mainly driven by two factors: the availability of inexpensive computer resources and the necessity to process and learn from the vast amount of data being generated every day, and referred as the *Big Data* era (McAfee et al., 2012). This amount of data collected by public entities and private companies, and awaiting to be analysed, poses new large-scale real-world problems that challenges scientists and industries around the world. All these real-world problems have usually some commonalities: large amount of available data, missing values, high dimensional hyper-parameter spaces and strong non-linear relationships of the collected variables. The research presented in this thesis is motivated by the challenge posed into addressing and providing solutions to large-scale real-world problems. A variety of machine learning methods are here proposed, implemented and compared into the quest to advance the state of the art of several challenging industrial and academic tasks. The original contribution to knowledge for each tackled problem is described in Section 1.2, the dissemination of the knowledge through peer reviewed articles is listed in Section 1.3, while a detailed outline of the thesis is described in Section 1.4.

1.2 Original Contribution to Knowledge

This dissertation investigates different aspects of the missing data imputation problem (Chapter 3) and three large-scale real-world problems tackled through the use of Deep Learning techniques (Chapter 4). The original contribution to knowledge can be summarised as follow:

- In Section 3.2 I compare three methods for dealing with large amount of missing values in intercepted radar signal data. The imputation performance is assessed on both binary and multi-class classification tasks for the identification of the signal emitters. Furthermore, I introduce two new evaluation metrics (namely Inner and Outer accuracies) to better assess the classification performance in the multi-class setting.

- In Section 3.3 I propose a novel multivariate data imputation approach (namely Feature Guided Data Imputation) for dealing with a variety of missingness types. I report results from the comparison with two single imputation techniques and four state-of-the-art multivariate methods on several datasets from the public domain.

- In Section 3.4 I investigate the impact of missing data (cold start problem) in a real-word learn to rank task (online travel agency properties ranking). After an initial investigation, I show how the imputation of missing values can benefit the ranking of properties which have been recently added to the catalogue.

- In Section 3.5 I tackle the problem of missing values imputation for big data, proposing an original missing data technique based on Distributed Neural Networks with Mini-batch Stochastic Gradient Descent on Spark. The proposal is tested on a real-world recommender system dataset where the missing data is generally a problem for new items, biasing the ranking toward popular items. The model is compared with both univariate and multivariate imputation techniques, and its performance validated using prediction accuracy and computational speed.

- In Section 4.1 I investigate the use of Deep Learning models for hypoxia detection during childbirth. Both Convolutional Neural Networks and Long Short Term Memory Neural Networks are compared with existing computerized approaches and current clinical practice on both private and publicly available datasets. Furthermore, a novel Multimodal Convolutional Neural Networks is proposed to accommodate inputs of different

types and dimensions.

- In Section 4.2 I explore the profitability of the application of Deep Learning techniques to the volatility forecasting problem. The proposed Multivariate Long Short Term Memory Neural Networks is quantitatively compared in different market regimes with classic univariate and multivariate Recurrent Neural Networks, and with the univariate parametric models Realized Generalized Autoregressive Conditionally Heteroskedastic and Multiplicative Error Models, which are widely used benchmarks in this field.

- In Section 4.3 I use Deep Learning techniques for the automation of threat objects detection from x-ray scans of passengers luggage and courier parcels. The classification is performed on raw data and after a variety of preprocessing steps. The Deep Learning methods performance are compared on two datasets with widely used classification techniques such as shallow neural networks and random forests.

The above-listed contributions have been disseminated by:

- Presenting the research outcomes to six international conferences and congresses;

- Preparing five journal papers, one of which has been published, and four are under review.

1.3 List of Publications

1.3.1 Within the scope of the thesis

JOURNALS

1. A. Petrozziello, A. Serra, L. Troiano, I. Jordanov, M. La Rocca, G. Storti, and R. Tagliaferri, Deep Learning for Volatility Forecasting, Elsevier Information Sciences (under review).

2. A. Petrozziello, I. Jordanov, A.T. Papageorghiou, C.W.G. Redman, and A. Georgieva, Multimodal Convolutional Networks to detect the fetus at risk of asphyxia during labour, IEEE Access.

3. I. Jordanov, N. Petrov and A. Petrozziello, Classifiers accuracy improvement based on missing data imputation, Journal of Artificial Intelligence and Soft Computing Research (2018).

CONFERENCE PROCEEDINGS

4. A. Petrozziello and I. Jordanov, Automated Deep Learning for Threat Detection in Luggage from X-ray Images, Springer Special Event on Analysis of Experimental Algorithms (SEA 2019).

5. A. Petrozziello and I. Jordanov, Feature Based Multivariate Data Imputation, 4th Annual Conference on machine Learning, Optimization and Data science (LOD 2018).

6. A. Petrozzielloa, I. Jordanov, A.T. Papageorghiou, C.W.G. Redman, and A. Georgieva, Deep Learning for Continuous Electronic Fetal Monitoring in Labor, IEEE 40th International Engineering in Medicine and Biology Conference (EMBC 2018).

7. A. Petrozziello, C. Sommeregger and I. Jordanov, Distributed Neural Networks for Missing Big Data Imputation, IEEE International Joint Conference on Neural Networks (IJCNN 2018).

8. A. Petrozziello and I. Jordanov, Column-wise Guided Data Imputation, 17th International Conference on Computational Science (ICCS 2017).

9. A. Petrozziello and I. Jordanov Data Analytics for Online Traveling Recommendation System: A Case Study, IASTED's 36th International Conference on Modelling, Identification and Control (MIC 2017).

10. I. Jordanov, N. Petrov and A. Petrozziello, Supervised Radar Signal Classification, IEEE International Joint Conference on Neural Networks (IJCNN 2016).

1.3.2 Outside the scope of the thesis

JOURNALS

11. F. Sarro and A. Petrozziello, Linear Programming as a Baseline for Software Effort Estimation, ACM Transactions on Software Engineering and Methodology (2018).

12. A. Petrozziello, G. Cervone, P. Franzese, S.E. Haupt, R. Cerulli, Source Reconstruction of Atmospheric Releases with Limited Meteorological Observations Using Genetic Algorithms, Applied Artificial Intelligence Journal (2017).

CONFERENCE PROCEEDINGS

13. F. Sarro, A. Petrozziello and M. Harman, Multi-Objective Effort Estimation, ACM 38th International Conference on Software Engineering (ICSE 2016).

1.4 Outline

This thesis is organized in five chapters. The first chapter discusses the motivation for conducting this research (Section 1.1), including a section on the original contribution (Section 1.2), a list of peer-reviewed publications that disseminates the key research outcomes (Section 1.3) and the organization of the thesis (Section 1.4).

Chapter 2 provides a background on the topics covered in Chapter 3 and Chapter 4. Section 2.1 describes the state-of-art techniques used in missing data imputation; Section 2.2 gives an introduction on recommender systems; Section 2.3 overviews the most important frameworks used for big data processing; Section 2.4 illustrates deep neural networks architectures; while Section 2.5 describes the most widely used evaluation criteria for classification, regression and learn to rank tasks.

Chapter 3 investigates the impact of missing values on a variety of machine learning tasks (i.e., classification, regression and learn to rank) and introduces new methods to tackle this problem for medium, large and big datasets. Section 3.1 overviews the literature on missing data imputation, focussing on the state-of-art methods. Section 3.2 studies a classification problem for the identification of radar signal emitters with a high percentage of missing values in its features. Section 3.3 proposes an aggregation model of the most suitable imputation techniques based on their performance for each individual feature of the dataset. Section 3.4 investigates the missing data and consequent long tail problem for recommender systems, while Section 3.5 introduces a novel distributed algorithm for the imputation of missing data at scale.

Chapter 4 investigates Deep Learning techniques applied to three real-world problems. Section 4.1 examines the use of Convolutional Neural Networks and Long Short Term Memory Networks for monitoring fetal health during childbirth, taking into account both contractions and fetal heart rate. Furthermore, a novel architecture is presented, namely Multimodal Convolutional Neural Network, which can handle both raw signals and additional features in one model. Section 4.2 explores the use of a Multivariate Long Short Term Memory Networks for the forecast of stock market volatility. The proposed architecture is compared with both Univariate Long Short Term Memory Networks and state-of-the-art techniques used in the financial sector. Section 4.3 considers the use of Convolutional Neural Networks and Stacked Autoencoders for the detection of threats (e.g., firearm components) from x-ray scans collected during airport security clearance process and courier parcels inspection. The investigated techniques are compared to shallow Neural Networks and Random Forests and their performance are reported over a variety of image pre-processing steps, and operational settings.

Chapter 5 concludes the thesis by summarising the contributions made in this research work and outlines ideas for further investigation (Section 5.3).

2 Background

This chapter provides the background needed to better understand the research pursued in Chapter 3 and Chapter 4.

Section 2.1 describes all the missing data imputation state-of-art techniques used through Chapter 3, focussing on their strengths, weaknesses, and hyper-parameters needed. Section 2.2 gives an introduction on recommender systems, topic discussed in Section 3.4 and Section 3.5. The section covers a variety of recommender systems, highlighting their use cases and respective challenges. Section 2.3 overviews the most important frameworks used for big data processing, describing, for each of them, peculiarities and limitations. Section 2.4 illustrates the three most used deep neural networks architectures: autoencoders, convolutional neural networks, and long short term memory neural networks. All vanilla implementations and new topologies are compared through Chapter 4. Finally, Section 2.5 describes the most widely used evaluation criteria for classification, regression and learn to rank tasks. Furthermore, baseline methods used as benchmark against new proposed techniques and statistical tests to ensure the statistical significance of the results are here reported.

2.1 Missing Data Techniques

Ideally, dealing with missing values requires an analysis strategy that leads to the least biased estimation, without losing statistical power. The challenge is the contradictory nature of those criteria: using the information contained in partial record (keeping the statistical power), while substituting the missing values with estimates, which inevitably brings biases. Mechanisms of missing data belong to three categories (Enders, 2010; Schmitt et al., 2015): Missing At Random (MAR), where the missingness may depend on observed data but not on unobserved data (in other words, the cause of missingness is considered); Missing Completely At Random (MCAR), which is a special case of MAR, where the probability that an observation is missing is unrelated to its value or to the value of any other variable; Missing Not At Random (MNAR),

where the missingness depends on unobserved data. The last group usually yields biased parameter estimates, while MCAR and MAR analyses yield unbiased ones (at the same time the main MCAR consequence is a loss of statistical power).

Many techniques have been proposed in the last few years to solve the missing data imputation problem and they can be divided into two main categories (Graham, 2009): deletion methods and model-based methods. The former includes pairwise and listwise deletion, the latter is divided into single and multivariate imputation techniques. Figure 2.1 shows the missing data methods taxonomy.

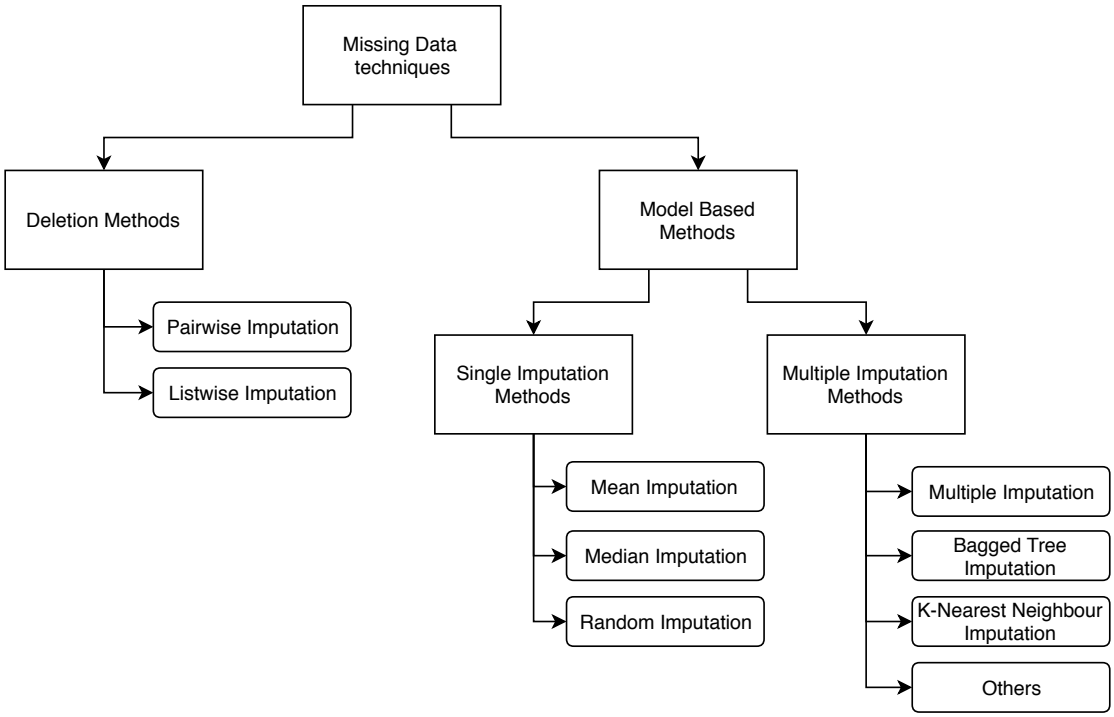

Figure 2.1: Missing data methodologies taxonomy.

The pairwise deletion keeps as many cases as possible using for each of them only the available variables (exploiting all available information). The main drawback is that analyses performed on sub-groups of variables is incomparable since each case is based on a different subsets of data, with different sample sizes and different standard errors. The listwise deletion (also known as complete case analysis) is a simple approach in which all records with missing data are omitted. The advantages of this approach include comparability across the

analyses and it leads to unbiased parameter estimates (assuming the data is MCAR) while the disadvantage is in the potential loss of statistical power (because not all information is used in the analysis, especially if a large number of cases is excluded).

The most common techniques used as a baseline for comparison and analysis of data imputation are random guessing, mean and median imputation (Sarro et al., 2016). The random guessing is a very simple benchmark to estimate the performance of a prediction method which inputs the missing data with random value drawn from the known values of the same feature. The mean (median) imputation replaces every missing value with the mean (median) of the attribute. However, those techniques fall into the single imputation category (the correlation between the variables is not taken into account), and are widely rejected by the scientific community (Osborne and Overbay, 2012), thus they are generally only used as benchmark for an initial comparison with newly proposed methods.

Different multivariate analysis techniques have been developed in the last 20 years, each of them showing different results based on the field and the type of data used. *Multiple Imputation* (MI) (Schafer, 1997), *Multiple Imputation Chained Equations* (MICE) (Azur et al., 2011), *Bagged Tree Imputation* (BTI) (Feelders, 1999; Rahman and Islam, 2011), *K-Nearest Neighbours Imputation* (KNNI) (Batista and Monard, 2002), *Single Value Decomposition Imputation* (SVDI) (Troyanskaya et al., 2001), *Bayesian Principal Component Analysis* (bPCA) (Oba et al., 2003) and others used through this thesis are here described.

Multiple Imputation (MI)

The multiple imputation is a general approach to the problem of data imputation that aims to address the uncertainty about the missing data by creating several different plausible imputed datasets and appropriately combining results obtained from each of them (Schafer, 1997).

The MI approach involves three distinct steps:

- sets of plausible data for the missing observations are created and filled

in separately to create many "complete" datasets;

- each of these datasets is analysed using standard statistical procedures;
- the results from the previous step are combined and pooled into one estimate for the inference.

The MI not only aims to fill in the missing values with plausible estimates, but also to plug in multiple times these values by preserving essential characteristics of the whole dataset. Therefore, all missing values are filled in with simulated values drawn from their predictive distribution given the observed data and the specified parameters Θ (vector of the normal parameters under which the missing data are randomly imputed: usually found by data augmentation or performing a maximum-likelihood estimation on the matrix with incomplete data using an expectation maximization (EM) algorithm). As with most multiple regression prediction models, the danger of over-fitting the data is real and this can lead to less generalisable results than the original data (Osborne and Overbay, 2012).

If X_c is a subset with no missing data, derived from the available dataset X, the procedure will start with X_c to estimate sequentially the missing values of an incomplete observation x^*, by minimizing the covariance of the augmented data matrix $X^* = (X_c, x^*)$. Subsequently, the data sample x^* is added to the complete data subset and the algorithm continues with the estimate of the next data sample with missing values.

Multiple Imputation Chained Equations (MICE)

The MICE is a method from the family of multiple imputation, operating under the assumption that the missing mechanism is MAR or MCAR. In the MICE process, each variable with missing data is regressed against all the others, guaranteeing that each variable is modelled independently to its distribution (Azur et al., 2011; Lee and Mitra, 2016).

The MICE method is divided into four stages:

- a simple imputation (e.g., mean) is performed for every missing value in the dataset and used as place-holder;

- the place-holders for one variable (Y) are set back to miss;
- use Y as the dependent variable in a regression model;
- use Y as independent variable in the regression of the next one.

The process is performed for every variable with missing entries and repeated many times until the convergence is reached. Graham et al. (2007) give a practical guide on how to select the number of iterations, however, depending on the size of the dataset, it is not always feasible to run the algorithm many times. As suggested by Bartlett et al. (2015), 10 iterations are usually enough for the convergence of the algorithm.

K-Nearest Neighbour Imputation (KNNI)

In the KNNI the missing values are imputed applying the mean, mode or median of the K most similar patterns, found by minimizing a distance function between a record with missing values and the complete subset (Batista and Monard, 2002). The use the Euclidean distance is recommended by Troyanskaya et al. (2001). The KNNI can be summarised in three steps:

- take the complete subset and use it to select the nearest neighbours;
- choose a distance metric and compute the nearest neighbours between each pattern with missing data and the complete set;
- impute the data, using the mean or the mode among the chosen neighbours.

An important parameter to select is the number of neighbours K. There are discordant opinions in the literature: Cartwright et al. (2003) suggest a low value (1 or 2) for small datasets; Batista and Monard (2002) advise a value of 10 for large datasets; while Troyanskaya et al. (2001) argue that the method is fairly insensitive to the choice of the number of neighbours. The KNNI has some advantages: the method can predict both, categorical variables (the most frequent value among the selected neighbours) and continuous variables (average among the neighbours); and when using this imputation technique, there is no need to train a model (as in the tree based imputation methods).

Bagged Tree Imputation (BTI)

The BTI is a machine learning technique for solving regression problems, which produces a robust prediction model using a vote (ensemble) among weak ones (Feelders, 1999; Rahman and Islam, 2011).

For each feature with missing data:

- train several tree models;
- impute the data using a regression function for each tree;
- use a vote among the trees to predict the missing value.

Bagging is used for generating multiple versions of a predictor in order to get an aggregated one. The aggregation uses the average over the predictor versions when imputing a numerical outcome, and employs a plurality vote when imputing a class. The multiple versions are formed by making bootstrap replicates of the training set and subsequently using these as new learning sets. Tests on real-world and simulated datasets, using classification and regression trees, and subset selection with linear regression, show that bagging can benefit the imputation accuracy (Rahman and Islam, 2011). Bagging also proved to be more efficient in the presence of label noise when compared to boosting and randomization (Dietterich, 2000; Saar-Tsechansky and Provost, 2007; Rahman and Islam, 2011; Frénay and Verleysen, 2014); it is also robust to outliers and can impute the data very accurately using surrogate splits (Feelders, 1999; Valdiviezo and Van Aelst, 2015). The latter feature (surrogate splits) is essential for handling missing data. For instance, say a decision tree is trained to predict variable d, using variables a, b and c, and if there are only values for a and b, the missing value of c will cause problems for the prediction of d. Making use of the surrogate splits, if the variable c is missing in a new data point, the algorithm defers the decision to another variable that is highly correlated to the missing variable c, which will allow the prediction to continue.

Singular Value Decomposition Imputation (SVDI) and Bayesian Principal Component Analysis (bPCA)

As the name suggests, the SVDI is a method that uses SVD to compute the missing values of a dataset Troyanskaya et al. (2001).

The algorithm is divided into four steps:

- fill the missing values with the column mean or zeroes (just as placeholders to run the SVD algorithm);
- compute a low rank-k approximation of the matrix;
- fill the missing values using the rank-k approximation;
- recompute the rank-k approximation with the imputed values and fill in again.

The process is iterated until a fixed epoch or when an improvement tolerance is reached. The main advantage of the SVDI is that it can work without a complete subset.

The bPCA imputation is an evolution of the SVDI (since the SVD is a PCA applied to normalised datasets with row-mean equal to 0) with the additional Bayesian estimation using a known prior distribution Oba et al. (2003).

The bPCA can be summarised in three steps:

- run a PCA on the initial dataset;
- perform a Bayesian estimation;
- use an EM algorithm until convergence to a specified tolerance.

An advantage of this approach is that no hyper-parameters tuning is needed, and the number of components is self-determined by the algorithm, but at the expense of a larger computational time. The Bayesian model takes into account the uncertainty in the parameters of the imputation model using a Bayesian treatment of PCA during the second step.

Random Forests Imputation (RFI)

Random Forests (RF), firstly introduced by Breiman (2001), is an evolution of the regression trees approach where multiples models are used together (ensemble) to predict the value of the substituted variable. Due to their flexibility, scalability, and robustness, the RF is considered one of the most successful machine learning models for classification and regression tasks (Fernández-Delgado et al., 2014). The RF have a wide range of benefits: they can easily handle categorical, continuous, discrete and boolean features, they are not very

sensitive to feature scaling, and can capture non-linearities and feature interactions without any additional effort in the data preparation (Wainberg et al., 2016). The method trains a set of decision trees separately, increasing the parallelisation and scalability while adding some randomness to ensure that each tree is different from the others. On the test set, the prediction of each tree is combined to reduce the variance, thus improving the performance metrics. The randomness is usually injected through two techniques: bootstrapping from the original dataset at each iteration; or using only a subset of features for each tree. To predict the outcome of an instance of the test set, all trees are aggregated, usually predicting as final value an average of the predictions over all trees.

Gradient Boosted Trees Imputation (BGTI)

The GBTI is an ensemble of decision trees that iteratively train single trees to minimize a given loss function (Ye et al., 2009). On each iteration, the algorithm uses the current set of models (ensemble) to predict the value of each training sample which is compared to the observed label. The dataset is re-labelled to give more importance to the training samples with low prediction accuracy, hence, in the next iteration, the algorithm will put more effort in correcting those problematic instances. The re-labelling process is carried minimising a loss function on the training set, in successive iterations. The two main loss functions for regression are the squared error ($\sum_{i=1}^{N}(o_i - p_i)^2$) and the absolute error ($\sum_{i=1}^{N}|o_i - p_i|$), where o_i is the observed label and p_i is the predicted one for a given pattern i, and N is the number of samples. Similarly, to RFI, the GBTI can handle a variety of features (e.g., categorical, continuous, discrete and boolean), no additional data scaling is needed and they can capture non-linear patterns and feature relationships. Since the GBTI can overfit during the training process, a validation set should be used to mitigate the possibility of memorizing the data instead of learning to generalise. The training is stopped when the improvement in the validation error is less than a certain threshold. Usually, the validation error decreases initially with the training error and increases later in the learning when the model starts to overfit (while the training

error continues to decrease).

While RFI and GBTI share many similarities (both are ensemble of decision trees), they have substantial differences in the learning process:

- the GBTI trains one model at time, while the RFI can train multiple in parallel;
- the GBTI requires shallower trees then the RFI, hence, less overall inference time;
- the RFI reduces the likelihood to overfit training a large number of trees. On the other hand, the GBTI increases it training large number of trees - in other words, the RFI reduces the prediction variance training more trees, while GBTI reduces the bias;
- the RFI is easier to tune since the performance increases monotonically with the number of trees (Meng et al., 2016), while the GBTI performance decreases with a larger number of trees.

Linear Regression Imputation (LRI)

In the LRI, the variables to be imputed (which are assumed to be in the continuous space) are considered as the dependent variable in a multivariate regression model (Anagnostopoulos and Triantafillou, 2014).

The model is trained on the complete subset and comprises three steps:

- take complete subset and fit a regression model: $\hat{y} = w_k x_i$, where w_k is the regression weight vector for feature k, and x_i the feature vector of item i (note that there is no parameter sharing between the features, so the optimization problem is separable in k independent tasks);
- impute each missing value with the fitted model;
- repeat steps one and two to generate multiple imputations.

Using the linear regression approach, a continuous variable may have an imputed value outside the range of observed values. The main advantages of the LRI are the ready implementation of regression models in Spark and the fact that it can easily scale with the size of the dataset. On the other hand, the main drawback of the method is the need of a different model for each feature con-

taining missing values.

2.2 Recommender Systems

The Recommender Systems (RS) (Resnick and Varian, 1997) are a branch of Information Retrieval (Baeza-Yates and Ribeiro-Neto, 1999) which popularity increased significantly with the advances of the Internet Of Things (Xia et al., 2012). Their application includes different market areas and domains (e.g., movies, music, news, books, research articles, search queries, social tags, restaurants, travels, and products in general). The interest in the research community particularly aroused in 2007 when Netflix released a big dataset with over a million users' preferences and offered a million dollars to the team which was able to increase the recommendation accuracy on their dataset (Koren, 2009). The RS is a machine learning model trained to produce a list of items based on two parts of information:

1. past behaviour of users in the system (e.g., items previously purchased, rated, viewed or liked in past sessions);
2. characteristics (features) of a specific item, used to recommend items with similar properties.

The RS using (1) is also called Collaborative Filtering (CF) (Koren, 2008; Koren et al., 2009; Su and Khoshgoftaar, 2009; Koren, 2009) and its main strength is the ability to exploit users' historical information to give a recommendation on a large number of items. On the other hand, the RS using (2) is called Content-Based Filtering (CBF) (Van Meteren and Van Someren, 2000), an approach that uses the item's feature space to recommend the most similar items based on a distance function (to be minimized) or a similarity function (to be maximized). Both methods CF and CBF struggle to give a good recommendation when a new item is added to the system (e.g., lack of historical features), or when some of the non-historical features are missing from the dataset (i.e., cold start problem (Lam et al., 2008)). Furthermore, the CBF only considers similar items, ignoring the possibility to explore the space of those far from the initial user's choice. To overcome some of the CF and CBF limitations and to give

even greater degree of diversity in the recommended list, a mix of the two approaches is used, namely Hybrid RS. During the training and retrieval phase of a Hybrid RS, and extra layer of features is added (which is denoted as *first-order interaction* between the users and items' features).

Only the CBF is here described in more details as its missing data problem is tackled in Section 3.4 and Section 3.5.

The CBF aims to discover similarities among the items of a catalogue, based on a set of features, either static and immutable, or historical and changing over time.

Given an item *i* selected by the user, the system should be able to recommend a list of items close to *i* in the item's feature space. Therefore, for each pair of items (i,j) it is necessary to minimize a similarity function:

$$s_{i,j} = sim([f_{i,1}, .., f_{i,n}], [f_{j,1}, .., f_{j,n}]) \quad , \tag{1}$$

where $s_{i,j}$ has [0,1] as co-domain, while $[f_{i,1}, .., f_{i,n}]$ and $[f_{j,1}, .., f_{j,n}]$ are the sets of features for the items *i* and *j* respectively.

Widely used similarity measures are the Peason correlation, cosine similarity, and Euclidean distance in case of continuous outcome - or, in case of binary features, the Jaccard similarity (Niwattanakul et al., 2013) and the Hamming distance (Norouzi et al., 2012) (or its variant Weighted Hamming distance) are valid alternatives.

The Jaccard similarity is defined in Eq. 2 while the Hamming distance and its weighted variant in Eq. 3 and Eq. 4 where *W* is a vector of the same length of f, containing the weight of each feature calculated with some popularity metric or expert judgement.

$$\text{jaccard}(i, j) = \frac{|\cap([f_{i,1}, .., f_{i,n}], [f_{j,1}, .., f_{j,n}])|}{|\cup([f_{i,1}, .., f_{i,n}], [f_{j,1}, .., f_{j,n}])|} \quad , \tag{2}$$

$$\text{hammingDistance}(i, j) = \sum \text{XOR}([f_{i,1}, .., f_{i,n}], [f_{j,1}, .., f_{j,n}]) \quad , \tag{3}$$

$$\text{weightedHammingDistance}(i,j) = \sum \text{XOR}([f_{i,1},..,f_{i,n}],[f_{j,1},..,f_{j,n}]) \cdot W \quad . \tag{4}$$

Both Eq. 3 and Eq. 4 represent distances, and only when opportunely scaled between 0-1, they become similarity measures.

Many challenges are open in the RS field, among those: data sparsity; cold start; missing values; scalability; duplication; outliers; diversity and long tail.

a) Data Sparsity and Cold Start

Most real-world RS are based on large datasets and their robustness and accuracy tend to increase with the use of big data. As a result of this, the RS user-item (item-item) matrix is extremely large and sparse, which brings problems in the general performance of the system. The cold start problem is a straight consequence of the data sparsity, where the introduction of a new user/item leads to random recommendations (or just popularity based recommendations), since there is no recorded historical data.

b) Missing values

The missing values problem concerns mainly the CBF algorithms, where new items added to the catalogue might miss historical features or any other important information due to human or machine fault.

To cope with this problem it is possible to apply canonical techniques of missing data imputation (Schafer and Graham, 2002), however, when the size of the catalogue or the number of features increases, ad-hoc parallelizable and distributed techniques are required.

c) Scalability

As the number of items and users grow, the RS tend to suffer of scalability problems. When the system has data related to millions of users and items, a RS with linear complexity is already too slow to meet the real-time criteria which are required in a web application (e.g., online shopping). To overcome this problem it is necessary to build parallel and distributed solutions, able to

linearly scale with the number of machines involved in the computation.

d) Duplication

The duplication problem occurs when an item is replicated multiple times in the catalogue with different names. Presence of many duplicates increases the sparsity of the data, impact the speed of the recommendation, and introduces the risk of recommending the same item multiple times. Effective de-duplication algorithms are necessary to reduce the size of the catalogue and increase the relevance of the recommended list.

e) Outliers

For CF and CBF the word outlier assumes different meanings. For the CF, an outlier is when a user neither agree nor disagree with any of the groups of users already in the catalogue, or when a user has tastes diametrically opposite to the others. On the other hand, for CBF an outlier is an item which does not share similarities with any other product in the system.

f) Diversity and long tail

The RS are supposed to increase diversity and help the users to find valuable items in the vastness of the catalogue. However, very often they tend to recommend the most popular items, due to lack of historical data for the newly added products, forming what is usually referred as long tail (Fleder and Hosanagar, 2009).

2.3 Big Data Frameworks

Here I describe the main frameworks that are used for the processing of large datasets (terabytes and more). Hadoop and Spark are described in greater details, as they are used in Section 3.4 and Section 3.5. Furthermore, a mention to other big data frameworks is given in Section 2.3.3.

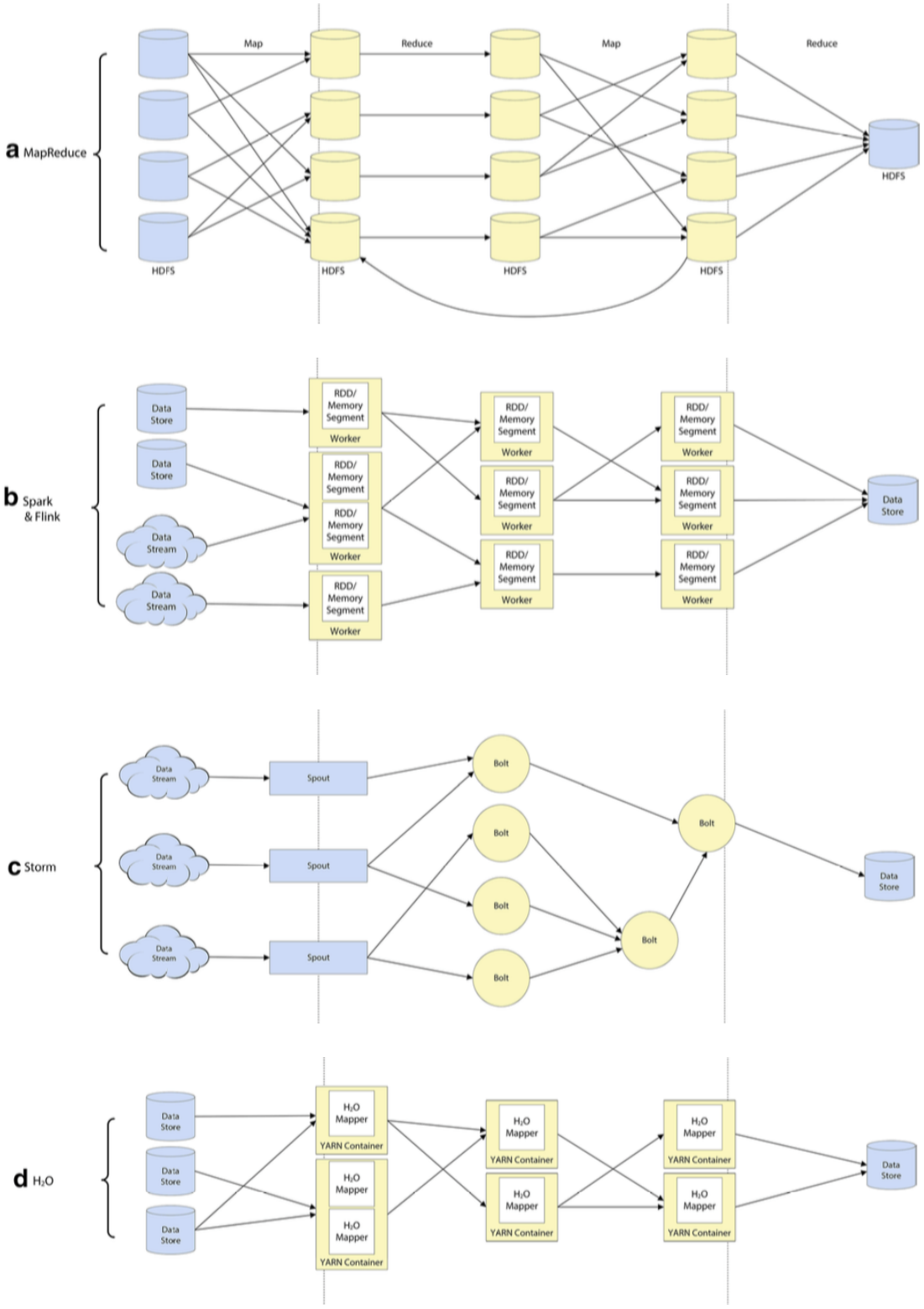

Figure 2.2: Processing engine flow charts: Map-Reduce (a), Spark/Flink (b), Storm (c), H_2O (d).

2.3.1 Apache Hadoop

Apache Hadoop is an open source framework for distributed storage and processing of big datasets. The main module consists of the storage part, known as Hadoop Distributed File System (HDFS) and the processing part, based on the Map-Reduce paradigm. Hadoop dispatches the packaged code to each machine of the cluster and processes the data taking advantage of the their locality (each node processes only the data that is in its local storage, reducing overhead and transfer bottlenecks). The Apache Hadoop framework core is composed of 4 modules:

- Hadoop Common: contains libraries and utilities needed by other Hadoop modules (White, 2012).
- Hadoop Distributed File System (HDFS): a distributed file-system that stores data on commodity machines, providing very high aggregate bandwidth across the cluster (Borthakur, 2007).
- Hadoop YARN: a resource-management platform responsible for the management of computing resources in clusters to optimize the scheduling of users' applications (Vavilapalli et al., 2013).
- Hadoop Map-Reduce: an implementation of the Map-Reduce paradigm for large scale data processing (Dean and Ghemawat, 2008).

However, nowadays the term Hadoop refers to the whole ecosystem that includes a set of additional packages, such as:

- Ambari: enables system administrators to provision, manage and monitor an Hadoop cluster (Wadkar and Siddalingaiah, 2014);
- HBase: open source, non-relational, distributed database providing BigTable-like capabilities for Hadoop (George, 2011);
- Mahout: free implementations of distributed or otherwise scalable machine learning algorithms focused primarily in the areas of collaborative filtering, clustering and classification based on Hadoop (Owen and Owen, 2012).

and many others.

A small Hadoop cluster includes at least one master and multiple worker nodes. The master node is composed of a Job Tracker, Task Tracker, NameNode and DataNode. A worker act like a DataNode and TaskTracker, although it is possible to have data-only or compute-only worker nodes.

In large clusters, the HDFS nodes are managed through a dedicate NameNode server to host the file system index and a secondary NameNode preventing the corruption and loss of data (losing the index of the chunks means losing the whole dataset stored on the HDFS). To reduce network traffic and overhead, the HDFS must provide location awareness: the name of the rack where the worker node is and all the information used to execute code on the same node where the data dwell. The HDFS usually stores and replicates large files (gigabytes or terabytes) on a number of nodes to provide a fault tolerance mechanisms: if one node fails during a map or a reduce task, the master automatically deploys the same task to another node containing a replica of the data. A last important note is that the HDFS was designed for mostly immutable files and may not be suitable for systems requiring concurrent write-operations or real-time tasks.

Map-Reduce is a paradigm for parallel programming (Dean and Ghemawat, 2008) designed to process big datasets over a cluster of commodity computers. The paradigm is totally transparent to the programmer and an easy way to implicitly parallelise applications without effort. As the name says, the process is divided into two steps (functions) for the programmer: map and reduce phases (Figure 2.2a). The map function reads each sample of the dataset as a key-value <k,v> input pair and gives an intermediate set <k,v> as output. Then, a middleware merges all the values associated with a specific key, producing a list (shuffle phase). The reduce phase aggregates each list, producing the final result.

While this paradigm works for many problems, its very design to express every problem as a sequence of map and reduce tasks is a big pitfall: if a job requires more than one map-reduce step, the intermediate results are stored on the HDFS, leading to heavy network traffic and bandwidth bottlenecks. This is the case for iterative and incremental algorithms, where multiple passes are

needed over the same dataset (which includes almost all machine learning techniques). Furthermore, while the start-up costs for map and reduce tasks is negligible for large datasets, it is a critical limitation if several map-reduce jobs have to be started for many small datasets. Lastly, the Map-Reduce paradigm also fails to support interactive data mining (where a set of queries needs to be run on the same dataset), and to handle real-time streaming data (which needs to maintain and share its state across multiple phases).

2.3.2 Apache Spark

Apache Spark is a general-purpose cluster-computing framework based on the idea of Map-Reduce while addressing some of the limitations already described. Spark supports iterative computation and uses the Resilient Distributed Datasets (RDD) to store the data in-memory, providing fault tolerance without data replication (Zaharia et al., 2010). The framework is implemented in Scala (Odersky et al., 2008) which is a hybrid programming language offering its users the high expressiveness of functional programming, and the easiness of the object oriented paradigm.

The data are initially stored in a storage system such as HDFS and read from the Spark handler to generate RDDs. Operations carried on RDDs are referred as transformations (e.g., map, reduce, filter, etc). The output of each transformation is a new RDD, and a sequence of transformations are stored in a graph and lazily evaluated only when the results are needed by the driver node (referred as actions).

The RDDs are immutable parallel data structures which simplifies consistency and supports resiliency through the use of computational graphs (the lineage of transformations needed to recover the data). In case of any failures, it applies these transformations on the base data to reconstruct any lost partition. A program cannot reference an RDD that it cannot reconstruct after a failure, which is critical for fault tolerance.

The main difference between Hadoop and the Spark is that the latter uses the lineage graph instead of the actual data itself to efficiently achieve fault toler-

ance. Memory remains a prime concern with the increasing volumes of data, not having to replicate the data across disks saves significant memory and storage spaces, while network and storage I/O account for a major fraction of the execution time. The RDDs offer great control of these, hence attributing to better performance. Figure 2.2b shows an abstraction of a Spark pipeline: the process stores the intermediate results in cache, reducing the read and write overhead, hence offering sub-second latency and strongly supports interactive ad-hoc querying on large datasets.

Spark supports a wide range of distributed computations and facilitates re-use of working datasets across multiple parallel operations. Among those there are graph processing (Xin et al., 2013), real time streaming data (Maarala et al., 2015) and machine learning applications.

A recent update introduced the concept of dataframes (a data structure formed of key-value columns). The dataframes can be created from an existing RDD, HDFS or other sources. Spark succeeded in numerous contests, showing performance 10 times faster than Map-Reduce with one third of the nodes (Zaharia et al., 2010).

2.3.3 Mention to other big data frameworks

In this section I briefly describe other widely used frameworks for the processing of big data, such as: Flink, Storm, and H_2O.

Apache Flink is a solution for batch and stream processing, it is scalable with in-memory option and has interfaces for Java and Scala. Born as an independent project, it can run without the Hadoop ecosystem, but can also be integrated with HDFS and YARN. As for in Spark, Flink processing model (Figure 2.2b) applies transformation to parallel data collection to generalize map, reduce, join, group and iterate functions (Ewen et al., 2013). Flink comes with an integrated machine learning (ML) library named ML-Flink, while still being compatible with the SAMOA library for streaming algorithms.

Apache Storm is a distributed stream processing computation framework aim-

ing to process large datasets. The Storm architecture (Figure 2.2c) consists of spouts and bolts. The former is the input stream, the latter is the computational logic: processing data in tuples taken from the spouts or other bolts. The network is presented as a directed graph witch can be defined in any programming language through the Thrift framework (Toshniwal et al., 2014). The fault tolerance is guaranteed with an acknowledgment (ACK) system:

- spouts keep the message in the output queue until the bolt sends an ACK;
- the message is continuously sent to the bolts until they are acknowledged, before being dropped from the queue.

The entire system is orchestrated by a master node (Nimbus) witch checks the heartbeat from the workers and re-assigns the jobs in case of faults. The biggest difference between the Map-Reduce JobTracker and Nimbus is that if the former dies, all running jobs are lost, but if Nimbus dies, it is automatically restarted (Gradvohl et al., 2014). Storm does not come with any ML library, but SAMOA can be easily integrated.

H_2O offers a full environment for parallel processing, analytics, math, machine learning, pre-processing and evaluation tools. The suite comes with a GUI and interfaces for Java, R, Python and Scala. As can be seen in Figure 2.2d, H_2O integrates Spark, Spark streaming and Storm. The suite offers total in-memory storage with distributed fork-join and divide-et-impera techniques for massive parallel computation.

Landset et al. (2015) made a comprehensive overview of the existing frameworks analysing scalability, speed, coverage, usability and extensibility, alongside a list of algorithms available for each framework. The authors pointed out that there is not one winner but the choice is based on the application and the type of task (i.e., batch, iterative batch or real-time streaming). Map-Reduce is the current standard, with the limitation to process batch tasks, Spark is a natural successor that adds iterative tasks and supports all the ML libraries that Map-Reduce does and even more. For real-time tasks, Storm and Flink offer true streaming: Flink is the best trade-off with sequential batch and streaming but it is a young project and yet with a small community. Furthermore, it does

not provide much choice in terms of ML algorithms. H_2O is the only end-to-end system, offering a web interface and a Deep Learning implementation.

Table 2.1 shows the compatibility of each engine, demonstrating: execution model, supported languages, supported ML libraries and some main characteristics, including: in-memory processing, low latency, fault tolerance and enterprise support.

Mahout has improved much with the latest version, giving more flexibility and allowing the user to write its own algorithms, same for SAMOA and MLlib. It is important to notice that the libraries are continuously updated and other features might be added.

Table 2.1: Data processing engines for Hadoop.

Engine	Execution Model	Supported Language	LM Libraries	In-Memory Processing	Low Latency	Fault Tolerance	Enterprise Support
Map-Reduce	Batch	Java	Mahout	-	-	✓	-
Spark	Batch Streaming	Java, Python R, Scala	Mahout MLlib, H_2O	✓	✓	✓	✓
Flink	Batch Streaming	Java, Scala	Flink-ML SAMOA	✓	✓	✓	-
Storm	Streaming	Any	SAMOA	✓	✓	✓	-
H_2O	Batch	Java, Python R, Scala	Mahout MLlib, H_2O	✓	✓	✓	✓

2.4 Deep Neural Networks

Neural networks (NN) take inspiration by the central biological system of animals. The basic unit of a network is the neuron, each one loosely or strongly connected to the others based on weights. The knowledge is taken by the external environment through an adaptive process of learning associated with the network and stored in its parameters, in particular in the weights of the connections. The networks are divided into layers. The first layer is connected with a middle layer called *hidden* and at each input is applied a transformation based on a learning function. The outputs are transferred to the output layer or to another hidden layer.

Based on the number of layers, a network can be identified as shallow or deep (Figure 2.3). A shallow network is provided with only one hidden layer while a

deep network benefits of different stacked layers, each one with its own learning function. Both threads have their roots in 2006 and are respectively named Extreme Learning Machine (ELM) (Huang et al., 2006) and Deep Learning Approach (DLA) (Hinton et al., 2006). Both methodologies have been largely applied in different fields with enormous success: image recognition (Sun et al., 2013; Cao et al., 2013; Neto et al., 2015; Li et al., 2018), speech recognition (Deng et al., 2013), time series forecasting (Kuremoto et al., 2014), natural language processing (Zhou et al., 2013), genomics (Sha-Sha et al., 2014), neuroscience (Plis et al., 2014) and others.

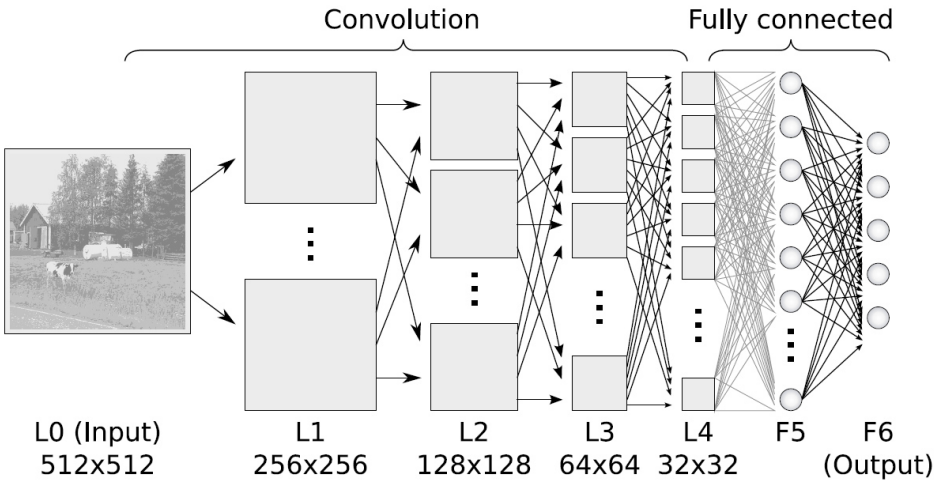

(a)

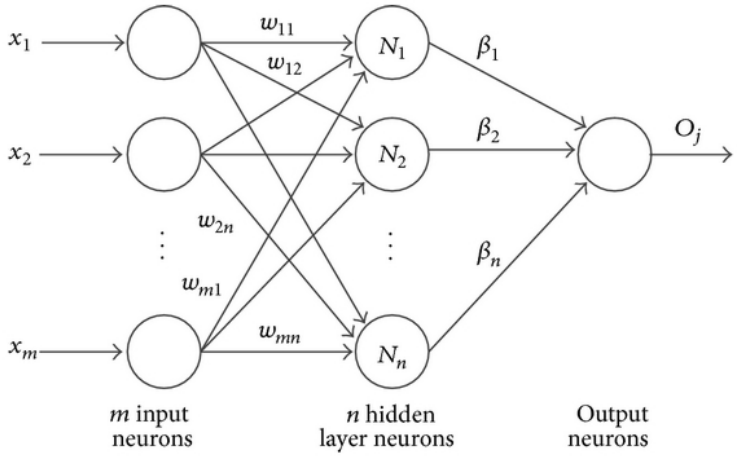

(b)

Figure 2.3: Topological differences between a DLA network (Figure 2.3a) (source: Institute for Computer Science VI, Autonomous Intelligent Systems, University of Bonn) and an ELM network (Figure 2.3b) (source: Hindawi Publishing Corporation).

The DLA (LeCun et al., 2015) is a multi-hidden layer feed-forward neural network where each layer computes a non-linear transformation of the previous one. A deep network has greater representational power than a shallow one with the same number of neurons (Le Roux and Bengio, 2008; Delalleau and Bengio, 2011). The DLA has been studied for many decades with poor results (Schmidhuber, 2015), the main problem was that an NN trained using supervised learning involves the resolution of a highly non-convex problem, with the complexity growing with the number of layers. Therefore, training with the classic gradient descent (or other methods like conjugate gradient and Quasi-Newton methods) no longer works well. A solution has been proposed by Bengio et al. (2007) applying a greedy layer-wise training where each layer is trained independently. The training for the DLA can be supervised (classification error as the objective function on each step), but more frequently is unsupervised (e..g, stacked autoencoders), with a fine-tuning phase to minimize the training set error. While the idea behind deep learning goes back to 1991, the expression DLA was coined in 2006 when the first step of unsupervised pre-training of deep feed-forward neural networks helped to accelerate supervised learning with backpropagation. The first breakthrough has been made with the introduction of Deep Belief Network (Hinton et al., 2006) composed of a stack of Restricted Boltzmann Machines (RBM) with a single layer of hidden units. Each RBM receives patterns from the previous layer and learns how to encode them in an unsupervised fashion. The results achieved on the MNIST dataset (1.2% error rate) by Hinton and Salakhutdinov (2006) helped arouse interest in the field, along with the Stacked Autoencoders (Bengio et al., 2007; Erhan et al., 2010) as another popular way of unsupervised pre-training. In the following years, the methodology rapidly expanded with the implementation of Convolutional Neural Networks (CNN) on GPUs, followed in 2007 by a mix of CNN and max-pooling layers trained with backpropagation as a winner of numerous machine learning competitions.

2.4.1 Convolutional Neural Networks

Convolutional Neural Networks are the state-of-the-art technique for image recognition, having the best results in different applications such as: control of unmanned helicopters (Kang et al., 2018), object detection (Zhao et al., 2019), x-ray cargo inspection Rogers et al. (2017), and many others. A CNN is composed of an input layer (i.e., the pixels matrix), an output layer (i.e., the class label) and multiple hidden layers. The hidden layers usually consist of convolutional layers, pooling layers, fully connected layers and a softmax output function. A convolutional layer learns a representation of the input applying 2D filters sliding on the image and capturing the information of contingent patches of pixels. The pooling layer then is used to reduce the input size, aggregating (e.g., usually using a max function) the information learned by the filters (e.g., a 3x3 pixels patch is passed in the learned filter and the 3x3 output is then pooled taking the maximum among the nine values). After a number of convolution and pooling layers, the final output is flattened into an array and passed to a fully connected neural network for classification.

2.4.2 Autoencoders

Stacked Autoencoders, also called auto-associative neural networks, are a machine learning technique trained to learn features at different level of abstraction in an unsupervised fashion. The autoencoder is composed of two parts: an encoder, which maps the input to a reduced space; and a decoder which task is to reconstruct the initial input from the lower dimensional representation. The new learned representation of the raw features can be used as input to another autoencoder (hence the name stacked). Once each layer is independently trained to learn a hierarchical representation of the input space, the whole network is fine-tuned (by performing backpropagation) in a supervised fashion to discriminate among different classes. In this thesis I use sparse autoencoders, which imposes a sparsity constraint on the hidden units, in order to learn a compact representation of the input data. The regularization parameter (ρ) is chosen to be a small value close to zero which represents the average activation

probability of each neuron. To do so we define the average activation of hidden unit j as:

$$\hat{\rho}_j = \frac{1}{m} \sum_{i=1}^{m} a_j x^{(i)} \tag{5}$$

where m is the number of training examples, a_j the activation of the hidden unit and x_i the input data, and impose the constraint $\hat{\rho}_j = \rho$.

To achieve this, an extra term is added to the optimization function that penalizes $\hat{\rho}_j$ deviating significantly from ρ.

2.4.3 Long Short Term Memory Networks

Long Short Term Memory Networks (LSTM) (Hochreiter and Schmidhuber, 1997; Gers et al., 1999) is a Recurrent Neural Network (RNN) architecture that acts as a Universal Turing Machine learner: given enough units to capture the state and a proper weighting matrix to control its evolution, the model can replicate the output of any computable function.

Because of this noticeable characteristic, LSTM is largely used in tasks of sequence processing such as those having place in natural language processing (Yao et al., 2014; Sundermeyer et al., 2015; Tran et al., 2016), speech recognition (Graves et al., 2013; Han et al., 2017; Suwajanakorn et al., 2017), automatic control (Gers et al., 2002b; Hirose and Tajima, 2017), omics sciences (Leifert et al., 2016; Lee et al., 2016), and others. The LSTM networks are gaining increasing interest and popularity in time series modelling and prediction, as they can model long and short range dependencies (Zaytar and El Amrani, 2016; Bianchi et al., 2017).

There are several variations of the original model proposed by Hochreiter and Schmidhuber (1997). Graves (2013) LSTM model is adopted in this thesis (Figure 2.4b) which is governed by the set of equations below:

$$i_t = \sigma(W_{xi}x_t + W_{li}l_{t-1} + W_{ci}c_{t-1} + b_i), \tag{6}$$

$$f_t = \sigma(W_{xf}x_t + W_{lf}l_{t-1} + W_{cf}c_{t-1} + b_f), \tag{7}$$

$$c_t = f_t c_{t-1} + i_t \tanh(W_{xc}x_t + W_{lc}l_{t-1} + b_c), \tag{8}$$

$$o_t = \sigma(W_{xo}x_t + W_{lo}l_{t-1} + W_{co}c_t + b_o), \tag{9}$$

$$l_t = o_t \tanh(c_t). \tag{10}$$

The core of the LSTM is represented by the c_t which acts as a memory accumulator of the state information at time t. The state evolves according to Eq. 8, subject to two elements: the *forget gate* and the *input gate*, represented at time t

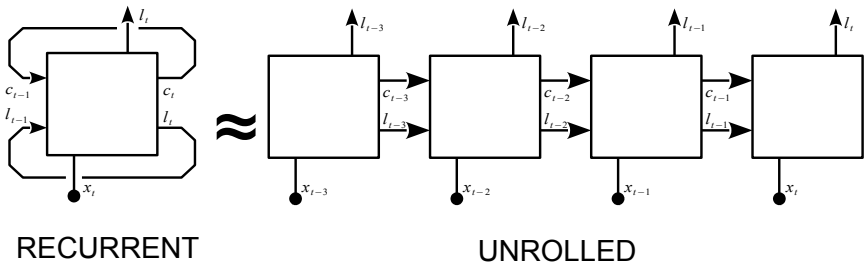

(a) unfolding of LSTM

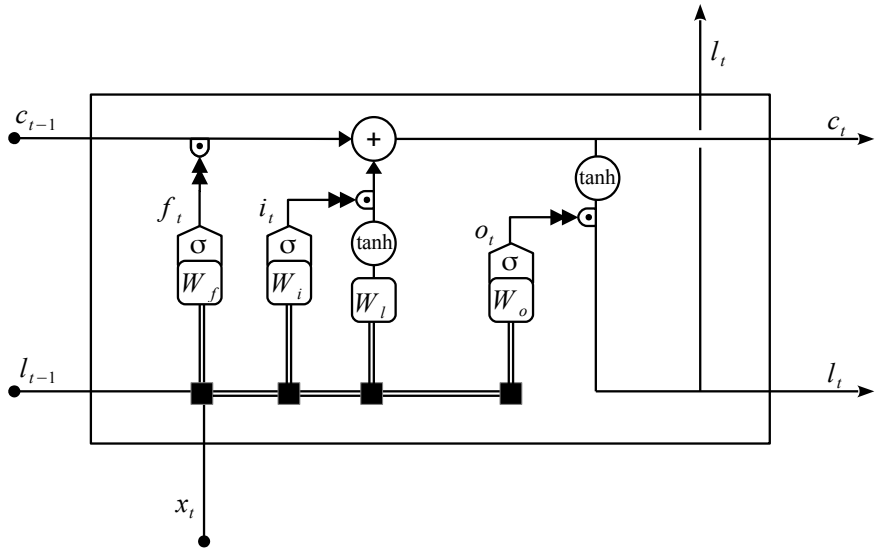

(b) LSTM cell

Figure 2.4: Graves (2013) LSTM architecture. On the left a diagram showing how the sequence is propagated through the LSTM cells, while on the right a representation of the internals of a specific cell.

by the variables f_t and i_t respectively. The role of f_t is to erase the memory c_{t-1} according to the current input x_t, the state l_{t-1} and the memory c_{t-1} (Eq. 7). The forget gate is counterbalanced by the input gate that, making use of the same information (Eq. 6) has instead the role of reinforcing or replacing memory by activating a combination x_t and l_{t-1} (Eq. 8). These last functions, as those governing the activation of f_t and i_t are learned as single-layer perceptrons using the logistic function σ (Eq. 6 and Eq. 7), or the tanh function (Eq. 8) as activation, where b_i, b_f and b_c are the respective biases. Once the memory is recomputed at time t, the LSTM emits the output o_t as a function of x_t, l_{t-1} and the memory c_t (Eq. 9). This latter function is also learned as a single-layer perceptron and finally, the LSTM computes the state l_t as given by Eq. 10. Figure 2.4a shows how a sequence is propagated through the LSTM.

The main advantage of this architecture is the of the memory c_t, refreshed under the control of gates so that the gradient is limited to the last stage (also known as constant error carousels (Gers et al., 1999; Gers and Schmidhuber, 2001)) and prevented from vanishing too quickly. This latter issue is a critical one and a well-known limitation of Recurrent Neural Networks (RNN) based on older architectures, such as the Elman's and Jordan's reference models (Pascanu et al., 2013; Jozefowicz et al., 2015).

Furthermore, LSTM learning function can be decomposed into multiple intermediate steps so that the information produced by one LSTM becomes the input to another. This kind of architecture is named stacked, and it has been applied in many real-world sequence modelling problems (Xu et al., 2015; Sutskever et al., 2014).

2.5 Evaluation Criteria

Correctly choose evaluation metrics to assess the performance of machine learning techniques is an important decision to make during the empirical design of the experimentation. Here I describe the most widely used metrics applied in literature for classification, regression and learn to rank tasks. Furthermore, I present baseline benchmarks, statistical significance tests and the use of execu-

Table 2.2: Confusion matrix for a binary problem.

		True Condition			
		Condition Positive	Condition Negative		
Predicted Condition	Predicted Condition Positive	True Positive TP	False Positive FP	Positive Predictive Value (Precision) $\frac{TP}{TP+FP}$	False Discovery Rate $\frac{FP}{TP+FP}$
	Predicted Condition Negative	False Negative FN	True Negative TN	False Omission Rate $\frac{FN}{TN+FN}$	False Omission Rate $\frac{TN}{TN+FN}$
		True Positive Rate (Sensitivity, Recall) $\frac{TP}{TP+FN}$	False Negative Rate FP / FP + TN	Accuracy (ACC) $\frac{TP+TN}{TP+FP+FN+TN}$	
		False Negative Rate $\frac{FN}{TP+FN}$	True Negative Rate (Specificity) $\frac{TN}{FP+TN}$		

tion time as metric to evaluate the performance of distributed algorithms.

2.5.1 Assessment of classification performance

Classification tasks usually aim to predict the class of each item in the dataset. Metrics are usually designed to evaluate binary or multi-class problems and should take into account class distributions (e.g., imbalanced datasets) and noisy labelling (e.g., uncertainty in the ground truth).

The most common metric to assess classification tasks is the prediction accuracy (Eq. 11).

$$\%Accuracy = \frac{\#CorrectClassifiedPattern}{\#TotalPatterns} \tag{11}$$

Although the accuracy gives a first insight into the general behaviour of a classifier, it does not provide much information about the distribution of the errors among the classes. Given a confusion matrix for a 2-class (binary) problem (Table 2.2), it is possible to build more insightful assessment metrics exploiting all the information available regarding the class error distributions.

As reviewed by Hossin and Sulaiman (2015), evaluation metrics can be divided into three types: threshold, probability, and ranking. Threshold based measures aim to minimise the number of misclassified patterns; probability based measures assess the reliability of the classifier on the estimated probabilities; and ranking based ones assess the top N classified instances.

Lavesson and Davidsson (2008) instead, categorize the measures based on their application: generalisation ability of the classifier (offline analysis); find the

best classifier among many (ranking analysis); and choose the best model to be tested on unseen data (online analysis). The focus here goes for the second application: when among many models we want to pick up the best one, particularly when there is a high discordance among multiple measures.

Here I describe some of the most widely used metrics for classification tasks which are used through the thesis.

Precision and Recall

In the probabilistic framework, the precision (Eq. 12) is the probability that a randomly selected pattern is positive, while the recall (Eq. 13) is the probability that a random positive pattern is selected. A higher score in both metrics shows that the classifier returns accurate results (high precision) as well as returning a majority of all positive results (high recall).

$$\text{Precision} = \frac{\text{TP}}{\text{TP + FP}} \tag{12}$$

$$\text{Recall} = \frac{\text{TP}}{\text{TP + FN}} \tag{13}$$

However, those measures maximised one by one will not give much information, and this is why they are usually combined in multiple ways: precision at a specified recall value (precision at a recall point); even precision and recall values (precision-recall break-even point); and average precision at evenly spaced recall thresholds (average precision).

ROC - Receiver operating characteristic

The receiver operating characteristic (ROC) is a plot of the True Positive Rate (TPR) against the False Positive Rate (TPR) (see Table 2.2 for more details) over all the thresholds. The FPR is defined as P(Pred = positive | True = positive) and is calculated as the fraction of positive samples that are correctly predicted (i.e Sensitivity). The FPR is defined as P(Pred = positive | True = negative) and is the fraction of all negatives samples predicted as positives (i.e., 1 - Specificity). The Area Under the Curve (AUC) is a summary plot of TPR and FPR across all

the threshold and is calculated as the integral of the AUC, with values between 0 (worst classifier) and 1 (best classifier); where 0.5 is considered the random classifier. The ROC measure has many positive aspects:

- each classifier is identified with one point in the bi-dimensional space;
- no assumption about the cost error (one class more important than the other);
- no assumption about the distribution of the classes (suitable for imbalanced classification).

While the ROC is usually used to assess binary problems, a multi-class extension has been introduced by Hand and Till (2001).

Both accuracy and ROC are used to assess the classification performance in Section 3.2, while precision/recall and ROC measures are analysed in Section 4.1 due to the high class imbalance.

2.5.2 Assessment of regression performance

Variety of metrics used for comparing and evaluating data imputation and predictive models can be found in the literature. Among them, the Mean Absolute Error (MAE), Mean Squared Error (MSE) and its variants as Root Mean Squared Error (RMSE) and Normalized Root Mean Squared Error (NRMSE), are the most largely used (Oba et al., 2003; Chang and Ge, 2011; Pan et al., 2011). The MSE measures the squared difference between predicted and actual values, while the two variants are also able to mitigate the magnitude problem (taking the root of the errors and normalizing them in the interval [0, 1]). The MAE (Eq. 14) is argued to be more accurate and informative than the RMSE (Eq. 15) (Willmott and Matsuura, 2005), successively refuted by (Chai and Draxler, 2014), who states that the two measures picture different aspects of the error and therefore they should both be used to assess the performance of a predictive model.

$$\mathrm{MAE} = \frac{1}{\mathrm{N}} \sum |\mathrm{predicted} - \mathrm{actual}| \tag{14}$$

$$\text{RMSE} = \sqrt{\frac{1}{N}\sum(\mathit{predicted} - \mathit{actual})^2} \tag{15}$$

The R^2 coefficient of determination (Draper and Smith, 2014) is closely related to RMSE but has an additional normalization term which maps its values into the (0, 1) interval. The R^2 (Eq. 18) can be expressed as function of the Sum of Squared Explained (Eq. 16) and Sum of Squared Total (Eq. 17):

$$\text{SSE} = \sum(\mathit{predicted} - \mathit{actual})^2 \tag{16}$$

$$\text{SST} = \sum(\mathit{predicted} - \mu(\mathit{actual}))^2 \tag{17}$$

$$R^2 = \frac{\text{SSE}}{\text{SST}} = 1 - \frac{N * \text{RMSE}^2}{\text{SST}} \tag{18}$$

with N being the number of samples.

Whigham et al. (2015) discuss the importance of comparing new techniques with baseline models (Section 2.5.4). In particular, two metrics are deemed suitable for this task: the Standard Accuracy (SA) and the Variance Relative Error (RE*).

The SA (Eq. 19) compares the prediction against the mean of a random sample taken from the training response values, while the RE* (Eq. 20) gives a score of 1 for a model predicting values with 0 variance. This metric is an appropriate baseline error measure since any model producing RE* greater than 1 would be considered weak, independently of the dataset (Whigham et al., 2015).

$$\text{SA} = \frac{\text{RMSE(predicted, actual)}}{\text{RMSE(random, actual)}} \tag{19}$$

$$\text{RE*} = \frac{\sigma^2(\mathit{predicted} - \mathit{actual})}{\sigma^2(\mathit{actual})} \tag{20}$$

The MSE is used in Section 4.2 to evaluate the models forecast accuracy; the

RMSE is used to assess the performance of imputation methods in Section 3.2 and Section 3.3; while its scale invariant version (R^2) is used in Section 3.5 due to the different magnitude in the imputed values across features. The MAE is adopted in Section 3.3 to have a better picture of the error shape, alongside the RMSE. Both SA and RE* measures are analysed in Section 3.3 to test the proposed technique against baseline models.

2.5.3 Assessment of learn to rank tasks performance

When two lists (rankings) need to be compared (e.g., in recommender systems), the use of Mean Average precision at X (MAP@X) is recommended (Chen et al., 2009).

The MAP@X measures the distance of a particular item rank from its position in the target list:

$$\text{MAP@X} = \frac{1}{N}\sum_{m=1}^{N} P(m) \quad , \tag{21}$$

where N is the number of items and $P(m)$ is the precision at cut-off X calculated as:

$$P(m) = \begin{cases} \frac{1}{|o_m - p_m|+1} & \text{if} \quad |o_m - p_m| \leqslant X \\ 0 \quad \text{otherwise} \end{cases} \quad , \tag{22}$$

with o_m and p_m as observed and predicted item ranks respectively.

The MAP@X measure is used in Section 3.4 to evaluate rankings performance.

2.5.4 Baseline sanity check

In this section I introduce some of the main baseline techniques used as benchmark against new methods. Many researchers in the machine learning community have strongly advocated comparing novel prediction systems against simpler existing alternatives (Cohen, 2013). As suggested by Whigham et al.

(2015) and Sarro and Petrozziello (2018), to be considered a baseline a method needs to satisfy ten criteria:

1. be simple to describe, implement, and interpret;
2. be deterministic in its outcomes;
3. be applicable to mixed qualitative and quantitative data;
4. offer some explanatory information regarding the prediction by representing generalised properties of the underlying data;
5. have no parameters within the modelling process that require tuning;
6. be publicly available via a reference implementation and associated environment for execution;
7. generally be more accurate than a random guess or an estimate based purely on the distribution of the response variable;
8. be robust to different data splits and validation methods;
9. do not be expensive to apply;
10. offer comparable performance to standard methods.

Baselines are useful to avoid conclusions stability (Briggs, 2008) where new models, only compared against current state-of-the-art techniques, show superior results only in a limited empirical setting (due to stochastic outcomes, parameters tuning, different implementation compared to the original one, etc). Furthermore, some of the before mentioned measures (i.e., SA, RE*) explicitly need a baseline model, or the performance of a random classifier, to be calculated.

There are many different valid baselines depending on the performed task.

For a classification problem, the following methods can be used as baseline:

- generates random predictions by respecting the training set class distribution;
- always predicts the most frequent label in the training set (useful for imbalanced datasets);
- always predicts the class that maximises the class prior;
- generates predictions from a uniform distribution;

- generates predictions based on a different distribution (e.g., gamma, exponential, log-normal, etc);

while for a regression tasks is advised to use one of the following baselines:

- always predicts the mean of the training target;
- always predicts the median of the training target;
- always predicts a given quantile of the training target;
- always predicts a constant value;
- always predicts random values;
- always predicts random values drawn from the training set.

Generally, if the performance of a new proposed technique is close to the one provided by a baseline, it is advised to revisit it before performing any comparison with the state of the art methods.

2.5.5 Statistical significance tests

In this section I describe the statistical tests used through the thesis to assess the significance of results.

The Wilcoxon test uses the rank of the data to determine if there is any difference between two samples, without making any assumption about the data distributions' nature (Dalgaard, 2008). If the p-value is greater than the significance threshold (usually being $\alpha = 0.05$), then there is no significant difference between the two samples.

The Cohen's d effect size (Eq. 23) shows how much, on average, one technique outperforms another. The measure applied to the two populations (1^{st} technique vs 2^{nd} technique) gives a response between 0 and 1 and is calculated as:

$$d = \frac{\mu^2_{group1} - \mu^2_{group2}}{\sigma_{both}} \quad \sigma_{both} = \sqrt{\frac{\sigma^2_{group1} + \sigma^2_{group2}}{2}} \quad , \tag{23}$$

where μ_{group1} and μ_{group2} are the average of the two techniques respectively, and σ_{both} is the average of their standard deviations.

Cohen et al. (2013) group the results in three categories: small with $d \in [0.2, 0.5)$;

medium $d \in [0.5, 0.8)$; and large $d \in [0.8, 1.0]$. If $d < 0.2$ the difference of the two groups is insignificant, even if the p-value shows statistical significance.

The Debold-Mariano (DM) test is used to assess models' conditional predictive ability (Diebold and Mariano, 2002). The test can be set as a one or two tails, and has three parameters: the error function $g(.)$ (i.e., absolute error or squared error), the predictive horizon (e.g., a value of 1 for one step ahead forecasts) and a significance threshold.

Given a loss function and two forecast models m_1 and m_2, the loss differential (d_t) between the two predictions is defined by

$$d_t = g(m_{1t}) - g(m_{2t}) \quad , \tag{24}$$

the DM test assumes the loss differentials to be covariate stationary, hence the expected value $\mu_d = E(d_t)$ to be constant and finite for each time point t (Diebold and Mariano, 2002).

Given the covariate stationarity of the expected value, the test hypothesis are:

$$H0 : \mu_d = 0, \quad H1 : \mu_d \neq 0 \tag{25}$$

where two models have equal accuracy if and only if d_t has zero expectation for all t.

2.5.6 Time as a performance measure

In this section are described the most used performance metrics based on execution time to compare parallel and distributed models implementation with the sequential counterparts. Kaminsky (2016) reviewed the most relevant contributions in this area (Amdahl, 1967; Gustafson, 1988) focussing on two measures: speedup and size-up. Let *N* be the size of a problem (e.g., number of samples for a machine learning task), *K* the number of processing units (e.g., processor cores for parallel applications or computing nodes for distributed ones) allotted for the task and *T(N,K)* the running time needed to complete it. T_{seq} indicates

the running time for a sequential implementation to complete the task ($K = 1$), while T_{par} the parallel or distributed version ($K > 1$). The term scaling refers to running the same task on an increasing number of processing units. There are two ways of scaling a task: strong scaling (speedup) or weak scaling (size-up). In the former, the number of processing units (K) increases while the size of the problem is fixed (N), with an expectation of $1/K$ as the amount of time needed to compute the task compared to the sequential setting. However, the gain is always suboptimal due to portions of the task not parallelisable and overheads related to communication costs and synchronization. In weak scaling, the size of the problem (N) increases with the processing units (K) and ideally the task should take the same amount of time to compute the solution for a problem with an input K times larger.

The speedup is the main metric to measure strong scaling and it is the ratio between the computational speed of the parallel or distributed version of the task and the sequential one:

$$\text{Speedup} = \frac{T_{seq}(N, 1)}{T_{par}(N, K)} \quad . \tag{26}$$

The numerator in Eq. 26 is the running time of the sequential version executed on a single core and not the parallel version executed on a single core. An ideal speedup should be equal to K, however, due to the overhead and non-parallelisable parts of the code, this value is usually smaller. The theoretical limit to the speedup is the reciprocal of the sequential part of the code, which can severely impact the performance limit. Efficiency tells how close the speedup is to the theoretical limit:

$$\text{Efficiency(N,K)} = \frac{\text{Speedup(N,K)}}{K} \quad , \tag{27}$$

where if the speedup is maximum (i.e., equal to K), then the efficiency is 1. Figure 2.5 shows a speedup analysis where a task of size N is completed in T seconds by the sequential version, while its distributed version ($K = 4$) takes T/K seconds (with a speedup = 4 and efficiency = 1). During the empirical study

of a parallel (distributed) implementation, it is appropriate to fix the size of the input (N) and to increase the number of computing units (K) to perform the speedup analysis for a given task.

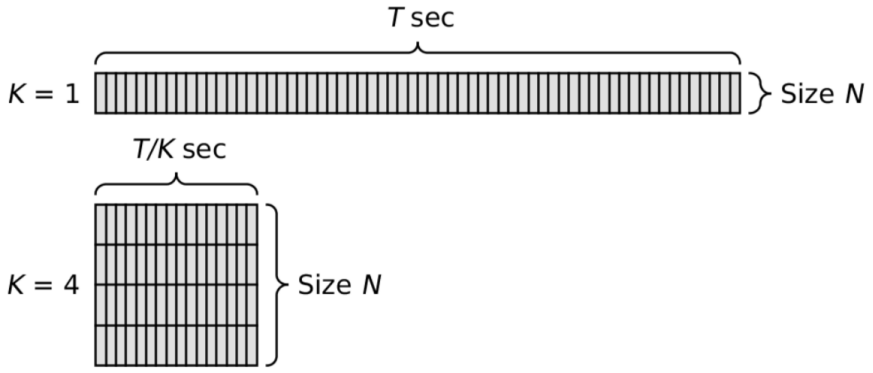

Figure 2.5: An example of speedup analysis (Source: Kaminsky (2016)).

The size-up is the main metric to measure weak scaling and is the ratio between the computational rate of the parallel or distributed version of the task and the computational rate of the sequential one:

$$\text{Size-up} = \frac{\mathrm{N(K)}}{\mathrm{N(1)}} \mathrm{x} \frac{\mathrm{T}_{seq}(\mathrm{N(1)}, 1)}{\mathrm{T}_{par}(\mathrm{N(K)}, \mathrm{K})} \quad . \tag{28}$$

As for the speedup, the numerator in Eq. 28 is the running time of the sequential version executed on a single core. If the problem size of the parallel (distributed) version is the same as the problem size of the sequential program (i.e., strong scaling, $\mathrm{N(K)} = \mathrm{N(1)} = \mathrm{N}$), then the first factor in Eq. 28 is 1, and Eq. 28 is equal to Eq. 26.

Figure 2.6 shows a size-up analysis where a task of size N is completed in T seconds by the sequential version, while its distributed version ($\mathrm{K} = 4$) and input size $\mathrm{K} * \mathrm{N}$ is also finished in T seconds (with a size-up = 4 and efficiency = 1). During a size-up analysis, the computing unit is usually fixed while the size of the input dataset is increased.

The speedup metric is considered in Section 3.5 to measure the scalability of our proposed method. The size-up has not been measured as we preferred to use the whole dataset for our experimentation while varying the number of

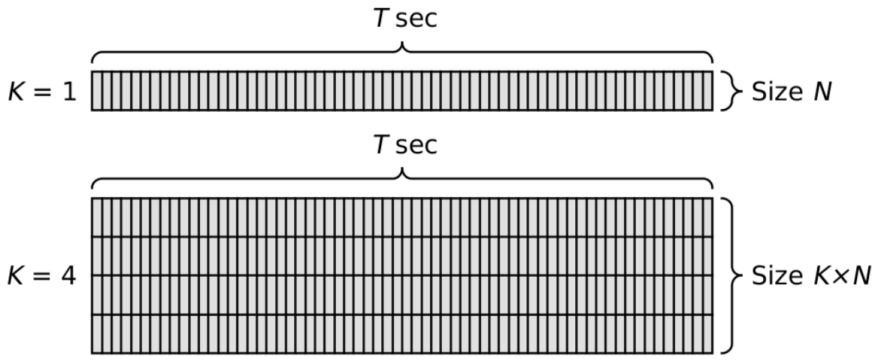

Figure 2.6: An example of size-up analysis (Source: Kaminsky (2016)).

machines.

2.6 Conclusion

This chapter laid down the necessary background needed to follow the research conducted in Chapter 3 and Chapter 4. In particular, an overview of missing data techniques used through Chapter 3 has been given; concepts of Recommender Systems used in Section 3.4 and Section 3.5 have been introduced; similarities and differences of the most widely used distributed frameworks used for processing large datasets have been highlighted (among those the Apache Spark framework used in Section 3.4 and Section 3.5); an overview on the deep neural networks covered the architectures explored in Chapter 4; finally, a list of all the evaluation criteria used in the empirical experimentation carried through the thesis has been presented.

3 Missing Data Imputation

In this chapter I tackle the missing data problem and its impact in small and big data. The literature review (Section 3.1) gives an overview of works investigating and comparing a variety of techniques, trying to find the best one for a given task (e.g., regression, classification, etc) and field of application (e.g, genetics, environment, etc). Following the literature review I focus on three gaps in missing data imputation: the "no free lunch theorem" for missing data imputation (i.e., there is no single method always able to outperform all the others); the missing data problem in Recommender Systems (also known as cold start problem); and the missing data problem at scale for big datasets.

After an initial study of missing data techniques in Section 3.2, I propose a feature based imputation technique which learns, for each in a dataset, the most suitable imputation technique (Section 3.3). Following, in Section 3.4, I investigate the impact of missing data in a real-world Recommender System ranking Online Travel Agency properties (i.e., hotels, motels, vacation rentals). Lastly, I introduce a novel imputation technique scaling to big datasets not fitting in the memory of one machine (Section 3.5).

3.1 Literature Review

A variety of imputation techniques has been used and implemented in the past years, e.g. Musil et al. (2002) compared five approaches (i.e., list-wise deletion, mean imputation, simple regression, regression with an error term, and the EM algorithm) on a relatively small dataset (450 patterns) with 20% of MAR. The mean imputation appeared the least accurate method and the EM was the most accurate, however, the authors addressed some limitations in approximating the original data for all compared methods. Shrive et al. (2006) used a survey dataset (1580 participants and 20 ranked questions) with 10% to 30% of artificial missing data to compare six imputation techniques (i.e., MI, single regression, individual mean, overall mean, participant's preceding response and random selection) under MAR and MNAR assumption. The MI achieved the best ac-

curacy for some of the experiments, followed by the individual mean. Again there was not just one imputation technique that outperforms all the others, and the authors stated that a good imputation method should balance accuracy and interpretability of the results. Chang and Ge (2011) compared ten imputation methods for handling missing value problem of micro-array data with bPCA, on the imputation of traffic flow data. The authors carried out this comparison to show that other methods (i.e., LSI gene, LSI array, LSI combined, LSI adaptive, EM gene and local least square imputation) can be more accurate than the bPCA, which is assumed to outperform most of the conventional approaches (i.e., KNNI and EM methods). The RMSE was used to compare the methods performance over datasets with 2% to 50% missingness rates. Liu and Brown (2013) used a dataset of 100 artificial patterns (50 elements with mean vector [1,0] and 50 with [-1,0]), and two small real-world datasets (i.e., Iris and Wine) to compare five iterative imputation methods (i.e., general iterative principal component imputation, singular value decomposition imputation, regularized EM with multiple ridge regression (r-EM), regularized EM with truncated total least squares, and MICE) on a multivariate analysis and classification problem. Instead of using the canonical imputation metric (e.g., MAE or RMSE) and classification accuracy, the authors introduced two new metrics, namely covariance criterion and classification criterion, which assess the change in the covariance matrix and the change in the classification error caused by the imputation. However, it is important to bear in mind that the population covariance and class assignments are usually unknown for practical, incomplete data. The authors concluded that no single imputation method emerged as the overall best in all examined cases. Judging from the obtained results from both real-world datasets, the r-EM imputation method was considered the best when the missingness rate is under 20%. For the cases with above 20%, the authors suggested careful consideration whether an imputation should be applied at all. Gómez-Carracedo et al. (2014) compared five imputation methods (i.e., list-wise deletion, unconditional mean, modified mean, principal component based imputation, EM and MI) on three air quality datasets with missingness rate between 4% and 24%. All the considered techniques performed similarly in this investi-

gation, although MI substituted values with larger variance, mostly attributed to the high rate of missingness, while the rest of the techniques estimated values with smaller variance. Schmitt et al. (2015) compared six imputation methods (i.e., mean imputation, KNNI, FKM, SVDI, bPCA and MICE) over four datasets and four performance measures (i.e., RMSE, unsupervised classification error, supervised classification error and execution time). Accordingly with Oba et al. (2003), bPCA outperformed mean imputation, KNNI, SVDI and MICE; while FKM was better than bPCA in all the metrics but the execution time, which can be considered a possible drawback in case of large datasets. All these reviewed works compared the algorithms trying to identify the one achieving the best overall accuracy for each dataset. The ensemble method (Dietterich, 2000) already showed good results when applied to other fields of machine learning, as in classification tasks (Breiman (2001)'s random forests) and in optimization problems (e.g., genetic algorithms (Wang et al., 2014; Petrozziello et al., 2017)). Similar results have been achieved when different imputation methods were ensembled to improve the estimation accuracy (Twala et al., 2006; Sorjamaa and Lendasse, 2010; Pan et al., 2011). Twala et al. (2006) used an ensemble of seven imputation algorithms (LD, EMSI, kNNSI, MMSI, EMMI, FC, and SVS) on eight small software effort estimation datasets (18 to 166 instances) with artificial MCAR and MAR. The experiment was done under a 5-fold cross validation; the ensemble was created through randomized decision trees and a training set was used to select the combination of two algorithms with the smallest error. Sorjamaa and Lendasse (2010) applied an ensemble of Self-Organized Map (SOM) weighted with nonnegative least squares algorithm to impute data on two real-world datasets, namely Corporate Finance and Climatology. The algorithm was compared with four imputation methods (Empirical Orthogonal Functions (EOF), EOF Pruning, Probabilistic PCA and single SOM). The assessment of the results was carried out comparing the MSE on the test set and the execution time. In both cases the ensemble of SOM achieved the lowest error and smaller computational time since calibration of the model through the validation phase was skipped. Pan et al. (2011) used an ensemble of six imputation methods (bPCA, Matrix CompletionMC, LLS, uKNN, wKNN, and LSimpute)

over six epistatic mini-array profiling datasets. Despite the good results, the ensemble was done via a weighted linear combination of the five methods, predetermining one of the algorithms as a reference and calculating the individual diversities of the other five algorithms.

As can be observed by the literature review, the proposed methodologies are often only tested on small datasets comprising up to a few thousands records. Furthermore, the majority of imputation techniques described in Section 2.1 only work as long as the full dataset can be stored in memory, which would constitute a problem for datasets containing hundreds of thousands of records (i.e., tall datasets), hundreds of features (i.e., wide datasets), or both. Little research has been done in the field of missing data imputation for big data. In the case where the missing rate is negligible compared to the size of the dataset, a deletion method is applicable without losing statistical strength. However, if the rate of missingness grows with the size of the dataset the imputation is necessary to preserve, or even increase, the statistical power of the data. The few advances in the field happened during the last couple of years have been possible due to the rising interest in distributed processing frameworks. Anagnostopoulos and Triantafillou (2014) use a Map-Reduce-like approach to scale the missing values imputation problem adopting the concept of signature (the record is assigned to a cluster based on its features value) and data locality (the record is allocated to the machine handling that specific cluster). Once the record has been allocated to the machine, a missing data technique can be locally used to impute its missing values. The proposed framework has been tested on two real datasets (namely D1 and D2) and one synthetic. The D1 dataset is composed of 500K samples and 90 features, while D2 has 50K records and 384 variables. The synthetic dataset has 20 features, five of which with missing values. The records for this dataset are generated on the fly and assigned to each machine to perform the imputation step. The authors show that it is possible to reduce the imputation time, and make the imputation feasible even for large datasets, distributing the computation on a cluster of machines. However, the impact on the imputation accuracy would depend on the chosen granularity (i.e., number

of machines) and the signature function (i.e., clustering technique). Singh and Toshniwal (2019) propose a data decomposition approach for RBF functions on Spark. The authors use a divide and conquer approach which split the data in small overlapping windows. Firstly the data are sorted applying an Euclidean distance on the features; secondly, for each window, an imputation model is trained; and lastly, all models are aggregated to get a global one. Although the model has been tested on eight datasets coming from the UCI repository, the biggest one utilized has less than fifty thousands records. As in the previous study, results showed that the the trade-off between accuracy, speed and feasibility is driven by the number of windows - with bigger windows yielding better generalization, while being constrained by the memory size.

3.2 Radar Signal Recognition with Missing Data

This section addresses a classification task for recognition of intercepted radar signals with high percentage of records containing missing values (Jordanov et al., 2016, 2018). The problem is to classify the signals into several functional groups by finding patterns in their pulse features (i.e., frequencies, modulation types, pulse repetition, scanning period, etc). To recover the missing data, three main approaches namely Multiple Imputation (MI), K-Nearest Neighbours Imputation (KNNI) and Bagged Tree Imputation (BTI) are investigated, tested and validated on two case studies: binary classification and multi-class classification. Three different classifiers (i.e., Random Forests (RF), Neural Networks (NN) and Support Vector Machines (SVM)) are then trained to solve the signal classification problem. Each of the approaches is tested and validated on a number of case studies and the results are evaluated and critically compared.

3.2.1 Background

Radar activity is generally grouped in two areas of application: military and civil. In the military sector, radar activity has found application in surveillance, navigation, and weapon guidance, while in the civil are, radars are widely used for traffic control, navigation, weather forecast, pollution control, space obser-

vation, and others (Richards, 2005; Jordanov and Petrov, 2016). The radar characteristics (i.e., range, resolution and sensitivity) are determined by its transmitter and waveform generator: most of the radars operate within the microwave region of the electromagnetic spectrum (with frequency ranging 200 MHz to 95 GHz), and are used for short range application with high resolution; other radars operate at a very low frequency bands and are usually preferred to cover longer distances (Richards, 2005). Radar classification and tracking of targets against a background of clutter are considered as a "general radar problem". For military purposes it includes interception, localisation, analysis and identification of radiated electromagnetic energy, also known as radar Electronic Support Measures (ESM). A real-time identification of the radar emitter associated with each intercepted pulse train is a very important function of the radar ESM. Typical approaches include sorting incoming radar pulses into individual pulse trains and comparing their characteristics with a library of parametric descriptions in order to get a list of likely radar types. This task is very difficult as there may be radar types with no records in the ESM library; overlaps of different radar parameters for the same type; increases in environment density; noise and propagation distortion that lead to incomplete or erroneous signals (Granger et al., 2001). Intercepted and collected pulse train characteristics typically include signal frequencies, type of modulation, pulse repetition intervals, etc. The collected information usually consists of a mixture of continuous, discrete and categorical data with frequent missing values (Table 3.1). Handling such high rate of missing data is a very important part of the data preprocessing before applying classification models (Saar-Tsechansky and Provost, 2007).

Table 3.1: Sample radar data. Missing values (i.e., values that could not have been intercepted or recognized) are denoted with "-". The rest of the acronyms are defined in Table 3.3.

ID	FN	RFC	RFmi	RFma	PRC	PRImi	PRIma	PDC	PDmi	PDma	ST	SPmi	SPma
84	SS	B	5300	5800	K	-	-	S	-	-	A	5.9	6.1
4354	AT	F	2700	2900	F	1351.3	1428.6 S	-	-	A	9.5	10.5	-
7488	3D	B	8800	9300	K	100	125	S	13	21	B	1.4	1.6
9632	WT	F	137	139	T	-	-	V	-	-	D	-	-
9839	3D	S	2900	3100	J	-	-	V	99	101	A	9.5	10.5

Table 3.2: Sample radar subset with imputed continuous values.

ID	FN	RFC	RFmi	RFma	PRC	PRImi	PRIma	PDC	PDmi	PDma	ST	SPmi	SPma
84	SS	B	5300	5800	K	963.2	5625	S	5.8	17	A	5.9	6.1
4354	AT	F	2700	2900	F	1351	1428	S	4	6.3	A	9.5	10.5
7488	3D	B	8800	9300	K	100	125	S	13	21	B	1.4	1.6
9632	WT	F	137	139	T	622.6	31312	V	61.1	93.1	D	12	47.8
9839	3D	S	2900	3100	J	2058	48128	V	99	101	A	9.5	10.5

3.2.2 Data pre-processing

The original dataset includes about 30000 sample of which 7693 fully intercepted and recognised radar signals that constitutes the complete subset (after applying list-wise deletion of the original dataset) (Jordanov and Petrov, 2014). As suggested in the literature, it is recommended to exclude samples containing more than 50% of missing values, for this reason, from the samples with missing data (example given in Table 3.1) I excluded those with above 60% missingness (as previously done in Jordanov and Petrov (2014)), which brought the dataset to 22000 samples and used MI, KNNI, and BTI for substituting the rest.

The data imputation with MI led to a dataset of 15656 samples - hence doubling the number of the available data (Table 3.2 shows the samples from Table 3.1 with the imputed values produced by the MI).

On the other hand, when using KNNI and BTI, all missing data were recovered, enabling us to utilise valuable information and use the statistical power of the data contained in the samples with missing values. As can be seen from Table 3.1, the first column includes the data sample identifier, the second shows the category label (the output of the classifier) and the rest of the table contains radar signal pulse train characteristics (the classifier's inputs). A more comprehensive summary of the data distribution is presented in Table 3.3, where an overview of the type, range and percentage of missing values for each parameter is given. The analysed data consists of both numerical (discrete and continuous) and categorical values, the latter of which are coded during the data pre-processing stage, converting them into numerical features. As can be seen from the table, the percentage of missingness varies from 11.2% for the radar frequency feature (RFmi) to 59.4% for the scan period characteristic (SP).

Table 3.3: Data description and percentage of missing values.
Type: I - integer; C - categorical; R - real values.

Field	Field Description	Type	Levels	% Missing
ID	Reference for the line of data	I	-	-
FN	Function performed by the radar (3D - 3D surveillance, AT - air traffic control, SS - surface search, WT - weather tracker, etc.)	C	142	1.4
RFC	Type of modulation used by the radar to change the frequency from pulse to pulse (A - agile, F - fixed, etc.)	C	12	20.7
RFmi	Min frequency used by the radar	R	-	11.2
RFma	Max frequency used by the radar	R	-	11.2
PRC	Type of modulation used by the radar to change the Pulse Repetition Interval (PRI), (F - fixed, etc.)	C	15	15
PRImi	Min PRI used by the radar	R	-	46.7
PRIma	Max PRI used by the radar	R	-	46.7
PDC	Type of modulation used by the radar to change the pulse duration (S - stable)	C	5	12.9
PDmi	Min pulse duration used by the radar	R	-	46.1
PDma	Max pulse duration used by the radar	R	-	46.1
ST	Scanning type - used method by the radar to move the antenna beam (A - circular, B - bidirectional, W - electronically scanned, etc.)	C	28	11.3
SPmi	Min scan period used by the radar	R	-	59.4
SPma	Max scan period used by the radar	R	-	59.4

Verboven et al. (2007) sequential imputation algorithm is used for MI, implemented in the *impSeq* function from the *rrcovNA* R package (its robust version *impSeqRob* was also tested; but it didn't produce better results probably due to the lack of outliers). For the KNNI, a K = 10 is used as advised by Batista and Monard (2002), while for BTI Ridgeway (2007) R *gbm* package is leveraged to implement the imputation function.

The pre-processing of the available data is of a great importance for the subsequent machine learning stage as it can affect significantly the overall success or failure of the used classification algorithm. This stage of the pre-processing aims to transform the data into a form suitable for feeding to the selected classifier, expecting to facilitate faster and more accurate machine learning training. The categorical features in the dataset are transformed into numerical ones. Three of the most broadly applied coding techniques are investigated and evaluated here: continuous; binary; and dummy variables. For the first type of coding, each category is substituted with a natural number, e.g., the 12 categories for the RFC input are encoded with 12 ordinal numbers, the 15 PRC categories - with 15 ordinal numbers, etc. A sample of a data subset coded with continuous values is given in Table 3.4. Binary coding, wherein each non-numerical value is substituted by $\log_2 N$ new binary variables (where N is the number of cate-

gories), is illustrated with 32 categories in Table 3.5. Finally, the non-numerical attributes are also coded using dummy variables (also known as one-hot encoding), where every level of a categorical variable is represented by a new unique variable. An example of one-hot encoding coding for 32 levels is shown in Table 3.6. In order to mitigate the impact of difference in magnitude of the inputs on the training algorithm, the data is scaled during the pre-processing phase. Correspondingly, each of the conducted experiments is evaluated using three forms of the input dataset: the original data (i.e., no scaling); normalized data (i.e., normalizing each feature within (0, 1) interval); and standardized data (i.e., standardizing the feature space with 0-mean and a unit variance).

For the identification and classification of the radar signals, the applied supervised learning uses from two to eleven output classes: in the first set of simulations I use 2 classes - civil and military (defined by experts in the field from a total of 125 functional categories); and in the second set of simulations, four civil and seven military classes, which gives eleven output labels to classify.

Table 3.4: Sample subset with imputed radar data and natural number coding of RFC, PRC, PDC, and ST.

ID	RFC	RFmi	RFma	PRC	PRImi	PRIma	PDC	PDmi	PDma	ST	SPmi	SPma
84	2	5300	5800	7	963.2	5625	1	5.8	17	1	5.9	6.1
4354	4	2700	2900	4	1351	1428	1	4	6.3	1	9.5	10.5
7488	2	8800	9300	7	100	125	1	13	21	2	1.4	1.6
9632	4	137	139	11	622.6	31312	2	61.1	93.1	4	12	47.8
9839	9	2900	3100	6	2058	48128	2	99	101	1	9.5	10.5

Table 3.5: Example of binary coding for 32-level categorical variable.

Label		Encoded Variables				
Index	Label	B1	B2	B3	B4	B5
1	2D	0	0	0	0	0
2	3D	0	0	0	0	1
3	AA	0	0	0	1	0
...	...	...	...	...	...	...
16	CS	0	1	1	1	1
...	...	...	...	...	...	...
32	ME	1	1	1	1	1

Table 3.6: Example of dummy coding for 32-level categorical variable.

Label		Encoded Variables								
Index	Label	D1	D2	D3	D4	D5	...	D16	...	D32
1	2D	1	0	0	0	0	...	0	...	0
2	3D	0	1	0	0	0	...	0	...	0
3	AA	0	0	1	0	0	...	0	...	0
...	...	...	...	...	...	...	...	...	...	...
16	CS	0	0	0	0	0	...	1	...	0
...	...	...	...	...	...	...	...	...	...	...
32	ME	0	0	0	0	0	...	0	...	1

3.2.3 Supervised radar classification techniques

There is a wide variety of approaches and methods used for radar emitter recognition and identification. Among those, Neural Networks, Support Vector Machine and Random Forest have been independently investigated in previous study and for this reason are here compared.

a) Neural Networks

Various approaches and methods have been investigated and used for radar emitter recognition and identification, and considerable part of this research incorporates Neural Networks (NN).

NN techniques have previously been applied to several aspects of radar ESM processing and more recently, many new radar and target recognition systems include neural networks as a key classifier (Gong et al., 2016). Examples of a variety of NN architectures and topologies used for radar identification, recognition and classification based on ESM data include popular multilayer perceptron, radial basis function (RBF) based NN, vector NN, single parameter dynamic search NN (Ibrahim et al., 2009; Ahmadlou and Adeli, 2010; Yin et al., 2011) and deep NN (Gong et al., 2016). For example, Granger et al. (2001) use initial clustering algorithm to separate pulses from different emitters according to position-specific parameters of the input pulse stream when implementing their "What-and-Where fusion strategy" and then apply fuzzy ARTMAP-NN to classify streams of pulses according to radar type, using their input parameters. They also do simulations with dataset that has missing input pattern components and missing training classes and incorporate a bank of Kalman filters

to demonstrate high level performance of their system on incomplete, overlapping and complex radar data. Ibrahim et al. (2009) investigate the potential of multilayer perceptron when used in "forward scattering radar applications" for target classification. The authors analyse collected radar signal data and extract features, which are then used to train NN for target classification. They also apply the KNN classifier to compare the results from the two approaches, concluding that the NN solution is superior. Shieh and Lin (2002) use a vector NN for emitter identification while Gong et al. (2016) used deep NN architectures for synthetic-aperture radar images recognition. In many cases the NN are hybridized with fuzzy systems, clustering algorithms, wavelet packets, Kalman filters, particle swarm optimization-based SVM, etc., which in turn leads to systems with increased accuracy (Granger et al., 2001; Shieh and Lin, 2002).

b) Support Vector Machines

Support Vector Machines (SVM) are a type of learning machines based on the statistical learning theory, that can use linear, polynomial, Gaussian, exponential and hybrid kernels for the classification. RBF networks, and even particle swarm optimisation has been used in some cases (Zhai and Jiang, 2015). SVM maximize the error margin between the classes searching for an optimal classification hyperplane in a higher dimensional space of the features. In other words if the feature space is linearly non-separable, the SVM use non-linear mapping to find a better discriminant hyperplane. The choice of a map function (kernel) is of critical importance and can substantially determine the classification results (Xin et al., 2010). One advantage of this approach is that it is possible to design and use a kernel for a specific problem that could be applied to the data without the need of a feature extraction process. The SVM have been used recently to classify radar pulse signals. For example, Eryildirim and Onaran (2011) use SVM to classify targets by using micro-Doppler features when analysing micro-motions of an object having single signature. Target recognition method based on SVM with hybrid differential evolution and self-adaptive particle swarm optimization is investigated by Zhai and Jiang (2015), reporting low error rate on the given task. Implementations of SVM exist in

almost every programming language and at least four R packages contain SVM related software (I used the R package E1071 which I found to work faster on multi-class problems (Karatzoglou et al., 2005)).

c) Random Forests

Random Forests (RF) is a powerful machine learning technique that operates by constructing a multitude of decision trees at training time and outputs the class that is the mode of the classes (classification) or mean prediction (regression) of the individual trees. Each tree is trained on a bootstrapped sample of the training data, and at each node, the algorithm only searches across a random subset of the variables to determine a split. For an input vector to be classified, it is submitted to each of the decision trees in the forest and the prediction is then formed using a majority vote. Key advantages of the RF include: their non-parametric nature; avoiding decision trees' habit of overfitting; high classification accuracy; and capability to determine variable importance (Breiman, 2001). However, as the split rules for classification are unknown, the RF can be considered to be a black box type classifier. In this implementation, I used the *randomForest* function (from the R *randomForest* package), which implements the Breiman's random forests algorithm.

3.2.4 Assessment baseline

To begin with, it is essential to determine which imputation method leads to the best substitution of the missing values. For this purpose, I designed two experiments, as described below.

a) Labels Imputation

In order to test the reliability of the investigated imputation models, 25% of the labels in the complete data subset (around 4000 samples), are randomly removed. The labels are subsequently imputed, using the three methods: MI, BTI and KNNI. Considering the random nature of the algorithms, I run the imputation 30 times for each of them. This is done for the two simulations: with 2 classes and with 11 classes. In the 2-class imputation case, the KNNI

method achieved the best performance with a 90% accuracy, followed by BTI with 84% and MI with 65% (Figure 3.1).

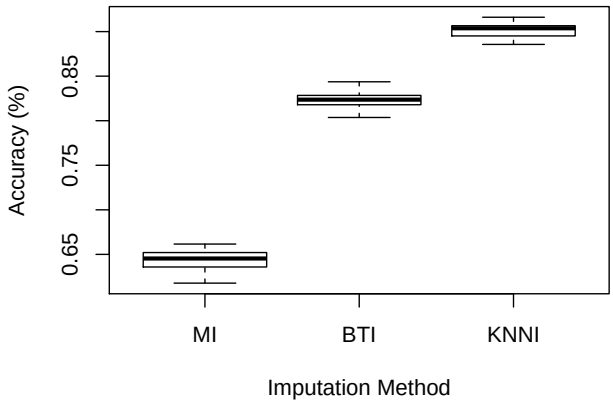

Figure 3.1: Label imputation for MI, BTI and KNNI over 30 runs for 2 classes. Each boxplot displays the minimum and maximum values (whiskers), the first and the third quartile (boundaries of the box represent 50% of the data), and the median (the thick line).

The KNNI achieved the best accuracy most likely due to the skewed nature of the data: in fact, 75% of the data belongs to the second class, this way, the unbalanced dataset helps the search of nearest neighbours to go towards the class with more samples. On the contrary, the MI and BTI methods assume balanced label distribution, which leads to limited accuracy of their imputation. In the 11-class case (Figure 3.2), the effect is even more evident, as the samples are not equally distributed among the classes, leading to a low accuracy for MI and BTI and a high variance for KNNI due to the randomness of the labels removed in each of the 30 runs.

b) Continuous features imputation

The second experiment aims to validate the algorithms' accuracy in presence of continuous features. Eight features from the complete subset (RFmi, RFma, PRImi, PRIma, PDmi, PDma, SPmi, SPma) are considered in this setup. As in the previous experiment, 25% of the data is removed for each feature and subsequently imputed. The RMSE between the imputed values and the real ones is selected to measure the methods' performance. The experiment is iterated

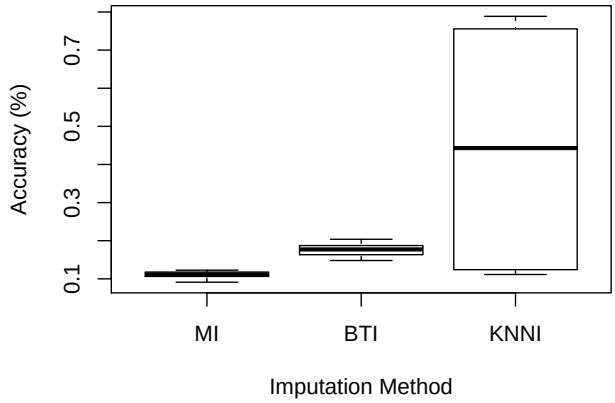

Figure 3.2: Label imputation for MI, BTI and KNNI over 30 runs for 11 classes. Each boxplot displays the minimum and maximum values (whiskers), the first and the third quartile (boundaries of the box represent 50% of the data), and the median (the thick line).

30 times and the Wilcoxon test for statistical significance (with $\alpha < 0.05$) along with the relative Cohen's d effect size, are calculated.

The considered imputation algorithms are also tested against the median imputation as a comparison baseline. As expected (Figure 3.3), all other algorithms outperformed the median imputation, producing smaller errors. In 23 out of 25 cases BTI is significantly better than MI and KNNI and with effect size d=1. The comparison between BTI and KNNI on PRImi and PRIma, despite a p-value < 0.025, showed slightly lower effect size, d=0.83 and d=0.78 respectively. Analysing the results for the two features led to the conclusion that the KNNI is again strongly affected by the data distribution, which is highly positively skewed for PRImi and PRIma (Figure 3.4). Figure 3.4 shows the normalized density function for four features, from which PRImi and PDmi have high positive skewness, concentrated in the first quartile. It seems, as for the label imputation, that a highly imbalanced distribution can affect the imputation process, explaining why each imputation method produces different accuracy for the features given in Figure 3.3 (although, BTI is the overall winner). The results for the Wilcoxon test subjected to the Benjamini-Hochberg and Bonferroni corrections (Dalgaard, 2008) for multiple statistical test are still significant

($\alpha = 0.05$).

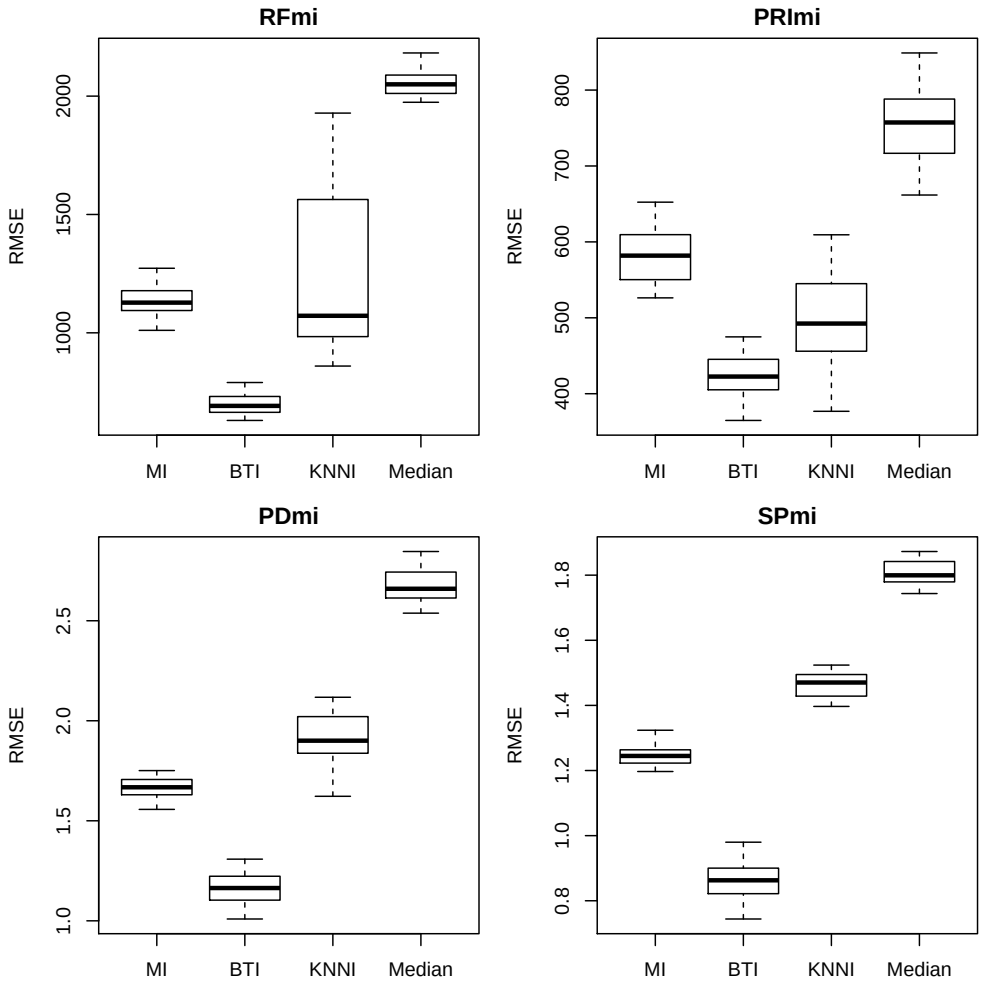

Figure 3.3: Root mean square error (RMSE) for the imputation of the continuous values (30 runs). Low median values represent preferable imputation methods. Non-overlapped boxplots indicate statistical difference between the algorithms. For a better visualisation, the features RFma, PRIma, PDma and SPma have been omitted due to the similar distribution and high correlation with the respective minimum.

3.2.5 Classification results

Two main experiments are conducted for investigating the efficiency of each classifier when solving the radar emitter recognition problem. The dataset is split into two subsets before the imputation: one for training (75% of the whole data) and second one for testing (25% of the whole data). The investigated neural network topologies include one hidden layer with fully connected neurons in the adjacent layers and batch-mode training is performed. For a given exper-

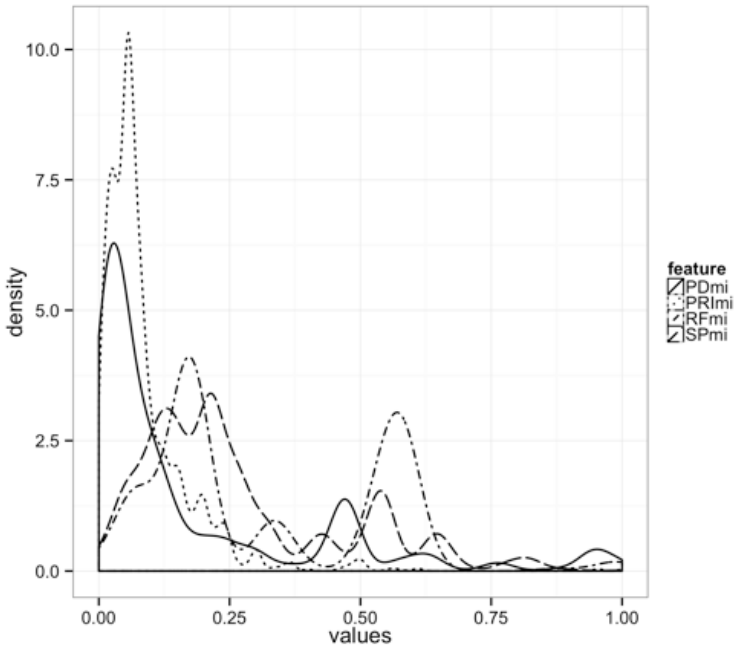

Figure 3.4: Density function for the features: RFmi, PRImi, PDmi, SPmi on the dataset without missing value. Each feature is normalized within (0, 1) interval. The distribution of PRImi and PDmi shows highly positive skewness. For a better visualisation, the features RFma, PRIma, PDma and SPma are omitted due to the similar distribution and high correlation with the respective minima.

iment with P learning samples, the error function is given by:

$$E_p = \frac{1}{2} \sum_{p=1}^{P} \sum_{i=i}^{L} (x_i^p - t_i^p)^2 \quad , \tag{29}$$

where for each sample $p = 1, ..., P$ and each neuron of the output layer $i = 1, ..., L$; a pair (x_i, t_i) of NN output and the target values is defined respectively. NN learning with Levenberg-Marquardt algorithm is then used and the training set is further divided into 80% for the training and 20% for the validation. The MSE is used for evaluating the NN learning performance. The stopping criterion is set to 500 training epochs, or gradient reaching value less than 1.0e-06, or 6 consequent failed validation checks, whichever occurs first. For the RF, the limit for the number of trees is set to 500 and the output class is decided by a vote among them. The SVM are provided with a radial basis kernel (other kernels were tried as well but led to worse results) and the algorithm hyper-parameters are optimised through the *tune.svm* function included in the

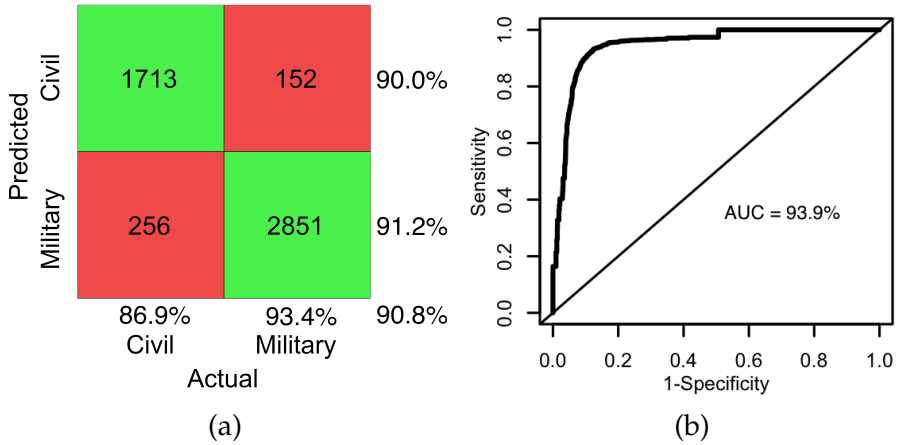

(a) (b)

Figure 3.5: Figure 3.5a Confusion matrix illustrating the RF classification results for the two classes, after using BTI with continuous value coding (Military and Civil). Figure 3.5b ROC Curve for the same simulation.

package, which increased the classifier accuracy with up to 4%.

For the first experiment, the NN topology is N-N-2, where N is the number of inputs and the output contains 2 binary neurons coded as: *10* for class *Civil*; and *01* for class *Military*. For the second experiment, the same topology is used with 11 output neurons (representing 4 civil and 7 military classes). After coding the categorical variables with the three methods described above, the accuracy of each classifier is investigated, evaluated and compared before and after the data normalisation and standardisation.

Sample confusion matrices are shown for the best accuracy achieved in the experiments for the 2 and 11 classes, after training with continuous input data. The RF demonstrates high accuracy, as can be seen from Figure 3.5a and Figure 3.6, showing the number of correct responses in the green squares and the number of incorrect responses in the red squares. The bottom right percentage illustrates the overall classifier accuracy (OCA) described in Eq. 11. Furthermore, it can be observed from Figure 3.6 that the number of hits, as well as the accuracy of the RF classifier, compared to the previous work (Jordanov and Petrov, 2014), has increased. Another important achievement is also illustrated in these figures: the class accuracy variance of the classification is now within the 34.8% to 90.8% interval; while in (Jordanov and Petrov, 2014) it was between 22.6% and 87.4%. This may be attributed to the higher number of available

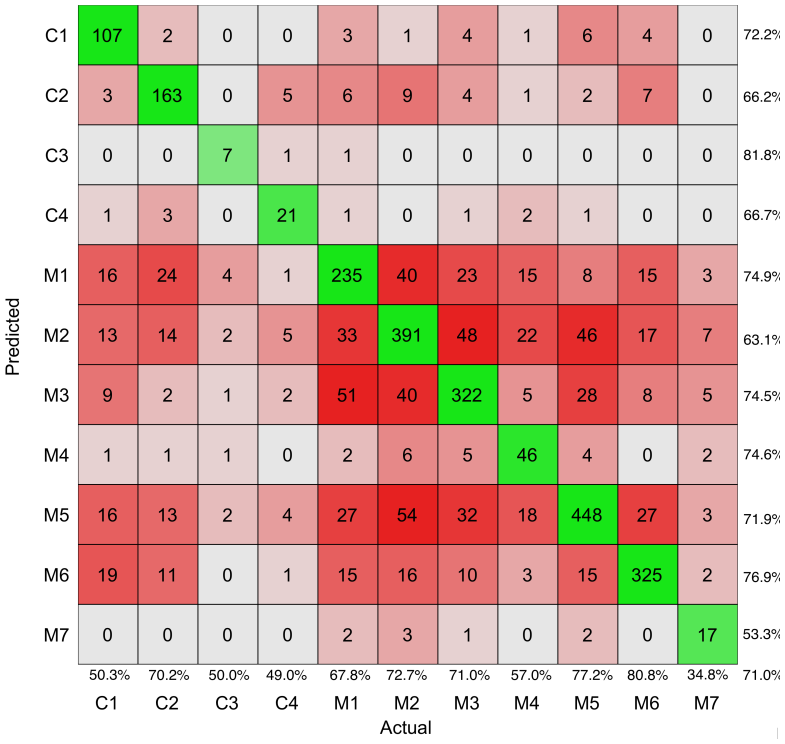

Figure 3.6: Confusion matrix illustrating the RF classification results for the 11 classes, after using BTI with continuous value coding. The batch includes 7 military (M1 - Multi-function, M2 - Battlefield, M3 - Aircraft, M4 - Search, M5 - Air Defence, M6 - Weapon and M7 - Info) and 4 civil classes (C1 - Maritime, C2 - Airborne Navigation, C3 - Meteorological, C4 - Air Traffic Control).

training and testing samples as a result of the BTI imputation, which increased the used dataset statistical power and improved the classification performance of the RF. The results shown in Figure 3.7 and Figure 3.8, illustrate moderate impact of the categorical coding on the classification. The continuous coding appears to be more efficient (1% better for the 2-class case, and 5% for the 11-class one). For the 2 classes, the best result (90.80%) is obtained when combining the RF classifier with the BTI and continuous values, and for the 11 classes, the same combination achieved again the best accuracy of 71.0% (Figure 3.6).

In Figure 3.7 and Figure 3.8, the SVM columns (the last three columns) have the same results for the scaled and standardized data, since the algorithm performs internally the two operations before the classification. In 98 out of 108 comparisons, BTI has demonstrated the best accuracy for all classifiers, while the KNNI achieved best results in 8 cases and MI in 2 comparisons only. Taking a closer look at the confusion matrix given in Figure 3.6, it can be seen that the num-

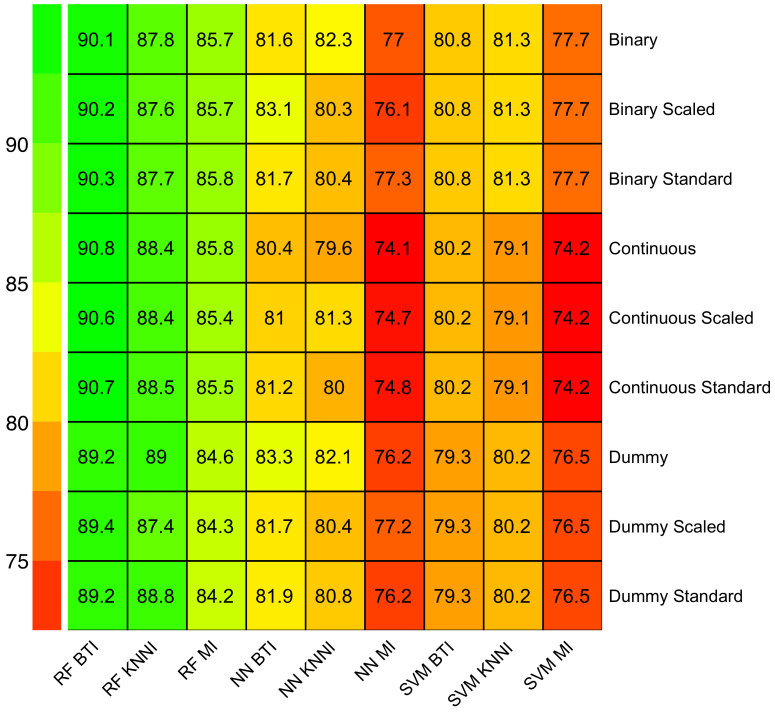

Figure 3.7: Classification performance results of the classifiers (RF, NN and SVM) in the case of 2 classes after using three different imputation techniques (BTI, KNNI and MI), for the three different groups of coding (binary, continuous and dummy). The colour scale to the left shows the achieved accuracy percentile.

ber of misclassified samples within the classes of the same family (e.g., civil) is higher than the number of misclassified samples as belonging to the other family classes (e.g., military). For example, if we take a look at M1 class (5th row in Figure 3.8), 24 samples of M1 class are wrongly classified as belonging to civil classes (C1 to C4), while 63 samples are mislabelled as of the other military classes (M2 to M7). It is even more evident from the last row (M7 class), for which all misclassified samples (seven) belong to the military family. Since it is not possible to give a cost for the misclassification of each class, a ROC curve analysis for multiclass problems is used to assess the classifiers accuracy under different conditions. Let's call a superclass the union of all classes belonging to the same general type or family (civil or military) for the 11-class problem: C = ∪(C1,..., C4); and M = ∪(M1,..., M7). I also define two types of misclassification errors: outer error (OE) and inner error (IE).

In the 11-class case, the OE occurs when: one of the civil samples belonging

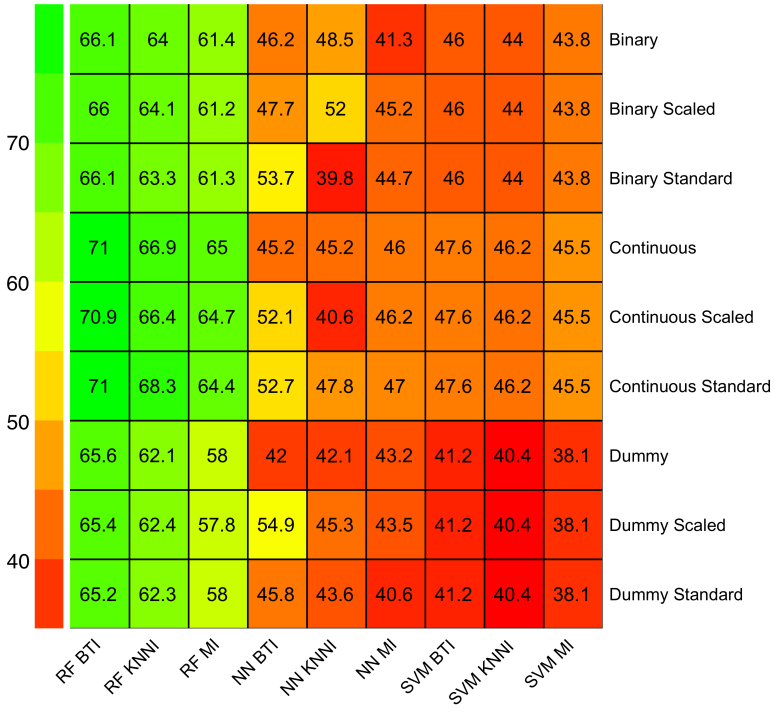

Figure 3.8: Classification performance results of the classifiers (RF, NN and SVM) in the case of 11 classes after using three different imputation techniques (BTI, KNNI and MI), for the three different groups of coding (binary, continuous and dummy). The colour scale to the left shows the achieved accuracy percentile.

to a C_i, i = 1,..., 4, class is misclassified as belonging to a military one M_j, j = 1,...,7; or when a military sample is mislabelled as a civil one. An IE occurs when a civil sample is misclassified as belonging to another civil class or when a military pattern is mislabelled with a different military label. Let's now denote the inner accuracy (IA) as the accuracy obtained calculating the ROC curve for a multi-class problem, as proposed by Hand and Till (2001), when applied only on classes belonging to the same superclass. In (Hand and Till, 2001), the area under the curve (AUC) is obtained by averaging the AUC of all considered pairwise classes. This approach measures how well each class is separated from the others, emphasising that certain pairs of classes can be well separated, even when the superclasses cannot be well separated.

Labelling the civil classes C_1, ..., C_k, (k = 4), I estimate the probability of each test sample x belonging to any class C_i as: $p(C_i|x)$, for i = 1, ..., k. For any pair of classes (C_i, C_j), it is possible to compute measure A using $p(C_i|x)$ or $p(C_j|x)$,

hence, $A(C_i|C_j)$ is the probability of a randomly selected member of class C_i to have lower estimated probability of belonging to class C_j, than a randomly selected member of class C_j. Because for a 2-class problem (class 0 and class 1): A(0|1) = A(1|0); and for a multi-class problem $A(C_i|C_j) \neq A(C_j|C_i)$, I use the average $A(C_i, C_j) = (A(C_i|C_j) + A(C_j|C_i))/2$, adopted as measure of separability between C_i and C_j. The overall performance of the classification in separating *k* classes is then the average of this measure over all class pairs:

$$IA = \frac{2}{k(k-1)}\left(\sum_{i<j} A(C_i, C_j) + \sum_{i<j} A(M_i, M_j)\right) \quad . \tag{30}$$

The difference 1 - IA represents on average, the percentage of wrongly labelled patterns in the same superclass. On the other hand, the outer accuracy (OA) is calculated applying the average AUC to all the pairs (C_i, M_j)

$$OA = \frac{\sum A(C_i, M_j)}{kn} \quad , \tag{31}$$

where $i = 1, ..., k$, $j = 1, ..., n$, and *k* and *n* are the number of civil and military classes respectively. Again, the difference 1 - OA represents the percentage of patterns, misclassified as belonging to the other superclass.

Results for IA, OA and OCA are given in Table 3.7, where in the first six rows the best OA and OCA accuracies for the RF, NN and SVM classifiers are shown (which performance is illustrated with Figure 3.8). The last two rows display the results for NN (with MI and continuous coding) and SVM (with BTI, binary coding and standardisation). The IA and OA can help to better understand the underlying distribution of the misclassified samples among the classes. Looking at the results in Figure 3.8, it is evident that for some of them, it is difficult to choose the best classifier due to the similar OCA values. In such cases the OA can provide insightful information and help identify the best one. For example, the OCA is identical (46%) for the NN (with MI and continuous coding) and SVM (with BTI, binary coding and standardization) classifiers. Nevertheless, looking at the OA column in Table 3.7 (last 2 cells), one can see that the

NN classifier has 11.1% better accuracy than the SVM one. In theory, it may be speculated that the probability of having a misclassified sample within the same superclass is higher (since they are coming from the same family of radar signals), than the probability of class being misclassified as belonging to the other superclass. Considering the values given in Table 3.7, it can be seen that the IA is generally lower than the OA, which is in agreement with the above presumption. Moreover, the RF, NN and SVM classifiers producing the best OCA (71%, 54.9%, and 47.6%: rows 2, 4, and 6, respectively) are not the best ones when OA is used as a metric (then their OCA are 68.3%, 52.7%, and 46.2%: rows 3, 5, and 7, respectively). This enforces the point that a second metric should be used when assessing classifiers performance.

Table 3.7: Classifiers Inner Accuracy (IA) and Outer Accuracy (OA) compared to the best Overall Classifier Accuracy (OCA) in the 11 class classification for RF, NN and SVM; best OA for RF, NN, SVM; and results for two classifiers with same OCA but different OA.

Classifier	IA	OA	OCA
RF BTI continuous (RFbest OCA)	87.1	88.7	71.0
RF KNNI continuous standardised (RFbest OA)	89.1	90.6	68.3
NN BTI dummy scaled (NNbest OCA)	74.1	74.2	54.9
NN BTI continuous scaled (NNbest OA)	81.0	84.3	52.7
SVM BTI continuous (SVMbest OCA)	64.8	67.7	47.6
SVM KNNI continuous scaled (SVMbest OA)	62.9	69.0	46.2
NN MI continuous	75.6	78.8	46.0
SVM BTI binary standardised	64.9	67.7	46.0

For example, the RF classifiers with highest OCA and OA are shown in the first 2 rows of Table 3.7. In the first (RFbest OCA) case (1st row), 29% of the patterns are misclassified (1450 of 5000) and 11.3% of them are assigned to the wrong superclass (164 patterns). In the second (RFbest OA) case (2nd row), 31.7% of the samples (1680 of 5000) are wrongly labelled and 9.4% of them (158) are assigned to the wrong superclass. As for the NN classifiers (3rd an 4th rows), the difference in the OCA is very small (2.2%), with 2255 and 2365 misclassified samples respectively, while the relative OA difference is substantial - 10.1%, with 582 and 371 misclassified patterns respectively. Similar results can be observed for the SVM classifier as well (6th and 7th rows). As discussed, the use of OA provides extra insight of the classifiers' performance, giving additional metric for

choosing the best classification model (considering the trade-off between OCA and OA).

3.2.6 Discussion

The above results showed that the performance of the used classifiers for recognition and identification of radar sources, based on datasets of radar signal characteristics depends a lot on the quality of the available data and dealing with the missingness in the datasets can improve the classifier overall accuracy. The implementation of imputation models tripled the number of complete records, which in turn led to improved performance of the classifiers. The BTI had best accuracy for all supervised classifiers (especially in the 11-class case). In the 2-class case, the best performance was achieved by the RF after BTI imputation and continuous coding (90.8%), followed by the NN (83.3%) and SVM (81.3%). In the 11-class, I use the ROC curve analysis for a multi-class problem, and obtain the area under the curve (AUC) by averaging the AUC of all considered pairwise classes. This approach showed that some pairs of classes can be well separated, even when the superclasses are not well separated. I also showed how the two new introduced metrics: inner (super) class error IE (Eq. 30); and the outer class error OE (Eq. 31), can be used to complement the OCA metric when choosing the best classifier. Especially in cases when the OCA has similar values for the classifiers, the OA should be used as an additional criterion for the choice of the most efficient and accurate method for the classification. This investigation found that the IE is usually smaller than the OE, which is in agreement with the presumption that it is more likely a class to be misclassified for another one from the same superclass (as being from the same family), than to be misclassified as belonging to the other superclass. Future work may include identification of more than two superclasses by implementing unsupervised learning and then using supervised one for assessing IE and OE metrics.

3.3 Scattered Feature Guided Data Imputation

All the imputation techniques described in the background section (Section 2.1) would select a single method that outperforms the others, based on a given metric. However, while a given approach might have a good performance across the whole dataset, it does not mean that its performance would be superior at the level of each individual feature. Here I propose an aggregation model of the most suitable methods from a multitude of imputation techniques, based on their performance for each individual feature of the dataset. Instead of selecting a single method which outperforms the others as a whole, a feature (column-wise) selection is used to choose the best imputation method for each individual attribute of the dataset. The proposed method, namely Scattered Feature Guided Data Imputation (sFGDI) is compared with two baseline techniques (random guessing and median imputation) and four state-of-the-art methods (MICE, BTI, KNNI, and bPCA). It is also extensively tested and validated on 13 publicly available datasets, with a large degree of diversity (size and number of attributes). The proposed method performance is assessed and compared with the other techniques using a Wilcoxon Signed-rank test for statistical significance.

3.3.1 Proposed method

The sFGDI is composed of two phases: a learning phase and an imputation phase.

During the learning phase, the algorithm is trained on artificially introduced missing data, and then, the combination of methods that performed best, is used to impute the missing values in the initial dataset. The complete subset (without missingness) is used for training the model, introducing a percentage of MCAR, MAR or MNAR (e.g., 25%) for each feature. Once the data are imputed with each technique, an error function (e.g., RMSE) is used to select the best imputation method for every feature of the dataset. To cope with the random nature of the algorithm and to ensure more robust choice, this process

is iterated given number of times, and the algorithm with the lowest median overall error for each feature is then chosen. For example, let's assume a set of m imputation methods ($M_1, ..., M_m \in S$) and dataset (X) composed of v variables and n samples, where k of them ($0 < k < n$) contain at least one missing value. Once the $n - k$ complete samples (X' subset) are separated from those with missing values, a percentage of missingness is introduced to each variable of X' (e.g., 25%). The missing data in X' are separately imputed using all methods of S, and the estimation error is calculated for each feature. This process is repeated I times (e.g., $I = 5$), and for every variable in X', the imputation algorithm scoring the lowest median error is selected (E). The selected techniques are then used to estimate the missing values of the whole set X. In particular, $\forall M_i \in E$, $i = 1, .., m$, the dataset X is entirely imputed, and only the imputed values for the features where M_i scored the lowest error are saved, discarding the others. Since X is imputed independently with each technique, the order of imputation is irrelevant, enabling the process to be parallelised. An example of how the techniques are selected is given in Table 3.8, while the pseudo-code for the sFGDI method is given in Algorithm 1.

Algorithm 1 The sFGDI algorithm.

procedure sFGDI
    Inputs: dataset (X), # of iterations (I)
    for $i = 1$ to I, i++ **do**:
        Add 25% MCAR, MAR or MNAR to each attribute of X';
        Impute the missing values in X' using each method (MICE, BTI, KNNI, bPCA, and Median);
        Calculate the methods errors (e.g., MSE, RMSE, EuclideanDistance, LogMSE) for each feature;
    for each feature **do**:
        Select the best imputation method using the median error over the I iterations;
    for each method which scored the best error for at least one feature: **do**:
        Impute all the missing values in X;
        Keep the imputed values in the features where the method produced the best error;
        Discard all the other values;
        Replace the missing data in X, with the values estimated by each algorithm

Table 3.8: Columns represent different imputation techniques, and each row is a run of imputation on the complete subset filled with MCAR, and the values in (*,*,*) are the RMSE for the three variables. The last row is the median error over all runs with the lowest errors are given in bold. In this case, the combination BTI, KNNI, bPCA is used to impute the missing data. All the missing values in the dataset are imputed independently with the three techniques, then, for the data imputed by BTI, only those belonging to the first feature are considered, and the rest discarded. The same is done for the second feature with KNNI and the third one with bPCA.

Run #	KNNI	BTI	MICE	bPCA	Median
1	(0.7, 0.2, 0.5)	(0.2, 0.2, 0.7)	(0.5, 0.6, 0.4)	(0.4, 0.4, 0.1)	(0.9, 0.7, 0.8)
2	(0.8, 0.3, 0.4)	(0.1, 0.4, 0.5)	(0.5, 0.4, 0.6)	(0.5, 0.4, 0.2)	(0.6, 0.5, 0.7)
3	(0.8, 0.3, 0.2)	(0.3, 0.5, 0.5)	(0.6, 0.6, 0.6)	(0.5, 0.4, 0.2)	(0.9, 0.6, 0.6)
Median Error	(0.8, **0.3**, 0.4)	(**0.2**, 0.4, 0.5)	(0.5, 0.6, 0.6)	(0.5, 0.4, **0.2**)	(0.9, 0.6, 0.7)

3.3.2 Empirical study design

The proposed method (sFGDI) is compared with known univariate baselines and multivariate state-of-the-art imputation methods (i.e., KNNI, BTI, MICE and bPCA) to assess its performance on the missing data imputation task. The experiments are carried for all of the three missing data mechanisms: MCAR, MAR and MNAR. In addition, to evaluate its sensitivity to various missing rates and training set sizes, the sFGDI is tested in four different settings (combining 25% and 50% MCAR with 5-fold and 30-fold cross validation). Lastly, a run time analysis is carried to observe the computational cost needed during the training and imputation phases. The results are reported in Section 3.3.3.

Thirteen publicly available datasets from UCI and KEEL repositories (Alcalá et al., 2010; Asuncion and Newman, 2007) are used in this work, namely Contraceptive, Yeast, Red wine, Car, Titanic, Abalone, White Wine, Page Block, Ring, Two Norm, Pen Based, Nursery, and Magic04. The selection of these datasets from the repositories classification area was driven by the intent to cover different application domains and data characteristics. In particular, the datasets differ in the number of instances (from several hundreds to several thousands), the number of features (3 to 20), and range and type of the features (discrete, continuous and categorical). The used datasets do not have missing values by default, guaranteeing total control over the experiments and the assessment

and evaluation of the results. Table 3.9 provides descriptive statistics for each dataset and more details about the features can be found in (Alcalá et al., 2010; Asuncion and Newman, 2007).

Table 3.9: Datasets used in the empirical study. The last three columns show the number and type of attributes (R - Real, I - Integer, C - Categorical).

Dataset	#Instances	R	I	C
Contraceptive	1474	0	9	0
Yeast	1484	8	0	0
RedWine	1599	11	0	0
Car	1728	0	0	6
Titanic	2201	3	0	0
Abalone	4174	7	0	1
WhiteWine	4898	11	0	0
PageBlock	5472	4	6	0
Ring	7400	20	0	0
TwoNorm	7400	20	0	0
PenBased	10992	0	16	0
Nursery	12960	0	0	8
Magic04	19020	10	0	0

As described in Section 2.5, MAE and RMSE are used here to assess the performance of the proposed method, while SA and RE* are adopted to compare the sFGDI with the imputation baselines.

To validate the proposed method, a k-fold cross validation is applied, splitting the dataset into independent training and test sets. The test set is generated using a uniform sampling without repetitions, and the rest of the data is left for training. Since the Shapiro Test showed that many of the patterns came from non-normally distributed populations, the statistical Wilcoxon Signed Rank Test was also used to prove which method is giving better performance. In this work, the following NULL hypothesis is tested: "Given a pair of models (M_i, M_j) with $i, j \in \{1, .., n\}, i \neq j$, the RMSEs (MAEs) obtained by model M_i are significantly smaller than the errors produced by model M_j", using confidence level $\alpha = 0.05$.

As reported in the literature review, it is not common in the missing data imputation literature to address and compare the performance of a newly proposed technique under all the missing mechanisms assumptions. Here I report the

process of missing data generation used in the empirical evaluation of sFGDI.

In the case of Missing Completely at Random (MCAR), the probability of the data being missing is unrelated to any other variable in the dataset at hand (e.g., the subject income is missing in a survey because he/she left before completing all the questions). In order to simulate this mechanism, for each feature value point in the dataset, a number is drawn from a uniform distribution in the $(0, 1)$ interval. If this number is smaller than assumed missing data threshold (e.g., 0.25), the feature value is set as missing in the original dataset. The Missing at Random (MAR) case represents missingness correlated to other factors contained in the dataset (e.g., the elder participants in a survey may be less willing to report their income). To simulate the MAR mechanism, a variance-covariance matrix is built for the considered dataset. For each variable, the probability of missingness is governed by the most correlated feature in the matrix (i.e., with the increase of the correlated feature values, the probability of missingness also increases). The Missing Not at Random (MNAR) mechanism happens when the probability of a value being missing is directly correlated to the feature itself (e.g., subjects with a very high income may be more reluctant to disclose it). To generate missing values for the MNAR mechanism, I draw values from a uniform distribution in the $(0, 1)$ interval, and sort them in decreasing order. I do the same for the variable values and pair them with the sorted random numbers (used as thresholds). For each threshold, I draw a new random number in $(0, 1)$ interval and if it is smaller than the threshold, I erase the feature value (this way the pairs with higher random numbers are more likely to be set as missing).

3.3.3 Results

All three mechanisms of missing data (i.e., MCAR, MAR, and MNAR) are considered in this study and the performance of the proposal compared to the state-of-the-art techniques. To calibrate the model during the training phase, 25% of missing data is added to each attribute of the training set, subsequently imputed using the five imputation techniques and the accuracy is evaluated us-

Table 3.10: Hyper-parameters setting.

Method	Hyper-parameters
KNNI	K = 10, Distance = Euclidean
BTI	#Trees = 200
MICE	#Iterations = 10
bPCA	Method = Bayesian, Nboot = 5, Lstart = 1000, L = 100
sFGDI	#Iteration of training set = 5, Error function = RMSE

ing both MAE and RMSE. This process is run 5 times and for each attribute, the imputation model achieving the lowest median error (preferred to the mean due to robustness to outliers) is selected. Lastly, the selected techniques are used to impute the data on the independent test set and the results are compared to all the other methods. Table 3.10 shows the hyper-parameters used for each algorithm in this study.

Table 3.11: Standardized Accuracy (SA) values achieved by sFGDI, the baseline (median imputation) and state-of-the-art (KNNI, BTI, MICE, and bPCA) techniques over the 13 datasets for 5-fold cross validation with 25% MCAR. Higher values represent better estimation over the random guess.

Dataset	sFGDI	KNNI	BTI	MICE	bPCA	Median
Contraceptive	**0.39**	0.24	0.36	0.18	0.38	0.26
Yeast	**0.33**	0.24	0.32	0.06	**0.33**	0.28
Red Wine	**0.37**	0.33	0.33	0.23	0.32	0.30
Car	**0.29**	0.12	**0.29**	-0.01	**0.29**	0.25
Titanic	**0.35**	0.26	0.34	0.05	0.34	0.28
Abalone	0.68	0.62	0.57	0.66	**0.72**	0.28
White Wine	**0.36**	0.34	0.34	0.16	0.34	0.28
Page Block	**0.49**	0.41	0.43	0.39	0.46	0.25
Ring	**0.31**	0.24	0.29	-0.02	0.29	0.28
Two Norm	**0.34**	0.24	0.32	0.07	**0.34**	0.30
Pen Based	0.54	**0.56**	0.49	0.47	0.45	0.27
Nursery	**0.30**	0.09	0.25	0.00	0.29	0.23
Magic04	**0.47**	0.42	0.41	0.32	0.45	0.28

The first set of experiments is performed imputing the missing data under the MCAR mechanism. As the MCAR is unrelated to any other variable in the dataset, it is simulated using a Bernoulli random variable, removing values with 25% chance of success. Figure 3.9 shows the mean cumulative RMSE for the four state-of-the-art methods over the Red Wine dataset (the other datasets can be found in the appendix). The segments in each bar represent the relative error expressed in percentages (if the errors were the same for each imputation method, each segment would occupy 25% of the bar). The methods are ordered from the smallest error (bottom of the bar) to the largest (top). As can

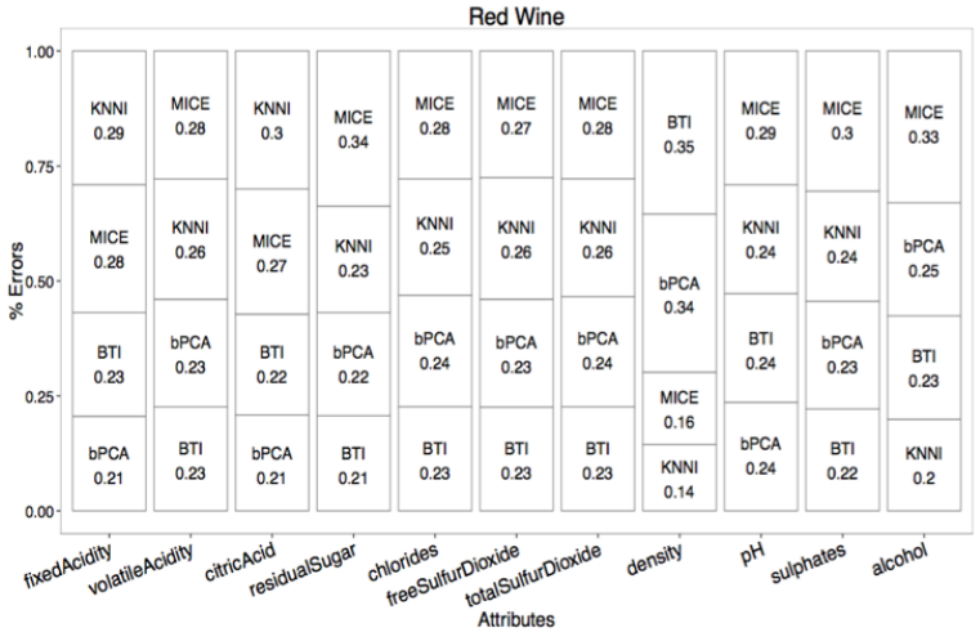

Figure 3.9: Cumulative error bar plot of the four considered imputation methods for the Red Wine dataset. For each dataset, the x-axis discrete values represent the attributes of the dataset, the y-axis represents a % error cumulative to 1 (a smaller segment means smaller RMSE). Each segment shows different imputation method, ordered from the shortest (bottom) to the highest (top). For each attribute, the bottom segment is the one which performed best. The values in the segments are rounded to the second significant digit for readability purpose, while the height of segments has not been rounded.

be seen, for each attribute there is a different winner, hence, if one method is selected as the overall best - it would not be superior for every feature of the dataset. As a whole, the KNNI prevailed on one dataset (i.e., Pen Based), the BTI on four datasets (i.e., Car, Red Wine, White Wine, and Ring), and the bPCA on six datasets (i.e., Contraceptive, Yeast, Titanic, Abalone, Two Norm, and Magic04). In very few cases, the dataset at hand would have the same best imputation model for all the features (i.e., Car and Two Norm), and normally different features of the dataset would have different best imputation models. This preliminary result encouraged the investigation and implementation of the aggregation of models idea.

The SA values given in Table 3.11 show superior results for the imputation carried out with the proposed model. It outperformed the baseline methods random guessing (SA_{Random} is always 0) and the median imputation ($SA_{\text{sFGDI}} >$

Table 3.12: RMSE (MAE) significance test for 5-fold cross validation with 25% (a) and 50% (b) MCAR in the test set. Each row shows how many times the model M_i is better (win), comparable (tie), or worse (loss) than the other models in a Wilcoxon Signed Rank Test, with NULL Hypothesis "Given a pair of models (M_i, M_j) with $i, j \in 1, .., n, i \neq j$, the RMSEs (MAEs) obtained by model M_i are significantly smaller than the errors produced by model M_j" using confidence level $\alpha = 0.05$.

	win	**tie**	**loss**
sFGDI	40 (37)	9 (12)	3 (3)
bPCA	31 (24)	9 (14)	12 (14)
BTI	26 (19)	12 (15)	14 (18)
KNNI	15 (19)	3 (11)	34 (22)
MICE	3 (4)	5 (8)	44 (40)

(a)

	win	**tie**	**loss**
sFGDI	36 (36)	9 (14)	7 (2)
bPCA	39 (31)	9 (16)	4 (5)
BTI	28 (21)	10 (16)	14 (15)
KNNI	12 (15)	3 (4)	37 (33)
MICE	1 (2)	2(5)	49 (45)

(b)

SA_{Median}). The mean imputation was omitted in favour of the median imputation, since the latter is considered less biased to outliers. Furthermore, Table 3.13 presents the RE* results over five different imputation methods and again, as can be seen from the values, the sFGDI method outperformed the median imputation, with $RE_{sFGDI} < 1$ in almost all case studies. It can be also seen from the table that the $RE_{MICE} > 1$, which means high variance in the imputed values, problem already discussed by Gómez-Carracedo et al. (2014). The RE_{KNNI}, instead, shows high variance (from 0.19 to 1.24) depending on the considered dataset and feature. In the Yeast dataset, two variables (i.e., Erl and Pox) are removed during the RE* calculation since the variance in the denominator is 0. To finally assure that the proposed method is outperforming the baselines, Wilcoxon test for statistical significance was run. The RMSE results proved the superiority of sFGDI over both random guessing and median imputation techniques with p-value < 0.05 over all 13 datasets. The Standardized Accuracy analysis (Table 3.11) shows that the sFGDI method not only outperforms the baselines, but it is also comparable, and even better than the state-of-the-art algorithms. As can be seen from the table, the SA_{sFGDI} is higher than the SA of the other methods in 41 out of the 52 cases, comparable in 9 out of the 52 cases, and worse in only 2 cases. To validate the significance of the difference, the Wilcoxon test was run to justify that the provided RMSEs by sFGDI are significantly smaller than the errors achieved by the state-of-the-art methods. The obtained results given in Table 3.12a show that the imputation improvement

achieved by sFGDI is significant (p-value < 0.05) in 40 out of the 52 cases (77%), comparable in 9 out of the 52 cases and worse in 3 cases only. As suggested by Willmott and Matsuura (2005), the same was tested using the MAE metric. The sFGDI showed superiority in 37 cases (71%), was comparable in 12 and worse in only 3 cases. The second-best imputation method (i.e., bPCA) for RMSE was significantly better in 31 out of the 52 cases (60%), comparable in 9 and worse in 12 case, which demonstrates an improvement for sFGDI of 17% over the best single method. For the MAE metric, bPCA results were significantly better in 24 out of the 52 cases (46%), comparable in 14 and worse in 14 cases, showing 25% superiority for the sFGDI over the best single method. Furthermore, Table 3.13 shows that sFGDI estimates the missing values with more stability (low variance) than KNNI, MICE, bPCA, and is comparable with BTI.

Table 3.13: RE* metric of sFGDI and four state-of-the-art imputation methods for the 13 datasets for 5-fold cross validation with 25% MCAR.. Each entry represents the number of times that a given algorithm scored a RE* < 1 (good estimator) on a total of 138 used features. The median imputation is not reported since scores an RE* = 1 every time.

Dataset (# features)	**sFGDI**	**KNNI**	**BTI**	**MICE**	**bPCA**
Contraceptive (9)	9	3	9	1	8
Yeast (6)	5	1	6	0	4
Red Wine (11)	10	6	11	4	9
Car (6)	6	0	5	0	0
Titanic (3)	3	1	3	0	3
Abalone (8)	8	7	8	7	8
White Wine (11)	10	7	10	1	8
Page Block (10)	10	10	10	4	9
Ring (20)	16	0	20	0	14
Two Norm (20)	20	0	20	0	20
Pen Based (16)	15	16	16	14	16
Nursery (8)	8	0	2	0	0
Magic04 (10)	9	8	9	5	9
Total (138)	129	59	129	36	108

To test the sensitivity to missingness, the same set of experiments is run with a 5-fold cross validation and 50% missingness in the test sets. Table 3.12b shows the Wilcoxon Test for RMSE and MAE in this new setting. As can be seen from the table, in the RMSE case, bPCA results are better than sFGDI in 5% of the cases, while under the MAE metric, sFGDI is better than bPCA in 10% of the

comparisons. As argued by Chai and Draxler (2014), if the error distribution is expected to be Gaussian, the RMSE is more suitable than the MAE to picture it. The RMSE penalizes variance, as it gives errors with larger absolute values more weight than the errors with smaller ones. Since in this setting, the two metrics are giving discordant results, to check which one is more suitable, a Shapiro Test was run to check the error normality. The results showed that the errors are not having Gaussian distribution, which implies that the MAE may give more accurate information about the errors and can be considered more trustworthy in this simulation. Following this hypothesis, the proposed method resulted as "at least comparable" in 14 out of the 52 cases, better than all the other models in 36 cases, and worse in only 2 out of the 52 cases. Finally, to check whether the proposed method is sensitive to the size of the training set, the same two experiments were repeated using a 30-fold cross validation. As can be seen from the data reported in Table 3.14a and Table 3.14b, the sFGDI is statistically superior between 1% and 15% RMSE against the best single method (bPCA), and is between 10% and 17% better when using MAE. Furthermore, it is also worth to mention that in all but one experiment (5 folds, 50% missingness, and RMSE), the sFGDI is on average never worse than the other single models, which supports the choice of this method without risk of worsening the imputation results.

Table 3.14: RMSE (MAE) significance test for 30-fold cross validation with: (a) 25%; and (b) 50% MCAR in the test set. Each row shows how many times model M_i is better (win), comparable (tie), or worse (loss) than the other models in a Wilcoxon Signed Rank Test, with NULL Hypothesis "Given a pair of models (M_i, M_j) with $i, j \in 1, .., n, i \neq j$, the RMSEs (MAEs) obtained by model M_i are significantly smaller than the errors produced by model M_j" using confidence level $\alpha = 0.05$.

	win	tie	loss
sFGDI	43 (41)	5 (7)	4 (4)
bPCA	35 (32)	8 (6)	9 (14)
BTI	26 (26)	11 (9)	15 (17)
KNNI	14 (18)	1 (5)	37 (29)
MICE	4 (5)	5 (8)	43 (39)

(a)

	win	tie	loss
sFGDI	43 (42)	5 (7)	4 (3)
bPCA	42 (37)	5 (8)	5 (7)
BTI	27 (25)	8 (8)	17 (19)
KNNI	10 (15)	4 (4)	38 (33)
MICE	1 (2)	3 (2)	48 (48)

(b)

Here I report the results of the experiments when the missingness is caused by MAR (Table 3.15) and MNAR (Table 3.16) mechanisms. The given in Table 3.15

Standardized Accuracy values for the MAR experiment show slightly superior performance of sFGDI when compared with the other imputation techniques. In particular, the proposed model outperforms the baseline random guessing ($SA_{\text{sFGDI}} > 0$) in all reported cases and the median imputation ($SA_{\text{sFGDI}} > SA_{\text{Median}}$) in 8 out of 13 datasets. Furthermore, it also demonstrates better accuracy in all 13 cases when compared to KNNI and MICE, and is better than BTI and bPCA in 11 and 10 cases respectively. It is also worth to note that the imputation under MAR condition is generally harder task (compared to MCAR), since the missingness is not uniformly distributed across the dataset and depends on the other variables as well (as discussed in Section 3.3.2). In addition, the sFGDI is better or at least comparable with the median imputation, while the other methods are worse or at most comparable to this baseline. As for all previous experiments, the Wilcoxon test was adopted to evaluate the significance in difference for RMSE and MAE metrics. Results in Table 3.17a show that the imputation improvement achieved by sFGDI is significant (p-value < 0.05) in 41 out of the 52 cases (79%), comparable in 10 and worse in only 1 case when using RMSE. On the other hand, the sFGDI resulted significantly better in 47 cases (90%), comparable in 5 and never worse when implementing the MAE metric. The second-best imputation method (BTI) for RMSE is significantly better in 36 out of the 52 cases (69%), comparable in 8 and worse in 8 cases, which shows an improvement of 10% for sFGDI over the second best method. For the MAE hypothesis, BTI results are significantly better in 31 out of the 52 cases (60%), comparable in 6 and worse in 15 cases, showing inferior accuracy (30%) compared to my method (90%). The same analysis performed under the MNAR condition also suggests that the use of a single imputation method for the whole dataset is not the best option. Again, the SA values (Table 3.16) are generally lower when compared to the MCAR mechanism (Table 3.11) as the missingness is caused by the considered variable itself (as explained in Section 5.4), increasing the likelihood of introducing bias when imputing the values.

Table 3.16 shows superior results for my method in 10 out of 13 datasets. In particular, the reported SA_{sFGDI} is better than SA_{KNNI} and SA_{MICE} for all con-

Table 3.15: Standardized Accuracy (SA) values achieved by sFGDI, the baseline (median imputation) and state-of-the-art (KNNI, BTI, MICE, and bPCA) techniques over the 13 datasets for 5-fold cross validation with 25% MAR. Higher values represent better accuracy over the random guess.

Dataset	sFGDI	KNNI	BTI	MICE	bPCA	Median
Contraceptive	**0.27**	0.11	0.26	-0.02	0.23	0.23
Yeast	**0.37**	0.29	0.36	0.04	0.36	0.36
Red Wine	**0.28**	0.13	0.18	0.01	0.15	**0.28**
Car	**0.32**	0.21	0.31	0.01	0.31	0.29
Titanic	**0.27**	0.18	**0.27**	-0.06	**0.27**	0.25
Abalone	**0.28**	-0.32	0.27	0.08	0.08	**0.27**
White Wine	**0.29**	0.11	0.18	-0.01	0.18	**0.29**
Page Block	**0.26**	0.16	**0.26**	0.12	0.22	**0.26**
Ring	**0.30**	0.24	0.29	-0.02	0.29	0.29
Two Norm	**0.30**	0.18	0.29	0.01	0.25	0.29
Pen Based	**0.27**	0.02	0.22	0.00	0.17	**0.27**
Nursery	**0.30**	0.18	0.24	0.01	0.29	0.23
Magic04	**0.26**	0.13	0.22	0.07	0.20	0.25

sidered datasets, while being never worse than SA_{BTI} and SA_{bPCA}. When compared to the baselines, the sFGDI is always superior than the Random Guess ($SA_{\text{sFGDI}} > 0$), better than the median imputation in 7 out of 13 cases, and worse only in 1 of the cases. The Wilcoxon analysis (Table 3.17b) shows the sFGDI being better than the second best method (BTI) in 25% and 33% of the cases for RMSE and MAE respectively. Comparing the proposed method with the other imputation techniques showed the sFGDI superiority over the bPCA, KNNI and MICE in 46%, 64% and 89% of the cases respectively for the RMSE, and in 50%, 67% and 90% respectively for the MAE metrics.

Table 3.16: Standardized Accuracy (SA) values achieved by sFGDI, the baseline (median imputation) and state-of-the-art (KNNI, BTI, MICE, and bPCA) techniques over the 13 datasets for 5-fold cross validation with 25% MNAR. Higher values represent better estimation over the random guess.

Dataset	sFGDI	KNNI	BTI	MICE	bPCA	Median
Contraceptive	**0.31**	0.17	0.30	0.03	**0.31**	0.27
Yeast	**0.27**	0.09	0.24	-0.02	0.22	0.22
Red Wine	**0.28**	0.14	0.25	-0.08	0.25	0.26
Car	**0.29**	0.16	0.15	-0.07	0.14	**0.29**
Titanic	**0.28**	0.00	0.26	-0.05	0.23	0.26
Abalone	**0.27**	-0.05	0.18	-0.10	-0.10	**0.27**
White Wine	**0.30**	0.12	0.18	0.00	0.19	0.29
Page Block	0.22	0.17	0.20	0.03	0.16	**0.23**
Ring	**0.29**	0.25	**0.29**	0.00	**0.29**	**0.29**
Two Norm	**0.30**	0.21	0.29	0.01	0.27	0.29
Pen Based	**0.28**	0.00	0.22	-0.01	0.20	**0.28**
Nursery	**0.28**	0.13	0.25	0.00	**0.28**	0.22
Magic04	**0.22**	0.06	0.18	-0.06	0.13	**0.22**

Despite being generally not recommended (Whigham et al., 2015), the median imputation showed comparable and even better results than the bPCA, BTI, KNNI, and MICE in both MAR and MNAR settings. At first sight, this result is contradictory to the MCAR experiment (given in Table 3.11). This could be explained by the fact that the multivariate model can benefit from the uniformly distributed missingness across the dataset (like in the MCAR mechanism), while for the MAR and MNAR (where the missingness depends on a single variable), the use of a univariate model (baselines) could be reducing the noise in the prediction (because of not considering uncorrelated features). However, as can be seen from the carried experiments, the use of combination of baselines and state-of-the-art techniques (as in the proposed approach) can improve the accuracy in almost all proposed scenarios with a very low risk of worsening the imputation. Last point to note is that while the sFGDI is superior in all setups, the bPCA and BTI are competing for the second best in the two scenarios (bPCA for MCAR; and BTI for MAR and MNAR).

Table 3.17: RMSE (MAE) significance test for 5-fold cross validation with 25% MAR (a) and 25% MNAR (b) in the test set. Each row shows how many times the model M_i is better (win), comparable (tie), or worse (loss) than the other models in a Wilcoxon Signed Rank Test, with NULL Hypothesis "The RMSEs (MAEs) provided by M_i are significantly smaller than the errors provided by the other models".

	win	**tie**	**loss**
FGDI	41 (47)	10 (5)	1 (0)
BTI	36 (31)	8 (6)	8 (15)
bPCA	28 (22)	6 (11)	18 (19)
KNNI	11 (13)	2 (6)	39 (33)
MICE	1 (1)	2 (5)	49 (46)

(a)

	win	**tie**	**loss**
FGDI	47 (48)	5 (4)	0 (0)
BTI	34 (31)	7 (7)	11 (14)
bPCA	23 (22)	6 (8)	23 (22)
KNNI	14 (13)	3 (6)	35 (33)
MICE	1 (1)	1 (5)	50 (46)

(b)

All the experiments presented in this work have been done on a 16 core machine with 32gb RAM and 64Gb SSD of storage. Figure 3.10 shows the training time for the four state-of-the-art techniques (KNNI, BTI, MICE, and bPCA) and the proposed sFGDI method over the 13 datasets, given in seconds. Due to the sFGDI parallelisation (each imputation algorithm can be run independently from the others), its training execution time is never significantly higher than the time needed for any other single technique. In particular, sFGDI train-

ing time (blue bar in Figure 3.10) is always comparable with the slowest technique, plus an overhead due to the different scheduled threads. Furthermore, the proposed method shows a consistent time execution overhead with datasets of different volume and feature sizes. This behaviour can be observed from the percentage change between the sFGDI and the slowest compared model. In particular, the percentage change results are smaller for bigger datasets (7.69, 6.15, 14.37, 11.76, 5.84, 10.74 and 4.76 for White Wine, Page Block, Ring, Two Norm, Pen Based, Nursery and Magic04 respectively) and larger for the small ones (22.5, 20, 43.90, 59.09, 56.25, 46.34 for Contraceptive, Yeast, Red Wine, Car, Titanic and Abalone respectively). This finding supports the recommendation of using the sFGDI regardless the size of the dataset (as long as the imputation is feasible for the single models used in the sFGDI). For the prediction runtime (applied on the test set), sFGDI showed to be comparable with the slowest method selected during the training phase.

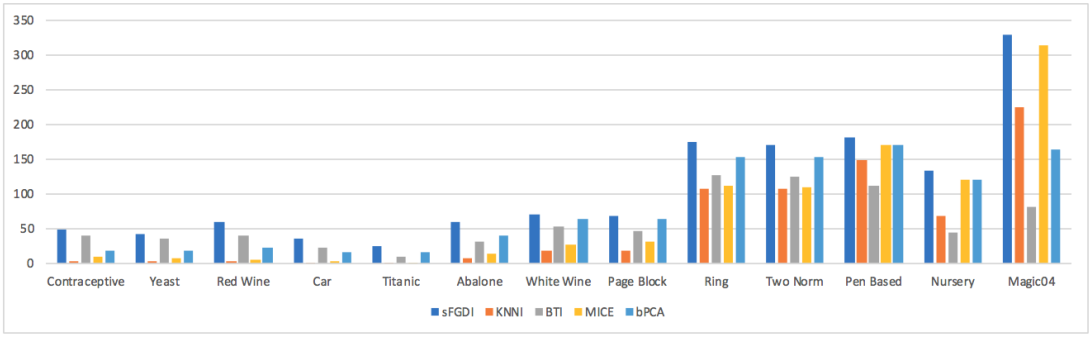

Figure 3.10: Training time in seconds (y-axis) of the five considered imputation methods over the 13 datasets (x-axis). The median imputation is omitted having always a training time less than 1 second.

3.3.4 Discussion

Missing data is an immanent problem in most real-world datasets used in machine learning tasks, statistical analysis, and any other processing approach requiring complete datasets. An initial analysis carried on 13 datasets showed that a model scoring the lowest overall error does not necessarily provide the best imputation for each feature of the dataset. The investigated here Scattered Feature Guided Data Imputation method aim is to remedy this, by aggregat-

ing different imputation methods in an attribute-wise fashion, considering the respective features. The sFGDI extracts the complete subset (without missing values), and selects through a learning process the most suitable imputation method for each feature. The imputation performance is evaluated with four widely used metrics for such tasks (i.e., RMSE, MAE, SA, and RE*). The results are statistically assessed using the Shapiro Test to check the distribution normality, and the non-parametric Wilcoxon Signed Rank Test. Under the MCAR mechanism, the Standardized Accuracy analysis demonstrates that the proposed model is always more accurate than the two baselines and produces better estimation from the state-of-the-art methods in 41 out of 52 cases. The Wilcoxon on MAE shows improvements between 10% and 25% for the sFGDI over the second best performing algorithm (bPCA) in four different settings. Furthermore, the Wilxocon test with RMSE metric confirms that the sFGDI is superior to bPCA in up to 15% of the cases for three different settings, and only in one experiment (5 folds and 50% missingness) it is 5% worse. In addition, sFGDI and BTI impute values with higher stability (RE* < 1) for 129 out of 138 tested features, followed by bPCA with 108 out of 138. Although the prediction under MAR and MNAR mechanisms is generally less accurate than the one under MCAR, the sFGDI still shows better performance when compared with the baselines and the state-of-the-art techniques. In particular, in the MAR case, the sFGDI is more accurate than the second best model (BTI) in 10% and 30% of the cases for RMSE and MAE respectively. Under the MNAR mechanism the proposed model is again better than BTI in 25% and 33% of the cases using the two evaluation metrics. Finally, the performed imputation run time analysis proves the approach feasibility regarding the needed training and testing time. The reported results strongly support the efficiency of the proposed method when implementing multivariate imputation as a way of dealing with missingness. Another advantage is that the sFGDI can be easily parallelised, having straightforward implementation allowing other imputation methods to be easily incorporated and aggregated. Future work will compare the imputation techniques when the datasets are subsequently used in a prediction task (e.g., regression and classification). Sensitivity analysis will be also carried out

to assess the impact of this imputation on the final results, to show the correlation between imputation accuracy and prediction errors (bias analysis).

3.4 Online Traveling Recommender System with Missing Values

In this section I tackle the problem of missing data and long tail for Recommender Systems.

As in all online services where users choices, items, and decisions are involved, there is a necessity for a Recommender System (RS). Since the online travel agencies (OTAs) provide the main service of booking holidays, business trips, and accommodations, a useful recommendation is what the user can benefit mostly from the system (money-wise and satisfactory-wise). Going through a big catalogue is a tedious and time-consuming operation and selecting the best deal among many choices is not a trivial task. For a travel RS where the user is allowed to navigate the catalogue and book the hotels without being logged in the system and the rated items are very few (compared to movie or music recommender systems), the use of a Collaborative Filtering (CF) approach is not feasible because the user-item matrix is way too sparse (and sometimes even the user information is not available). For this reason, a Content Based Filtering (CBF) is applied in this work, focusing on two of its main problems: missing values and long tail.

An important event in the market of holidays lodging is represented by the explosive popularity of private renting, also called Vacation Rentals (VR), gained in the past few years (Zervas et al., 2017). The primary problem with this massive influx of new properties is the lack of related historic data which results in their unfair ranking in the system. For the new VR, the lack of features is not only historical (e.g., historical prices, purchases, popularity, etc.), but also in absence of basic characteristics (e.g., star rating and guest rating). For example, star rating (which is given for public properties by an Institutional body) is not regularized for private lodgings. On top of that, the guest rating would be

missing for some time after the first appearance of the property, until recording at least a few users' rating.

Different missing data imputation techniques and ad-hoc feature engineering can be used to enhance the CBF, allowing more diversity and fairer ranking of new items. This investigation includes analysis of the VR market. Experiments and results of the missing values imputation and item similarities prediction are also reported.

3.4.1 Data pre-processing and feature engineering

Although all the information related to amenities, destinations and properties is available during the navigation of the website, the datasets used in this work are owned by *Hotels.com*.

The collected data is coming mainly from *four* sources:

- *Clickstream*: This dataset contains all users' website interactions (e.g., clicks, bookings, etc.);
- *Amenities*: includes the characteristics of all the properties (e.g., Wi-Fi, pool, TV, etc.);
- *Destinations*: records of all points of interest (e.g., cities, landmarks, airports, train and metro stations, etc.);
- *Properties*: comprises all the relevant information in the system (e.g., property ID, name, latitude, longitude, etc).

The *clickstream* dataset is stored in an HDFS and accessed through Apache Hive queries (Thusoo et al., 2009), which is a surrogate of SQL, optimized to work on a distributed cluster. The data stored in the *clickstream* table contains all users interactions during the website navigation (around 80M rows (200Gb) are daily collected and stored in this table). Each row can represent a search, a click on a property, or a booking. This table is mainly used for exploratory analysis of the data and for gaining insights of the functionality of the RS regarding different searches and property types.

The *amenities* dataset contains mostly static information about the amenities

available in each property.

The *destinations* table contains a worldwide list of points of interest. Each record is categorized as continent, country, city, landmark, airport, metro station or train station and identified through its latitude and longitude.

The last dataset stores basic information about the properties - e.g., property ID, property name, property type, city name, country, latitude, longitude, guest rating, star rating, number of reviews, etc.

The first operation performed on the clickstream data is the filtering of records coming from bots, spiders, and crawlers. An easy way of achieving this goal is to eliminate all the samples coming from users with a high rate of clicks in a short time window (e.g., more than 5 clicks per second) or on a wider time frame (e.g., more than 200 interactions in 1 hour). More sophisticated anti-bot techniques include checking the *user agent identifier*, or whether the pages have been accessed in a sequential fashion, following progressive URLs on the website. However, the click-through-time ($\frac{\#\text{clicks}}{\text{time}}$) interaction is a good proxy to identify the real users (Yu et al., 2010). The second filter isolates the interactions useful for the scope of this research, such as: search pages, property pages, and booking pages. This subset is referred as *cleansed clickstream*.

The *amenities* dataset is divided into four categories: dining (e.g., restaurants, bar, etc.), room (e.g., TV, Wi-Fi, etc.), property (e.g., reception, elevator, etc.) and recreation (e.g., spa, pool, etc.) amenities.

The cleaning of this dataset is performed in two steps:

- removing all the amenities starting with ”No ” and ”- no” from each category;
- removing the 2% most popular and 15% least popular amenities.

The first one filters out all the amenities that are not provided by the property or those requiring a fee (e.g., No Free Parking, No Free Water, No Free Wi-Fi, etc). The second filter removes, for each category, the most frequently listed amenities (e.g., Free Wi-Fi appears in 190K out of 290K properties) and the least frequently listed ones (roughly getting rid of the top 2% and bottom 15% of

the list). The obtained cleansed subset contains around 5 million records (16 amenities on average for each property) and 500 unique amenities.

From the *properties* dataset, only the active ones on the website are considered (around 290K).

The *destinations* table is cross-joined with the active properties in order to calculate the geographical distance between each pair. The resultant set contains 200 million records of *property-destination* pairs.

Table 3.18: For each category, the amenities contained in less than *Bottom 15%* properties and more than *Top 2%* properties, are discarded. In the *Dining* category no amenities have been discarded since there are only *four*: *Venue*, *Restaurant*, *Bar* and *Reception*.

Category	Bottom 15%	Top 2%
Dining	None	None
Room Amenities	1015	183000
Property Amenities	465	170000
Recreation	535	53000

The *cleansed clickstream* data is daily aggregated on a property level to get an insight of how each item is ranked by the RS, for each category of users and searches (all the information in a search are considered as segments). Table 3.19 shows a descriptive structure of the dimensions contained in the *cleansed clickstream*, while Table 3.20 illustrates possible explorable segments. The data can be further aggregated on a monthly basis to get more information of the long tail or for properties with limited number of available rooms (e.g., it is unfair to compare the number of bookings of a hotel with 300 rooms and bookings of an apartment with 2 rooms).

The set of cleansed amenities is joined with the *properties* table on the property ID and subsequently the amenities of each hotel are grouped in a vector. This structured table (Table 3.21), composed of two columns (Property ID and array of amenities) is used to compute hotels similarity in Section 3.4.4.

For the geographical features, once the property and destination tables are cross-joined, the resultant *property-destination* table contains for each pair of hotel and destination: the respective IDs (property ID, destination ID); respective coordinates on the map (latitudes and longitudes); and the destination type (Ta-

Table 3.19: Description of the aggregated dimensions from the *cleansed clickstream* dataset.

Dimension	Description	Example
# Reviews	Number of reviews received by a property	500
Review Score	Avg. Review score given by the users (0 to 5)	3.5
Star Rating	Star Rating classification for each property (0 to 5)	4
Avg. Rank	Average ranking in the RS (1 to #Properties)	5
Median Rank	Median ranking in the RS (1 to #Properties)	3
Nightly USD Avg. price	Average booked price for each property for one night	140 USD
Deal of the Day	Number of times a property is in first position for a special deal	20
Travel Advertisement	Number of times a property is in first position as sponsored property	15
# Impressions	Number of times a property is impressed by the users in the search page	550
# Clicks	Number of times a property is clicked by the users from the search page	300
# Bookings	Number of times a property is booked by the users	20
Clicks / Impressions	Rate of clicks based on the number of impressions	0.35
Bookings / Clicks	Rate of bookings based on the number of clicks	0.10
Top10 probability	Probability for a property to be ranked in the top 10 (#Top10 / #Impressions)	0.70

Table 3.20: Description of the aggregated segments from the *cleansed clickstream* dataset.

Segment	Description	Example
Property type	Specific category for each property	Hotel, Motel, Vacation Rental, Condo
Experiment	Number of experiment for A/B testing	1191
Variant	Number of variant for each experiment	0 for control, different from 0 for variants
Sorting Order	Selected sorting order by the user	Default (recommended), Lowest Price, etc.
Filters	Boolean to identify the filters usage	TRUE
# Adults	Number of adults selected by the user	1, 2, 3+
Children	Boolean to specify the presence of children	FALSE
# Rooms	Number of rooms selected by the user	1, 2, 3+
Platform	Type of device used by the user	Mobile, Desktop
User region	User region identification	NA, EMEA, APAC, LATAM

ble 3.22). The Haversine function ((Robusto, 1957)) is then used to calculate the distance between two points, and is defined as:

$$haversine(\Delta\phi, \Delta\lambda) = \sin^2(\Delta\phi/2) + \cos(\phi_1) \cdot \cos(\phi_2) \cdot \sin^2(\Delta\lambda/2) \quad , \tag{32}$$

$$distKm = r \cdot 2 \cdot atan2(\sqrt{haversine}, \sqrt{1 - haversine}) \quad , \tag{33}$$

where $\Delta\phi$ is $(lat_{property} - lat_{destination})$ and $\Delta\lambda$ is $(lon_{property} - lon_{destination})$ are expressed in radians, and r is the earth radius ($r = 6371$km). The Haversine is preferred to the Euclidean distance when calculating the distance between two coordinates since it takes into account the spherical shape of the earth (considering the fact that 1° of distance near the equatorial line is bigger

than 1° closer to the poles).

Once the distance is calculated for each pair, only those those smaller than 200km are stored in the final table (about 170 million pairs). From this dataset the following features are computed for each property: #landmarks in 1km radius; #landmarks in 5km radius; presence of top 10 rated landmarks in 1km radius; train station in half km radius; train station in 1km radius; metro station in half km radius; metro station in 1km radius; distance from city center; distance from the closest airport. Those features are subsequently used to calculate the geographical clusters used in Section 3.4.3.

Table 3.21: Cleansed and aggregated amenities for each property.

Property ID	Amenities
001	[Wifi, Pool, Kitchen]
002	[Wifi, Bar, Restaurant, Bathtub]
004	[Wifi, Parking, Spa]
...	...
600	[Breakfast, Slippers, Egyptian Cotton Sheets]

Table 3.22: Cleansed and cross-joined table between *active properties* and *destinations*. Each row represents a pair of hotel-destination and the relative distance in kilometers calculated with the Haversine distance.

Property ID	Destination ID	Destination type	Property latitude	Property longitude	Destination latitude	Destination longitude	Haversine distance (Km)
001	465	Landmark	51.506	-0.140	51.504	-0.140	0.22
001	478	Metro station	51.506	-0.140	51.499	-0.133	0.87
001	459	Train station	51.506	-0.140	51.503	-0.112	1.97
002	459	Train station	51.500	-0.116	51.503	-0.112	0.38
...	...	...	...	...	...	...	...
002	665	Airport	51.500	-0.116	51.876	-0.374	45.36

3.4.2 Exploratory analysis

The distribution of the *guest* and *star* ratings across the different property types are given in Figure 3.12. For the VR, the *guest rating* is missing in more than 55% of cases (Figure 3.12b), while for the *star rating* in 19% (Figure 3.12a).

Figure 3.11 shows the distribution of each property type (Table 3.23) along the first 50 ranks, grouped in 10 bins. As can be seen from the figure, the VR (purple bars) and *Alternative Hotels* (red bars) are under-ranked in the first 2 bins (positions 1 to 10) with less than 3% of the property density each (in total), while they show higher density than the other property types in positions 26 to 50 (bins 6

Table 3.23: List of property types.

Property Type	# of properties
Hotel	203899
Vacation Rentals (e.g., *Apartment, Condos, Villa, Penthouse, etc.)*	31394
Motel	14245
Alternative Hotels (e.g., *Apart-Hotel, Resort, Boutique Hotel, Inn, etc.)*	7915
Truly Alternative (e.g., *Ranch, Farmhouse, Cruise, Lodge, Riad, Pousada, etc.)*	3918

to 10). The low density of VR in the first 10 ranks can be associated with the lack of features data and the long tail problem, caused by the biased ranking towards recommended popular properties. The distribution of the guest and star ratings across the different property types is given in Figure 3.12.

For the VR, the guest rating is missing in more than 50% of the cases, while for the star rating it is within 20%. Although the *Alternative Hotels* category is under-ranked in the first 10 positions (having a missing rate of 25% and 15% for guest rating and star rating respectively), it only represents 3% of all properties (Table 3.23). For this reason, the long tail problem for this category is not addressed in this dissertation - thus I focus my investigation on the emerging market of VR only (Zervas et al., 2017), in particular discussing and analysing the problem of missing data. To confirm the relationship between the two ratings and the rank position, and to evaluate the impact of the missing values, a Spearman correlation analysis is considered (Cohen et al., 2013). As can be seen from Table 3.24, the analysis shows positive correlation between the impressions, clicks, and bookings, with the rank position. The correlation between impressions and rank (0.59) can be expected, since it is most likely that the top of the list is more likely seen by the users. The positive Spearman value between clicks and rank (0.43) means that the customers are more inclined to click properties from the top of the list. Although the smaller positive Spearman correlation between bookings and rank (0.13) shows that the users are more likely to book properties suggested by the RS, the slightly higher booking correlation with the guest and star ratings (0.21 and 0.19 respectively), suggests these as better drivers when choosing a property. It is also evident from Table 3.24 that bookings correlation values are smaller, as the number of purchases is very small compared to the others (impressions and clicks), which makes difficult

to find clear relationships with the other drivers. The positive correlation between guest rating and rank (0.45) indicates that the RS is more likely to push the well rated properties to the top of the list and the non-rated ones to the list bottom. As a natural consequence, the users are more likely to click and book properties with good ratings (positive clicks/bookings-guest rating/star rating correlation). The use of the star rating and guest rating as drivers in the users choices is similar, which can be proved by the high correlation between the two (0.62).

Table 3.24: *Spearman Correlation* between *Impressions*, *Clicks*, *Bookings*, *Rank*, *Guest Rating* and *Star Rating*.

Feature 1	Feature 2	Correlation
Impressions	*Guest Rating*	0.50
Clicks	*Guest Rating*	0.47
Bookings	*Guest Rating*	0.21
Impressions	*Star Rating*	0.49
Clicks	*Star Rating*	0.47
Bookings	*Star Rating*	0.19
Impressions	*Rank*	0.59
Clicks	*Rank*	0.43
Bookings	*Rank*	0.13
Guest Rating	*Rank*	0.45
Star Rating	*Guest Rating*	0.62

3.4.3 Empirical study design

Following the exploratory analysis of the available data, I found out that only 2% of all VR have median rank within the top 10 positions and missing data rate of 50% for the guest rating Figure 3.12b, and 19% for the star rating Figure 3.12a. This naturally led to the question whether the VR are unfairly ranked by the RS and if this is related to the missing data problem. The co-clicks (Yu et al., 2014) is an item-item similarity metric based on the number of users who clicked two items in their search session. Although being a good similarity metric (using the implicit feedback of the users to pin similar properties), due to the lack of historical data, it is impossible to be calculated for properties recently added to the catalogue. To tackle this problem, three other non-historical similarity metrics (i.e., based on amenities - Jaccard similarity and Weighted Hamming distance;

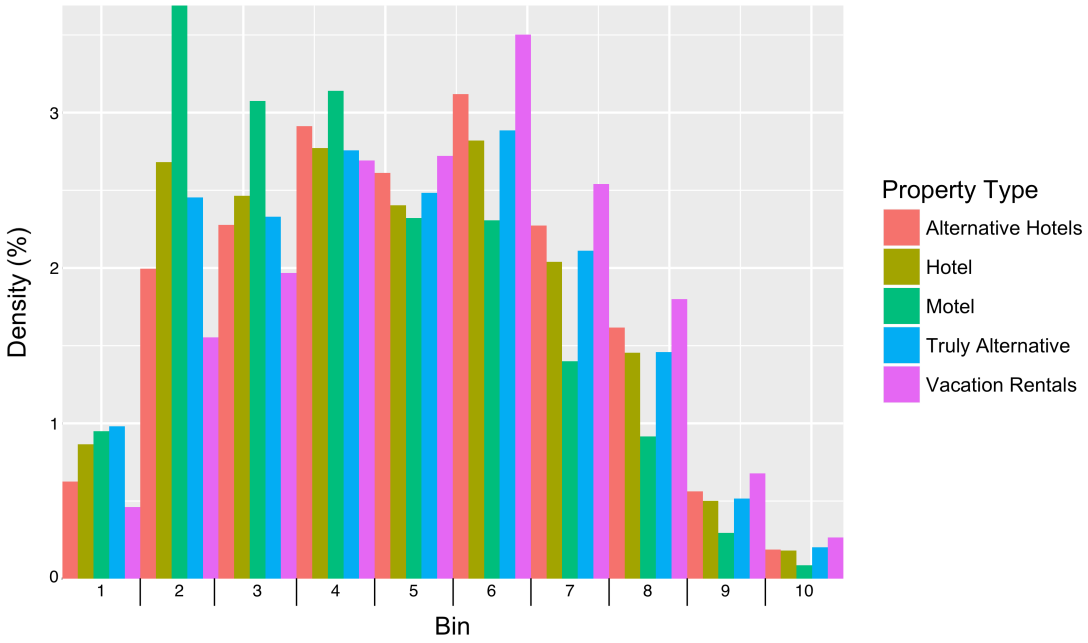

Figure 3.11: Density plot showing for each *property type*, the density of properties in each rank. Each *bin* contains 5 positions of the rank from 1 to 50.

and based on geographical features - Fuzzy-C-Mean clustering centroid distance) are discussed, compared, and analysed in Section 3.4.4, aiming to define the best approximation metric when the co-clicks data is missing. Following the Spearman analysis of the historical data, I found that the guest and star ratings are major decision making criteria for viewing and booking a property. However, when a new property is introduced in the catalogue these features are missing (e.g., for the VR in Figure 3.12: 50% and 19% missingness for the guest and star ratings respectively). To mitigate this problem, the missing guest and star ratings are imputed with two baselines (i.e., mean and median imputation) and three state-of-the-art techniques for missing data imputation (i.e., KNNI, RFI and GBTI), using non-historical features (e.g., geographical features, amenities, etc). The application of these methods is discussed in Section 3.4.4, followed by the analysis of the results. As previously showed, the Vacation Rentals (VR) are one of the unfairly ranked property types due to the missing values and long tail (Figure 3.11) problems. As last goal of this investigation,

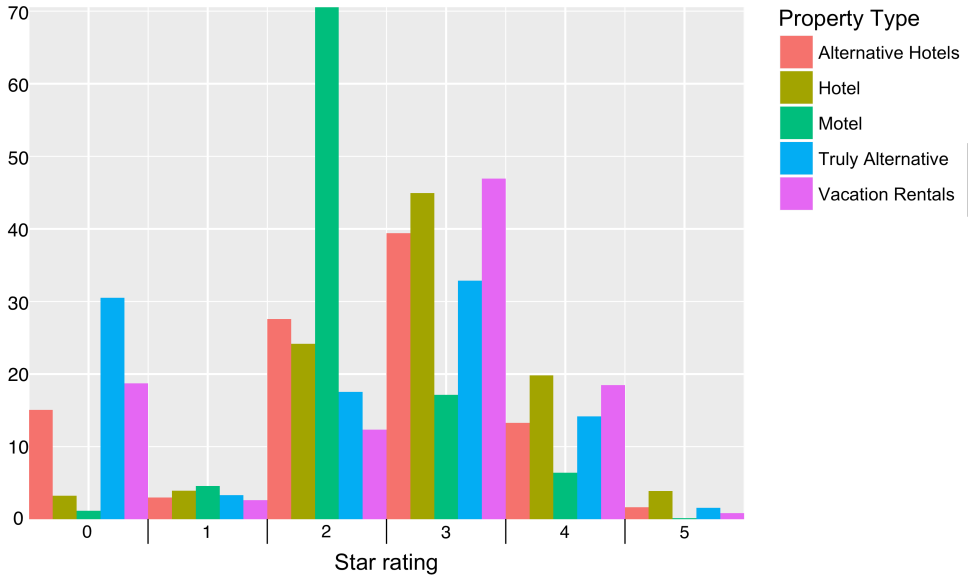

(a)

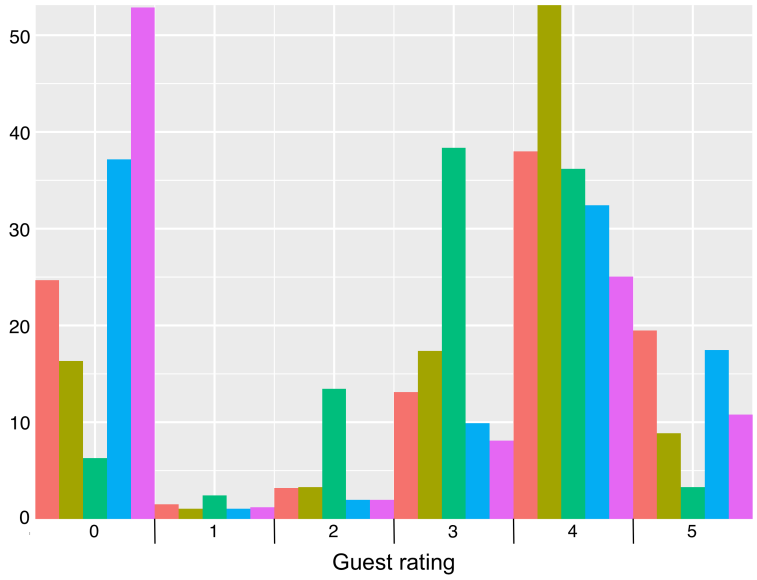

(b)

Figure 3.12: Distribution of star rating (Figure 3.12a) and guest rating (Figure 3.12b) (ranging 1 to 5 with 0 used to represent missing ratings) across all property types (e.g., *Hotel*, *Vacation Rentals*, *Motels*, etc). The distribution is expressed in percentage (y-axis). Please not that the y-axes are given with different scales.

the geographical clusters, plus the imputed features, are used to boost the VR ranking from the tail to the head of the list (the top 10 positions). The boost promotes the VR which are most similar to the hotels in the top 10 positions of the ranking. The similarities are calculated computing the Euclidean distance of the hotels and VR imputed features (guest rating and star rating), and the Haversine distance of the relative latitudes and longitudes. Furthermore, to reduce the number of computed pairwise similarities, only pairs of hotel-VR belonging to the same geographical cluster (computed in Section 3.4.1) are considered. Algorithm 2 describes the main steps to perform for boosting VR to the top of the list based on similarities and an example is given in Table 3.25.

Table 3.25: Example of a search where no VR are displayed in the top 10 positions (head of the list). In this case, Algorithm 1 is applied to boost one of the feasible VR to the top 10 rankings. The hotel ranked 10th (5th row) is the one selected randomly from the head, to be compared with the rest of the list (the tail). Three VR are given (ranks: 12, 48 and 50): the VR with rank 12 (7th row) is not eligible for boosting, since it belongs to a different geographical cluster (Hotel Blue belongs to cluster 3, while Queens Apartment belongs to cluster 1). From the two remaining VR (9th and 11th rows), the most similar one to the Hotel Blue is selected to be boosted. To select the best option, a look up table containing pair similarities (Euclidian distances) is kept and used when needed. E. g., Beautiful Apartment and Kings Condo have 0.90 and 0.15 as distance score respectively, resulting in Kings Condo boosting to position 10, while all properties rated 11-49 are shifted down 1 position.

Id	Name Type	Cluster	Rank
5000	Hotel Brown Hotel	1	1
2050	Hotel Red Hotel	2	2
...	... ...	...	...
2500	Hotel Blue Hotel	3	10
7500	Hotel White Hotel	1	11
5300	Queens Apartment Vacation Rental	1	12
...	... ...	...	...
3000	Kings Condo Vacation Rental	3	48
9800	Young Hostel Hostel	2	49
2350	Beautiful Apartment Vacation Rental	3	50

Since the boosting of the properties is only considering the "hotel to VR similarity", a further optimization can be done minimizing the price difference as a second objective. Because these two objectives are contradictory, a Pareto optimization approach (Sarro et al., 2016) is used to achieve the best trade-off between the two criteria. The optimal solution is expressed as a Pareto front

Algorithm 2 VR Boosting.

procedure BOOSTVR
    Rank the properties with the RS;
    Select property *i* from the top 10 rankings with *property type* != "Vacation Rental";
    for X (properties ranked > 10) **do**:
        Select only the properties with *property type* = "Vacation Rental" (X');
        From X' select only the properties in the same geographical cluster of *i* (X'');
    for each pair (i, j) with $j \in X''$ **do**:
        Calculate $sim(i, j)$ based on guest rating, star rating, latitude and longitude;
    Select the most similar property *j* to *i*;
    Replace *i* with j;

(Figure 3.13) representing non-dominated points of hotel-VR pairs (for which no objective can be improved without worsening the other). In a formal way, point *x* Pareto dominates point *y* iff the following two conditions hold:

$$f_i(x) \leqslant f_i(y) \forall i \in \{1, 2, ..., M\} \quad , \tag{34}$$

$$f_i(x) < f_i(y) \text{ for at least one objective } j \in 1, 2, ..., M, \tag{35}$$

where the number of objectives M = 2 in this case. Solution x is called Pareto optimal if there is no other solution z which Pareto dominates it (Figure 3.13). The collection of all Pareto optimal solutions is called the Pareto optimal set, and the Pareto optimal front is the projection of these solutions in the objective space (Zhai and Jiang, 2015; Yuan et al., 2016; Rostami and Neri, 2017; Miranda and Von Zuben, 2017).

Regarding the evaluation of the results for the imputation of guest rating and star rating, the MAE is used as error function as it is of easier interpretability, reflecting on average how many error stars there are between the observed value and the predicted one (e.g., MAE = 0.5 means an average error of a half star).

As recommended by Chen et al. (2009), I use MAP@X metric to compare the ranking lists (with X = 1 and X = 5).

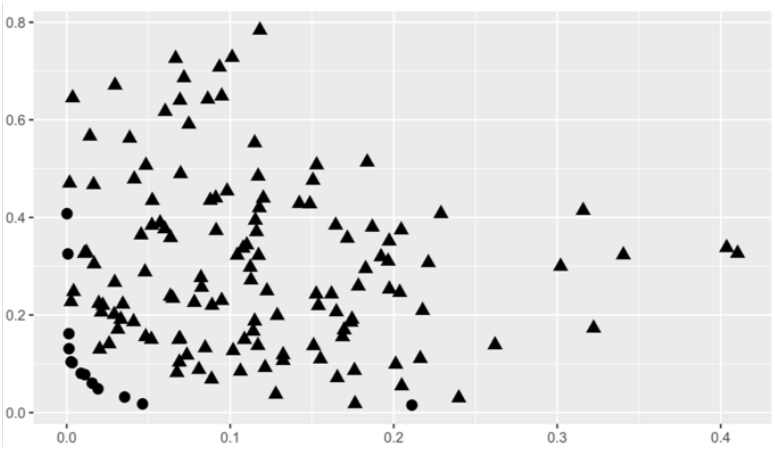

Figure 3.13: Pareto front example for one search. The dots represent non-dominated Pareto solutions in the similarity (y-axis) and difference in price (x-axis) objectives respectively.

A k-fold cross validation is applied splitting the dataset into independent training, validation and test subsets. The test set is generated using a uniform sampling without repetitions, and the rest of the data is left as a training and validation sets. Furthermore, the ML-Spark pipelines (Meng et al., 2016) are used to ensure correctness and replicability of the experiments. In machine learning, the concept of pipeline (or workflow) is very important to guarantee that the same set of steps are involved when a new dataset is processed. Figure 3.14 shows a pipeline in ML-Spark from the pre-processing to the regression phase. The ML-Spark library represents such workflow as a sequence of steps to be performed in a specific order. Due to the laziness of Spark transformations, the pipeline is created as a recipe, stored in the memory and the computation is deferred to the point where the *fit(·)* method is invoked (see Section 2.3.2 for more details).

3.4.4 Results

As mentioned earlier, the co-clicks is an item-item measure which takes into account the properties co-clicked by the user in a specific time frame. Let us assume that in a year, a group of 1 million users are navigating through the London properties catalogue. Every time a user clicks on multiple items during the search, the number counting the co-clicked pairs increases by one. All

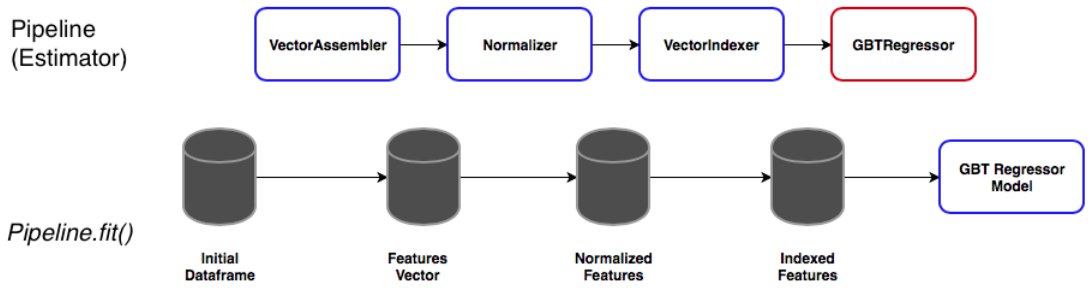

Figure 3.14: Workflow for a machine learning pipeline on ML-Spark. The top flow shows the abstract steps that are performed on the data. The bottom represents the transformation applied to the data when the *fit(·)* method is invoked on a dataframe.

the values are scaled within [0, 1] range for estimating the similarity. The main problem of this similarity measure, based on implicit feedback from the user, is that for each new item added to the catalogue, there is no historical data available, resulting in 0 similarity with all other items. The first objective of this research is to find an approximation function (based on non-historical features), which can be used as a proxy of the co-clicks (when they are not available). To achieve this, two sets of engineered features based on amenities and geographical position are investigated. I carried out two experiments using the amenities: the first one implements the Jaccard similarity metric (Niwattanakul et al., 2013; Park and Kim, 2017) and the second one - the Weighted Hamming distance. The Jaccard similarity (within [0, 1] interval, where 0 means completely dissimilar and 1 represents identical), is defined in Eq. 3 where f_i and f_j are the two sets of amenities related to properties i and j. The Jaccard similarity only considers the number of shared amenities, without giving any preference to the amenity popularity. On the other hand, the Weighted Hamming distance (within $[0, \text{inf}]$ range, when used as similarity measure a lower value means more similar) takes into account the number of properties in which the amenity is available (Eq. 4), where W is the amenity weight vector. Each element of W is calculated as Inverse Document Frequency (IDF):

$$w_k = \text{idf}(k, D) = \log\left(\frac{N}{|d \in D : k \in d|}\right) \quad , \tag{36}$$

with D representing all amenity sets, N the total number of items (properties), and $|d \in D : k \in d|$ the number of properties in which the amenity k is available. For the geographical features, a Fuzzy-C-Means (Pal et al., 2005; Koohi and Kiani, 2016; Farokhi et al., 2016) (or soft clustering) algorithm is implemented to group the properties and subsequently the Euclidean distance of their membership functions is used to calculate their similarities. To cluster the properties, a three stage Spark pipeline is built: vectorization; standardization; and clustering. The vectorization transforms a dataframe with one column per feature in a one column dataframe containing a vector of features. The 0-mean and unit-variance standardization is then applied to each feature in the vector and the clustering groups the properties, based on a given parameter c (number of clusters). The choice of c is empirically tested with values between 5 and 100, with incremental step of 5. The final choice resulted in c = 10 for two main reasons: the MAP@X accuracy was not significantly improving for values greater than 10; and the clusters were meaningful (e.g., properties in the city centre all in the same cluster, or near commute connections all in another cluster, etc). While the Jaccard and Weighted Hamming are metrics able to measure the similarity between two properties based on the quantity (the former) and quality (the latter) of shared amenities, the Fuzzy-C-Means is solely depending on the geographical characteristics, calculated using the latitude, longitude and their derived geo-features (given in Section 3.4.1). For the co-clicks similarity prediction, the MAP@x (x = 5) is used as accuracy measure. Table 3.26 shows the probabilities of ranking property pairs with the three-similarity metrics against the co-clicks ranking property at first place and in the top five positions. In particular, the second column of the table gives the probability of a property being ranked first by the co-clicks to be also ranked at the top by the other three metrics, while the third column illustrates the probability when comparing the first five positions of the rankings. In other words, column three show the accuracy of the Jaccard similarity, Weighted Hamming distance and Fuzzy-C-Means rankings against the co-clicks similarity with rank from 1 to 5 (the first five are chosen because they appear at the top of the screen). As can be seen from Table 3.26, the accuracy when using the amenities as similarity measure is very

low (11% and 25% for the Jaccard similarity and 9% and 22% for the Weighted Hamming distance respectively). The poor results can be explained by the correlation between the co-clicks and the position of the properties in the raking (two closely ranked items would have higher probability of being co-clicked in the same session), while the amenities similarity (either Jaccard or Weighted Hamming distance) only correlates properties based on the number and type of matching amenities. For the Fuzzy-C-Means ranking, the achieved accuracy is much higher (35% and 60% for the two ranking groups respectively) and this could be related to the fact that usually the listed properties are geographically close (in each search session the shown properties are from the queried destination). While the co-clicks still give a better insight of the properties similarity, implicitly reflecting the users behaviour and choice; the geographical clustering offers a good approximation with a 35% of correctly ranked items in first position (rank = 1), and 60% in the top 5 rankings, when the co-clicks similarity information is missing (due to the lack of historical data for the new properties).

Table 3.26: MAP@5 accuracy scored by the three proposed similarity measures compared only with the pairs of properties with co-clicks rank $\in$ [1,5]. The second column shows the probability of a property ranked first by the co-clicks similarity, to be ranked in the first 5 positions by the other similarity metrics. The third column shows the accuracy of a property ranked in the first 5 positions by the co-clicks similarity and all the other similarity metrics.

Method	co-clicks rank = 1	co-clicks $1 \leqslant$ rank $\leqslant 5$
Jaccard similarity ranking	0.11	0.25
Weighted Hamming distance ranking	0.09	0.22
Fuzzy-C-Means ranking	**0.35**	**0.60**

Two of the most frequently used features when selecting a property from a catalogue are the users rating and the quality of the property (e.g., star rating). Very often this information is missing when a new item is added to the website and both the RS and the user are most likely to underestimate its potential. To provide fairer ranking (as a second objective of this research), the two ratings are imputed using available non-historical features (e.g., amenities and geographical position). From the initial dataset, I took out all the instances with missing

guest or star rating, which resulted in a complete subset (with no missing values). This set was then further split into 70% training and 30% testing subsets respectively. Subsequently, missingness is introduced artificially in the guest and star ratings, producing an incomplete testing set - used for the assessment of imputation methods performance. Two baselines (mean and median imputation) and the three state-of-the-art approaches for missing data imputation are applied: K-Nearest neighbours Imputation (KNNI), Random Forests Imputation (RFI) and Gradient Boosted Trees Regression (GBTI). All methods are described in the background section and are here implemented using the Apache Spark framework.

For the KNNI a value of K = 10 is used as suggested in (Batista and Monard, 2002). The main disadvantage of this method when applied to big data is the low scalability due to $O(N^2)$ comparison needed and its questionable robustness of the results (e.g., compared to ensemble methods). Both RFRI and GBTI used in this work minimise the MAE function and use a 10% validation set to avoid overfitting. The ML-Spark library implementation is used for both tree models.

Firstly, the two baselines are used to calculate the mean (median) of the guest rating (star rating) on the training set and substitute it in the test set. Secondly, the model based imputation approaches are used. For each instance of the test set (all with missing ratings), KNNI is used to calculate the ten most similar neighbours from the training set, minimizing the Euclidean distance on the weighted amenities and geographical features. The imputed value then is the average of these ten guest and star ratings. For the RFI and GBTI, a four stage Spark pipeline is set up to ensure replicable experiments: vectorization, standardization, cross validation, and regression. The cross-validation step splits the complete dataset into a set of folds which are used as a training and validation subsets. E.g., with 10 folds, the cross validator generates 10 (training, validation) dataset pairs, each of which uses 9/10 of the data for training and 1/10 for validation iterating through them during the training phase. The regression step involves the two algorithms described in Section 2.1 (i.e., RFRI and GBTI).

Table 3.27 contains results from applying the above imputation techniques on guest and star ratings. As expected, the two baselines (mean and median imputation) achieved the lowest accuracy with MAE of 1.21 and 1.01 for the guest rating, and 0.70 and 0.75 for star rating. From the implemented state-of-the-art algorithms, KNNI produced the worst accuracy (0.70 and 0.50 for star and guest rating respectively). This approach also appeared to be very slow, because of the large number of samples in the training set (about 200K samples). The GBTI technique with standardized features achieved the best result (0.36 for star rating and 0.34 for guest rating), followed by the RFI with the same setup (0.39 and 0.47 for star and guest rating respectively). The same experiments were repeated removing the amenities from the dataset to assess the importance of this feature. While the use of amenities as a feature failed the prediction of the co-clicks similarity (Table 3.26), their use in the ratings imputation improved the overall accuracy (Table 3.27). These contradictory results can be explained by the fact that the amenities partially define the quality of the property (e.g., a property with amenities such as pool and spa has higher likelihood to be rated as a 5 star). On the other hand, the geographical position seems to be useful for determining the guest rating (e.g., properties close to stations, airports or famous landmarks have greater probability of receiving a higher rating).

Table 3.27: Guest rating and star rating imputation errors. The MAE is used as error function to compare the imputation results of two baselines (mean and median imputation) and three state-of-the-art approaches (KNNI, RFI, and GBTI). The experiments are performed with (v) or without (-) amenities and standardisation.

Method	Amenities	Standardization	Guest Rating		Star Rating	
			MAE	SD	MAE	SD
Mean	v	-	1.21	1.17	0.70	0.65
Median	v	-	1.01	0.99	0.75	0.71
KNNI	v	-	0.70	0.66	0.50	0.45
RFI	v	-	0.40	0.37	0.42	0.40
	-	-	0.44	0.40	0.50	0.46
	v	v	0.39	0.35	0.47	0.44
GBTI	v	-	0.37	0.34	0.39	0.36
	-	-	0.40	0.37	0.44	0.42
	v	v	**0.34**	**0.31**	**0.36**	**0.33**

Here I combine the geographical features, amenities and imputed guest and star ratings to re-rank the properties in two million searches collected in one month (Table 3.28) using Algorithm 2.

The third row of the table shows 65% searches without VR in the top 10 rankings (35% of the searches already contain at least one VR in the top 10, so they are not affected by the algorithm). From the 65% searches, only those with VR ranked higher than 10 (rank > 10) are considered, resulting in total eligible searches of 31% (row 4). Subsequently, from the 31% of searches, the feasible VR are subject to three main rules: do not boost VR too far from the paired hotel (row 5); do not boost VR which is not similar enough to its paired hotel (row 6); and only consider hotels ranked in positions 5 to 10 for the pairs (row 7). Following these rules brings the number of eligible searches (row 8) to 291705 (13%), with 1801023 (the number of hotel-VR pairs that satisfy the distance and similarity metrics) possible boosts (6 possible boosts per each search on average).

Table 3.28: Offline experimentation on one month of real world searches. The total number of searches and the eligible searches for a boost after applying different filters are shown. The last two rows give the total number of possible boosts and the number.

Types of searches	#Searches	%Searches
Total searches	2206479	100
Without VR in top 10	1446976	65
VR with rank > 10	697418	31
Searches with eligible VR within chosen *distance*	324289	14
Searches with eligible VR within chosen distance, and $sim < \alpha$ (0.05)	316977	14
Searches with eligible VR within chosen distance, $sim < \alpha$ (0.05) and hotels ranked between 5 and 10	291705	13
Types of boosts	#Boosts	%Boosts
Total number of possible boosts	1801023	100
Total number of optimal boosts (in the Pareto front)	449070	25

At this point the Pareto optimization using the two objectives (pair similarity and pair price difference) is applied considering only non-dominated solutions. This approach reduced the number of possible boosts by 75% (1.54 possible boosts per search on average), excluding all dominated Pareto solutions. The selection of similarity threshold (row 6 of Table 3.28), beside the use of human

expertise, can be done applying statistical test to ensure that the similarity and price difference are statically significant (p-value < 0.05) (the difference is small enough to consider a boost). To do so, all the points from each Pareto front are standardized with 0-mean and unit-variance. From the set of standardized points, I consider only those with std < 2 (assuming normal distribution, this corresponds to the 95^{st} percentile). Figure 3.15 shows the standardized Pareto front for a one-day searches. All solutions with std > 2 are not considered. A statistical t-test is finally used to compare the distribution of the features in the top 10 ranks (e.g., guest rating, star rating, price, distance from city centre, distance from airports, etc). The t-test showed that the boosting of one Pareto optimal VR in each search doesn't statistically change these distributions (p-value < 0.05). The same t-test repeated when boosting dominated Pareto VR solutions, showed statistical changes in the features' distribution of the top 10 ranks (p-value $\geqslant 0.05$). This results leads to the conclusion that the sub-optimal VR solutions are not recommended during the boosting phase due to the statistically different features from those of the compared hotels.

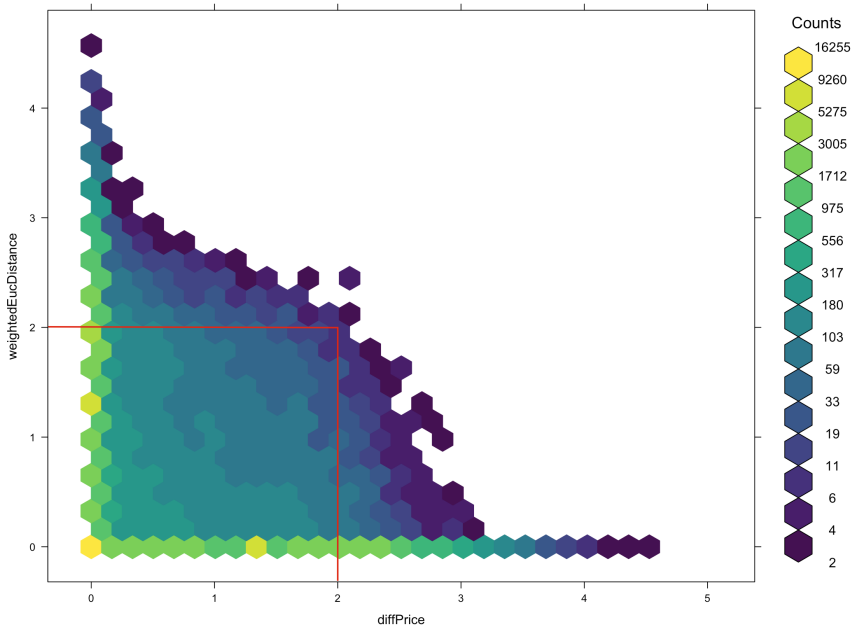

Figure 3.15: All Pareto front solutions standardized with 0-mean and unit-variance. Only the solutions with std $\leqslant 2$ are used for the boost (all hexagons in the (2, 2) square). This plot illustrates a sample of only one-day searches (about 70000). The x and y axes represent the difference in price and property similarity respectively.

3.4.5 Discussion

The missing data problem for travel Recommender Systems is investigated giving focus on the VR market. After an initial exploratory analysis, the dataset of properties at hand showed 50% and 19% missingness for guest rating and star rating respectively. Furthermore, the properties similarity, namely the co-clicks, is always missing when a new property is added in the catalogue (because there is no historical data of users co-clicks with other properties). To deal with that, non-historical features (amenities and geographical position) are introduced, analysed and used to determine the best proxy of the co-clicks (when not available). Results from the applied three similarity measures (Jaccard, Weighted Hamming and Fuzzy-C-Means rankings) showed the Fuzzy-C-Means to be the best approximation metric with 35% of correctly ranked items in first position, and 60% for the top 5 rankings, indicating a correlation between the co-clicked properties and their position on the map. The applied data imputation techniques for mitigating the guest and star ratings missingness (two baselines: mean and median imputation; and three state-of-the-art models: KNNI, RFI, and GBTI), resulted in recommending the GBTI as the most suitable one for this task, achieving the lowest MAE (0.36 and 0.34 for guest and star rating respectively), followed by the RFI and KNNI. As expected, the baselines scored the lowest accuracy, with an error greater than 1 for guest rating and 0.75 for the star rating (both ranging one to five). Furthermore, the importance of amenities as a feature for this task is assessed repeating the same experiment using only the geographical features. While the use of amenities failed the prediction of the co-clicks similarity (with an accuracy between 9% and 25%), their use in the ratings imputation always improved the overall accuracy. Lastly, the VR long tail is considered as a multi-objective problem, optimising the hotel-VR similarity and their difference in price as the two objectives. From an initial 2 million considered searches, only 35% had at least one VR in the top 10 rankings, while after the Pareto optimization, the percentage increased to 48%. Furthermore, the boost of optimal solutions (non-dominated) does not change the distributions of the features in the head of the list. Future work would analyse the

behaviour of the RS when the engineered and imputed features are used during the recommendation process for the VR properties. In addition to that, new error functions will be tested to assess and distinguish the current under/over estimation of the imputed ratings by the model based techniques.

3.5 Large Scale Missing Data Imputation

When Big Data is considered, the problem of the missing data imputation is still of primary importance for the successful implementation of machine learning techniques (e.g., recommendation tasks where millions of users and thousands of items are involved). Usually, the probability of having missing data increases with the number of features in the dataset and with the number of samples, making the imputation task in big data context extremely important. However, if the missing entries are few compared to the scale of the dataset, a deletion method is applicable without losing statistical strength. On the other hand, if the number of missing values grows with the size of the dataset the imputation is necessary to preserve, or even increase, the statistical power of the data (or in general to not lose too many samples during the pre-processing stage). Unfortunately, almost all the imputation techniques proposed in literature (Musil et al., 2002; Schmitt et al., 2015; Petrozziello and Jordanov, 2017a, 2018) require the whole dataset to be provided for the model at imputation time, which means that adequate memory allocation is needed, making the task unfeasible for datasets composed of hundreds of features and millions of samples. Not many methods have been proposed to cope with the missing data problem in the big data field (Anagnostopoulos and Triantafillou, 2014) due to the inherent complexity of the task (both related to time and memory constraints). Neural Networks are state of the art machine learning approach for several different domains with recent advances in image processing (Sun et al., 2013), pattern and speech recognition (Deng et al., 2013), that involve fitting of large architectures (with thousands of weights) to large datasets (several gigabytes to few terabytes). Given the scale of these machine learning problems, training can take up to days or even weeks on a single machine using the commonly applied

optimization techniques (e.g., stochastic gradient descent (SGD)) (Bottou, 2010). For this reason, research focussed on the distribution of machine learning algorithms across multiple machines. Different attempts have been made to speed up the training of NN using asynchronous jobs (Chilimbi et al., 2014). In the parameter server model (Li et al., 2014), one master holds the latest model parameters in memory, serving the workers nodes on request. The nodes compute the gradient on a mini batch drawn from the local hard drive. The gradients are then shipped back to the server, which updates the model parameters. With the introduction of the Map-Reduce paradigm, different frameworks emerged to leverage resources of a cluster (e.g., Apache Hadoop and Apache Spark). Here, I propose a Distributed Neural Network Imputation (D-NNI) framework (Figure 3.16), leveraging the idea of mini-batch training in a distributed fashion over Spark to reduce training time, while making at the same time the imputation of new values possible even for larger datasets. The proposed imputation approach (Petrozziello et al., 2018b) is tested on a real-world dataset composed of 400K samples (Petrozziello and Jordanov, 2017b), and 645 features (of which 57 including missing values).

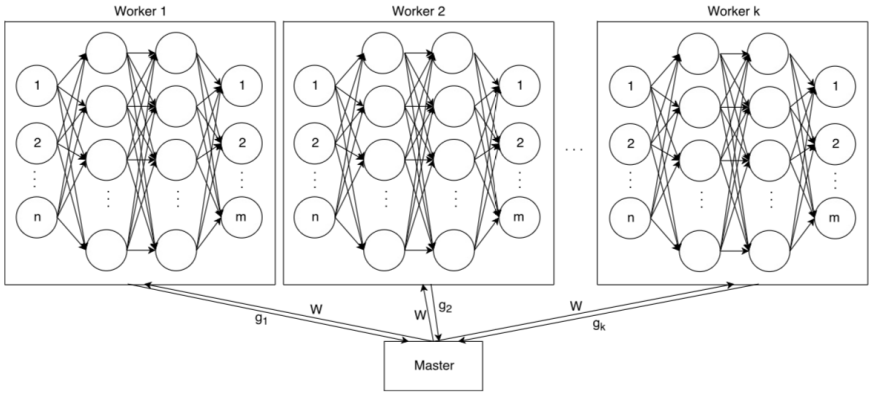

Figure 3.16: Distributed Neural Network architecture in Spark (Section 3.5.1).

3.5.1 A distributed Neural Network architecture on Spark

The implementation of the imputation stage through distributed neural networks builds on Apache Spark and the open source Neuron library (Unknown, 2017) (a lightweight Neural Network library written in Scala providing all the

Table 3.29: Neural Network Trait.

```
trait NN {
   def initNetwork(nInputs:Int, nOutput:Int):Unit
   def setWeights(weights: DenseVector[Double])
   def apply(denseVector: DenseVector[Double],
       memKey:String)
   def apply(denseMatrix: DenseMatrix[Double],
       memKey:String)
   def backpropagate(loss:DenseVector[Double],
       memKey:String)
   def backpropagate(loss: DenseMatrix[Double],
       memKey:String)
   def getGradient()
   def getWeights()
   def getNumberOfWeights()
   def getLastLayerWsize()
}
```

building blocks (e.g., layers, optimizers, back-propagation, etc.), to create our own distributed version (Table 3.29 shows the Neural Network Scala interface). By building on top of Spark, I utilise the advantages of modern batch computational frameworks, which includes: the high-throughput loading and pre-processing of data; and the ability to keep data in memory between operations. Furthermore, the implementation of the D-NNI as a Spark pipeline stage allows the imputation to be easily included as a pre-processing stage of any dataset. Table 3.30 and Table 3.31 show code snippets of how the imputation stage is created. In particular, Table 3.30 presents how the layout of the network is defined (using a sequence of layers, with the initial one representing the input, and the last one the output (which can be as large as the number of imputed features)), while Table 3.31 demonstrates the creation of a Spark pipeline imputation stage. The *NeuralNetworkImputationStage* object exposes several methods to: set the input columns (i.e., the features used during the learning phase); the target columns (the ones containing missing values); the predicted columns (the stage returns a new dataframe containing additional columns with the imputed values); and the additional parameters used during the imputation procedure (i.e., the NN layout as defined in Table 3.30, the optimizer hyper-parameters, the weights initialization procedure, the loss function, etc).

In this work I use a data-parallelization schema with synchronization and a

Table 3.30: Example of network specification for D-NNI.

```
networkLayout: Seq[layerConf] =  Seq(
   layerConf("linear", 20, 10),
   layerConf("Relu", 10, 10),
   layerConf("linear", 10, 5),
   layerConf("Relu", 5, 5),
   layerConf("linear", 5, 1),
   layerConf("sigmoid", 1, 1)
)
```

Table 3.31: Create a Missing Imputation Stage in a Spark pipeline, the *fit(·)* method is used to train the imputation model, once the model is trained (i.e., imputationModel object), the missing values can be imputed using the *transform(·)* method of the model.

```
val imputationModel = new NeuralNetworkImputationStage()
   .setFeatureColumnName("features")
   .setTargetColumnName("missingFeatures")
   ,setPredictColumnName("imputedFeatures")
   .setOptimizerParameters(optimizerSGD(10, 5, 0.0001)
   .setNetworkLayout(networkLayout)
   .trainWithMatrices(true)
   .setWeightInitializationType("heUniform")
   .useValidation(true)
   .setValidationPerc(0.10)
   setLossFunction("l2distance")
   .fit(data)
val newData = imputationModel.transform(data)
```

central coordinator, labelled naive parallelization by Moritz et al. (2015). In every iteration, each worker node c in the cluster C computes a local gradient g_c for a batch of data b_c, then these vectors are (tree-) aggregated,

$$g = \frac{1}{C} \sum_{c} g_c(b_c) \quad , \tag{37}$$

and sent back to the master which performs the SGD update step and broadcasts the new weights (W) to all $c \in C$ (Figure 3.16). In the absence of network overhead and aggregation cost this setup scales linearly with the number of worker nodes. Under more realistic conditions, the optimal number of nodes depends on the size of b_w and the network overhead.

Table 3.32: Sample of the dataset containing the features used for the properties recommendation. Missing values (values that are not available for a short history) are denoted with a "-".

ID	nDays in Catalog	Latitude	Longitude	Am. 1	..	Am. 500	# landmarks	Dist Airport	Avg Price last 3 days	#bookings last 180 days	#bookings last 365 days	Pct bookings month 1
140759	5730	37.78	-122.40	0		0	92	19.27	1.47	511	2254	0.05
431602	1484	-2.42	-54.73	0		0	1	5.29	0.94	0	84	0
17905696	133	21.73	-79.99	0		1	1	>500	0	-	-	-
189642	5730	32.91	-97.01	1		1	1	3.36	0.65	889	4250	0.09
679498048	28	41.38	2.18	0		0	137	0.24	1.43	-	-	-
637314944	111	27.79	-82.79	1		0	0	16.03	1.39	-	-	-
636663872	112	47.80	7.67	1		1	2	24.87	2.91	30	-	-

3.5.2 Empirical study design

To test the proposed technique I partially re-use the dataset of Section 3.4.1. In addition to the already seen *amenities*, *properties* and *destinations* tables, I also included a dataset of *historical prices* displayed on the website, calculated using three different time spans: a 1-day; a 3-day; and a 7-day average. This additional information is joined to the others on the property ID to have all needed information for a each specific property. A subset of features of this final dataset is showed in Table 3.32, while a summary of the features contained in each dataset is given in Table 3.33.

The proposal is compared with two baselines (mean and mdian imputation by market) and two state-of-the-art techniques (Linear Regression Imputation (LRI) and K-Nearest Neighbour Imputation (KNNI) which are easy to distribute and already available in the Apache Spark framework (also described in Section 2.1), while the results are assessed on the R^2 coefficient (Eq. 18) as both RMSE and MAE are scale dependent and therefore of hard comparability across a large set of features.

Table 3.33: Summary of the features used in the OTAs dataset.

Feature Type	# of Features
Amenities	500
Properties	20
Destinations	11
Displayed Prices	57

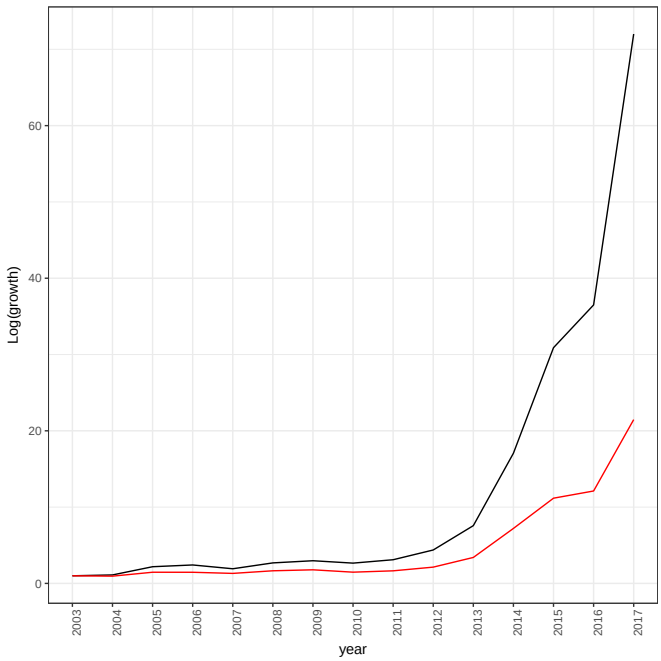

Figure 3.17: Log growth of the properties in the catalogue (black line) and log growth of missing data (red line).

3.5.3 Results and discussion

The empirical experiment on the RS for OTA dataset is carried to test the imputation accuracy and time feasibility of the proposed technique. Before the imputation, the data is split into a training set (70%) and a test set (30%). The investigated NN topology includes two hidden layers (n-n-n-k), with n being the number of inputs (n = 657) and k the number of outputs (k = 57). After each hidden layer, a ReLU activation function is used to transform the data (a ReLU is also applied in the output layer as all the missing values belong to features in $R_{\geqslant 0}$. The training set is further divided into 80% for training and 20% for validation, and the R^2 coefficient is used to evaluate the learning performance. The stopping condition includes 2000 training epochs, gradient reaching value less than 1.0E-06, or 6 consequent failed validation checks, whichever occurs first.

Figure 3.18 shows the R^2 metric across the 57 considered features. As can be seen, the D-NNI outperforms the other techniques (larger R^2 value) for many of the imputed features. The range of R^2 for the D-NNI spans from 0.07 to 0.95 with a median of 0.56. The second best method (LRI) has its lowest imputation performance at 0 (same as all the other compared techniques), the best

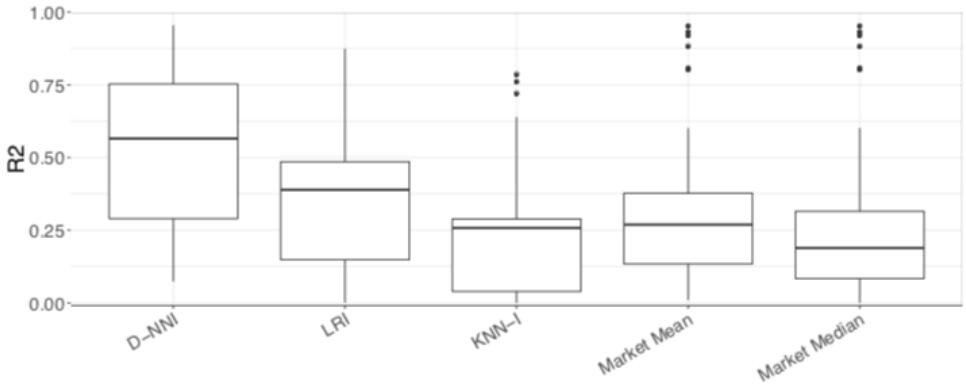

Figure 3.18: Boxplot for the R^2 measure on the 57 imputed variables.

at 0.87 and a median R^2 of 0.38. Following are the mean imputation, KNNI and median imputation with 0.27, 0.26 and 0.18 median R^2 respectively. It is also worth to notice that the mean and median imputation techniques have a few outliers reaching an R^2 above 0.80, this is happening with features skewed toward one value (low variance), hence closer to the mean (median) of the imputed one. The R^2 for each feature with missing values is also presented in Figure 3.19. As can be seen, the prediction accuracy of the D-NNI is always greater of those provided by the LRI and KNNI. For the mean (median) imputation, the D-NNI is better in 51 out of 57 cases, while still being comparable in the six remaining features (i.e., pct_gt_ly_amer_posa_h, pct_gt_ly_emea_posa_h, etc. (see Figure 3.19). Figure 3.20 shows one of the best (i.e., gt_ly_h) and worst (i.e., pct_gt_stay_month_4_h) imputed features for the D-NNI, illustrating the NN ability to predict with high accuracy continuous features (Figure 3.20a), while struggling with the zero inflated ones (Figure 3.20b) (but still achieving better imputation accuracy compared to the other models).

Furthermore, in Table 3.34 the running times over 10 runs for the five imputation techniques are displayed when using the following Amazon Web Service cloud cluster configuration: Master (r4.xlarge, 30gb, 4 cores) and 8 Workers (15gb, 8 cores). The average and standard deviation in minutes are reported, showing the D-NNI as the slowest method to impute, with a large variance across different runs (depending on the convergence speed for the training phase). The second slowest method is the LRI. Here, the 57 features contain-

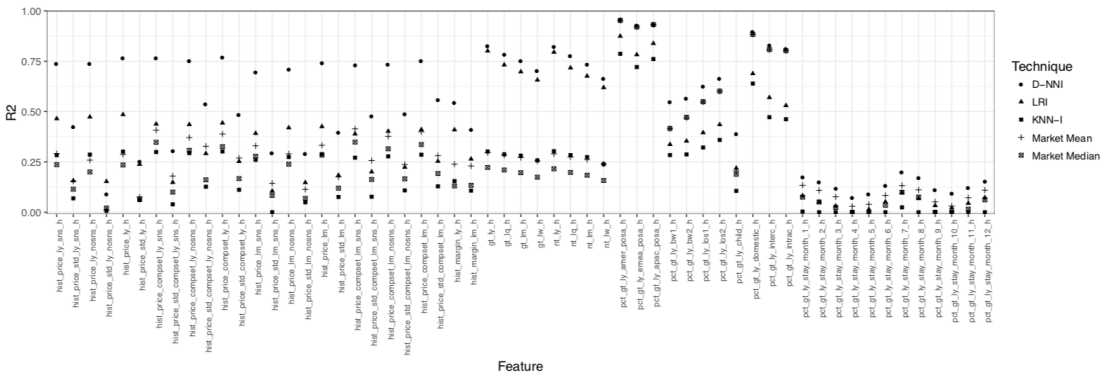

Figure 3.19: Boxplot for the R^2 measure on the 57 imputed variables.

ing missing values are independently fitted, reason for the achieved imputation speed. It would be expected a linear decrease in speed using up to 57 workers (where each node of the cluster is fitting a different feature). The fastest imputation models appeared to be the mean (median) imputation, where the prediction only finds the average (median) of each feature with missing values. The KNNI speed is not reported as the imputation was not possible with the considered cluster configuration (not enough memory to fit the N^2 pair matrix). When increasing the cluster size to 20 nodes, the KNNI imputation took 40 minutes, with a standard deviation of 8 minutes, mainly due to communication latency among the workers.

Table 3.34: Average and std run time (in minutes) over 10 runs.

	D-NNI	LRI	KNNI	Mean Imputation	Median Imputation
Avg	24	12	-	< 1	< 1
(Std)	(±10)	(±5)	-	(± 0)	(± 0)

Table 3.35: Speedup ratio of the NN compared to the sequential model, for number of samples in batch (10% to 70%) against number of workers (2 to 8).

	10	20	30	40	50	60	70
2	2.89	2.40	1.69	1.45	1.27	1.21	1.12
4	3.85	3.62	2.13	2.21	1.97	1.93	1.68
8	3.35	2.95	1.96	2.12	1.71	3.06	2.63

To measure the D-NNI sensitivity to the batch size and the number of workers, I consider a grid of values from 10 to 70 for the first parameter, and 2 to 8 for the second one. For each training run I compute the achieved speedup (Eq. 26)

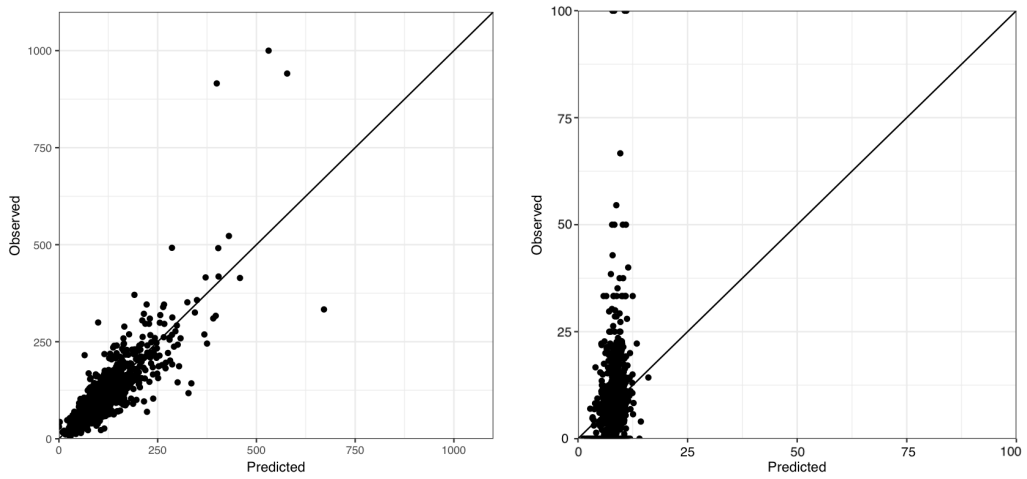

(a) (b)

Figure 3.20: Predicted (x-axis) and observed (y-axis) values for the D-NNI. Figure 3.20a (left) shows the historical yearly gross transactions of each property, while Figure 3.20b (right) depicts the yearly percentage transactions for one month (April).

relative to training on a single node (sequential NN with SGD). In Table 3.35 the imputation speedup for the D-NNI model under 21 different settings is reported. Table 3.35 exhibits several trends, with the top row representing the case of two machines. As can be seen, the speedup decreases when incrementing the batch size, which is due to the training taking the largest part of the total computational time, while the communication between nodes is negligible. The same trend still holds in the case of 4 machines (2^{nd} row). In the 3^{rd} row, the trend shows reduction of the speedup up to the batch size of 50%. The subsequent increase of the ratio (for 60% and 70%) could be due to the time being evenly split between training and communication, and from randomness due to fluctuation in the convergence of the optimization process.

Another interesting trend can be observed when inspecting the table by columns. Is true almost for all cases that the use of 4 nodes gives the best speedup over 2 and 8. This could be explained by the quantity of data used for training. When a certain threshold for the number of workers is passed, the overhead for communication and synchronization can become larger than the actual processing time. This is enforced by the fact that the trend is less accentuated when moving toward bigger batches. For 40% and 50%, the speedup for 4 and 8 nodes

is almost identical, while for 8 nodes the speedup is higher when using more than 50% of data in each batch.

3.6 Conclusion

Here, the missing data problem affecting machine learning tasks has been investigated. This chapter explored a variety of use cases where the effective imputation of missing values can benefit the learning process. An extensive search through related works in missing data imputation allowed to identify a series of gaps which have been tackled and different novel solutions have been proposed. The main proposals are: the analysis of the impact of missing data on the radar classification task in both the binary and multi-class settings; the "Scattered Feature Guided Data Imputation" which focuses on finding the best performing imputation algorithm for each feature of a dataset through a learning procedure; the study of the impact of missing data in Recommender Systems and the proposal of a bi-objective Pareto front algorithm to boost unfairly ranked properties after imputation of their missing values; and the "Distributed Neural Network Imputation" which allows to impute missing data at scale (datasets not fitting on one machine) through the use of the Spark framework and a cluster of machines.

4 Deep Learning Methods for Real-World Problems

In this chapter I investigate the use of Deep Learning approaches applied to three real-world problems. In the first one, I use both Convolutional Neural Networks and Long Short Term Memory Networks for the detection of hypoxia during labour. Those models are compared with current clinical practice and computerized approaches and a new architecture, namely Multimodal Convolutional Neural Network is proposed Petrozziello et al. (2018a, 2019). The second part of this chapter explores the profitability of Multivariate Long Short Term Memory Networks for the forecast of stock market volatility. The method is compared with univariate and multivariate Recurrent Neural Networks, as well as with state of the art univariate techniques from the financial field. Lastly, Convolutional Neural Networks and Stacked Autoencoders are used to detect threats from hand-luggage and courier parcel x-ray images (Petrozziello and Jordanov, 2019).

4.1 Deep Learning for fetal monitoring in labour

During labour, materno-fetal respiratory exchange is transiently compromised by uterine contractions leading to reduced oxygen supply to the foetus. The foetus responds by adjusting its cardiac output, redistributing blood to prioritise the heart and brain, and adapting metabolically. Failure of fetal compensation leads to brain injury or death. The cardiotocogram (CTG, Figure 4.1) continuously displays the fetal heart rate and uterine contractions on a paper strip. This is examined visually in real time to detect the foetus that may benefit from emergency operative delivery (Caesarean or instrumental vaginal birth). The CTG is exceptionally complex, showing patterns that variably reflect periodic changes in fetal sleep state, responses to the stresses of uterine contractions, responses to maternal position, anaesthesia, pregnancy complications, infection, stage of labour, in addition to features that reflect terminal decompensation.

Hence, fetal assessment in labour is challenging and progressed little in the past 45 years (Timmins and Clark, 2015). In the developed world, the long

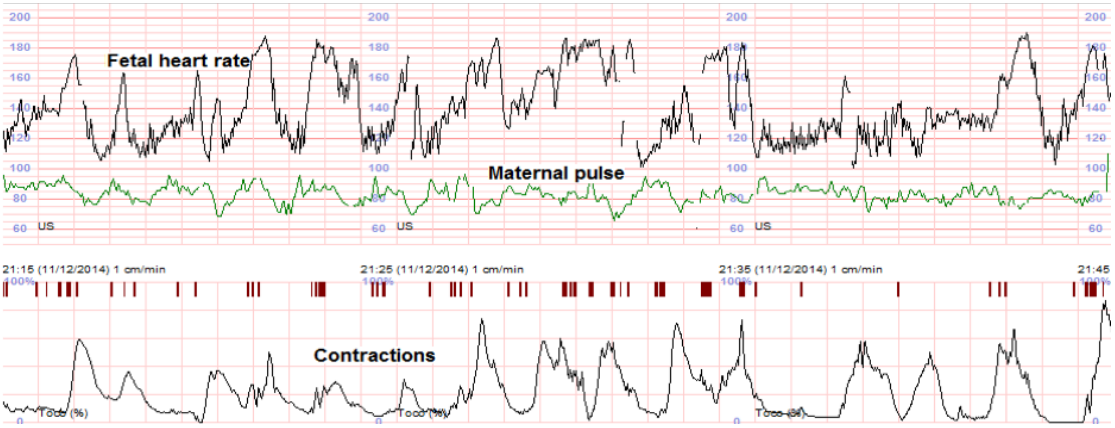

Figure 4.1: Cardiotocogram (CTG) in labour (a 30min snippet).

time series of the CTG are still assessed by eye (Figure 4.1). In the UK, during labour at term, about 100 healthy babies die and about 1100 sustain brain injury (Kurinczuk et al., 2010; Walsh et al., 2008). Nearly 50% of the total NHS litigation bill is due to obstetric claims (3.1bn in 2000-2010), the majority relating to shortcomings in labour management and cardiotography interpretation (Figure 4.1) (Authority, 2012). Each neonatal death or permanent brain damage is devastating for the family. The cost of insurance against litigation per birth in the UK is 20% of the total delivery cost (Davies, 2015). At the same time, around 100 unnecessary emergency deliveries are performed each day in the UK alone, with major financial and potentially life-long consequences, such as increased risks of uterine rupture and/or stillbirth in next pregnancies, maternal incontinence, and post-traumatic stress disorder (unpublished estimate based on the database provided by Oxford, UK). Worldwide, about 2.6 million stillbirths occurred in 2015. Intrapartum stillbirths predominantly occur in low resource settings and overall are considered to be mostly preventable by CTG monitoring in labour (Lawn et al., 2016), which is largely not available in the developing world. However, due to its high false positive rate, even in the developed world, CTG is often not offered in labours considered to be *low-risk*.

The work presented here arises from prior work with the Oxford digital archive of 59279 term deliveries: a uniquely large birth cohort spanning nearly 20 years and growing daily. Georgieva et al. (2017) have already developed a basic prototype diagnostic system (OxSys 1.5) that objectively quantifies the CTG in the

context of clinical risk factors; and relates these to perinatal outcome. OxSys 1.5 already compares favourably to clinical assessment (on retrospective data), with higher sensitivity for fetal compromise (37.6% vs. 32.2%, $p < 0.05$) and lower intervention rate in normal outcomes, i.e. false positive rate (14.5% vs. 16.4%, $p < 0.001$). However, OxSys 1.5 employs only two diagnostic rules based on feature extraction and clinical risk factors. The main CTG feature used by OxSys 1.5 is the decelerative capacity (DC) of the phase rectified signal averaging (PRSA) algorithm - a combined measure of the frequency, depth, and slope of any dips in the fetal heart rate (Georgieva, 2016; Georgieva et al., 2017). The large size of the data archive confers scope for substantial improvement. Deep Learning approaches have been successful with various real-world problems at "learning" the most relevant unbiased and new information from large datasets (LeCun et al., 2015). Hence, the aim is to apply Deep Learning to interrogate the CTG archive and establish optimal ways to classify the CTG into *high* and *low* risk.

In Section 4.1.5 (point 2) I report results of my pilot simulations and experiments of applying Long Short Term Memory (LSTM) and Convolutional Neural Networks (CNN) to CTG assessment: I analyse the CTGs from 35429 labours (85% were used for training with cross validation and 15% were set aside for testing). I demonstrate that increasing the training set size and considering information about the quality of the contraction signal improved the performance of the classifier. However, I only focused on the last hour of CTG monitoring without distinguishing or adapting to the stage of labour (an important clinical confounder to CTG interpretation) or including information about signal loss in the fetal heart rate signal. However, fetal heart rate signals are notorious for their poor signal quality owing to signal loss; erroneous pick up of maternal heart rate; signal noise or gaps in monitoring. Although both LSTM and CNN demonstrated promising performance worthy of further developments, CNN showed slightly superior results to LSTM. The LSTM is generally more suitable for forecast tasks over classification ones, and it suffered from vanishing gradient problems during back-propagation when learning on the long CTG records.

On the other hand, CNN proved to work effectively with long temporal data through the use of moving filters and max-pooling.

In Section 4.1.5 (points 3 and 4) I build on the pilot study and aim to improve my initial application of CNNs to CTG interpretation by: developing Multimodal CNN (MCNN) for CTG interpretation that allow the input of signal quality features (in this work) and other inputs (out of the scope here); developing Stacked MCNN to analyse separately the CTG before and after the onset of active pushing (first and second stage labour), while feeding the risk assessment from the first stage model into the second stage model; assessing the impact of the fetal heart rate signal quality on the models performance.

I also extend the range of the testing to a new external dataset: Signal Processing and Monitoring (SPaM) Workshop 2017 challenge dataset.

4.1.1 Datasets

1) Oxford data

I analysed the data from all monitored labours at the John Radcliffe Hospital, Oxford between 1993 and 2011 that met the following inclusion criteria:

- term delivery of a foetus at 36 weeks gestation or more;
- intrapartum (in-labour) CTG comprising fetal heart rate and contractions (Figure 4.1), longer than 15minutes, ending within three hours of birth (only *high risk* women are monitored in the UK - roughly 50% of births);
- validated cord gas analysis at the time of birth, indicating the adequacy of fetal blood oxygenation. In practice the acidity of the blood, measured by pH, is the most appropriate way of grading this problem and indicates an increased risk for long term compromise of the baby. Cord gases are analysed at the discretion of the clinician - in about 65% of all continuously monitored births in the Oxford unit.

Excluded are babies with breech presentation and congenital abnormalities. There are four exclusive groups according to the outcome of labour:

- severe compromise (comprising one or more of any stillbirth, any neona-

tal death, seizures, resuscitation followed by $\geqslant$ 48hrs in neonatal intensive, regardless of the arterial cord pH);

- moderate compromise: arterial cord pH at birth below 7.05;
- intermediate arterial cord pH between 7.05 and 7.15: the status of the outcome of an intermediate pH is uncertain. This is especially the case when delivery has been expedited for concerns about fetal welfare, when more severe problems could have occurred if the labour continued without intervention. These outcomes are labelled as intermediate/uncertain.
- normal: arterial cord pH$\geqslant$7.15.

A low arterial cord pH (increased acid content) reflects the duration of reduced fetal oxygenation at the time of birth. However, cases with severe compromise often have normal cord pH values at birth (about 60% of cases). These represent a heterogeneous group of pathologies in which the pathway to brain injury in utero is not fully understood. Cases with low pH (with or without severe compromise) represent a more homogeneous set indicating the fetal injury occurred as a consequence of oxygen deficiency specifically during labour and at birth. This is a group more likely to exhibit changes in the CTG to allow detection/prediction. For this reason, and for consistency with the open access datasets who define compromise as pH<7.05 (see below), I split the testing set to parts A and B and report the results separately (but still training the networks using all the data). Test Set A comprises of all Normal cases (n=4249) and all moderate compromises plus the severe compromises with cord pH<7.05 (n=180). Test Set B comprises of all intermediate/uncertain cases (n=845) and all severe compromises with pH $\geqslant$ 7.05 (n=40). This inclusion/exclusion criteria results in 35429 births with CTG in labour and details about the labour outcome. In these, the testing subset of CTGs were identified by a random selection of 15% of cases within each outcome group, ensuring similar rates of compromise in training and testing. Overall, there are 1796 (5%) traces shorter than one hour where I coded the missing values with zeros. The CTG data is originally available at 4Hz for the fetal heart rate and 1Hz for the uterine signal (as default output from the monitors). Signal loss or noise in the heart rate sig-

nal is common and here basic pre-processing is applied before smoothing the heart rate to 0.25Hz. Therefore, one hour of data corresponded to 900 heart rate and 900 contraction signal samples.

2) External open access datasets

Data-driven CTG interpretation is a narrow field with only several teams worldwide working on this clinical problem. In the past five years there has been a strong will from a few teams to begin creating open access databases that would allow comparison between different approaches, as well as providing at least some data for others to use as training data. Currently, there are two such datasets available and I tested the proposed algorithms on both: firstly, because routine data coming from other hospitals/countries would be inevitably influenced by varying clinical practice and ability to perform emergency intervention, providing therefore external validation; and secondly, because in the future, I would hope practitioners could use the same open-access datasets to test and compare new approaches.

The Signal Processing and Monitoring (SPaM) in Labour Workshop 2017 database comprises 300 labours collected from three participating centres (Lyon, Brno and Oxford). Each centre provided 100 cases: 80 with normal pH and 20 with pH<7.05, i.e. it was selected specifically to have a higher than usual rate of compromised cases (i.e. 20% which is five times higher than that in the Oxford cohort). To avoid any contamination between the SPaM data coming from Oxford and the Oxford training data, the proposed Deep Learning approaches are only tested on the 200 SPaM cases coming from Lyon (France) and Brno (Czech Republic).

The Czech Technical University / University Hospital Brno (CTU-UHB) comprises 552 cases of which 40 (7%) have cord acidemia at birth below 7.05 (more details on the dataset are provided in (Chudacek et al., 2014)).

4.1.2 Proposed Deep Learning models

To tackle the problem of an unbalanced training dataset (4% compromised babies vs. 96% healthy ones), I adopt a weighted binary cross-entropy error function:

$$CE = -t\log(s) - (1-t)\log(1-s) \quad , \tag{38}$$

where t_1 and s_1 are the ground-truth and the scores respectively.

The class weights is set such that one misclassification from the compromised group contributes to the error as much as 24 misclassifications from the healthy group (reflecting the incidence of 1 in 24 of compromised cases in the data). In the pilot experimentation, I also tested down-sampling and bootstrapping techniques to handle the imbalanced dataset in the training phase but with worse generalization performance on unseen data.

1) Preliminary Convolutional Neural Networks (CNN) and Long Short Term Memory Network (LSTM)

As a first experimentation, I implemented both CNN and LSTM models. The proposed single channel CNN has one input layer with size 2x900 points, corresponding to one hour of fetal monitoring at 0.25Hz (fetal heart rate and contractions). The network comprises five convolutional layers (with max-pooling and ReLU activation function) Figure 4.2. The last max-pooling layer is flattened and fed as input to a fully connected layer. The class probability is then computed using a softmax activation function. Batch normalization and dropout are used through the network (Wan et al., 2013). I assess the quality of the CTG contraction signals by an established autoregressive model (Cazares et al., 2001), imposing the following restriction: >40min of acceptable quality, of which >20min is of excellent quality. To avoid overloading the network with noise, only the uterine signals that met this condition is used in the networks (24%), whereas the remainder are substituted with zero.

The implemented LSTM follows the model presented by Graves (2013). The

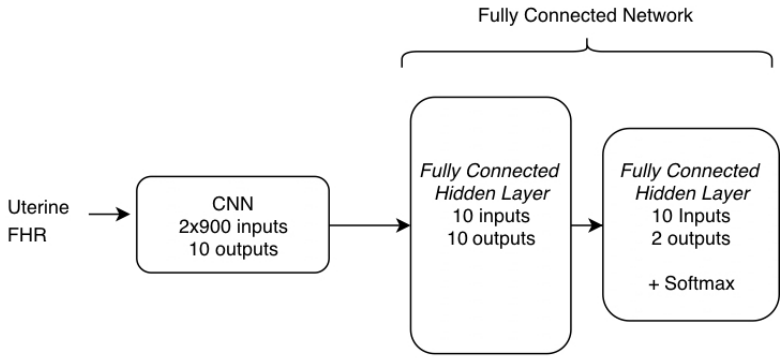

Figure 4.2: Convolutional Neural Network topology. FHR - fetal heart rate; CNN - convolutional neural network.

main advantage of this architecture is its ability to capture both long and short time dependencies in time series, which have proven to be effective in many domains (including medical applications) (Choi et al., 2016). The LSTM has two inputs: fetal heart rate and contraction signals; and two outputs: healthy and compromised newborns. The LSTM architecture includes hyperbolic tangent as a hidden activation function and a hard sigmoid as a recurrent activation (default activation functions for LSTM, as advised by Hochreiter and Schmidhuber (1997)). To get a binary class probability, a softmax function is used in the output layer (Figure 4.3). The data is normalized before being inputted in the LSTM.

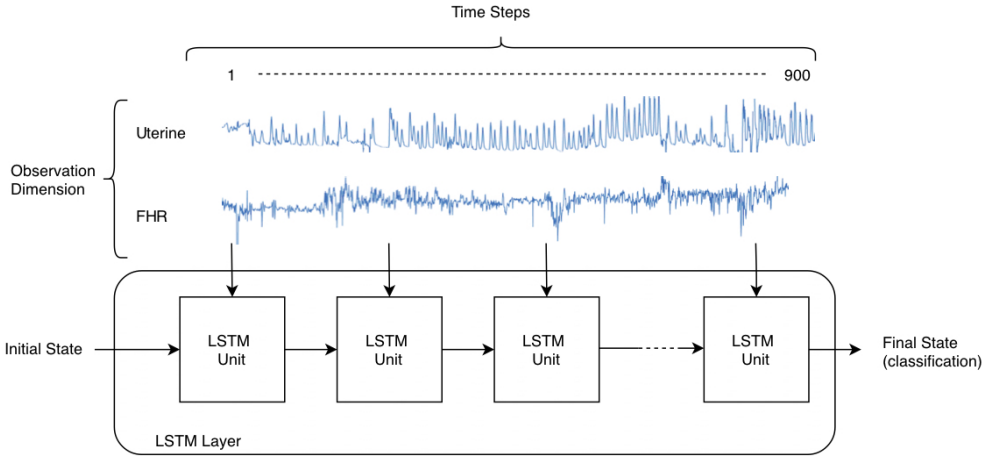

Figure 4.3: Long Short Term Memory Network topology. FHR - fetal heart rate; LSTM - Long Short Term Memory.

2) Multimodal Convolutional Neural Networks (MCNN)

Here I propose a Multimodal Convolutional Neural Network (MCNN), com-

prising different inputs layers and independent learning branches (Figure 4.4). The MCNN allowed me to use a variety of input sources: fetal heart rate, uterine contraction and a fetal heart rate quality score vector. The heart rate and uterine signals are fed into two distinct 5-layer convolutional networks branches, while the heart rate quality is used as a score multiplier of the heart rate convolutional branch, giving a weight for each output (each quality score is calculated on a 15 minutes window with 5 minutes overlap as per the default OxSys pre-processing (Cazares et al., 2001)). In particular, the signal quality in each 15min window is calculated using the raw 4Hz data as the ratio of valid signal data points out of the total number of signal points in the window. As is in the canonical CNN, the last layer uses a softmax transformation to get the class probability of each sample. The convolutional layer hyper-parameters (i.e., number of filters and filter length) are independently optimized for each layer, granting more flexibility during the network creation. A Bayesian hyper-parameters optimization with Gaussian Process (Bergstra et al., 2011) is used, and its parameters and optimal values are reported in Section 4.1.5.

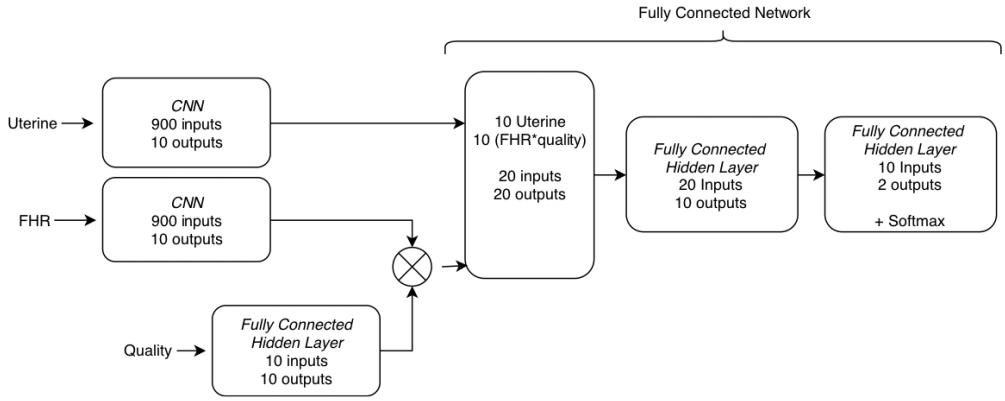

Figure 4.4: Multimodal Neural Convolutional Network topology. FHR - fetal heart rate; CNN - convolutional neural network.

3) Stacked MCNN

The ability of the network to correctly predict the labour outcome using data from the end of the CTG, which may often coincide with imminent delivery, is a relevant result from a classification perspective. But it is important to note that, at this time, the alert may be too close to the delivery, not allowing enough time for appropriate intervention. To address this problem, I split the time se-

ries into two parts, the first one being the last 60 minutes of 1^{st} labour stage (900 data points); and the second one being the last 30 minutes of 2^{nd} labour stage (450 data points). I only consider 30 minutes in the 2^{nd} stage of labour because significant physiological changes are expected in a shorter time span and because often the second stage does not last longer than 30 min. As in the pilot study, deliveries with less than 900 and 450 data points for 1^{st} and 2^{nd} stage respectively, are zero padded at the front. In the Stacked MCNN, the class probability from the MCNN applied to the 1^{st} stage of labour is used as additional input into the MCNN analysing the 2^{nd} stage of labour (Figure 4.5). The Stacked MCNN is then tested and, if the baby is delivered by intervention in the 1^{st} stage of labour and thus had no monitoring in the 2^{nd} stage, the probability of the first MCNN is considered as the relevant MCNNs outcome prediction for this baby.

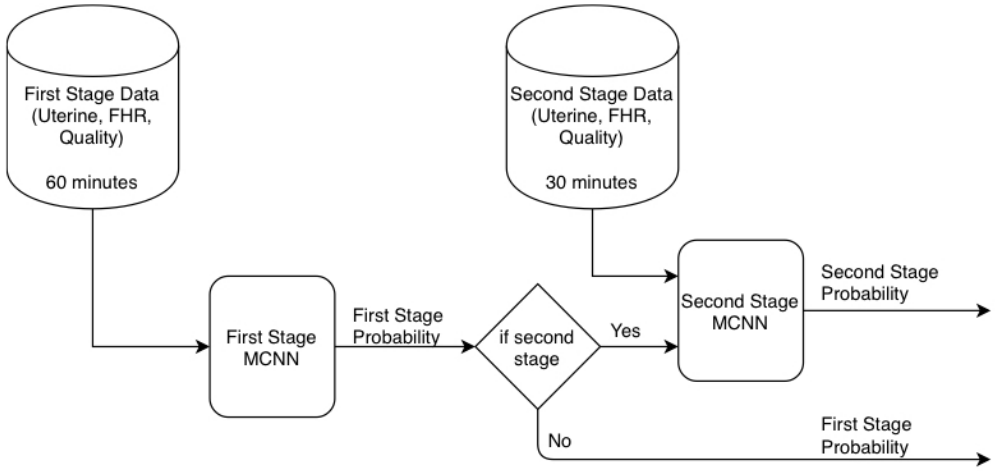

Figure 4.5: Stacked MCNN topology for 1^{st} and 2^{nd} stage classification. FHR - fetal heart rate. MCNN - multimodal convolutional neural network.

4.1.3 State of the art methods

1) Clinical practice

The primary reason for operative delivery (Caesarean, Forceps or Ventouse delivery) is noted in the patient records by the attending clinician at the time of birth, when applicable. This information is used to define true and false positive rates as follows: TPR - the number of operative deliveries for *presumed fetal*

compromise where there is a compromise as a proportion of the total number of compromises; FPR - the number of operative deliveries for *presumed fetal compromise* where there is no compromise as a proportion of the total number of normal cases.

2) Phase Rectified Signal Averaging (PRSA), also known as Decelerative Capacity (DC)

A signal processing method proposed by Bauer et al. (2006) for the analysis of adult fetal heart rate variability. Successively adapted and optimized for fetal heart rate monitoring in labour (Georgieva et al., 2014; Rivolta et al., 2014). Here, the maximum PRSA (maxPRSA) value per CTG segment of interest (i.e. 60 or 30min corresponding to 10 or 4 15min windows respectively) is considered.

3) OxSys 1.5

A current prototype of the Oxford system for data-driven fetal monitoring in labour (Georgieva et al., 2017). This is under development and newer versions will be available with time. OxSys 1.5 uses only two fetal heart rate features (DC and the number of accelerations). It also uses two clinical risk factors - the presence/absence of thick meconium or pre-eclampsia. OxSys analyses the entire fetal heart rate with a 15min sliding window (5min sliding step) and produces an alert if the risk for the foetus is high.

4.1.4 Performance metrics

Each of the proposed models are trained following a 3-fold cross validation schema to avoid overfitting. Five runs of each algorithm are performed to address the neural networks randomness and the median performance metrics for the five runs is reported. The networks is evaluated using standard performance metrics for classification tasks, such as AUC-ROC, TPR and FPR. The AUC-ROC is suitable for unbalanced datasets because it is not biased by the size of each class. Results are reported for TPR with a fixed FPR of 5, 10, 15 and 20 percent, relating to the FPR in clinical practice of 16% - 21% (Georgieva et al.,

2017; Abry et al., 2018).

4.1.5 Results

1) Parameters Optimization

For all proposed models, I use Bayesian optimization with Gaussian Process, a popular model for parameter optimization (Bergstra et al., 2011) to maximize the models' TPR at 15% FPR. A high FPR is one of the most important defects of CTG analysis, Georgieva et al. (2017) recently reported a figure of 16.3% for Oxford, reduced to less than 15% by Oxsys 1.5. Hence, 15% is chosen as the upper acceptable limit of the FPR for the analyses. A total of 40 iterations, with an initial random search of 10 samples are performed. Then hyper-parameters are optimized, representing the number of filters and filter length of each convolutional layer. Average results from the 3-fold cross validation are reported. Figure 4.6 shows the hyper-parameters landscape after 40 iterations. To display the 10 hyper-parameters in a two-dimensional plot, the median value across the five convolutional layers is selected for the filter length and the number of filters respectively. The colour represents TPR at 15% FPR for every set of chosen hyper-parameters in the interval [10, 50] for the number of filters and in [5, 30] for the filter length. As can be seen, the filter length (y-axis) is the main contributor toward the improvements in the fitness function. In particular, the network performs better with few short filters (less than 20 filters with a length smaller than 15 (i.e. 60 seconds)). This leads to the conclusion that the quick variations into fetal heart rate and contraction are more relevant than long term changes.

2) Comparison of CNN and LSTM

Table 4.1 shows the AUC and TPR (at a fixed 15% and 20% FPR) for training and testing sets. The CNN outperformed the LSTM in all proposed metrics and both models performed on the testing set similarly to their performance on the training set, showing they generalize well on unseen data. The ROC curves in Figure 4.7b present a small gap in performance in the first 0.1 FPR (easy to predict cases), while subsequently increasing difference for FPR of 0.1 to 0.2.

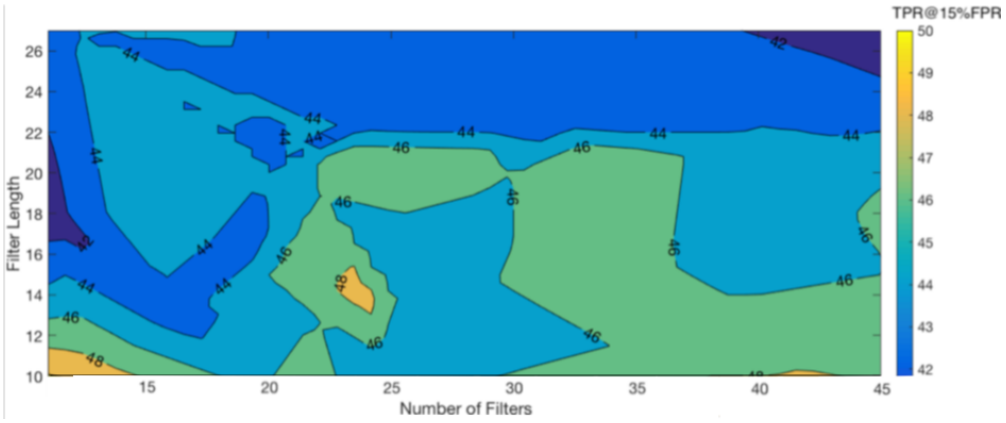

Figure 4.6: Optimization contour plot. To represent the ten dimensions into a 2-D plot, the x-axis and y-axis are the median number of filters and the median filter length across the five convolutional layers respectively. The colour represents the TPR@15%FPR for every set of ten hyper-parameters chosen during the optimization.

The proposed Deep Learning architectures are also compared with the current clinical practice performance and the computerized OxSys 1.5 by Georgieva et al. (2017). Figure 4.7a illustrates the FPR and TPR for the four compared techniques. The CNN showed better sensitivity, at a lower false positive rate, compared to clinical practice and OxSys 1.5. Lastly, an empirical experiment was carried out to test robustness and validate the importance of the amount of CNN training data. Figure 4.8 shows the test sensitivity at fixed FPR achieved when using 10%, 50%, and 100% of the data during training.

Table 4.1: Selected training and testing results for the two neural networks models.

Model	Data	AUC	TPR@15% FPR	TPR@20% FPR
CNN	Train	0.73	0.44	0.52
	Test	0.68	0.36	0.45
LSTM	Train	0.68	0.41	0.46
	Test	0.61	0.30	0.34

AUC: Area Under the ROC Curve; TPR: True Positive Rate; FPR: False Positive Rate

3) Comparison of CNN, MCNN, MaxPRSA, OxSys 1.5 and Clinical Practice

Firstly, the proposed approach (MCNN) was trained on the last 60min of CTG recording, its performance is shown in Figure 4.9 (Test Set A and Test Set B) and Table 4.2 (Test Set A). The MCNN outperformed the pilot neural network

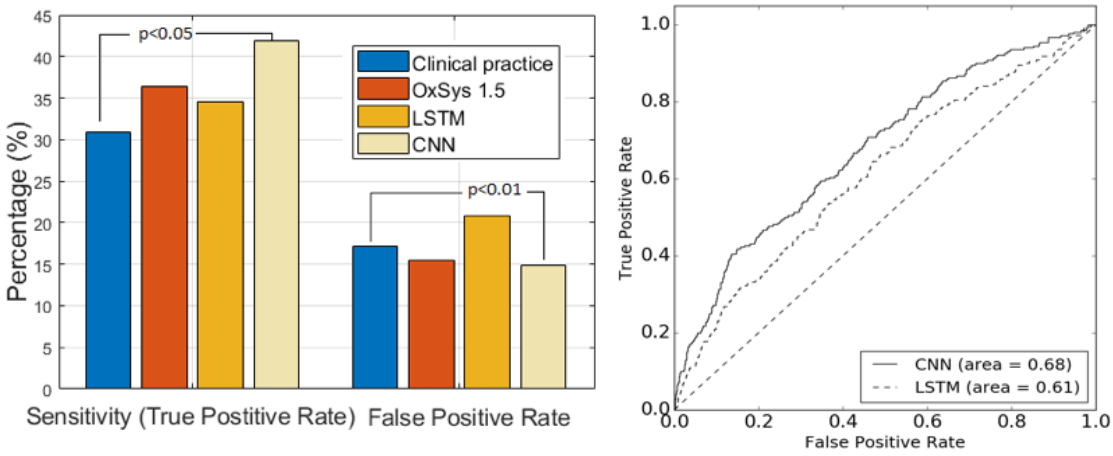

(a) (b)

Figure 4.7: Left: Comparison of the two Deep Learning models, OxSys 1.5 and Clinical practice o the test set (x^2 test for comparison of proportions); Right: ROC curves CNN vs LSTM models (Oxford test set: 5314 cases).

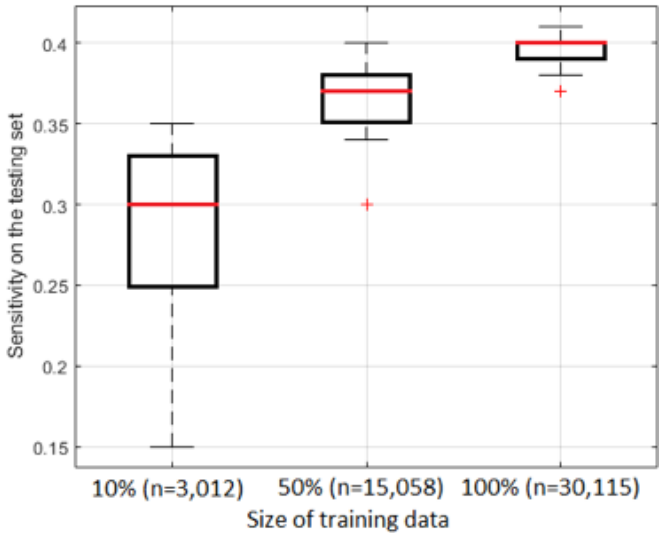

Figure 4.8: Robustness of CNN with respect to the size of training dataset over 30 runs (FPR is fixed at 15%).

model, the single-channel CNN. The MCNN also outperformed clinical practice, maxPRSA (Georgieva et al., 2014) and Oxsys 1.5 (Georgieva et al., 2017), increasing the TPR with the same or lower FPR. On Test Set B, CNN and MCNN had poor sensitivity and OxSys 1.5 was strikingly better than all other methods, including clinical practice. This is not surprising, because these 40 severe compromises without acidemia are a small and heterogeneous group better detected with individualised rules for CTG interpretation in the clinical context (as in OxSys 1.5).

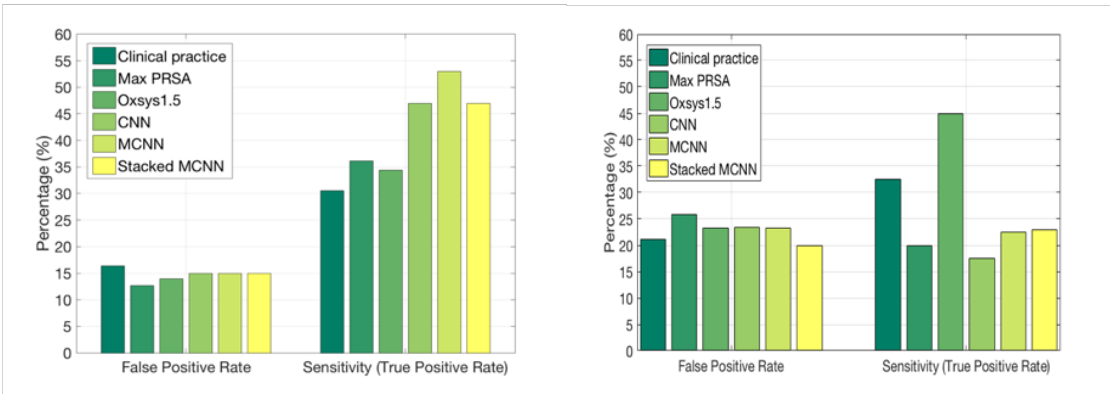

(a) Test Set A, n=4429 (Normal/Moderate plus Severe Compr with pH<7.05)

(b) Test Set B, n=885 (Intermediate/Severe Compr. with pH⩾7.05)

Figure 4.9: Performance on last 60min of CTG: Clinical practice, MaxPRSA, Oxsys 1.5, CNN, MCNN, Stacked MCNN (median of 5 runs). The FPR was fixed at 15% for the CNN and MCNN in order to be comparable to the FPR of clinical practice.

Table 4.2: Comparison of the proposed models (median of 5 runs) on Test Set A (n=4429). Compromise: acidemia (arterial cord pH at birth <7.05); Normal: healthy new-born with arterial cord pH>7.15. FPR: false positive rate. First labour stage: established labour before the onset of pushing. Second labour stage: pushing until birth.

	AUC	True Positive Rate (TPR %)			
		At 5% FPR	At 10% FPR	At 15% FPR	At 20% FPR
Test on last 60min of CTG, regardless of labour stage (4429 CTGs)					
CNN (trained on last 60min of CTG)	0.73	26	37	47	54
MCNN (trained on last 60min of CTG)	0.77	32	44	53	58
Test on last 60min of 1st stage (4177 CTGs)					
CNN (trained on last 60min of CTG)	0.59	18	24	30	35
MCNN (trained on last 60min of 1st stage)	0.65	17	27	33	40
MCNN (trained on last 60min of CTG)	0.60	19	28	33	39
Test on last 30min of 2nd stage (3138 CTGs)					
MCNN (trained on last 30min of 2nd stage)	0.71	22	36	43	47
Test on last 60min of first stage and/or the last 30min of 2nd stage as available (4348 CTGs)					
Stacked MCNN (trained on last 60min of 1st stage and last 30min of 2nd stage)	0.67	23	36	43	47
Stacked MCNN (trained on last 60min of CTG and last 30min of 2nd stage)	0.73	28	41	47	53

Furthermore, I investigated the effect of labour stage on network performance and whether it could improve if we analysed separately the end of the first and second stages of labour. Firstly, the same experiment carried in the previous section was replicated here but with training and testing only on data from the first or second stage separately (two CNN and two MCNN models). The results in Table 4.2 show that the networks trained and tested on 2^{nd} stage data had higher TPR than the ones in 1^{st} stage, which is to be expected because the considered data are closer to the time of delivery when the outcome *label* is assigned. Secondly, I trained a simple Stacked MCNN as shown in Figure 4.5, using the MCNN model trained on 1^{st} stage data to generate the probability for compromise and then fed this as an additional feature into a 2^{nd} stage MCNN (trained and tested on 2^{nd} stage with probability input from 1^{st} stage when available). The Stacked MCNN furtherly increased the AUC metric from 0.60 to 0.73 when compared to the MCNN trained on last hour in the 1^{st} stage and from 0.71 when compared to the same MCNN in the 2^{nd} stage (Table 4.2). If second stage data was not available (i.e. there was a Caesarean section in the first stage), then the probability generated from the first stage analysis is used for the final classification. In particular, in Test Set A, 6% of the data did not have any 1^{st} stage, while 29% did not have any 2^{nd} stage. MCNN had AUC of 0.77 and Sensitivity of 53% for FPR@15% (Table 4.2) but, when the same MCNN configuration was trained and tested only on the last one hour of 1^{st} stage (not the last hour of CTG recording), the AUC fell to 0.65 and the Sensitivity of 33% at FPR@15%. Reduction in performance is to be expected when analysis moves away from the time of birth and thus the outcome label (which is assigned at birth): a compromise that was undetected in first stage may mean that the fetus was still compensating well and the classification as normal was actually correct at the time. On the other hand, when the MCNN model was trained and tested only on the last 30min of 2^{nd} stage (if 2^{nd} stage was reached), the MCNN achieved AUC of 0.70 and Sensitivity of 42%. So, the Stacked MCNN improved on the individual MCNN performance in each labour stage but remained slightly suboptimal when compared to the MCNN trained and tested on the last hour (Table 4.2), AUC 0.74 vs 0.76 and Sensitivity for FPR@15% 47%

vs 53%. Only the median values were reported here because all networks had very small performance variability over the five independent runs (0.1 and $\pm$3.5 from the median for the AUC and TPR metrics respectively when trained on the last 60min of CTG trace; $\pm$0.2 and $\pm$3.5 when trained on last 60min of first stage). Finally, I concluded that the best performance was achieved with the MCNN trained on the last 60min of CTG (regardless of stage).

4) Effect of the fetal heart rate signal quality on the classification threshold and MCNN performance

Signal loss and noise are common in the fetal heart rate during labour monitoring. Basic pre-processing removed the noise and replaced it with missing values (Georgieva et al., 2017). Thus I examined the influence of signal loss (after de-noising) on the performance of my best model (MCNN trained on the last 60min of CTG): I defined four groups of heart rate signal quality (Table 4.3) based on the quality score vector (which consists of 10 values for 60min monitoring corresponding to each 15min window moving with a 5min step). I found that MCNN had consistently higher number of *alerts* (i.e. high-risk classifications) when there was more signal loss/noise (i.e. poorer signal quality). Importantly, for every quality group there was a different probability cut off point on the ROC curve (Figure 4.10) in order to obtain FPR at 15%. Without the quality breakdown, it is only possible to select one (sub-optimal) cut point for the different groups. It can be seen that the AUC is particularly low for the group with poorest signal quality, clearly demonstrating the obvious - poor signal quality leads to poor performance. Future work will focus on how to better integrate the signal quality information into the MCNN, so that it is better adjusted for.

5) Testing on external data

In addition to the Oxford Testing Set (>5000 CTGs), I tested my best model (MCNN trained on the last 60min of CTG) and the corresponding Stacked MCNN using two open access external datasets (SPaM'17, Table 4.4 and CTU-UHB, Table 4.5). Currently, a publication is awaited for the SPaM'17 challenge that will present all competing algorithms and performance in detail. However, the re-

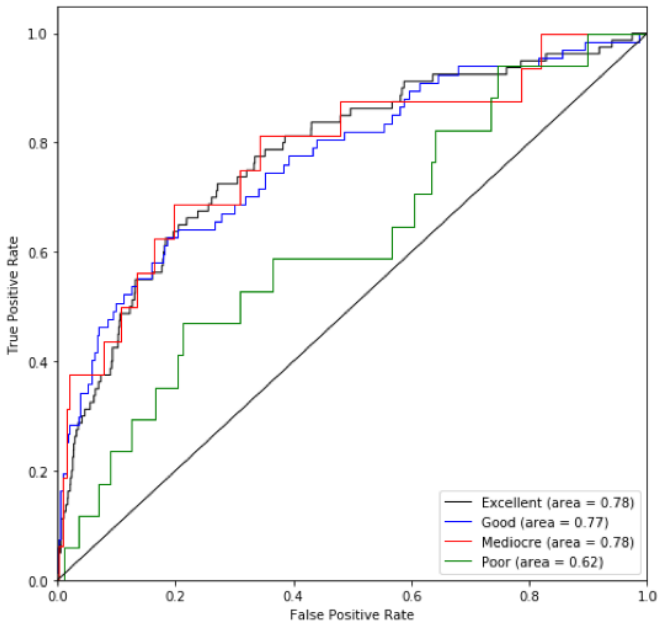

Figure 4.10: ROC curves for the four quality groups (Testing Set A, n = 4429).

Table 4.3: Quality groups on Test Set A. For each quality group is reported the percentage of data belonging to that group and the TPR/FPR median (min - max) for the five runs. The median threshold for the MCNN classification for the five models was 0.50 with minimum and maximum of 0.47 and 0.53 respectively (cases with higher than threshold MCNN value are classed as *high-risk* by the model).

Fetal Heart Rate quality (% of CTGs from Test Set A, $n = 4429$)	TPR (%)	FPR (%)
Excellent (52%)	43 (41 - 44)	9 (8 - 10)
Good (31%)	57 (57 - 61)	15 (14 - 18)
Mediocre (9%)	69 (56 – 69)	25 (25 - 29)
Poor (8%)	59 (59 - 76)	37 (29 - 44)

sults were reported at the meeting in early Nov 2017 and I used them as a general comparison. Both external sets have fetal compromise defined as cord pH<7.05 and hence Test Set A is the testing set somewhat comparable to them. The proposed models performed better on the SPaM dataset when compared to Test Set A, but this is to be expected with such a selected set with high incidence of cord pH<7.05 (20%, as opposed to 4% in Test Set A). It is interesting to note that most of the methods performed substantially better on the data from Lyon, when compared to the one from Brno and this is what can be also observed with the proposed MCNNs (Table 4.4). On the Lyon data, four methods from

the SPaM challenge had TPR of 75% at FPR ranging between 20% - 24% and one method achieved 95% TPR at 40%FPR. Therefore, both the MCNN and the Stacked MCNN performed better - with 83% and 80% at 20%FPR (median values, Table 4.4). On the SPaM Brno data, the methods achieved TPR of 45% - 65% with corresponding FPR of 12% - 29%FPR and this was only slightly improved by my models.

Table 4.4: Testing on the SPaM'17 dataset. Reported is the median performance for five models.

	AUC	True Positive Rate (TPR %)			
		At 5% FPR	At 10% FPR	At 15% FPR	At 20% FPR
MCNN (Lyon)	0.92	63	70	78	83
MCNN (Brno)	0.82	35	50	55	65
Stacked MCNN (Lyon)	0.91	60	70	75	80
Stacked MCNN (Brno)	0.77	30	40	50	60

Table 4.5: Testing on the CTU-UHB dataset. Note this dataset also comes from the same Brno Hospital but there is no overlap with the SPaM17 data.

	AUC	True Positive Rate (TPR %)			
		At 5% FPR	At 10% FPR	At 15% FPR	At 20% FPR
MCNN	0.81	33	48	58	65
Stacked MCNN	0.82	33	45	58	65

The MCNN and Stacked MCNN methods performed a little bit better on the CTU-UHB dataset than on the SPaM subset coming from the same hospital (Brno). I found two published methods reporting results on the CTU-UHB database (even though the data was not strictly used as an unseen testing set) and compared to them: Spilka et al (Spilka et al., 2016) reported 40% TPR at 14% FPR and Georgoulas et al (Georgoulas et al., 2017) reported 72%TPR at 35%FPR. The proposed Deep Learning approaches performed substantially better: the MCNN had 58% (53% - 60%) at 14%FPR and 80% (75% - 85%) at 35%FPR; and the Stacked MCNN had 55% (53% - 60%) at 14%FPR and 83% (75% - 88%) at 35%FPR.

4.1.6 Discussion

The CTG analysis during labour still relies on visual examination of long and complex heart rate patterns: a massive clinical challenge which has seen virtually no improvements in the past decades (Timmins and Clark, 2015). There have been developments of computer-based methods who are designed to mimic clinical interpretation and assist the visual CTG assessment by highlighting/alerting features of interest, but these have shown no benefit in clinical practice (Brocklehurst et al., 2017; Nunes et al., 2017). Data-driven CTG analysis is still a narrow and challenging field with only a few teams working with CTG datasets of about 3000 CTGs, in contrast, here I present my work on Deep Learning methods employing more than 35000 CTG samples.

The motivation behind the initial pilot study (point 2) on CNN and LSTM was to move away from classic feature extraction approaches and examine whether Deep Learning has the potential to detect information in the EFM that is currently "hidden". Both architectures showed good generalizability - retaining similar performance on training and testing (Table 4.1). On the Oxford data, CNN performed better than the LSTM (Table 4.1, Figure 4.7a, Figure 4.7b). Also, CNN outperformed the results of clinical practice (Figure 4.7a) and showed robust performance (Figure 4.8). As can be seen from Figure 4.8, the sensitivity of CNN increased and its variance decreased with larger size of the training set. Direct comparison with OxSys 1.5 suggested that CNN achieved better results, but this must be interpreted with caution because OxSys 1.5 is based on the entire dataset and analyses the entire EFM trace, incorporating clinical risk factors. The CNN's TPR of 44% @15%FPR (Figure 4.7a) is significantly higher than the TPR in clinical practice (31%) but needs to exceed 60% if we want tangible clinical benefits. Furthermore, I developed Multimodal Convolutional Neural Networks (MCNN) and Stacked MCNN models for the prediction of fetal compromise, using CTG traces from >35000 labours (85% for training and 15% for testing). The Stacked MCNN, is a more clinically relevant model allowing the analysis of the CTGs from first and second labour stages separately and feeding the estimated probability for compromise from

first stage into the analysis of the second labour stage. The MCNN is a more flexible network architecture, compared to the single channel CNN, allowing inputs with different dimensions. Thus, in addition to the fetal heart rate and contraction signals, a third input is used, indicating the signal quality vector containing the rate of signal loss in the fetal heart rate trace. The MCNNs' convolutional layer hyper-parameters (i.e., number of filters and filter length) were independently optimized for each layer, granting more flexibility during the network optimization when compared to the CNN model (Section 4.1.5, point 2). The optimization of the convolutional layers (Figure 4.6) showed the MCNN to work better when using many short filters on the contrary of what was found in Section 4.1.5 (point 1) where the CNN was working better with few large filters. This is probably due to the fact that each layer here was independently optimized, allowing for different filter length and number of filters. This finding could also be explained by the different architecture proposed here, where each input is treated separately before the fully connected layer. On the Oxford Testing Set of >5000 births, I compared the results of the proposed models with: clinical practice as well as the current Oxford prototype system OxSys 1.5 by Georgieva et al. (2017), the maximal Phase Rectified Signal Averaging (maxPRSA, (Georgieva et al., 2014)) and single channel CNN. Even though I trained the models with all available training data, I reported the testing results on the testing set split into two exclusive groups (Set A and Set B) according to the definition of compromise demonstrating the usefulness of such separation, as explained below. Firstly, for the prediction of acidemia (cord pH<7.05) with or without severe compromise (Test Set A, n = 4429 births), all neural networks performed substantially better than clinical practice, MaxPRSA or OxSys 1.5, with TPR at least 20% higher than that of clinical practice for the same or lower FPR, i.e. TPR of 53% vs 31% for MCNN and clinical practice respectively (Figure 4.9a). The best performing model was the newly proposed MCNN, trained on the last 60min of CTG regardless of the labour stage (Figure 4.9a and Table 4.2). Thus, the MCNN outperformed also the Stacked MCNN (53% vs 47% TPR at 15%FPR, Figure 4.9a). There are several explanations for this. The main challenge with analysing the second stage separately is the different duration

for each labour (most labours have between 10min to 150min of 2^{nd} stage). The proposed Stacked MCNN analysed strictly only the last 30min, padding with zeros at the beginning if there was less than 30min recording in the 2^{nd} stage. This introduced a gap of CTG data not analysed by the Stacked MCNN model, potentially losing information. Future work will examine more flexible models of the stacked approach, allowing for iterative analysis of the entire CTG available. Even though it could not outperform the MCNN trained on last 60min labour, the Stacked MCNN model performed well and provided a first attempt to analyse the CTG by estimating the probability of compromise at a point in time by using probability estimates from CTG data at an earlier time. I believe that as a concept and with future work, such stacked models could provide a clinically relevant model suitable for use at the bedside, building on the time series nature of the CTG (often >15hours long). Furthermore, I showed that noisy and inaccurate signal (i.e., high number of missing measurements) negatively impacts the performance of the models (Figure 4.10, Table 4.3). My models were more likely to class a trace as abnormal if the heart rate had poor quality, indicating that future models could benefit from adjustments to remove this bias. Secondly, for the detection of severe compromise without acidemia (Test Set B, n = 845 births, Figure 4.9b), all neural networks had low TPR. OxSys 1.5 was the best at 45% followed by clinical practice at 33% and the Deep Learning models around 20% TPR, for the same FPR. The Severe compromises without acidemia are a heterogeneous and challenging group to detect. They seem better suited to be detected by tailored diagnostic rules such as the ones in OxSys 1.5, which incorporates clinical risk factors and analyses the entire CTG trace from the beginning (for example, some pre-existing fetal injuries are detected by OxSys 1.5 early on in the CTG and are irrelevant to the proposed here models). I conclude that future work should focus on improving performance on both test sets separately, with highest gain from CNN-based approaches potentially for detecting the more homogeneous problem of acidemia. The current FPR in clinical practice of >15% is unacceptably high and future work will consider improving my network models working towards a new generation OxSys system, incorporating the best from both - Deep Learning *black box*

models and from heuristic domain-based knowledge. Finally, I used two open access datasets for testing my methods, allowing a comparison with work from other researchers and setting a standard for future comparisons: SPaM dataset (Brno and Lyon subsets, a total of 200 high quality CTGs with 20% incidence of compromise, cord pH<7.05); and the CTU-UHB dataset (552 CTGs with 7% incidence of cord pH<7.05). I concluded that the MCNN models convincingly outperformed the methods which competed in the SPaM challenge and any limited results reported on the CTU-UHB dataset. This was so even though both for the SPaM and CTU-UHB, many researchers did not use the data as set-aside testing sets but also used it for training/tuning one way or another.

4.2 Deep Learning for stock market volatility forecasting

Quantifying the potential loss of assets is a big part of risk management, trading in financial markets and asset allocation. To be able to measure these losses and make investment decisions, investors need to estimate risks (Blume, 1971). Since volatility has some well-known statistical regularities that make it inherently forecastable, it is among one of the most accepted and used measures of risk in the financial market. These regularities include the volatility clustering effect, leading to positive and persistent autocorrelations of volatility measures, the leverage effect, which is related to the negative correlation between past returns and current volatility values, the dynamic cross-correlation between the volatilities of different assets that give rise to the well-known phenomenon of volatility spillovers. In addition, it is worth reminding that volatility is a key ingredient for computing more refined risk measures such as the Value at Risk or the Expected Shortfall.

As the prediction of volatility is a major factor in risk analysis, many efforts have been made to implement parametric as well as non-parametric predictive methods for forecasting future volatility. Depending on the reference information set, the proposed approaches can be classified into two broad categories. Of these, the first includes approaches fitted to time series of daily log-returns. In

the parametric world, this class of methods includes the Generalized Autoregressive Conditionally Heteroskedastic (GARCH) models of Bollerslev (1986) and their numerous univariate and multivariate extensions (Bauwens et al., 2006) while, in the non-parametric world, I recall a consistent number of papers applying non-parametric approximators (such as smoothing splines (Langrock et al., 2015; Zhang and Teo, 2015) or neural networks to time series (Wang et al., 2015; Kourentzes et al., 2014)) of squared returns taken here as an unbiased, but noisy volatility proxy.

The second and more recent class of approaches for volatility forecasting replaces this noisy volatility proxy with more efficient realized volatility measures (Andersen and Teräsvirta, 2009) built from time series of high-frequency asset prices. Notable examples of parametric models falling into this second class of approaches are the class of Multiplicative Error Models (MEM) by Engle and Russell (1998) and the Realized GARCH (R-GARCH) models (Hansen et al., 2012). The main structural difference between MEM and R-GARCH models is that, differently from the R-GARCH which uses bivariate information on log-returns and realised volatility, the MEM are directly fitted to a univariate realised volatility series, and log-returns are eventually used only as external regressors for capturing leverage effects. Similarly, in a non-parametric environment, neural networks (McAleer and Medeiros, 2011) or other non-parametric filters (Chen et al., 2018) can be applied to time series of realised volatility measures to forecast future volatility. See also (Han and Zhang, 2012) non-parametric volatility modelling for non-stationary time series.

All above-discussed approaches are univariate. Nevertheless, the presence of phenomena such as common features and volatility spillovers make the analysis of multivariate volatility panels potentially very profitable. In a parametric setting, however, the number of required model parameters is rapidly exploding as the cross-sectional dimension of the panel increases, making the estimation infeasible even for moderately large dimensions, unless some heavy, and untested parametric restrictions are imposed. Typically, it is often assumed that all the volatilities in the panel share the same dynamic dependence structure

and volatility spillovers are not present (Pakel et al., 2011). Those assumptions are clearly unrealistic and they greatly reduce the ability of parametric models, albeit multivariate, to describe the complexity of the dynamic structure which is observed in financial time series.

Feed-forward neural networks are a favourite class of multivariate, non-parametric models used to study dependencies and trends in the data, e.g. using multiple inputs from the past to predict the future time step (Chakraborty et al., 1992). However, when using traditional neural network models, much effort is devoted to make sure that what is presented for training in the input layer is already in a format that allows the network to recognise the significant patterns. This process usually requires some ad-hoc procedures and soon becomes one of the most time-consuming part of neural network modelling. In a Deep Learning framework instead, by adding more and more layers between input and output (hence "deep"), the model allows richer intermediate representations to be built and most of that feature engineering process can be achieved by the algorithm itself, in an almost automatic fashion. This latter point both improves prediction accuracy and strongly widens the domains of applications. As a drawback, Deep Learning models require a large amount of data to outperform other approaches and are computationally expensive to train. However, the availability of parallel computing, both on CPUs and GPUs, sharply reduces the computational burden making even complex Deep Learning training processes feasible. Moreover, in financial applications a large amount of data can be quickly gathered, making Deep Learning applications appropriate and viable.

The main focus of this work is on proving the effectiveness of using Deep Learning techniques for multivariate time series forecasting. In particular, a stacked LSTM is applied for forecasting the volatility of financial time series. The LSTMs have several advantages with respect to the modelling approaches used so far in the literature. Firstly, they can be seen as non-parametric statistical models, and consequently, they do not suffer from the misspecification problems which typically affects parametric modelling strategies. Secondly,

they can overcome the curse of dimensionality problem which affects both standard non-parametric estimation techniques and several multivariate parametric models (Poggio et al., 2017), making the use of LSTMs feasible even for high dimensional temporal datasets. Moreover, they do not require any undesirable reduction of the parameter space through untestable, unrealistic restrictions, which might significantly reduce the ability of the model to reveal some well-known stylized facts about multivariate financial time series (such as spillovers and complex dynamics). Finally, they can profit from modelling complex non-linear and long-term dependencies, leading to improved accurate predictions (Gers et al., 2002a).

4.2.1 Data

Two datasets are used for the empirical experimentation. The first dataset used by Hansen et al. (2012), includes 28 assets from the Dow Jones Industrial Average (DJI 500) index plus one exchange-traded index fund SPY, that tracks the S&P 500 index. The sample spans the period from 1^{st} January 2002 to 31^{st} August 2008. The second dataset is related to 92 stocks belonging to the NASDAQ 100 index within the period 1^{st} December 2012 to 29^{th} November 2017. Further detail on the two datasets can be found in Table 4.6 and Table 4.7 respectively[1].

Each asset is represented by two different time series, the realized measure, namely volatility, and the related open-close return. The realized measure v_t is given by a realized kernel estimator computed using the Parzen kernel function. This estimator is similar to the realized variance, and more importantly, it is robust to market micro-structure noise and is more accurate than the quadratic variation estimator. The implementation of the realized kernel follows the method proposed by Barndorff-Nielsen et al. (2011) that guarantees a positive estimate.

[1]The data is publicly available on the following Zenodo repository https://zenodo.org/record/2540818

Table 4.6: Dow Jones Industrial Average assets used as case study. Capitalization is given with respect to 4th August 2017 values.

Symbol	Name	Sector	Capitalization (USD)
AA	Alcoa Corp	Materials	6.89B
AIG	American International Group	Financials	58.79B
AXP	American Express	Financials	75.99B
BA	Boeing	Industrials	140.50B
BAC	Bank of America	Financials	245.97B
C	Citigroup	Financials	187.94B
CAT	Caterpillar	Industrials	67.58B
CVX	Chevron	Energy	208.66B
DD	EI du Pont de Nemours	Materials	71.17B
DIS	Disney	Consumer Discretionary	168.52B
GE	General Electric	Industrials	223.20B
GM	General Motors	Consumer Discretionary	51.39B
HD	Home Depot	Consumer Discretionary	182.62B
IBM	IBM	Information Technology	135.28B
INTC	Intel	Information Technology	170.57B
JNJ	Johnson & Johnson	Health Care	357.45B
JPM	JPMorgan Chase	Financials	329.58B
KO	Coca-Cola	Consumer Staples	194.07B
MCD	McDonald's	Consumer Discretionary	125.37B
MMM	3M	Industrials	123.92B
MRK	Merck	Health Care	172.59B
MSFT	Microsoft	Information Technology	559.80B
PG	Procter & Gamble	Consumer Staples	231.51B
T	AT&T	Telecommunication Services	235.96B
UTX	United Technologies	Industrials	97.04B
VZ	Verizon	Telecommunication Services	199.52B
WMT	Wal-Mart	Consumer Staples	242.61B
XOM	Exxon Mobil	Energy	339.86B
SPY	SPDR S&P500 ETF Trust	-	(Net Assets) 242,54B

4.2.2 Experimental setup

The proposed model is a 2-layer stacked LSTM made of $2n$ and n units respectively, with n being the number of assets, according to the input and output size. This means 58/29 for DJI 500 and 184/92 for NASDAQ 100. The output of the first LSTM is given as input to a dense activation layer designed to provide the model's output (Figure 4.11 shows a schematic description of the model). The hidden activation function is an hyperbolic tangent, while the recurrent activation is a hard sigmoid (default activation functions for LSTM, as advised by Hochreiter and Schmidhuber (1997)). To avoid negative forecasts (the realized volatility is always continuous positive), a softplus function is used in the output layer.

Two topologies of LSTM are tested and evaluated: univariate and multivariate.

LSTM-1: A univariate architecture (one model independently trained for each asset) taking as input only one asset at the time (open-close return and volatility

Table 4.7: NASDAQ 100 assets used as case study.

Sector	Symbol
Capital Goods	ILMN, KLAC, PCAR, PCLN, TSLA
Consumer Non-Durables	CTAS, HAS, MDLZ, MNST
Consumer Services	AMZN, CHTR, CMCSA, COST, DISCA, DISCK, DISH, DLTR, EXPE, FAST, FOXA, FOX, LBTYA, LBTYK, LVNTA, NFLX, ORLY, PAYX, QVCA, ROST, SBUX, SIRI, TSCO, ULTA, VIAB, WYNN
Health Care	ALGN, ALXN, AMGN, BIIB, CELG, ESRX, GILD, HOLX, HSIC, IDXX, INCY, ISRG, MYL, SHPG, XRAY
Miscellaneous	AKAM, CTRP, EBAY, MELI, NTES
Public Utilities	VOD
Technology	AAPL, ADBE, ADI, ADP, ADSK, AMAT, ATVI, AVGO, BIDU, CA, CERN, CHKP, CSCO, CTSH, CTXS, EA, FB, FISV, GOOGL, INTC, INTU, LRCX, MCHP, MSFT, MU, MXIM, NVDA, QCOM, STX, SWKS, SYMC, TXN, VRSK, WDC, XLNX
Transportation	JBHT

for a chosen past window $(r_{t-k}, .., r_{t-1}, v_{t-k}, .., v_{t-1})$ and producing as output the one-step-ahead volatility (v_t).

LSTM-n: A multivariate architecture, where a single model is trained using all the assets. This version takes as input the open-close return and volatility for a given past window $(r^i_{t-k}, .., r^i_{t-1}, v^i_{t-k}, .., v^i_{t-1})$, $i = 1, \ldots, n$ and outputting the n one-step-ahead volatilities (v^i_t, $i = 1, \ldots, n$), where $n = 29$ for DJI 500 and $n = 92$ for NASDAQ 100.

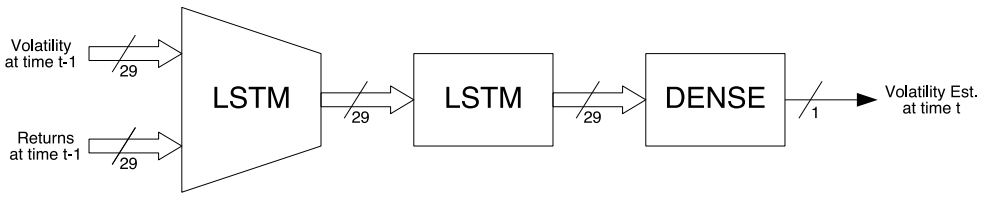

Figure 4.11: The proposed model for DJI 500 is a stack of two LSTM with 58 and 29 neurons each and a dense activation layer on the top. The size of the dense layer is one in the univariate approach (LSTM-1) and 29 in the multivariate one (LSTM-29).

The model is pre-trained by using the first 300 days of the dataset with a look-back window of 20 days. Subsequently, a rolling forecast is applied from day 301 onward. In particular, every time the one-step-ahead volatility is predicted, its observed features (realized return and volatility) are used to refine the network state, before moving the time window one step. This procedure allows having an up-to-date network, every time new information is available.

The hyper-parameters of the network have been optimised using a grid search,

Table 4.8: Hyper-parameters for the LSTM. The optimal value of each hyper-parameter has been selected through a grid search on the defined range.

Hyper-parameter	Range of optimization	Optimal value
Dropout	[0, 0.6] every 0.1	0.2
Number of training epochs on pre-training data	[100, 400] every 50	300
Number of training epochs on rolling window	[10, 30] every 5	20
Look-back	[5, 100] every 5	20
Loss function	MSE and QLIKE	QLIKE

and their search boundaries and optimal values are reported in Table 4.8. The optimal number of training epochs on the initial data was found to be in line with the optimal number of days used for pre-training (i.e., 300 days), while the number of epochs for the rolling period had its best value consistent with the size of the look-back (i.e., 20 days, equivalent to four weeks of trading data). I observed that a smaller number of epochs would produce an under-fitted network (smooth forecast trending with the average of the last few data points), while a longer training would produce an over-fitting network (giving a lot of weight to the most recently shown data point). Furthermore, a larger look-back would impact the convergency (probably due to the vanishing gradient problem). In addition, dropout, a standard regularization technique used for Deep Learning models, was used to avoid over-fitting, and its best value was found to be around 0.20, as also suggested by Wan et al. (2013). Lastly, I used two loss functions to train the model: MSE and QLIKE.

Both online and offline evaluations have been considered to assess the model performance. In the online evaluation case, two alternative fitness functions have been used to train the LSTM models: the widely used MSE for regression and forecasting tasks (described in Section 2.5.2); and the QLIKE loss function, particularly suitable for volatility forecasting (Patton, 2011). For the offline evaluation case, a test data set (not used for training) for out-of-sample evaluation using MSE, QLIKE and the Pearson correlation index is considered.

Given a vector $\hat{Y}$ of N forecasts and the vector Y of observed values, the QLIKE is defined a follows:

$$\text{QLIKE} = \frac{1}{N}\sum_{i=1}^{N}(\log(\hat{Y}_i) + \frac{Y_i}{\hat{Y}_i}). \tag{39}$$

Both MSE and QLIKE measures are proposed in the evaluation framework since they are considered to be robust for assessing volatility forecast performance (Patton, 2011). A robust measure must ensure that using a proxy for the volatility (the realized kernel in this case) gives the same ranking as using the true (unobservable) volatility of an asset.

Moreover, the Pearson correlation coefficient is computed between the forecast volatility of each estimated model and the realized one, to assess the ability of the models to follow the assets trends.

Lastly, the Diebold-Mariano (DM) test is used to assess models' conditional predictive ability. The one tail DM is used with squared error, predictive horizon equal to 1 (for one step ahead forecast) and a significance threshold at 0.05, to test the following NULL hypothesis 'Model M_i has better predictive ability than model M_j with a size level equal to $\alpha = 0.05$'.

Before training the model, the data are normalised and standardised with 0-mean and 1-variance. Since the features are in $\mathbb{R}^+$, for each sample (r_t, ν_t), its negative $(-r_t, -\nu_t)$ is added to the data (to have a perfectly bell shaped distribution). The resulting distribution is already mean-centred, hence the values are divided by their standard deviation and finally, the added negative values are dropped to restore the original set of observations.

4.2.3 Compared methods

a) Realized Garch (R-GARCH)

The Realized GARCH introduced by (Hansen et al., 2012) has extended the class of GARCH models by replacing, in the volatility dynamics, the squared returns with a much more efficient proxy such as a realized volatility measure. The structure of the R-GARCH(p, q) in its linear formulation is given by:

$$r_t = \mu + \sqrt{h_t}\, z_t, \tag{40}$$

$$h_t = \omega + \beta\, h_{t-1} + \gamma\, \nu_{t-1}, \tag{41}$$

$$\nu_t = \xi + \varphi\, h_t + \tau(z_t) + u_t, \tag{42}$$

where $z_t \sim$i.i.d.$(0,1)$ and $u_t \sim$i.i.d.$(0,\sigma_u^2)$ with z_t and u_t being mutually independent. The first two equations are the *return equation* and the *volatility equation* that define a class of GARCH-X models, including those estimated in (Engle, 2002; Barndorff-Nielsen and Shephard, 2005; Visser, 2011). The GARCH-X acronym refers to the fact that v_t is treated as an exogenous variable. It is worth noting that most variants of ARCH and GARCH models are nested in the R-GARCH framework. The measurement equation is justified by the fact that any consistent estimator of the Integrated variance can be written as the sum of the conditional variance plus a random innovation, where the latter is captured by $\tau(z_t) + u_t$. The function $\tau(z_t)$ can accommodate leverage effects, because it captures the dependence between returns and future volatility. A common choice (Hansen et al., 2012), that has been found to be empirically satisfactory, is to use the specification:

$$\tau(z_t) = \tau_1 z_t + \tau_2(z_t^2 - 1). \tag{43}$$

Substituting the measurement equation into the volatility equation, it can be easily shown that the model implies an AR(1) representation of h_t:

$$h_t = (\omega + \xi\gamma) + (\beta + \varphi\gamma)h_{t-1} + \gamma w_{t-1}, \tag{44}$$

where $w_t = \tau(z_t) + u_t$. Furthermore it is assumed that the expectation of $E(w_t) = 0$. The coefficient $(\beta + \varphi\gamma)$ reflects the persistence of volatility, whereas γ summarizes the impact of the past realized measure on future volatility.

The general conditions required to ensure that the volatility process h_t is stationary and the unconditional variance of r_t is finite and positive are given by:

$$\omega + \xi\gamma > 0, \tag{45}$$

$$0 < \beta + \varphi\gamma < 1. \tag{46}$$

If the conditions in Eq. 45 are fulfilled, the unconditional variance of r_t, taking expectations of both sides in Eq. 44, can be easily shown to be equal to $(\omega + \xi\gamma)/[1 - (\beta + \varphi\gamma)]$. Finally, as for standard GARCH models, the positivity of h_t ($\forall t$) is achieved under the general condition that ω, γ and β are all positive.

b) GJR-MEM

Multiplicative Error Models (MEM) were first proposed by Engle (2002) as a generalization to non-negative variables of the Autoregressive Conditional Duration models of Engle and Russell (1998). Namely, let ν_t be a discrete time process on $[0, \infty)$ (e.g. a realized measure). A general formulation of the MEM is

$$\nu_t = \mu_t \epsilon_t, \tag{47}$$

$$\mu_t = \mu(\boldsymbol{\psi}_\mu, \mathcal{J}_{t-1}), \tag{48}$$

where $(\epsilon_t|\mathcal{J}_{t-1}) \overset{iid}{\sim} D^+(1, \sigma^2)$. It can be easily seen that

$$E[\nu_t|\mathcal{J}_{t-1}] = \mu_t, \tag{49}$$

$$var[\nu_t|\mathcal{J}_{t-1}] = \sigma^2 \mu_t^2, \tag{50}$$

where the conditional expectation of the realized measure (μ_t) provides an estimate of the latent conditional variance h_t.

The GJR-MEM model is obtained by borrowing from the GARCH literature (Glosten et al., 1993; Engle, 2002) the following dynamic equation for μ_t:

$$\mu_t = \omega + \alpha\nu_{t-1} + \beta\mu_{t-1} + \gamma\nu_{t-1}I(r_{t-1} < 0), \tag{51}$$

which allows to reproduce volatility clustering as well as leverage effects.

Coming to the specification of the distribution of ϵ_t, any unit mean distribution with positive support could be used. Possible choices include Gamma, Log-

Normal, Weibull, Inverted-Gamma and mixtures of them. In this experiments I consider the Gamma distribution which is a flexible choice able to fit a variety of empirical settings. If $(\epsilon_t|\mathcal{I}_{t-1}) \sim \Gamma(\theta, \phi)$, its density would be given by

$$f(\epsilon_t|\mathcal{I}_{t-1}) = \frac{1}{\Gamma(\theta)\phi^\theta}\epsilon_t^{\theta-1}\exp\left(-\frac{\epsilon_t}{\phi}\right) \tag{52}$$

However, since $E(\epsilon_t|\mathcal{I}_{t-1}) = \theta\phi$, to ensure unit mean, it is needed to impose the constraint $\phi = 1/\theta$ giving rise to the following density

$$f(\epsilon_t|\mathcal{I}_{t-1}) = \frac{1}{\Gamma(\theta)}\theta^\theta\epsilon_t^{\theta-1}\exp\left(-\theta\epsilon_t\right). \tag{53}$$

Model parameters can be then estimated maximizing the likelihood function implied by the unit mean Gamma assumption. It is worth noting that these estimates have a quasi maximum likelihood interpretation since it can be shown that, given that μ_t is correctly specified, they are still consistent and asymptotic normal even if the distribution of ϵ_t is misspecified.

c) Elman Recurrent Neural Networks (RNN)

The Elman Network (also known as Simple Recurrent Network) is one of the most basic RNN architectures known in literature. Its topology consists of three layers (i.e., input, hidden, and output) with the addition of a set of context units (i.e., the network state). The state saves a copy of the previous values of the hidden units allowing interactions with the current inputs. Thus this architecture can be considered a very simplified version of the LSTM, where only information of the most recent past is stored.

$$h_t = \sigma_h(W_h x_t + U_h h_{t-1} + b_h), \tag{54}$$

$$y_t = \sigma_y(W_y h_t + b_y) \tag{55}$$

4.2.4 Results and discussion

In this section, the proposed approach to forecast stock market volatility, based on deep neural networks, is implemented in two variants: univariate (LSTM-1) and multivariate (LSTM-29 and LSTM-92). The method is compared with two state of the art methodologies, namely R-GARCH (Hansen et al., 2012) and GJR-MEM (Glosten et al., 1993). Here I discuss empirical results from an out-of-sample forecasting comparison, using returns and realized measures for the 28 Dow Jones Industrial Average stocks and one exchange-traded index fund, SPY, which tracks the S&P 500 index over a period of 1250 days and for the 92 stocks belonging to the NASDAQ 100 index over a period of 956 days.

a) Dow Jones Industrial Average 500

Table 4.9: Evaluation Metrics for the DJI 500 dataset: The MSE, QLIKE and Pearson measures are reported for each asset and for each compared model.

Asset	LSTM-1			LSTM-29			R-GARCH			GJR-MEM		
	MSE	QLIKE	Pearson	MSE	QLIKE	Pearson	MSE	QLIKE	Pearson	MSE	QLIKE	Pearson
AA	4.77	1.98716	0.59	3.65	1.97534	0.69	4.83	2.01253	0.60	4.05	1.97021	0.65
AIG	6.71	1.40473	0.61	4.84	1.35021	0.72	6.40	1.43038	0.61	5.40	1.35342	0.70
AXP	3.19	1.12222	0.77	1.70	1.10570	0.87	2.11	1.11389	0.84	2.00	1.10602	0.85
BA	0.88	1.40893	0.56	0.81	1.40138	0.62	0.85	1.41024	0.59	0.80	1.40229	0.62
BAC	3.93	0.91670	0.73	2.86	0.88778	0.81	5.19	0.96517	0.71	3.35	0.89910	0.77
C	5.86	1.21826	0.74	2.48	1.18877	0.89	3.62	1.22085	0.83	2.92	1.19124	0.86
CAT	1.12	1.56860	0.65	1.03	1.55595	0.69	1.18	1.56885	0.62	1.10	1.55946	0.66
CVX	1.36	1.32972	0.69	1.05	1.32618	0.76	1.20	1.32096	0.72	1.07	1.31349	0.75
DD	1.56	1.31255	0.64	1.10	1.29515	0.76	1.33	1.32252	0.72	1.11	1.29064	0.75
DIS	1.01	1.35000	0.52	0.86	1.33076	0.63	0.88	1.33510	0.61	0.83	1.32302	0.63
GE	0.57	0.92743	0.66	0.50	0.92145	0.72	0.54	0.93285	0.69	0.50	0.91087	0.71
GM	11.44	2.14155	0.62	9.83	2.10353	0.68	11.45	2.10482	0.62	10.79	2.09708	0.64
HD	2.58	1.56234	0.68	1.83	1.55630	0.78	1.99	1.55294	0.76	1.81	1.54174	0.77
IBM	0.65	1.00420	0.64	0.51	0.99950	0.73	0.65	1.01651	0.64	0.54	0.98996	0.70
INTC	1.42	1.77012	0.62	1.52	1.77107	0.62	1.51	1.77072	0.59	1.40	1.76207	0.62
JNJ	0.33	0.60274	0.52	0.32	0.60311	0.54	0.35	0.65656	0.48	0.34	0.60319	0.51
JPM	4.92	1.31900	0.76	3.86	1.30975	0.80	4.27	1.32231	0.78	3.24	1.29987	0.84
KO	0.28	0.76443	0.59	0.27	0.76449	0.61	0.34	0.83988	0.56	0.27	0.75574	0.60
MCD	1.32	1.35511	0.49	1.40	1.37356	0.48	1.32	1.36301	0.49	1.41	1.35786	0.47
MMM	0.64	1.05299	0.56	0.55	1.05117	0.65	0.68	1.09912	0.55	0.54	1.04440	0.64
MRK	9.45	1.55236	0.25	8.63	1.54827	0.38	9.75	1.57830	0.26	10.30	1.53410	0.28
MSFT	0.77	1.20058	0.60	0.63	1.20299	0.69	0.63	1.20704	0.68	0.57	1.18384	0.70
PG	0.25	0.76355	0.56	0.25	0.76961	0.58	0.31	0.80720	0.52	0.25	0.75837	0.57
SPY	0.17	0.16199	0.72	0.17	0.15189	0.75	0.16	0.13691	0.75	0.14	0.12674	0.78
T	1.97	1.44030	0.63	1.64	1.43042	0.70	2.12	1.46438	0.63	1.72	1.42659	0.69
UTX	0.85	1.17023	0.50	0.69	1.16343	0.62	0.97	1.18749	0.47	0.74	1.15846	0.59
VZ	1.40	1.26611	0.54	1.05	1.26430	0.70	1.15	1.29074	0.67	1.02	1.25300	0.70
WMT	0.71	1.12620	0.64	0.67	1.12532	0.68	0.88	1.16037	0.60	0.70	1.11630	0.65
XOM	0.95	1.24535	0.71	0.89	1.24840	0.73	0.92	1.23848	0.71	0.87	1.23240	0.73

A detailed comparison of the methods performance is given in Table 4.9 with respect to each asset. The LSTM-29 approach reaches the lowest MSE error for 18 out of the 29 assets when compared with LSTM-1, R-GARCH and GJR-

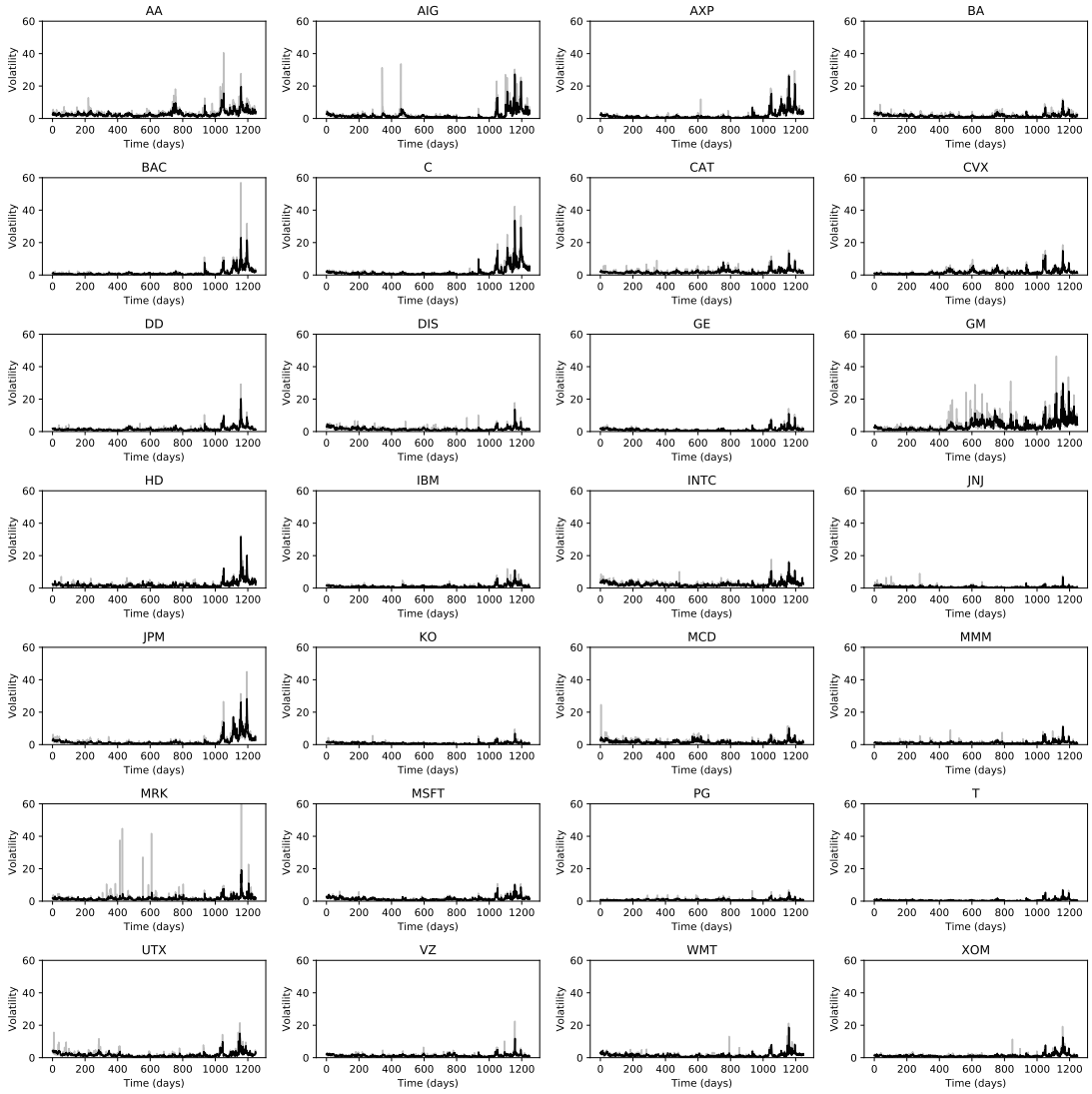

Figure 4.12: LSTM-29 one step ahead predictions for all assets of the DJI 500 dataset (excluded the index fund SPY). The observed time series are given in gray and the predicted volatility values in black.

MEM methods. In particular, the LSTM-29 has a lower error compared to the proposed univariate model for 25 out of 29 assets, equal in 2 and worse in 2 cases. Compared to R-GARCH, the LSTM-29 is better again in 25 out of 29 cases, equal for 1, and worse for 3 assets. Lastly, the multivariate LSTM is better, equal and worse than GJR-MEM in 16, 3 and 10 cases respectively. The one step ahead prediction given by the LSTM-29 is presented in Figure 4.12.

Having a closer look at the MSE values from Table 4.9, the LSTM-29 is not better than the other benchmarks on assets with very low errors and hence volatility, in the considered period (e.g., JNJ, KO, PG, and SPY).

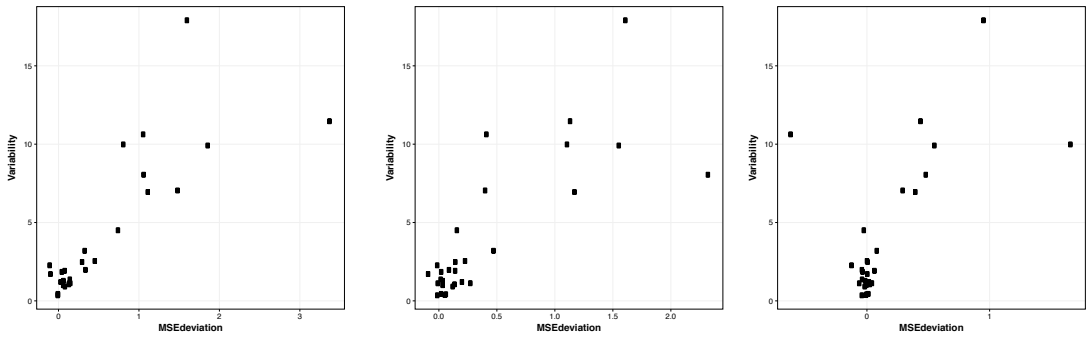

(a) LSTM-1 (b) R-GARCH (c) GJR-MEM

Figure 4.13: Relationship between difference in MSE (for LSTM-29 vs: LSTM-1 (Figure 4.13a); R-GARCH (Figure 4.13b); and GJR-MEM (Figure 4.13c)) (y-axis) and variance of volatility (x-axis). Each dot represents an asset. LSTM-29 gets better in periods of high volatility.

Figure 4.13 is a scatter plot illustration comparing for each asset, the performance of the LSTM-29 and the other models measured in terms of MSE difference (i.e., positive values representing smaller errors and better LSTM-29 performance) versus asset volatility in terms of its variance (i.e., higher values of variance representing stronger fluctuation in daily volatilities) over the out of sample period (1250 days).

As can be seen from Figure 4.13, the LSTM-29 is generally comparable with the other models at lower volatility, while outperforming the LSTM-1 and the two state-of-the-art R-GARCH and GJR-MEM approaches in higher volatility regimes. This result is confirmed by the Pearson's correlation index with values 0.825 against LSTM-1, 0.800 against R-GARCH, and 0.608 against GJR-MEM over the 29 assets.

To verify whether the proposed approach has statistically superior predictive ability, a Diebold-Mariano test is performed using a predictive horizon equal to 1 (one-step-ahead forecast). As it can be observed from the results reported in Table 4.10, the LSTM-29 has a better predictive ability for 10 out of 29 assets compared to the LSTM-1, 16 over 29 against the R-GARCH, and 6 out of 29 assets for the GJR-MEM, when considering a p-value strictly lower than 0.05. It is also worth noticing that in the remaining cases LSTM-29 is never worse than the compared models.

Table 4.10: Debold-Mariano statistic for the DJI 500 dataset (with a p-value given in brackets) for the LSTM-29 against LSTM-1, R-GARCH and GJR-MEM. The p-values are marked with a * for 10% confidence level, with ** for 5% and with *** for 1%.

Asset	LSTM-29 vs.					
	LSTM-1		R-GARCH		GJR-MEM	
AA	-2.42	(0.008***)	-3.21	(0.001***)	-2.53	(0.006***)
AIG	-2.86	(0.002***)	-2.35	(0.009***)	-1.21	(0.114)
AXP	-2.68	(0.004***)	-2.76	(0.003***)	-2.06	(0.020**)
BA	-1.33	(0.092*)	-1.92	(0.028**)	0.25	(0.597)
BAC	-2.27	(0.012**)	-3.11	(0.001***)	-1.65	(0.049**)
C	-3.12	(0.001***)	-3.33	(0.000***)	-2.17	(0.015**)
CAT	-1.01	(0.157)	-2.45	(0.007***)	-1.28	(0.100*)
CVX	-1.60	(0.055*)	-1.54	(0.061*)	-0.20	(0.420)
DD	-1.77	(0.039**)	-2.51	(0.006***)	-0.18	(0.429)
DIS	-1.55	(0.060*)	-0.62	(0.267)	0.64	(0.739)
GE	-0.85	(0.198)	-0.85	(0.197)	-0.10	(0.460)
GM	-2.12	(0.017**)	-2.91	(0.002***)	-2.05	(0.020**)
HD	-1.67	(0.048**)	-1.03	(0.153)	0.14	(0.556)
IBM	-1.81	(0.035**)	-2.31	(0.011**)	-0.89	(0.187)
INTC	0.64	(0.740)	0.05	(0.520)	1.27	(0.898)
JNJ	-0.10	(0.458)	-1.27	(0.100*)	-1.69	(0.046**)
JPM	-1.29	(0.099*)	-1.37	(0.085*)	1.28	(0.900)
KO	-0.28	(0.389)	-2.9	(0.002***)	-0.44	(0.331)
MCD	1.27	(0.898)	1.52	(0.935)	-0.14	(0.443)
MMM	-1.46	(0.072*)	-2.36	(0.009***)	0.33	(0.628)
MRK	-0.97	(0.165)	-1.47	(0.071**)	-1.58	(0.057*)
MSFT	-0.93	(0.176)	0.02	(0.509)	1.38	(0.916)
PG	-0.36	(0.360)	-3.00	(0.001***)	0.00	(0.501)
SPY	-0.09	(0.463)	0.33	(0.629)	1.92	(0.972)
T	-1.76	(0.040**)	-2.72	(0.003***)	-1.20	(0.116)
UTX	-0.87	(0.192)	-1.72	(0.043**)	-0.94	(0.173)
VZ	-1.45	(0.074*)	-1.02	(0.153)	0.58	(0.718)
WMT	-0.74	(0.230)	-2.26	(0.012**)	-0.61	(0.272)
XOM	-0.54	(0.293)	-0.40	(0.343)	0.43	(0.665)

Furthermore, to test the dependence of forecasting accuracy on volatility conditions, I evaluated the errors (mean, median, standard deviation (std) and median absolute deviation (MAD)) for four volatility clusters: very low (VL); low (L); high (H); and very high (VH) (Table 4.11). The clusters are calculated taking the 50, 75 and 95 percentiles of the smoothed volatility over time, using a 10-day centred moving average and moving variance of all the assets. Specifically,

Table 4.11: Average with Std (in brackets) errors, Median with MAD (in brackets) errors for the four models at different volatility regimes (VL, L, H and VH) on the DJI 500 dataset. The four volatility regimes are determined using the percentiles at 50, 75, 95 over the all assets. The first comparison (rows 2 to 5) is using a centered moving average of the volatilities over time (5 time steps before and 5 time steps after the current one), while the second one (rows 6 to 9) is using a centered moving variance of the volatilities over time (5 time steps before and 5 time steps after the current one).

		LSTM-1		LSTM-29		R-GARCH		GJR-MEM	
		Mean (Std)	Median (MAD)	Mean (Std)	Median (MAD)	Mean (Std)	Median (MAD)	Mean (Std)	Median (MAD)
Moving Average	Very Low	0.151 (0.657)	0.037 (0.051)	0.161 (0.677)	0.038 (0.053)	0.165 (0.709)	0.036 (0.050)	0.157 (0.636)	0.045 (0.062)
	Low	0.596 (3.290)	0.136 (0.186)	0.620 (3.234)	0.139 (0.191)	0.642 (3.367)	0.135 (0.188)	0.610 (3.232)	0.151 (0.205)
	High	2.867 (35.254)	0.385 (0.535)	2.796 (35.338)	0.385 (0.539)	3.034 (35.414)	0.414 (0.580)	2.941 (35.751)	0.418 (0.579)
	Very High	33.056 (144.510)	3.638 (5.130)	22.447 (104.469)	3.043 (4.333)	29.615 (125.571)	4.394 (6.264)	24.845 (105.169)	3.966 (5.640)
Moving Variance	Very Low	0.124 (0.259)	0.038 (0.053)	0.138 (0.292)	0.039 (0.055)	0.138 (0.305)	0.038 (0.053)	0.131 (0.260)	0.045 (0.063)
	Low	0.472 (0.971)	0.142 (0.196)	0.502 (1.021)	0.143 (0.200)	0.520 (1.091)	0.140 (0.195)	0.486 (0.951)	0.162 (0.222)
	High	2.253 (7.640)	0.344 (0.486)	2.126 (6.702)	0.335 (0.476)	2.423 (7.642)	0.366 (0.523)	2.160 (6.768)	0.384 (0.538)
	Very High	36.406 (159.551)	2.685 (3.848)	25.946 (125.006)	2.331 (3.362)	32.934 (142.879)	3.615 (5.222)	28.853 (125.875)	3.382 (4.868)

Table 4.12: Debold-Mariano statistic for the DJI 500 dataset (with a p-value given in brackets) for the LSTM-29 against LSTM-1, R-GARCH and GJR-MEM for the four volatility regimes.

		LSTM-29 vs.		
		LSTM-1	R-GARCH	GJR-MEM
Moving Average	Very Low	6.65 (1.000)	-2.12 (0.017)	2.21 (0.987)
	Low	2.56 (0.995)	-2.30 (0.011)	1.07 (0.859)
	High	-1.79 (0.037)	-5.23 (< 0.001)	-1.91 (0.028)
	Very High	-7.11 (< 0.001)	-6.87 (< 0.001)	-2.58 (0.005)
Moving Variance	Very Low	10.64 (1.000)	0.06 (0.524)	4.83 (1.000)
	Low	5.06 (1.000)	-2.51 (0.006)	2.55 (0.995)
	High	-2.88 (0.002)	-7.75 (< 0.001)	-1.13 (0.13)
	Very High	-7.02 (< 0.001)	-6.66 (< 0.001)	-3.00 (0.001)

for the moving average, I consider the following ranges: 0 to 0.50 (up to 50%) for VL; 0.50 to 0.85 (up to 75%) for L; 0.85 to 2.80 (up to 95%) for H; and 2.80 to 13.92 (up to 100%) for VH. For the moving variance the ranges are: 0 to 1.18 (up to 25%) for VL; 1.18 to 1.79 (up to 75%) for L; 1.79 to 4.38 (up to 95%) for H; and 4.38 to 15.60 (up to 100%) for VH. As can be seen from the DM test results in Table 4.12, the LSTM-1 performs better than the multivariate counterpart for relatively low volatility periods, while having inferior performance for higher volatility ones. The LSTM-29 is never worse than the R-GARCH, slightly worse than the GJR-MEM for low volatilities and always statistically better in high volatility settings.

However, it is worth noticing that the difference between LSTM-1 and LSTM-29 seen from Table 4.11 is in practice negligible, valuing 0.010 (VL) and 0.024

(L) for the mean, 0.014 (VL) and 0.030 (L) for the median. The real impact is made by the LSTM-29 within the VH volatility regime, where the difference to LSTM-1, R-GARCH, GJR-MEM is respectively 10.61, 7.17, 2.40 for the mean and 0.59, 1.35, 0.92 for the median. Considering that the risk in trading assets is considerable at higher volatility, the VH cluster is also the most important to pay attention to.

In all regimes, the LSTM-29 has a tendency to provide larger values of volatility when compared to R-GARCH and GJR-MEM estimates, and to be more conservative from a risk management perspective.

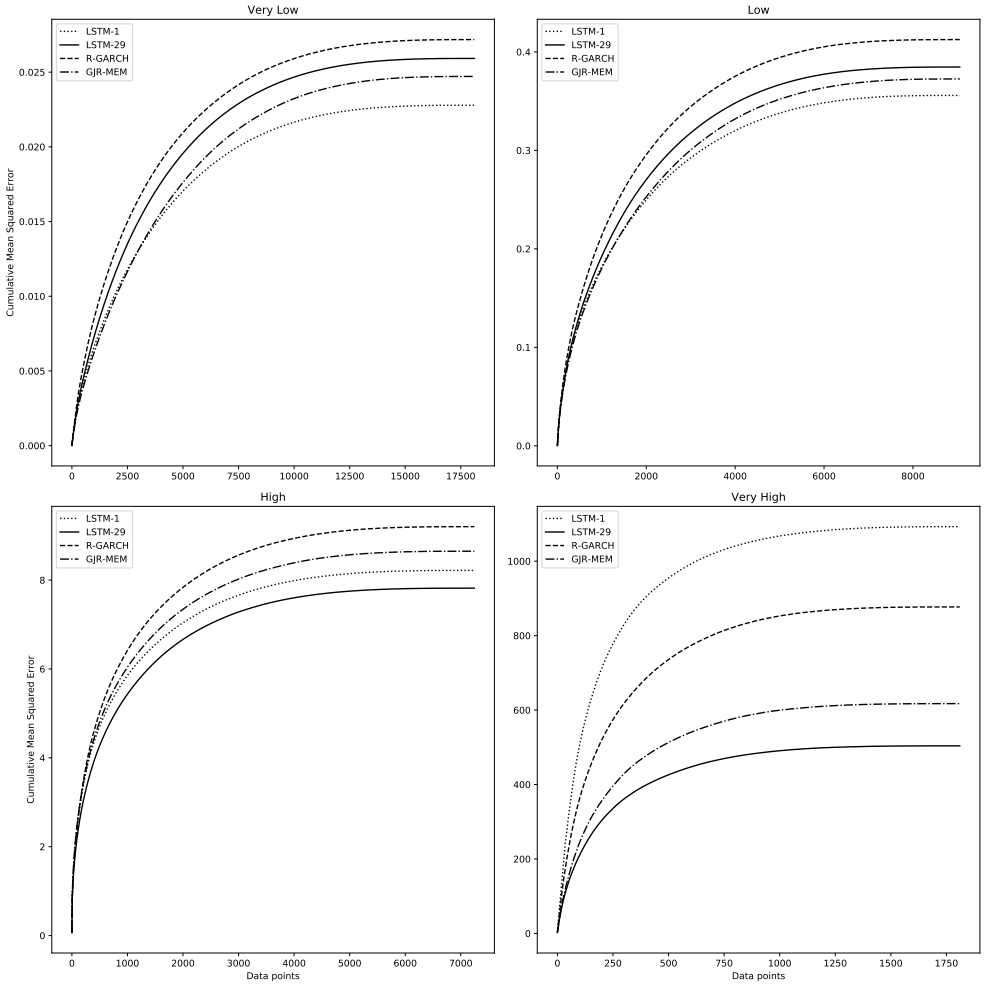

Figure 4.14: Cumulative MSE for the four models at different volatility regimes (VL, L, H, and VH). The four volatility levels are calculated using the percentiles at 50, 75 and 95 over the 29 assets. The different scale on the y-axis is due to the magnitude of the error in the four volatility regimes.

Figure 4.14 outlines the cumulative MSE recorded by the considered models

in the four different volatility regimes. These curves are plotted by sorting the errors in decreasing order so that larger errors come first, which is the reason of the up-sloped shapes of the curves: they outline the tendency of models to accumulate larger errors along the experimentation. One can observe that the LSTM-29 performance is always better than the other models in regimes of H and VH volatility. In VL and L volatility regimes, the LSTM-29 is a little worse than GJR-MEM, but still better than R-GARCH in all considered regimes. This is not surprising as the R-GARCH and GJR-MEM are econometric models of volatility, while LSTM is unaware of the underlying stochastic process. Instead, the LSTM-1 achieved a better accuracy for VL and L regimes, but performed poorly for the VH volatility regime. For completeness, the LSTM-29 was also trained without the index fund SPY, showing consistent results.

Table 4.13: MSE before and during the crisis on the DJI 500 dataset for the four models. The best performing model for the two considered time periods is given in bold.

Asset	Before Crisis				During Crisis			
	LSTM-1	LSTM-29	R-GARCH	GJR-MEM	LSTM-1	LSTM-29	R-GARCH	GJR-MEM
AA	2.66	**2.38**	2.79	2.44	15.90	**10.35**	15.56	12.61
AIG	3.24	2.85	3.48	**2.62**	25.07	**15.38**	21.88	20.13
AXP	0.71	**0.65**	0.68	0.73	16.35	**7.30**	9.61	8.72
BA	0.58	**0.57**	0.62	0.59	2.48	**2.04**	2.06	1.91
BAC	0.37	**0.34**	0.39	0.37	22.78	**16.24**	30.63	19.10
C	0.51	0.39	0.43	**0.37**	34.19	**13.49**	20.52	16.44
CAT	0.85	**0.82**	0.88	0.84	2.45	**2.07**	2.72	2.44
CVX	0.91	0.78	0.78	**0.73**	3.69	**2.51**	3.44	2.84
DD	0.55	**0.48**	0.53	**0.48**	6.92	**4.36**	5.58	4.43
DIS	0.65	**0.63**	0.67	0.64	2.97	2.09	2.02	**1.81**
GE	**0.21**	0.25	0.23	**0.21**	2.48	**1.82**	2.23	2.06
GM	7.15	**6.39**	7.36	7.05	34.18	**28.10**	33.16	30.61
HD	0.70	0.75	0.69	**0.68**	12.39	**7.46**	8.80	7.76
IBM	0.25	0.25	0.26	**0.22**	2.78	**1.86**	2.73	2.22
INTC	**0.85**	0.97	0.93	0.88	4.46	4.41	4.63	**4.15**
JNJ	**0.30**	0.31	0.32	0.33	0.48	**0.39**	0.51	0.44
JPM	0.62	**0.59**	0.64	0.60	25.71	**18.88**	21.29	15.11
KO	**0.18**	0.19	0.22	**0.18**	0.76	**0.70**	0.94	0.78
MCD	**1.20**	1.26	1.20	1.32	1.96	2.17	1.97	**1.94**
MMM	0.46	0.41	0.46	**0.40**	1.61	1.29	1.86	**1.27**
MRK	**6.37**	6.43	6.50	7.18	25.81	**20.38**	27.01	26.92
MSFT	0.33	0.36	0.34	**0.31**	3.13	2.06	2.16	**1.97**
PG	**0.20**	**0.20**	0.22	**0.20**	0.56	0.53	0.78	**0.52**
SPY	0.06	0.07	0.06	**0.05**	0.71	0.64	0.68	**0.55**
T	1.27	**1.22**	1.72	1.32	5.70	3.87	4.22	**3.86**
UTX	0.35	0.36	0.39	**0.34**	3.51	**2.44**	4.05	2.86
VZ	**0.59**	0.64	0.66	0.60	5.71	**3.24**	3.71	**3.24**
WMT	**0.36**	0.37	0.40	**0.36**	2.57	**2.27**	3.44	2.46
XOM	0.67	0.63	0.59	**0.57**	2.42	**2.30**	2.72	2.43

To investigate whether the proposed model is able to predict exceptional events, I considered its predictive performance during the 2007-2008 crisis (in particular, the time span of 200 data points, starting from the 1^{st} July 2007).

Table 4.13 shows the MSE scored by each model in the initial 1050 days (pre-crisis) and the last 200 days (in-crisis). As already shown in Figure 4.14, the LSTM-1 and GJR-MEM are slightly better in the forecast within low volatility regimes (pre-crisis), closely followed by the LSTM-29. On the other hand, during the crisis period, the LSTM-29 performed better than LSTM-1 and R-GARCH in 28 out of 29 cases, and in 20 out of 29 cases when compared to GJR-MEM. Furthermore, R-GARCH was never able to achieve the best forecast for any of the assets during both the pre-crisis and in-crisis periods.

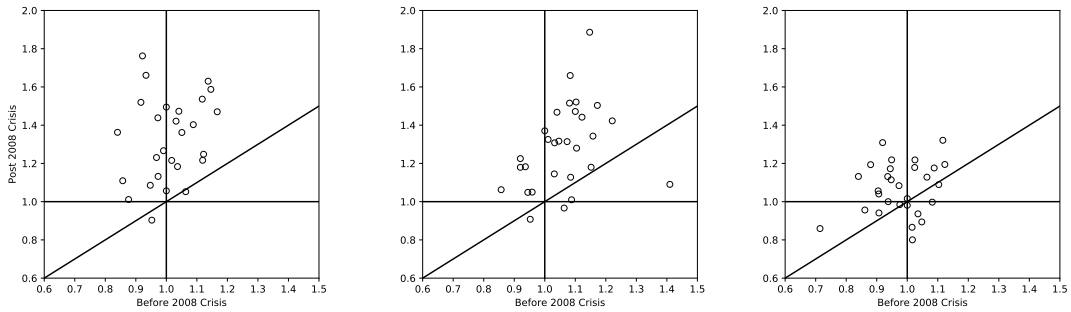

(a) LSTM-1 (b) R-GARCH (c) GJR-MEM

Figure 4.15: Relationship between MSE ratios pre-crisis on the x-axis (up to 1 July 2007) and in-crisis on the y-axis (after 1 July 2007). LSTM-29 is compared to LSTM-1 in Figure 4.15a, to R-GARCH in Figure 4.15b and to GJR-MEM Figure 4.15c. Each dot is an asset; the bisect line is used as reference.

In order to evaluate how much model A is better then model B, their MSE ratio is computed as:

$$\mathtt{ratioMSE}(A, B) = \frac{\mathrm{MSE}_A}{\mathrm{MSE}_B}$$

which gives a value greater than 1, if model B has better accuracy than model A, and lower than 1 otherwise. This metric has been applied in order to compare the four models performance during the pre-crisis and in-crisis periods.

As can be seen from Figure 4.15a, the LSTM-29 is performing better than LSTM-1 for 28 out of 29 assets (i.e., all except for the MCD - the only point below the reference line) during the in-crisis period, with up to 1.8 MSE ratio.

When compared to the R-GARCH model (Figure 4.15b), the LSTM-29 is showing similar performance. Again, the MCD is better predicted by the R-GARCH in both periods and three other assets are with worsened MSE ratio but are still better predicted by the LSTM-29. The remaining 25 assets showed an improved performance of LSTM-29 during the in-crisis period.

Lastly, the comparison with GJR-MEM (Figure 4.15c), shows the LSTM-29 with increased accuracy on 15 assets during the 200 high risk days. Five assets are with slightly worsened prediction during the in-crisis period, five assets have close prediction accuracy (at near 1 ratio) and three assets (i.e., INTC, MSFT, and SPY) are better predicted by the GJR-MEM for both before and during the crisis.

Overall, the above discussed empirical results suggest that the use of the LSTM approach for volatility forecasting could be particularly profitable in turbulent periods where the economic pay-off derived from generation of more accurate volatility forecasts is potentially more substantial than those in more tranquil periods.

b) NASDAQ 100 Results for the NASDAQ 100 dataset are reported in Table 4.14, Table 4.15, and Figure 4.16. The latter shows the models' cumulative MSE profile in the four volatility regimes for the NASDAQ 100 dataset. As already observed with the DJI 500 (Figure 4.14), the proposed method generally achieves better accuracy when compared to the R-GARCH and GJR-MEM. In this experiment, the univariate LSTM-1 not only outperforms the state-of-the-art methods, but also the multivariate counterpart (LSTM-92) in all volatility regimes.

Table 4.14 reports the errors (mean, median, standard deviation (std) and median absolute deviation (MAD)) for the four volatility regimes. As it can be seen from Figure 4.16, the LSTM-1 has smaller errors when compared to all other methods, for both moving average and moving variance volatilities over time. The mean/std are particularly high due to the difference in magnitudes across the 92 assets, which is also evident when using the more robust median/MAD metrics.

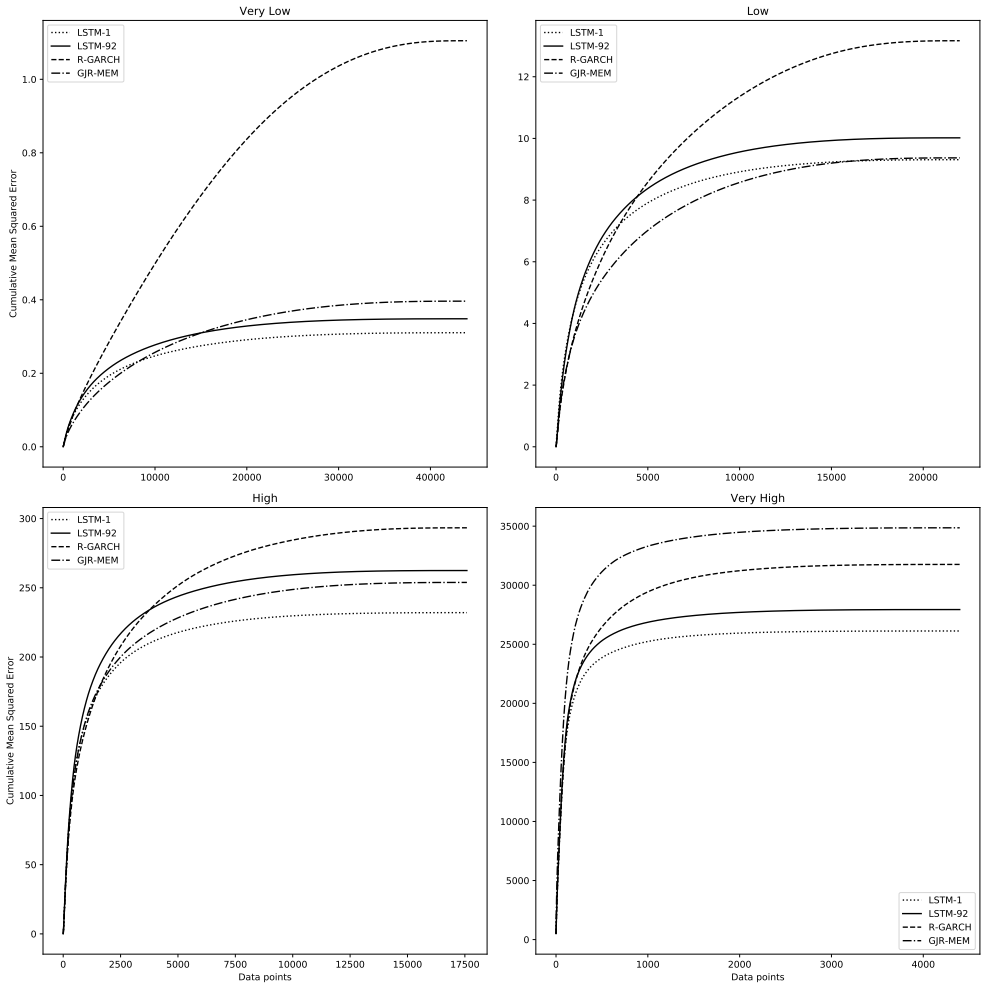

Figure 4.16: Cumulative MSE for the four models at different volatility regimes (VL, L, H, and VH). The four volatility levels are calculated using the percentiles at 50, 75 and 95 over the 92 assets. The different scale on the y-axis is due to the magnitude of the error in the four volatility regimes.

Furthermore, the DM test (Table 4.15) is used to statistically assess the difference in errors between the best model (LSTM-1) and the others (LSTM-92, R-GARCH and GJR-MEM). The DM test shows the LSTM-1 to be statistically better than the R-GARCH in all volatility regimes (p-value < 0.05), better than LSTM-92 in three volatility regimes (i.e., VL, H and VH) for moving variance, and in another three regimes (i.e., L, H and VH) for the moving variance. In the case of GJR-MEM, the LSTM-1 results are statistically better in two volatility settings (i.e., VL and H).

c) Comparison with Recurrent Neural Networks (RNN)

Eventually, I compare the proposed deep model with the classic Elman Net-

Table 4.14: Average with Std (in brackets) errors, Median with MAD (in brackets) errors for the four models at different volatility regimes (VL, L, H and VH) on the NASDAQ 100 dataset. The four volatility regimes are determined using the percentiles at 50, 75, 95 over the all assets . The first comparison (rows 2 to 5) is using a centered moving average of the volatilities over time (5 time steps before and 5 time steps after the current one), while the second one (rows 6 to 9) is using a centered moving variance of the volatilities over time (5 time steps before and 5 time steps after the current one).

		LSTM-1		LSTM-29		R-GARCH		GJR-MEM	
		Mean (Std)	Median (MAD)	Mean (Std)	Median (MAD)	Mean (Std)	Median (MAD)	Mean (Std)	Median (MAD)
Moving Average	Very Low	0.557 (3.311)	0.082 (0.112)	0.590 (2.960)	0.084 (0.118)	1.051 (2.765)	0.566 (0.649)	0.629 (2.675)	0.183 (0.237)
	Low	3.051 (20.954)	0.312 (0.432)	3.165 (15.148)	0.355 (0.495)	3.629 (13.814)	1.105 (1.361)	3.061 (14.050)	0.606 (0.802)
	High	15.233 (94.568)	0.836 (1.181)	16.201 (96.318)	1.048 (1.481)	17.127 (92.106)	2.296 (3.089)	15.933 (94.485)	1.555 (2.111)
	Very High	161.635 (1771.79)	3.022 (4.330)	167.151 (1771.46)	3.714 (5.322)	178.215 (1742.53)	7.645 (10.896)	186.709 (2023.93)	5.054 (7.166)
Moving Variance	Very Low	0.497 (2.376)	0.090 (0.123)	0.502 (1.355)	0.093 (0.130)	1.007 (1.923)	0.569 (0.659)	0.546 (1.147)	0.193 (0.252)
	Low	2.565 (9.518)	0.339 (0.474)	2.750 (7.390)	0.385 (0.544)	3.322 (6.759)	1.199 (1.474)	2.608 (6.313)	0.639 (0.860)
	High	12.955 (52.915)	0.682 (0.976)	13.964 (51.865)	0.848 (1.220)	15.120 (48.385)	2.051 (2.803)	13.207 (47.936)	1.333 (1.848)
	Very High	173.773 (1778.15)	1.178 (1.697)	179.051 (1778.06)	1.555 (2.249)	188.216 (1748.81)	3.272 (4.662)	200.715 (2029.43)	2.652 (3.761)

Table 4.15: Debold-Mariano statistic for the NASDAQ 100 dataset (with a p-value given in brackets) for the LSTM-1 against LSTM-92, R-GARCH and GJR-MEM for the four volatility regimes.

		LSTM-1 vs.		
		LSTM-92	R-GARCH	GJR-MEM
Moving Average	Very Low	-3.35 (0.001)	-40.06 (< 0.001)	-7.44 (< 0.001)
	Low	-1.13 (0.259)	-5.54 (< 0.001)	-0.1 (0.923)
	High	-7.91 (< 0.001)	-12.49 (< 0.001)	-3.41 (0.001)
	Very High	-4.42 (< 0.001)	-5.27 (< 0.001)	-1.59 (0.113)
Moving Variance	Very Low	-0.48 (0.632)	-38.15 (< 0.001)	-4.75 (< 0.001)
	Low	-3.6 (< 0.001)	-13.24 (< 0.001)	-0.87 (0.383)
	High	-5.85 (< 0.001)	-10.53 (< 0.001)	-1.42 (0.155)
	Very High	-4.29 (< 0.001)	-4.62 (< 0.001)	-1.7 (0.089)

work (also known as Simple Recurrent Network) Elman (1990) on both DJI 500 and NASDAQ 100. The Elman RNN topology only stores the previous values of the hidden units, thus being only able to exploit information from the most recent past. This comparison is carried out to further justify the use of the more complex LSTM model. Table 4.16 presents the mean/std and median/MAD of the two methods (both univariate and multivariate) for the two datasets. As can be seen, the LSTMs performances are generally better than the RNN counterparts, achieving lower estimate errors for all analysed volatility regimes and across all metrics (with only few exceptions for RNN-29 with moving variance). Furthermore, Figure 4.17 illustrates the cumulative errors for the DJI 500 (Figure 4.17a) and NASDAQ 100 (Figure 4.17b) datasets. As can be observed, the error profiles of both univariate and multivariate LSTM are better (lower cumulative error) than those achieved by the two compared RNN models. This

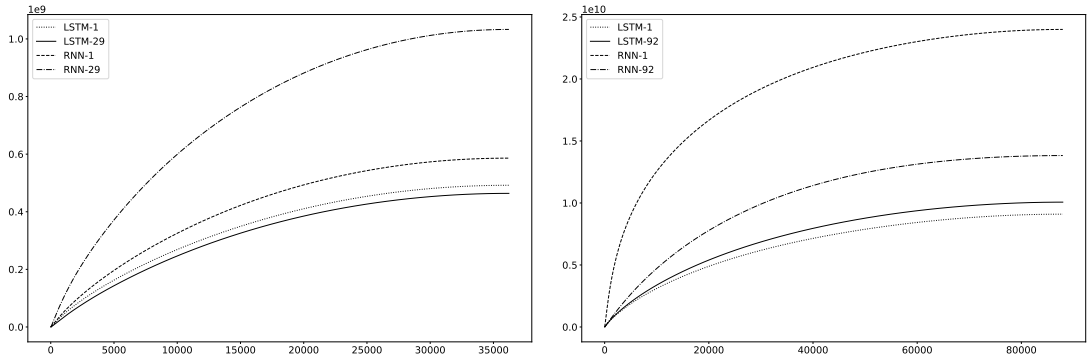

(a) DJI 500 (b) NASDAQ 100

Figure 4.17: Cumulative MSE for the LSTM and RNN methods (both univariate and multivariate).

result further acknowledges the ability of more complex time series models to exploit both short and long term dependencies in the available data.

Table 4.16: Average with Std (in brackets) errors, Median with MAD (in brackets) errors for the four models at different volatility regimes (VL, L, H and VH) on the DJI 500 and NASDAQ 100 datasets. The four volatility regimes are determined using the percentiles at 50, 75, 95 over the all assets. The first comparison (rows 2 to 5) is using a centered moving average of the volatilities over time (5 time steps before and 5 time steps after the current one), while the second one (rows 6 to 9) is using a centered moving variance of the volatilities over time (5 time steps before and 5 time steps after the current one).

		DJI 500							
		LSTM-1		LSTM-29		RNN-1		RNN-29	
		Mean (Std)	Median (MAD)	Mean (Std)	Median (MAD)	Mean (Std)	Median (MAD)	Mean (Std)	Median (MAD)
Moving Average	Very Low	0.151 (0.657)	0.037 (0.051)	0.161 (0.677)	0.038 (0.053)	0.176 (0.687)	0.04 (0.056)	0.503 (7.577)	0.061 (0.086)
	Low	0.596 (3.29)	0.136 (0.186)	0.62 (3.234)	0.139 (0.191)	0.679 (3.289)	0.155 (0.213)	3.074 (82.297)	0.222 (0.309)
	High	2.867 (35.254)	0.385 (0.535)	2.796 (35.338)	0.385 (0.539)	3.714 (41.474)	0.446 (0.629)	8.303 (140.693)	0.707 (0.995)
	Very High	33.056 (144.510)	3.638 (5.130)	22.447 (104.469)	3.043 (4.333)	38.993 (231.107)	4.405 (6.253)	61.709 (312.965)	6.707 (9.585)
Moving Variance	Very Low	0.124 (0.259)	0.038 (0.053)	0.138 (0.292)	0.039 (0.055)	0.148 (0.307)	0.041 (0.058)	0.06 (0.634)	0.015 (0.373)
	Low	0.472 (0.971)	0.142 (0.196)	0.502 (1.021)	0.143 (0.2)	0.572 (1.156)	0.165 (0.231)	0.084 (1.165)	0.02 (0.727)
	High	2.253 (7.640)	0.344 (0.486)	2.126 (6.702)	0.335 (0.476)	2.796 (9.868)	0.409 (0.582)	0.234 (3.082)	0.028 (1.182)
	Very High	36.406 (159.551)	2.685 (3.848)	25.946 (125.006)	2.332 (3.362)	43.480 (244.150)	3.4191 (4.942)	0.647 (8.114)	0.017 (3.328)
		NASDAQ 100							
		LSTM-1		LSTM-92		RNN-1		RNN-92	
		Mean (Std)	Median (MAD)	Mean (Std)	Median (MAD)	Mean (Std)	Median (MAD)	Mean (Std)	Median (MAD)
Moving Average	Very Low	0.557 (3.311)	0.082 (0.112)	0.590 (2.960)	0.084 (0.118)	2.427 (54.195)	0.069 (0.097)	0.928 (4.180)	0.086 (0.125)
	Low	3.051 (20.954)	0.312 (0.432)	3.165 (15.148)	0.355 (0.495)	16.100 (199.779)	0.315 (0.445)	4.349 (16.878)	0.413 (0.601)
	High	15.233 (94.568)	0.836 (1.181)	16.201 (96.318)	1.048 (1.481)	108.482 (1315.065)	0.970 (1.395)	19.953 (98.638)	1.246 (1.822)
	Very High	161.635 (1771.79)	3.022 (4.330)	167.151 (1771.46)	3.714 (5.322)	764.556 (6103.58)	4.134 (6.019)	177.407 (1761.22)	4.342 (6.374)
Moving Variance	Very Low	0.497 (2.376)	0.090 (0.123)	0.502 (1.355)	0.093 (0.130)	1.584 (32.389)	0.077 (0.108)	0.879 (3.226)	0.098 (0.142)
	Low	2.565 (9.518)	0.339 (0.474)	2.750 (7.390)	0.385 (0.544)	10.237 (121.438)	0.341 (0.488)	4.28 (12.877)	0.449 (0.656)
	High	12.955 (52.915)	0.682 (0.976)	13.964 (51.865)	0.848 (1.220)	78.006 (695.522)	0.794 (1.155)	18.125 (60.955)	0.983 (1.444)
	Very High	173.774 (1778.15)	1.178 (1.697)	179.051 (1778.06)	1.555 (2.249)	924.192 (6491.16)	1.612 (2.356)	185.557 (1767.47)	1.896 (2.787)

4.3 Deep Learning for threat detection in luggage from x-ray images

Identifying and detecting dangerous objects and threats in baggage carried on board of aircrafts plays important role in ensuring and guaranteeing passen-

gers security and safety. The security checks relay mostly on X-ray imaging and human inspection, which is a time consuming, tedious process performed by human experts assessing whether threats are hidden in closely packed bags, occluded by other objects. Furthermore, a variety of challenges make this process tedious, among those: very few bags actually contain threat items; the bags can include a wide range of items, shapes and substances (e.g., metals, organic, etc.); the decision needs to be made in few seconds (especially in rush hour); and the objects can be rotated, thus presenting an unrecognisable view. Due to the complex nature of the task, the literature suggests that human expert detection performance is only about 80-90% (Michel et al., 2007). Automating the screening process through incorporating intelligent techniques for image processing and object detection can increase the efficiency, reduce the time and improve the overall accuracy of dangerous objects recognition. This work aims to develop a framework to automatically detect firearms from x-ray scans using Deep Learning techniques. The classification task focusses on the detection of steel barrel bores to determine the likelihood of firearms being present within an x-ray image using a variety of classification approaches. Two datasets of dual view x-ray scans are used to assess the performance of the classifiers: the first dataset contains images of hand-held travel luggage, while the second dataset comprises scans of courier parcels. Two Deep Learning techniques, namely Convolutional Neural Networks and Stacked Autoencoders, and two widely used classification techniques (Feed Forward Neural Networks and Random Forests) are here compared.

4.3.1 Related Work

Research on threat detection in luggage security is grouped based on three imaging modalities: single-view x-ray scans (Riffo and Mery, 2012), multi-view x-ray scans (Mery et al., 2015, 2013), and computed tomography (CT) (Flitton et al., 2015). Classification performance usually shows improvements with the number of utilised views, with detection performance ranging from 89% true positive rate (TPR) with 18% false positive rate (FPR) for single view imag-

ing [1] to 97.2% TPR and 1.5% FPR in full CT imagery (Flitton et al., 2015). The general consensus in the baggage research community is that classification of x-ray images is more challenging than visible spectrum data (Parande and Soma, 2015), and that direct application of methods used frequently on natural images (such as SIFT, RIFT, HoG) does not always perform well when applied to x-ray scans (Jaccard et al., 2016). However, identification performance can be improved by exploiting the characteristics of x-ray images by: augmenting multiple views; using a coloured material image or using simple (gradient) density histogram descriptors (Rogers et al., 2017; Li and Yu, 2018; Shen et al., 2018). To our knowledge, no attempt has been made to use Deep Learning in the classification of x-ray images of baggage and parcels. Bastan et al. (2013) discuss some of the potential difficulties when learning features using Deep Learning techniques, including out-of-plane rotations and images of varying size. Here, I handle the varying image size problem by combining the two views in one unique sample, while I do not explicitly tackle the out-of-plane rotation problem, instead I rely on data augmentation techniques and on a dataset containing the threat objects recorded in different poses.

4.3.2 Dataset

The original dataset consists of over 22000 images of which approximately 10000 contained a threat item (i.e. a whole firearm or component). The threat images are produced using a dual view x-ray machine: one view from above, and one from the side. Each image contains metadata about the image class (i.e., benign or threat), and firearm component (i.e., barrel only, full weapon, set of weapons, etc). From the provided image library, a sample of 3546 threat images were selected containing a firearm barrel (amongst other item), and 1872 benign images only containing allowed objects. The aim of the classification is to discriminate only the threat items - as common objects are displayed in both benign and threat samples (Figure 4.18 and Figure 4.19). During the pre-processing phase, each image is treated separately and the two views are combined before the classification stage.

4.3.3 Threat identification framework

The proposed framework for automated weapon detection consists of three modules: pre-processing, data augmentation and threat detection. The pre-processing stage comprises four steps: green layer extraction, greyscale smoothing, black and white (b/w) thresholding and data augmentation.

Figure 4.18: A sample image containing a steel barrel bores (top left cylinder in the top row) from the baggage dataset. The left image is the raw dual view x-ray scan, in the middle the grey scale smoothed one, and on the right the b/w thresholded one.

The original x-ray scans are imported in the framework as 3-channel images (RGB) and scaled to 128x128 pixels in order to have images of same size for the machine learning procedure, and to meet memory constraints during training. From the scaled image, the green colour channel is extracted as the one found having the greatest contrast in dense material. The resulting greyscale image is intended to more accurately reflect the raw x-ray data (i.e. measure of absorption (Baruchel et al., 2010)). This step is performed to enable subsequent filtering and better identification of a threshold for dense material and eventually to facilitate the recognition of the barrel. A smoothing algorithm is applied on the greyscale image in order to reduce the low-level noise within the image while preserving distinct object edges. A number of smoothing algorithms were tested and a simple 3x3 kernel Gaussian blur (Aurich and Weule, 1995) was found to generate the best results. On the smoothed image a thresholding technique to isolate dense material (e.g., steel) is applied. The chosen threshold

is approximated within the algorithm to the equivalent of 2mm of steel, which ensures that metal objects such as firearm barrels and other components are kept. This step removes much of the benign background information within the image, such as organic materials and plastics. The resulting image is normalised to produce an image where the densest material is black and areas of the image that were below the threshold are white. At this point, some instances, where the produced image lacks any significant dense material, the sample can be directly classified as benign. From cursory examination of the operational benign test set, this is a significant proportion of the samples for the baggage dataset, while only filtering out a small portion of images on the parcels one (mainly because in the courier parcels there is a higher variety of big and small metallic objects compared to hand-held travel luggage). When applying Deep Learning techniques on images, it is often useful to increase the robustness of the classification by adding realistic noise and variation to the training data (i.e., augmentation (Ding et al., 2016)), especially in case of high imbalance between classes (Shen et al., 2018). There are several ways in which this can be achieved: object volume scaling: scaling the object volume V by a factor v; object flips: objects can be flipped in the x or y directions to increase appearance variation; object shift: objects can be shifted in the x or y directions to increase appearance variation. For every image in the training set, multiple instances are generated combining different augmentation procedures and those are used during the learning phase of the models. Lastly, the two views of each sample are vertically stacked to compose one final image. Here are reported the four machine learning techniques compared in this work, two from the Deep Learning area widely used for image classification, namely CNN and Stacked Autoencoders; and two shallow techniques, namely shallow NN and RF (also used for the detection of threats in cargo images Jaccard et al. (2016)).

4.3.4 Experimentation and Results

After the pre-processing and filtering of images not containing enough dense material, we are left with 1848 and 1764 samples for classification for the bag-

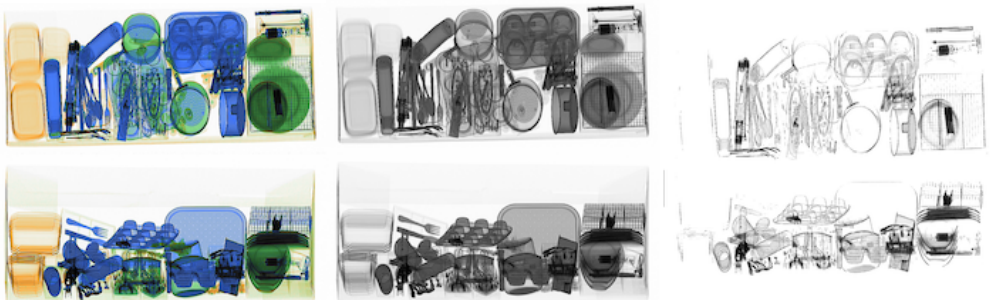

Figure 4.19: A sample image containing a steel barrel bores (top right cylinder in the top row) from the parcel dataset. The left image is the raw dual view x-ray scan, in the middle the grey scale smoothed one, and on the right b/w thresholded one. The parcel dataset usually contains a higher amount of steel objects and the barrels are better concealed.

gage and parcel datasets respectively. The baggage dataset has 672 images from the benign class and 1176 containing threats; while the parcel dataset has 576 and 1188 samples for the benign and threat classes respectively. Each dataset is split in 70% for training and 30% left as independent test set. Due to their different operational environments, the baggage and parcel scans are trained and tested separately. In this experiment I use a three layer stacked autoencoder with 200, 100, 50 neurons respectively, followed by a softmax output function to predict the classes probability. For the CNN I employ a topology with three convolutional layers (with 128, 64 and 32 neurons) followed by a fully connected neural network and a softmax output function. The RF is trained with 200 trees while the shallow NN has a topology of N-N-2, where N is the input size. Since both RF and shallow NN cannot be directly trained on raw pixels, a further step of feature extraction is performed. In particular, I use histograms of oriented Basic Image Features (oBIFs) as a texture descriptor as suggested in (Jaccard et al., 2016), which has been applied successfully in many machine vision tasks. Basic Image Features are a scheme for the classification of each pixel of an image into one of seven categories depending on local symmetries. These categories are: flat (no strong symmetry), slopes (e.g. gradients), blobs (dark and bright), lines (dark and bright), and saddle-like. Oriented BIFs are an extension of BIFs including the quantized orientation of rotationally asymmetric features (Newell and Griffin, 2011), which encode a compact representation of images. The oBIF feature vector is then fed as input into the RF and shal-

low NN classifiers. To evaluate the classification performance I employ three metrics: area under the ROC curve (AUC), the false positive rate at 90% true positive rate (FPR@90%TPR), and the F1-score. The AUC is widely used metric for classification tasks, the FPR@90%TPR is one cut-off point from the AUC and describes the amount of false positive we can expect if we want to catch 90% of all threats. The cut-off at 90% is suggested by [6] for the classification of x-ray images in a similar context. The F1-score is also a widely used measure score for classification of imbalanced datasets and takes into account the precision (the number of correctly identified threats divided by the number of all threats identified by the classifier) and the recall (the number of correctly identified threats divided by the number of all threat samples). For the experimentation I report the classification performance on the raw data and after applying two pre-processing steps: grey scale smoothing and b/w thresholding.

Table 4.17: Baggage dataset results for the AUC, FPR@90%TPR and F1-Score metrics. The results are reported for the four classification techniques and three pre-processing step: raw data, grey scale smoothing and b/w thresholding.

Metric	Technique	Raw	Smoothing	B/w thresholding
AUC	CNN	93	95	96
	Autoencoder	75	78	90
	oBIFs + NN	85	87	94
	oBIFs + RF	66	72	80
FPR@90%TPR	CNN	9	7	6
	Autoencoder	70	60	26
	oBIFs + NN	50	31	14
	oBIFs + RF	86	66	53
F1-Score	CNN	91	93	93
	Autoencoder	60	65	81
	oBIFs + NN	64	67	79
	oBIFs + RF	36	41	56

As it can be seen from Table 4.17, the CNN outperformed the other methods with AUC ranging between 93 and 96 depending on the pre-processing stage. The second best method is the shallow NN with AUC values between 85 and 94, while the worst performance is achieved by the RF with 66-80% AUC. Similar results are achieved when considering the FPR@90% TPR and F1-score metrics. The CNN achieved the best FPR (6%) when training on the b/w thresholded images, while still having only 9% FPR when employing raw data. On the other

hand, the NN, while achieving 14% FPR with the last stage of pre-processing, its performance drop drastically when employing the raw data and the smoothed one, with 50% and 31% FPR respectively. Same can be seen when using the F1-score, with the CNN achieving up to 93% followed by the autoencoders and shallow NN with 81% and 79% respectively. Once again, it is worth to notice that the CNN is the only technique able to score high classification accuracy across all pre-processing stages, while the other methods necessitate more time spent on engineering and extracting features.

Table 4.18: Parcel dataset results for the AUC, FPR@90%TPR and F1-Score metrics. The results are reported for the four classification techniques and three pre-processing step: raw data, grey scale smoothing and b/w thresholding.

Metric	Technique	Raw	Smoothing	B/w thresholding
AUC	CNN	80	79	84
	Autoencoder	65	66	75
	oBIFs + NN	65	69	84
	oBIFs + RF	63	63	79
FPR@90%TPR	CNN	46	46	37
	Autoencoder	66	69	70
	oBIFs + NN	71	75	40
	oBIFs + RF	91	88	56
F1-Score	CNN	86	83	87
	Autoencoder	40	43	55
	oBIFs + NN	36	32	63
	oBIFs + RF	34	42	58

Table 4.18 shows the performance metrics on the parcel dataset. As can be observed, the achieved performance are generally lower across all the techniques. This can be explained by the largest variety of metal items contained in the courier parcels when compared to objects contained in a hand-held airport luggage. Once again the CNN outperformed the comparison methods, with an AUC ranging 79% to 84%, followed by the NN 65% to 84%, RF 63 to 79% and Autoencoders 66% to 75%. The AUC achieved on the parcel dataset by the shallow NN, RF and Autoencoders are much closer than those achieved on the baggage one, where there is a more clearer separation on the best performing method. Once again the CNN achieved the lowest FPR (37%), followed by the shallow NN with 40% FPR, the RF with 56% FPR and the autoencoders 69% FPR. Lastly, the F1-score is again the metric with the larger difference in values

across methods, with the CNN achieving up to 87% F1-score, followed by shallow NN with 63%, RF with 58% and Autoencoders with 55%. Also in this case, the CNN is the only technique which is able to classify threats with high accuracy just using the raw images, where all other techniques would perform very poorly (e.g., the AUC on raw data for the CNN is: 15 percentage points better than the NN, while holding exact same performance with the b/w thresholded one; 25 percentage points better in FPR@90%TPR when compared to the NN; and 50 percentage points better for the F1-score).

4.4 Conclusion

In this chapter a variety of Deep Learning techniques have been applied to three real world problems. Although the tackled problems belong to very different fields (i.e., monitoring fetal health during childbirth; predicting volatility stock market; and aid human experts in the detection of threats in x-ray images), they all share a research literature were feature engineering and extraction aimed to improve the prediction performance has the largest focus. Here, I investigate the profitability of Deep Learning methods, were the effort goes into the selection of the architecture, rather than in the feature engineering (in almost all presented cases the Deep Learning models were able to cope with the raw data or with minimum pre-processing).

5 Conclusion

Several methods and approaches have been proposed, implemented, tested, validated and evaluated in the search of optimal and reliable solutions to several real-world machine learning tasks (i.e., classification, regression, values imputation and learn to rank). In their essence, the studied cases have been summarised below.

5.1 Missing data Imputation

In this thesis I explored a variety of use cases where the effective imputation of missing values can benefit the learning process. The problem of the identification of radar signal emitters with a high percentage of missing values in its features has been investigated. Three different missing data techniques have been applied and their impact analysed in different classification settings (i.e., binary and multi-class) and when applying a variety of classifiers. Furthermore, I introduced two new metrics to better discriminate between intra-class and outer-class errors due to the hierarchical nature of our radar types (i.e., civil and military).

From the reported literature review, multiple studies showed discordant results on which imputation technique performs the best depending on the individual problem or dataset at hand (confirming the no free lunch theorem). After an initial analysis on 13 publicly available datasets, I found that not only there is often a different best performing technique for each dataset, but also for each individual feature within a dataset. Based on those findings, I proposed an aggregation of imputation techniques tailored to maximize the imputation accuracy of each feature in the dataset. The proposal is extensively compared to five other imputation techniques and its effectiveness showed under all three missing data mechanisms.

The impact of missing data and long tail problems for a real-world learn to rank task (sorting online travel agency properties) has also been investigated. After an initial analysis of the dataset, I identified a class of poorly ranked properties

(i.e., Vacation Rentals) due to their short historical data and missing important features such as guest and star rating. Due to the large size of the dataset, I imputed the missing values of the two features using regression techniques available in Spark. The complete dataset has then been re-ranked, showing a significant boost in the overall position of the Vacation Rental type.

Furthermore, I tackled the missing historical data problem found in the Online Travel Agency properties. In order to do that, a novel missing data imputation technique based on Distributed Neural Network on Spark has been introduced. The proposal has been compared with three imputation techniques also implemented in Spark, in order to cope with the size of the dataset (500K properties and 1000 features). The proposal showed lower imputation error for all 57 features with missing data, while also having a good speedup (scaling well with the number of machines used in the cluster).

5.2 Deep Learning Methods for Real-World Problems

In the second part of the thesis, I applied Deep Learning techniques to three real-world problems. Although the tackled problems belong to very different fields, they all share a research literature were feature engineering and extraction has the largest focus, aimed to improve the prediction performance. Here I consider Deep Learning techniques in order to make predictions with raw data or minimal pre-processing.

Firstly, I used both LSTM and CNN to detect foetus complications during childbirth. In general, the Deep Learning models showed good generalization accuracy (in particular the newly proposed MCNN), outperforming in some instances existing computerized approaches and current clinical practice when tested on internal and external data. Nevertheless, the investigated model is still at its early stage of development and there is significant future research that should improve the performance further.

Secondly, I investigated the profitability of using LSTM for forecasting daily

stock market volatility employing an application to a panel of 29 assets representative of the Dow Jones Industrial Average index over the period 2002-2008, in addition to the market factor proxied by the SPY, and to 92 assets belonging to the NASDAQ 100 index within the period Dec 2012 to Nov 2017. The findings suggest that LSTM can outperform some widely popular univariate parametric benchmarks, such as the R-GARCH and GJR-MEM, in condition of high volatility, while still being comparable for low/medium volatility periods. These conclusions have been confirmed evaluating the results by different perspectives. An attractive feature of the LSTM is that it easily allows taking into account volatility spillover phenomena which are dynamic dependence relationships among the volatilities of different stocks. Such dependency is hard to shape with conventional parametric approaches, due to a large number of parameters that should be handled by the model itself. Indeed even simple models such as standard vector auto-regressive techniques are easily affected by the curse of dimensionality. On the other hand, LSTM belongs to the emerging class of Deep Learning approaches that proved their capability to cope with complex and highly nonlinear dependencies among the considered variables.

Lastly, I introduced a Deep Learning framework for the automatic identification of steel barrel bores in operational settings such airport security clearance process and courier parcel inspection. In particular I compare two Deep Learning techniques (i.e., CNN and Stacked Autoencoders), and two widely used state-of-the-art classification methods (i.e., shallow NN and RF) on two datasets. I evaluate performance using three widely used metrics for classification tasks: AUC, FPR@90%TPR and the F1-Score. Results show that the CNN is not only able to consistently outperform all other compared techniques over the three metrics and the two datasets, but it is also able to achieve good prediction accuracy using the raw data (whether the other techniques need multiple steps of data pre-processing and feature extraction to improve their performance). Furthermore, the CNN also achieved higher performance than those reported in literature for human experts (although the used datasets have not been evaluated by experts, hence an accurate direct comparison cannot be performed).

5.3 Further Research Directions

Further investigation of the studied research topics can be made in the following directions:

- Radar Signal Recognition with Missing Data: comparison with other techniques for handling missing data; experimentation on a broader variety of classifiers; identification of more than two superclasses by implementing unsupervised learning and then employing supervised one for assessing inner error (IE) and outer error (OE) metrics.

- Scattered Feature Guided Data Imputation: compare the imputation techniques when the datasets are subsequently used in a prediction task (e.g., regression and classification); perform a sensitivity analysis to assess the impact of this imputation on the final results in order to show the correlation between imputation accuracy and prediction errors (bias analysis); test the proposal on big data through aggregation of distributed techniques.

- Online Traveling Recommendation System with Missing Values: analyse the behaviour of the recommender system when the engineered and imputed features are used during the recommendation process for the VR properties; test new error functions to assess and distinguish the current under/over estimation of the imputed ratings by the model based techniques.

- Large Scale Missing Data Imputation: test different neural network topologies; validate the model on different datasets; use the imputed data in a subsequent task (e.g., recommendation) and study how the imputed data affect the overall performance of the second task.

- Deep Learning for fetal monitoring in labour: investigate more flexible models of the stacked approach, allowing iterative analysis of the entire CTG available; better embed the quality of the signal in the training process, instead of manually adjusting the classification thresholds to

the level of signal loss; introduce more suitably structured information about the clinical risk factors; combine the Multimodal Convolutional Neural Network with domain-specific knowledge and/or existing algorithms that complement each other to yield risk assessment for different types of fetal compromises.

- Deep Learning for stock market volatility forecasting: test different LSTM topologies with more stacked layers and different activation functions; test the performance of the LSTM decreasing the initial training set period (currently 300 days); study the impact of the LSTM predictions on financial phenomena such as the Value at Risk and the Expected Shortfall.

- Deep Learning for threat detection in luggage from x-ray images: explore different topologies for the CNN and Stacked Autoencoders; test the framework on bigger datasets and compare it with human expert performance; test a recurrent CNN model to work on a moving image (as it would be presented in a real operational setting).

References

Abry, P., Spilka, J., Leonarduzzi, R., Chudáček, V., Pustelnik, N., and Doret, M. (2018). Sparse learning for intrapartum fetal heart rate analysis. *Biomedical Physics & Engineering Express*, 4(3):034002.

Ahmadlou, M. and Adeli, H. (2010). Enhanced probabilistic neural network with local decision circles: A robust classifier. *Integrated Computer-Aided Engineering*, 17(3):197–210.

Alcalá, J., Fernández, A., Luengo, J., Derrac, J., García, S., Sánchez, L., and Herrera, F. (2010). Keel data-mining software tool: Data set repository, integration of algorithms and experimental analysis framework. *Journal of Multiple-Valued Logic and Soft Computing*, 17(255-287):11.

Amdahl, G. M. (1967). Validity of the single processor approach to achieving large scale computing capabilities. In *Proceedings of the April 18-20, 1967, spring joint computer conference*, pages 483–485. ACM.

Anagnostopoulos, C. and Triantafillou, P. (2014). Scaling out big data missing value imputations: pythia vs. godzilla. In *Proceedings of the 20th ACM SIGKDD international conference on Knowledge discovery and data mining*, pages 651–660. ACM.

Andersen, T. G. and Teräsvirta, T. (2009). Realized volatility. In *Handbook of financial time series*, pages 555–575. Springer.

Asuncion, A. and Newman, D. (2007). Uci machine learning repository.

Aurich, V. and Weule, J. (1995). Non-linear gaussian filters performing edge preserving diffusion. In *Mustererkennung 1995*, pages 538–545. Springer.

Authority, N. L. (2012). Ten years of maternity claims: an analysis of nhs litigation authority data. *London: NHS Litigation Authority*.

Azur, M. J., Stuart, E. A., Frangakis, C., and Leaf, P. J. (2011). Multiple imputation by chained equations: what is it and how does it work? *International journal of methods in psychiatric research*, 20(1):40–49.

Baeza-Yates, R. and Ribeiro-Neto, B. (1999). *Modern information retrieval*, volume 463. ACM press New York.

Barndorff-Nielsen, O. E., Hansen, P. R., Lunde, A., and Shephard, N. (2011). Multivariate realised kernels: consistent positive semi-definite estimators of the covariation of equity prices with noise and non-synchronous trading. *Journal of Econometrics*, 162(2):149–169.

Barndorff-Nielsen, O. E. and Shephard, N. (2005). Variation, jumps, market frictions and high frequency data in financial econometrics. *Nuffield College Economics Working Paper*, 1(1):1–5.

Bartlett, J. W., Seaman, S. R., White, I. R., Carpenter, J. R., and Initiative, A. D. N. (2015). Multiple imputation of covariates by fully conditional specification: accommodating the substantive model. *Statistical methods in medical research*, 24(4):462–487.

Baruchel, J., Buffiere, J.-Y., and Maire, E. (2010). X-ray tomography in material science. *Materials characterization*, 61(12):1305–1316.

Bastan, M., Byeon, W., and Breuel, T. M. (2013). Object recognition in multi-view dual energy x-ray images. In *BMVC*, volume 1, page 11.

Batista, G. E. and Monard, M. C. (2002). A study of k-nearest neighbour as an imputation method. *HIS*, 87(48):251–260.

Bauer, A., Kantelhardt, J. W., Barthel, P., Schneider, R., Mäkikallio, T., Ulm, K., Hnatkova, K., Schömig, A., Huikuri, H., and Bunde, A. (2006). Deceleration capacity of heart rate as a predictor of mortality after myocardial infarction: cohort study. *The lancet*, 367(9523):1674–1681.

Bauwens, L., Laurent, S., and Rombouts, J. V. (2006). Multivariate garch models: a survey. *Journal of applied econometrics*, 21(1):79–109.

Bengio, Y., Lamblin, P., Popovici, D., and Larochelle, H. (2007). Greedy layer-wise training of deep networks. *Advances in neural information processing systems*, 19:153.

Bergstra, J. S., Bardenet, R., Bengio, Y., and Kégl, B. (2011). Algorithms for hyper-parameter optimization. In *Advances in neural information processing systems*, pages 2546–2554.

Bianchi, F. M., Maiorino, E., Kampffmeyer, M. C., Rizzi, A., and Jenssen, R. (2017). An overview and comparative analysis of recurrent neural networks for short term load forecasting. *arXiv preprint arXiv:1705.04378*.

Blume, M. E. (1971). On the assessment of risk. *The Journal of Finance*, 26(1):1–10.

Bollerslev, T. (1986). Generalized autoregressive conditional heteroskedasticity. *Journal of econometrics*, 31(3):307–327.

Borthakur, D. (2007). The hadoop distributed file system: Architecture and design. *Hadoop Project Website*, 11(2007):21.

Bottou, L. (2010). Large-scale machine learning with stochastic gradient descent. In *Proceedings of COMPSTAT'2010*, pages 177–186. Springer.

Breiman, L. (2001). Random forests. *Machine learning*, 45(1):5–32.

Briggs, D. C. (2008). Comments on slavin: Synthesizing causal inferences. *Educational Researcher*, 37(1):15–22.

Brocklehurst, P., Field, D. J., Juszczak, E., Kenyon, S., Linsell, L., Newburn, M., Plachcinski, R., Quigley, M., Schroeder, L., and Steer, P. (2017). The infant trial. *The Lancet*, 390(10089):28.

Cao, F., Liu, B., and Park, D. S. (2013). Image classification based on effective extreme learning machine. *Neurocomputing*, 102:90–97.

Cartwright, M., Shepperd, M. J., and Song, Q. (2003). Dealing with missing software project data. In *Software Metrics Symposium, 2003. Proceedings. Ninth International*, pages 154–165. IEEE.

Cazares, S., Moulden, M., Redman, C. W., and Tarassenko, L. (2001). Tracking poles with an autoregressive model: a confidence index for the analysis of the intrapartum cardiotocogram. *Medical engineering & physics*, 23(9):603–614.

Chai, T. and Draxler, R. R. (2014). Root mean square error (rmse) or mean absolute error (mae)?–arguments against avoiding rmse in the literature. *Geoscientific Model Development*, 7(3):1247–1250.

Chakraborty, K., Mehrotra, K., Mohan, C. K., and Ranka, S. (1992). Forecasting the behavior of multivariate time series using neural networks. *Neural networks*, 5(6):961–970.

Chang, G. and Ge, T. (2011). Comparison of missing data imputation methods for traffic flow. In *Transportation, Mechanical, and Electrical Engineering (TMEE), 2011 International Conference on*, pages 639–642. IEEE.

Chen, W., Liu, T.-Y., Lan, Y., Ma, Z.-M., and Li, H. (2009). Ranking measures and loss functions in learning to rank. In *Advances in Neural Information Processing Systems*, pages 315–323.

Chen, X. B., Gao, J., Li, D., and Silvapulle, P. (2018). Nonparametric estimation and forecasting for time-varying coefficient realized volatility models. *Journal of Business & Economic Statistics*, 36(1):88–100.

Chilimbi, T. M., Suzue, Y., Apacible, J., and Kalyanaraman, K. (2014). Project adam: Building an efficient and scalable deep learning training system. In *OSDI*, volume 14, pages 571–582.

Choi, E., Schuetz, A., Stewart, W. F., and Sun, J. (2016). Using recurrent neural network models for early detection of heart failure onset. *Journal of the American Medical Informatics Association*, 24(2):361–370.

Chudacek, V., Spilka, J., Bursa, M., Janku, P., Hruban, L., Huptych, M., and Lhotska, L. (2014). Open access intrapartum ctg database. *BMC pregnancy and childbirth*, 14(1):16.

Cohen, J. (2013). *Statistical power analysis for the behavioral sciences*. Routledge.

Cohen, J., Cohen, P., West, S. G., and Aiken, L. S. (2013). *Applied multiple regression/correlation analysis for the behavioral sciences*. Routledge.

Dalgaard, P. (2008). *Introductory statistics with R*. Springer Science & Business Media.

Davies, S. (2015). Annual report of the chief medical officer, 2014, the health of the 51%: Women. *London: Department of Health*.

Dean, J. and Ghemawat, S. (2008). Mapreduce: simplified data processing on large clusters. *Communications of the ACM*, 51(1):107–113.

Delalleau, O. and Bengio, Y. (2011). Shallow vs. deep sum-product networks. In *Advances in Neural Information Processing Systems*, pages 666–674.

Deng, L., Li, J., Huang, J.-T., Yao, K., Yu, D., Seide, F., Seltzer, M., Zweig, G., He, X., and Williams, J. (2013). Recent advances in deep learning for speech research at microsoft. In *Acoustics, Speech and Signal Processing (ICASSP), 2013 IEEE International Conference on*, pages 8604–8608. IEEE.

Diebold, F. X. and Mariano, R. S. (2002). Comparing predictive accuracy. *Journal of Business & economic statistics*, 20(1):134–144.

Dietterich, T. G. (2000). Ensemble methods in machine learning. In *Multiple classifier systems*, pages 1–15. Springer.

Ding, J., Chen, B., Liu, H., and Huang, M. (2016). Convolutional neural network with data augmentation for sar target recognition. *IEEE Geoscience and remote sensing letters*, 13(3):364–368.

Draper, N. R. and Smith, H. (2014). *Applied regression analysis*, volume 326. John Wiley & Sons.

Elman, J. L. (1990). Finding structure in time. *Cognitive science*, 14(2):179–211.

Enders, C. K. (2010). *Applied missing data analysis*. Guilford Press.

Engle, R. (2002). New frontiers for arch models. *Journal of Applied Econometrics*, 17(5):425–446.

Engle, R. F. and Russell, J. R. (1998). Autoregressive conditional duration: a new model for irregularly spaced transaction data. *Econometrica*, pages 1127–1162.

Erhan, D., Bengio, Y., Courville, A., Manzagol, P.-A., Vincent, P., and Bengio, S. (2010). Why does unsupervised pre-training help deep learning? *The Journal of Machine Learning Research*, 11:625–660.

Eryildirim, A. and Onaran, I. (2011). Pulse doppler radar target recognition using a two-stage svm procedure. *IEEE Transactions on Aerospace and Electronic Systems*, 47(2):1450–1457.

Ewen, S., Schelter, S., Tzoumas, K., Warneke, D., and Markl, V. (2013). Iterative parallel data processing with stratosphere: an inside look. In *Proceedings of the 2013 ACM SIGMOD International Conference on Management of Data*, pages 1053–1056. ACM.

Farokhi, N., Vahid, M., Nilashi, M., and Ibrahim, O. (2016). A multi-criteria recommender system for tourism using fuzzy approach. *Journal of Soft Computing and Decision Support Systems*, 3(4):19–29.

Feelders, A. (1999). Handling missing data in trees: Surrogate splits or statistical imputation? In *Principles of Data Mining and Knowledge Discovery*, pages 329–334. Springer.

Fernández-Delgado, M., Cernadas, E., Barro, S., and Amorim, D. (2014). Do we need hundreds of classifiers to solve real world classification problems? *The Journal of Machine Learning Research*, 15(1):3133–3181.

Fleder, D. and Hosanagar, K. (2009). Blockbuster culture's next rise or fall: The impact of recommender systems on sales diversity. *Management science*, 55(5):697–712.

Flitton, G., Mouton, A., and Breckon, T. P. (2015). Object classification in 3d baggage security computed tomography imagery using visual codebooks. *Pattern Recognition*, 48(8):2489–2499.

Frénay, B. and Verleysen, M. (2014). Classification in the presence of label noise: a survey. *Neural Networks and Learning Systems, IEEE Transactions on*, 25(5):845–869.

George, L. (2011). *HBase: the definitive guide: random access to your planet-size data*. " O'Reilly Media, Inc.".

Georgieva, A. (2016). Advances in computing are driving progress in fetal monitoring. *BJOG: An International Journal of Obstetrics & Gynaecology*, 123(12):1955–1955.

Georgieva, A., Papageorghiou, A., Payne, S., Moulden, M., and Redman, C. (2014). Phase-rectified signal averaging for intrapartum electronic fetal heart rate monitoring is related to acidaemia at birth. *BJOG: An International Journal of Obstetrics & Gynaecology*, 121(7):889–894.

Georgieva, A., Redman, C. W., and Papageorghiou, A. T. (2017). Computerized data-driven interpretation of the intrapartum cardiotocogram: a cohort study. *Acta obstetricia et gynecologica Scandinavica*, 96(7):883–891.

Georgoulas, G., Karvelis, P., Spilka, J., Chudáček, V., Stylios, C. D., and Lhotská, L. (2017). Investigating ph based evaluation of fetal heart rate (fhr) recordings. *Health and technology*, 7(2-3):241–254.

Gers, F. A., Eck, D., and Schmidhuber, J. (2002a). Applying lstm to time series predictable through time-window approaches. In *Neural Nets WIRN Vietri-01*, pages 193–200. Springer.

Gers, F. A. and Schmidhuber, J. (2001). Long short-term memory learns context free and context sensitive languages. In *Artificial Neural Nets and Genetic Algorithms*, pages 134–137. Springer.

Gers, F. A., Schmidhuber, J., and Cummins, F. (1999). Learning to forget: Continual prediction with lstm. *Neural Computation*, pages 850–855.

Gers, F. A., Schraudolph, N. N., and Schmidhuber, J. (2002b). Learning precise timing with lstm recurrent networks. *Journal of machine learning research*, 3(1):115–143.

Glosten, L. R., Jagannathan, R., and Runkle, D. E. (1993). On the relation between the expected value and the volatility of the nominal excess return on stocks. *The journal of finance*, 48(5):1779–1801.

Gómez-Carracedo, M., Andrade, J., López-Mahía, P., Muniategui, S., and Prada, D. (2014). A practical comparison of single and multiple imputation methods to handle complex missing data in air quality datasets. *Chemometrics and Intelligent Laboratory Systems*, 134:23–33.

Gong, M., Zhao, J., Liu, J., Miao, Q., and Jiao, L. (2016). Change detection in synthetic aperture radar images based on deep neural networks. *IEEE transactions on neural networks and learning systems*, 27(1):125–138.

Gradvohl, A. L. S., Senger, H., Arantes, L., and Sens, P. (2014). Comparing distributed online stream processing systems considering fault tolerance issues. *Journal of Emerging Technologies in Web Intelligence*, 6(2):174–179.

Graham, J. W. (2009). Missing data analysis: Making it work in the real world. *Annual review of psychology*, 60:549–576.

Graham, J. W., Olchowski, A. E., and Gilreath, T. D. (2007). How many imputations are really needed? some practical clarifications of multiple imputation theory. *Prevention Science*, 8(3):206–213.

Granger, E., Rubin, M. A., Grossberg, S., and Lavoie, P. (2001). A what-and-where fusion neural network for recognition and tracking of multiple radar emitters. *Neural Networks*, 14(3):325–344.

Graves, A. (2013). Generating sequences with recurrent neural networks. *arXiv preprint arXiv:1308.0850*.

Graves, A., Jaitly, N., and Mohamed, A. R. (2013). Hybrid speech recognition with deep bidirectional lstm. In *Automatic Speech Recognition and Understanding (ASRU), 2013 IEEE Workshop on*, pages 273–278. IEEE.

Gustafson, J. L. (1988). Reevaluating amdahl's law. *Communications of the ACM*, 31(5):532–533.

Han, H. and Zhang, S. (2012). Non-stationary non-parametric volatility model. *The Econometrics Journal*, 15(2):204–225.

Han, S., Kang, J., Mao, H., Hu, Y., Li, X., Li, Y., Xie, D., Luo, H., Yao, S., and Wang, Y. (2017). Ese: Efficient speech recognition engine with sparse lstm on fpga. In *Proceedings of the 2017 ACM/SIGDA International Symposium on Field-Programmable Gate Arrays*, pages 75–84. ACM.

Hand, D. J. and Till, R. J. (2001). A simple generalisation of the area under the roc curve for multiple class classification problems. *Machine learning*, 45(2):171–186.

Hansen, P. R., Huang, Z., and Shek, H. H. (2012). Realized garch: a joint model for returns and realized measures of volatility. *Journal of Applied Econometrics*, 27(6):877–906.

Hinton, G. E., Osindero, S., and Teh, Y.-W. (2006). A fast learning algorithm for deep belief nets. *Neural computation*, 18(7):1527–1554.

Hinton, G. E. and Salakhutdinov, R. R. (2006). Reducing the dimensionality of data with neural networks. *Science*, 313(5786):504–507.

Hirose, N. and Tajima, R. (2017). Modeling of rolling friction by recurrent neural network using lstm. In *Robotics and Automation (ICRA), 2017 IEEE International Conference on*, pages 6471–6478. IEEE.

Hochreiter, S. and Schmidhuber, J. (1997). Long short-term memory. *Neural computation*, 9(8):1735–1780.

Hossin, M. and Sulaiman, M. (2015). A review on evaluation metrics for data classification evaluations. *International Journal of Data Mining & Knowledge Management Process*, 5(2):1.

Huang, G.-B., Zhu, Q.-Y., and Siew, C.-K. (2006). Extreme learning machine: theory and applications. *Neurocomputing*, 70(1):489–501.

Ibrahim, N., Abdullah, R., and Saripan, M. (2009). Artificial neural network approach in radar target classification. *Journal of Computer Science*, 5(1):23.

Jaccard, N., Rogers, T. W., Morton, E. J., and Griffin, L. D. (2016). Tackling the x-ray cargo inspection challenge using machine learning. In *Anomaly Detection and Imaging with X-Rays (ADIX)*, volume 9847, page 98470N. International Society for Optics and Photonics.

Jordanov, I. and Petrov, N. (2014). Sets with incomplete and missing datann radar signal classification. In *2014 International Joint Conference on Neural Networks (IJCNN)*, pages 218–224. IEEE.

Jordanov, I. and Petrov, N. (2016). Intelligent radar signal recognition and classification. In *Recent Advances in Computational Intelligence in Defense and Security*, pages 101–135. Springer.

Jordanov, I., Petrov, N., and Petrozziello, A. (2016). Supervised radar signal classification. *Proceedings on the International Joint Conference on Neural Networks (IJCNN 2016)*.

Jordanov, I., Petrov, N., and Petrozziello, A. (2018). Classifiers accuracy improvement based on missing data imputation. *Journal of Artificial Intelligence and Soft Computing Research*, 8(1):31–48.

Jozefowicz, R., Zaremba, W., and Sutskever, I. (2015). An empirical exploration of recurrent network architectures. In *Proceedings of the 32nd International Conference on Machine Learning (ICML-15)*, pages 2342–2350.

Kaminsky, A. (2016). *BIG CPU, BIG DATA: Solving the World's Toughest Computational Problems with Parallel Computing*. CreateSpace Independent Publishing Platform.

Kang, Y., Chen, S., Wang, X., and Cao, Y. (2018). Deep convolutional identifier for dynamic modeling and adaptive control of unmanned helicopter. *IEEE transactions on neural networks and learning systems*, 1(99):1–15.

Karatzoglou, A., Meyer, D., and Hornik, K. (2005). Support vector machines in r. *WU Vienna University of Economics and Business*.

Kohavi, R. and Provost, F. (1998). Glossary of terms. *Machine Learning*, 30(2-3):271–274.

Koohi, H. and Kiani, K. (2016). User based collaborative filtering using fuzzy c-means. *Measurement*, 91:134–139.

Koren, Y. (2008). Factorization meets the neighborhood: a multifaceted collaborative filtering model. In *Proceedings of the 14th ACM SIGKDD international conference on Knowledge discovery and data mining*, pages 426–434. ACM.

Koren, Y. (2009). The bellkor solution to the netflix grand prize. *Netflix prize documentation*, 81:1–10.

Koren, Y., Bell, R., and Volinsky, C. (2009). Matrix factorization techniques for recommender systems. *Computer*, 42(8):30–37.

Kourentzes, N., Barrow, D. K., and Crone, S. F. (2014). Neural network ensemble operators for time series forecasting. *Expert Systems with Applications*, 41(9):4235–4244.

Kuremoto, T., Kimura, S., Kobayashi, K., and Obayashi, M. (2014). Time series forecasting using a deep belief network with restricted boltzmann machines. *Neurocomputing*, 137:47–56.

Kurinczuk, J. J., White-Koning, M., and Badawi, N. (2010). Epidemiology of neonatal encephalopathy and hypoxic–ischaemic encephalopathy. *Early human development*, 86(6):329–338.

Lam, X. N., Vu, T., Le, T. D., and Duong, A. D. (2008). Addressing cold-start problem in recommendation systems. In *Proceedings of the 2nd international conference on Ubiquitous information management and communication*, pages 208–211. ACM.

Landset, S., Khoshgoftaar, T. M., Richter, A. N., and Hasanin, T. (2015). A survey of open source tools for machine learning with big data in the hadoop ecosystem. *Journal of Big Data*, 2(1):1–36.

Langrock, R., Michelot, T., Sohn, A., and Kneib, T. (2015). Semiparametric stochastic volatility modelling using penalized splines. *Computational Statistics*, 30(2):517–537.

Lavesson, N. and Davidsson, P. (2008). Generic methods for multi-criteria evaluation. In *SDM*, pages 541–546. SIAM.

Lawn, J. E., Blencowe, H., Waiswa, P., Amouzou, A., Mathers, C., Hogan, D., Flenady, V., Frøen, J. F., Qureshi, Z. U., and Calderwood, C. (2016). Stillbirths: rates, risk factors, and acceleration towards 2030. *The Lancet*, 387(10018):587–603.

Le Roux, N. and Bengio, Y. (2008). Representational power of restricted boltzmann machines and deep belief networks. *Neural computation*, 20(6):1631–1649.

LeCun, Y., Bengio, Y., and Hinton, G. (2015). Deep learning. *Nature*, 521(7553):436–444.

Lee, B., Baek, J., Park, S., and Yoon, S. (2016). Deeptarget: end-to-end learning framework for microrna target prediction using deep recurrent neural networks. In *Proceedings of the 7th ACM International Conference on Bioinformatics, Computational Biology, and Health Informatics*, pages 434–442. ACM.

Lee, M. C. and Mitra, R. (2016). Multiply imputing missing values in data sets with mixed measurement scales using a sequence of generalised linear models. *Computational Statistics & Data Analysis*, 95:24–38.

Leifert, G., Strauß, T., Grüning, T., Wustlich, W., and Labahn, R. (2016). Cells in multidimensional recurrent neural networks. *The Journal of Machine Learning Research*, 17(1):3313–3349.

Li, G. and Yu, Y. (2018). Contrast-oriented deep neural networks for salient object detection. *IEEE transactions on neural networks and learning systems*, 1(99):1–14.

Li, H., Zhao, H., and Li, H. (2018). Neural-response-based extreme learning machine for image classification. *IEEE transactions on neural networks and learning systems*, 1(99):1–14.

Li, M., Andersen, D. G., Park, J. W., Smola, A. J., Ahmed, A., Josifovski, V., Long, J., Shekita, E. J., and Su, B.-Y. (2014). Scaling distributed machine learning with the parameter server. In *OSDI*, volume 14, pages 583–598.

Liu, Y. and Brown, S. D. (2013). Comparison of five iterative imputation methods for multivariate classification. *Chemometrics and Intelligent Laboratory Systems*, 120:106–115.

Maarala, A. I., Rautiainen, M., Salmi, M., Pirttikangas, S., and Riekki, J. (2015). Low latency analytics for streaming traffic data with apache spark. In *Big Data (Big Data), 2015 IEEE International Conference on*, pages 2855–2858. IEEE.

McAfee, A., Brynjolfsson, E., Davenport, T. H., Patil, D., and Barton, D. (2012). Big data: the management revolution. *Harvard business review*, 90(10):60–68.

McAleer, M. and Medeiros, M. C. (2011). Forecasting realized volatility with linear and nonlinear univariate models. *Journal of Economic Surveys*, 25(1):6–18.

Meng, X., Bradley, J., Yuvaz, B., Sparks, E., Venkataraman, S., Liu, D., Freeman, J., Tsai, D., Amde, M., and Owen, S. (2016). Mllib: Machine learning in apache spark. *JMLR*, 17(34):1–7.

Mery, D., Riffo, V., Zscherpel, U., Mondragón, G., Lillo, I., Zuccar, I., Lobel, H., and Carrasco, M. (2015). Gdxray: The database of x-ray images for nondestructive testing. *Journal of Nondestructive Evaluation*, 34(4):42.

Mery, D., Riffo, V., Zuccar, I., and Pieringer, C. (2013). Automated x-ray object recognition using an efficient search algorithm in multiple views. In *Proceedings of the IEEE conference on computer vision and pattern recognition workshops*, pages 368–374.

Michel, S., Koller, S. M., de Ruiter, J. C., Moerland, R., Hogervorst, M., and Schwaninger, A. (2007). Computer-based training increases efficiency in x-ray image interpretation by aviation security screeners. In *2007 41st Annual*

IEEE International Carnahan Conference on Security Technology, pages 201–206. IEEE.

Miranda, C. S. and Von Zuben, F. J. (2017). Necessary and sufficient conditions for surrogate functions of pareto frontiers and their synthesis using gaussian processes. *IEEE Trans. Evolutionary Computation*, 21(1):1–13.

Moritz, P., Nishihara, R., Stoica, I., and Jordan, M. I. (2015). Sparknet: Training deep networks in spark. *arXiv preprint arXiv:1511.06051*.

Musil, C. M., Warner, C. B., Yobas, P. K., and Jones, S. L. (2002). A comparison of imputation techniques for handling missing data. *Western Journal of Nursing Research*, 24(7):815–829.

Neto, F. M., Cambuim, L. F., Macieira, R. M., Ludermir, T. B., Zanchettin, C., and Barros, E. N. (2015). Extreme learning machine for real time recognition of brazilian sign language. In *Systems, Man, and Cybernetics (SMC), 2015 IEEE International Conference on*, pages 1464–1469. IEEE.

Newell, A. J. and Griffin, L. D. (2011). Natural image character recognition using oriented basic image features. In *2011 International Conference on Digital Image Computing: Techniques and Applications*, pages 191–196. IEEE.

Niwattanakul, S., Singthongchai, J., Naenudorn, E., and Wanapu, S. (2013). Using of jaccard coefficient for keywords similarity. In *Proceedings of the International MultiConference of Engineers and Computer Scientists*, volume 1, pages 13–15.

Norouzi, M., Fleet, D. J., and Salakhutdinov, R. R. (2012). Hamming distance metric learning. In *Advances in neural information processing systems*, pages 1061–1069.

Nunes, I., Ayres-de Campos, D., Ugwumadu, A., Amin, P., Banfield, P., Nicoll, A., Cunningham, S., Sousa, P., Costa-Santos, C., and Bernardes, J. (2017). Central fetal monitoring with and without computer analysis. *Obstetrics & Gynecology*, 129(1):83–90.

Oba, S., Sato, M.-a., Takemasa, I., Monden, M., Matsubara, K.-i., and Ishii, S. (2003). A bayesian missing value estimation method for gene expression profile data. *Bioinformatics*, 19(16):2088–2096.

Odersky, M., Spoon, L., and Venners, B. (2008). *Programming in scala*. Artima Inc.

Osborne, J. W. and Overbay, A. (2012). *Best practices in data cleaning*. Sage.

Owen, S. and Owen, S. (2012). *Mahout in action*. Manning Shelter Island.

Pakel, C., Shephard, N., and Sheppard, K. (2011). Nuisance parameters, composite likelihoods and a panel of garch models. *Statistica Sinica*, pages 307–329.

Pal, N. R., Pal, K., Keller, J. M., and Bezdek, J. C. (2005). A possibilistic fuzzy c-means clustering algorithm. *IEEE transactions on fuzzy systems*, 13(4):517–530.

Pan, X.-Y., Tian, Y., Huang, Y., and Shen, H.-B. (2011). Towards better accuracy for missing value estimation of epistatic miniarray profiling data by a novel ensemble approach. *Genomics*, 97(5):257–264.

Parande, M. and Soma, S. (2015). Concealed weapon detection in a human body by infrared imaging. *International Journal of Science and Research*, 4(9):182–188.

Park, S. and Kim, D.-Y. (2017). Assessing language discrepancies between travelers and online travel recommendation systems: Application of the jaccard distance score to web data mining. *Technological Forecasting and Social Change*, 123:381–388.

Pascanu, R., Mikolov, T., and Bengio, Y. (2013). On the difficulty of training recurrent neural networks. In *International Conference on Machine Learning*, pages 1310–1318.

Patton, A. J. (2011). Volatility forecast comparison using imperfect volatility proxies. *Journal of Econometrics*, 160(1):246–256.

Petrozziello, A., Cervone, G., Franzese, P., Haupt, S. E., and Cerulli, R. (2017). Source reconstruction of atmospheric releases with limited meteorological observations using genetic algorithms. *Applied Artificial Intelligence*, 31(2):119–133.

Petrozziello, A. and Jordanov, I. (2017a). Column-wise guided data imputation. In *Procedia Computer Science*. Elsevier.

Petrozziello, A. and Jordanov, I. (2017b). Data analytics for online travelling recommendation system: a case study. In *Proceedings of the IASTED International Conference Modelling, Identification and Control (MIC 2017), Innsbruck, Austria*, pages 106–112.

Petrozziello, A. and Jordanov, I. (2018). Feature based multivariate data imputation. In *International Conference on Machine Learning, Optimization, and Data Science*, pages 26–37. Springer.

Petrozziello, A. and Jordanov, I. (2019). Automated deep learning for threat detection in luggage from x-ray images. In *Special Event on Analysis of Experimental Algorithms*, pages 1–8.

Petrozziello, A., Jordanov, I., Papageorghiou, T. A., Redman, W. C., and Georgieva, A. (2018a). Deep learning for continuous electronic fetal monitoring in labor. In *2018 40th Annual International Conference of the IEEE Engineering in Medicine and Biology Society (EMBC)*, pages 5866–5869. IEEE.

Petrozziello, A., Jordanov, I., and Sommeregger, C. (2018b). Distributed neural networks for missing big data imputation. In *2018 International Joint Conference on Neural Networks (IJCNN)*, pages 1–8. IEEE.

Petrozziello, A., Redman, C., Papageorghiou, A., Jordanov, I., and Georgieva, A. (2019). Multimodal convolutional neural networks to detect fetal compromise during labor and delivery. *IEEE Access*.

Plis, S. M., Hjelm, D. R., Salakhutdinov, R., Allen, E. A., Bockholt, H. J., Long, J. D., Johnson, H. J., Paulsen, J. S., Turner, J. A., and Calhoun, V. D. (2014). Deep learning for neuroimaging: a validation study. *Frontiers in neuroscience*, 8.

Poggio, T., Mhaskar, H., Rosasco, L., Miranda, B., and Liao, Q. (2017). Why and when can deep-but not shallow-networks avoid the curse of dimensionality: a review. *International Journal of Automation and Computing*, 14(5):503–519.

Rahman, G. and Islam, Z. (2011). A decision tree-based missing value imputation technique for data pre-processing. In *Proceedings of the Ninth Australasian Data Mining Conference-Volume 121*, pages 41–50. Australian Computer Society, Inc.

Resnick, P. and Varian, H. R. (1997). Recommender systems. *Communications of the ACM*, 40(3):56–58.

Richards, M. A. (2005). *Fundamentals of radar signal processing*. Tata McGraw-Hill Education.

Ridgeway, G. (2007). Generalized boosted models: A guide to the gbm package. *Update*, 1(1):2007.

Riffo, V. and Mery, D. (2012). Active x-ray testing of complex objects. *Insight-Non-Destructive Testing and Condition Monitoring*, 54(1):28–35.

Rivolta, M. W., Stampalija, T., Casati, D., Richardson, B. S., Ross, M. G., Frasch, M. G., Bauer, A., Ferrazzi, E., and Sassi, R. (2014). Acceleration and deceleration capacity of fetal heart rate in an in-vivo sheep model. *PloS one*, 9(8):e104193.

Robusto, C. (1957). The cosine-haversine formula. *The American Mathematical Monthly*, 64(1):38–40.

Rogers, T. W., Jaccard, N., and Griffin, L. D. (2017). A deep learning framework for the automated inspection of complex dual-energy x-ray cargo imagery. In *Anomaly Detection and Imaging with X-Rays (ADIX) II*, volume 10187, page 101870L. International Society for Optics and Photonics.

Rostami, S. and Neri, F. (2017). A fast hypervolume driven selection mechanism for many-objective optimisation problems. *Swarm and evolutionary computation*, 34:50–67.

Saar-Tsechansky, M. and Provost, F. (2007). Handling missing values when applying classification models. *Journal of machine learning research*, 8(Jul):1623–1657.

Sarro, F. and Petrozziello, A. (2018). Linear programming as a baseline for software effort estimation. *ACM transactions on software engineering and methodology (TOSEM)*, 27(3):12.

Sarro, F., Petrozziello, A., and Harman, M. (2016). Multi-objective software effort estimation. In *Proceedings of the 38th International Conference on Software Engineering*, pages 619–630. ACM.

Schafer, J. L. (1997). *Analysis of incomplete multivariate data*. CRC press.

Schafer, J. L. and Graham, J. W. (2002). Missing data: our view of the state of the art. *Psychological methods*, 7(2):147.

Schmidhuber, J. (2015). Deep learning in neural networks: An overview. *Neural Networks*, 61:85–117.

Schmitt, P., Mandel, J., and Guedj, M. (2015). A comparison of six methods for missing data imputation. *Journal of Biometrics & Biostatistics*, 2015.

Sha-Sha, W., Hui-Juan, L., Wei, J., and Chao, L. (2014). A construction method of gene expression data based on information gain and extreme learning machine classifier on cloud platform. *International Journal of Database Theory & Application*, 7(2).

Shen, Y., Ji, R., Wang, C., Li, X., and Li, X. (2018). Weakly supervised object detection via object-specific pixel gradient. *IEEE transactions on neural networks and learning systems*, 1(99):1–11.

Shieh, C.-S. and Lin, C.-T. (2002). A vector neural network for emitter identification. *IEEE Transactions on Antennas and Propagation*, 50(8):1120–1127.

Shrive, F. M., Stuart, H., Quan, H., and Ghali, W. A. (2006). Dealing with missing data in a multi-question depression scale: a comparison of imputation methods. *BMC medical research methodology*, 6(1):1.

Singh, B. and Toshniwal, D. (2019). Mowm: Multiple overlapping window method for rbf based missing value prediction on big data. *Expert Systems with Applications*.

Sorjamaa, A. and Lendasse, A. (2010). Fast missing value imputation using ensemble of soms. In *Aalto University School of Science and Technology*.

Spilka, J., Chudacek, V., Huptych, M., Leonarduzzi, R., Abry, P., and Doret, M. (2016). Intrapartum fetal heart rate classification: Cross-database evaluation. In *XIV Mediterranean Conference on Medical and Biological Engineering and Computing 2016*, pages 1199–1204. Springer.

Su, X. and Khoshgoftaar, T. M. (2009). A survey of collaborative filtering techniques. *Advances in artificial intelligence*, 2009:4.

Sun, Y., Wang, X., and Tang, X. (2013). Hybrid deep learning for face verification. In *Computer Vision (ICCV), 2013 IEEE International Conference on*, pages 1489–1496. IEEE.

Sundermeyer, M., Ney, H., and Schlüter, R. (2015). From feedforward to recurrent lstm neural networks for language modeling. *IEEE Transactions on Audio, Speech, and Language Processing*, 23(3):517–529.

Sutskever, I., Vinyals, O., and Le, Q. V. (2014). Sequence to sequence learning with neural networks. In *Advances in neural information processing systems*, pages 3104–3112.

Suwajanakorn, S., Seitz, S. M., and Kemelmacher-Shlizerman, I. (2017). Synthesizing obama: learning lip sync from audio. *ACM Transactions on Graphics (TOG)*, 36(4):95.

Thusoo, A., Sarma, J. S., Jain, N., Shao, Z., Chakka, P., Anthony, S., Liu, H., Wyckoff, P., and Murthy, R. (2009). Hive: a warehousing solution over a map-reduce framework. *Proceedings of the VLDB Endowment*, 2(2):1626–1629.

Timmins, A. E. and Clark, S. L. (2015). How to approach intrapartum category ii tracings. *Obstetrics and Gynecology Clinics*, 42(2):363–375.

Toshniwal, A., Taneja, S., Shukla, A., Ramasamy, K., Patel, J. M., Kulkarni, S., Jackson, J., Gade, K., Fu, M., and Donham, J. (2014). Storm@ twitter. In *Proceedings of the 2014 ACM SIGMOD international conference on Management of data*, pages 147–156. ACM.

Tran, N.-T., Luong, V.-T., Nguyen, N. L.-T., and Nghiem, M.-Q. (2016). Effective attention-based neural architectures for sentence compression with bidirectional long short-term memory. In *Proceedings of the Seventh Symposium on Information and Communication Technology*, pages 123–130. ACM.

Troyanskaya, O., Cantor, M., Sherlock, G., Brown, P., Hastie, T., Tibshirani, R., Botstein, D., and Altman, R. B. (2001). Missing value estimation methods for dna microarrays. *Bioinformatics*, 17(6):520–525.

Twala, B., Cartwright, M., and Shepperd, M. (2006). Ensemble of missing data techniques to improve software prediction accuracy. In *Proceedings of the 28th international conference on Software engineering*, pages 909–912. ACM.

Unknown (2017). Neuron package for scala. https://github.com/bobye/neuron. Accessed: 2017-11-28.

Valdiviezo, H. C. and Van Aelst, S. (2015). Tree-based prediction on incomplete data using imputation or surrogate decisions. *Information Sciences*, 311:163–181.

Van Meteren, R. and Van Someren, M. (2000). Using content-based filtering for recommendation. In *Proceedings of the Machine Learning in the New Information Age: MLnet/ECML2000 Workshop*, pages 47–56.

Vavilapalli, V. K., Murthy, A. C., Douglas, C., Agarwal, S., Konar, M., Evans, R., Graves, T., Lowe, J., Shah, H., and Seth, S. (2013). Apache hadoop yarn: Yet another resource negotiator. In *Proceedings of the 4th annual Symposium on Cloud Computing*, page 5. ACM.

Verboven, S., Branden, K. V., and Goos, P. (2007). Sequential imputation for missing values. *Computational Biology and Chemistry*, 31(5):320–327.

Visser, M. P. (2011). Garch parameter estimation using high-frequency data. *Journal of Financial Econometrics*, 9(1):162–197.

Wadkar, S. and Siddalingaiah, M. (2014). Apache ambari. In *Pro Apache Hadoop*, pages 399–401. Springer.

Wainberg, M., Alipanahi, B., and Frey, B. J. (2016). Are random forests truly the best classifiers? *The Journal of Machine Learning Research*, 17(1):3837–3841.

Walsh, C. A., McMenamin, M. B., Foley, M. E., Daly, S. F., Robson, M. S., and Geary, M. P. (2008). Trends in intrapartum fetal death, 1979-2003. *American journal of obstetrics and gynecology*, 198(1):47–e1.

Wan, L., Zeiler, M., Zhang, S., Le Cun, Y., and Fergus, R. (2013). Regularization of neural networks using dropconnect. In *International Conference on Machine Learning*, pages 1058–1066.

Wang, L., Zeng, Y., and Chen, T. (2015). Back propagation neural network with adaptive differential evolution algorithm for time series forecasting. *Expert Systems with Applications*, 42(2):855–863.

Wang, S., Minku, L. L., and Yao, X. (2014). A multi-objective ensemble method for online class imbalance learning. In *2014 International Joint Conference on Neural Networks (IJCNN)*, pages 3311–3318. IEEE.

Whigham, P. A., Owen, C. A., and Macdonell, S. G. (2015). A baseline model for software effort estimation. *ACM Transactions on Software Engineering and Methodology (TOSEM)*, 24(3):20.

White, T. (2012). *Hadoop: The definitive guide*. " O'Reilly Media, Inc.".

Willmott, C. J. and Matsuura, K. (2005). Advantages of the mean absolute error (mae) over the root mean square error (rmse) in assessing average model performance. *Climate research*, 30(1):79–82.

Xia, F., Yang, L. T., Wang, L., and Vinel, A. (2012). Internet of things. *International Journal of Communication Systems*, 25(9):1101.

Xin, R. S., Gonzalez, J. E., Franklin, M. J., and Stoica, I. (2013). Graphx: A resilient distributed graph system on spark. In *First International Workshop on Graph Data Management Experiences and Systems*, page 2. ACM.

Xin, Z., Ying, W., and Bin, Y. (2010). Signal classification method based on support vector machine and high-order cumulants. *Wireless Sensor Network*, 2(01):48.

Xu, K., Ba, J., Kiros, R., Cho, K., Courville, A., Salakhudinov, R., Zemel, R., and Bengio, Y. (2015). Show, attend and tell: Neural image caption generation with visual attention. In *International Conference on Machine Learning*, pages 2048–2057.

Yao, K., Peng, B., Zhang, Y., Yu, D., Zweig, G., and Shi, Y. (2014). Spoken language understanding using long short-term memory neural networks. In *Spoken Language Technology Workshop (SLT), 2014 IEEE*, pages 189–194. IEEE.

Ye, J., Chow, J.-H., Chen, J., and Zheng, Z. (2009). Stochastic gradient boosted distributed decision trees. In *Proceedings of the 18th ACM conference on Information and knowledge management*, pages 2061–2064. ACM.

Yin, Z., Yang, W., Yang, Z., Zuo, L., and Gao, H. (2011). A study on radar emitter recognition based on spds neural network. *Information Technology Journal*, 10(4):883–888.

Yu, F., Xie, Y., and Ke, Q. (2010). Sbotminer: large scale search bot detection. In *Proceedings of the third ACM international conference on Web search and data mining*, pages 421–430. ACM.

Yu, X., Ma, H., Hsu, B.-J. P., and Han, J. (2014). On building entity recommender systems using user click log and freebase knowledge. In *Proceedings of the 7th ACM international conference on Web search and data mining*, pages 263–272. ACM.

Yuan, Y., Xu, H., Wang, B., and Yao, X. (2016). A new dominance relation-based evolutionary algorithm for many-objective optimization. *IEEE Transactions on Evolutionary Computation*, 20(1):16–37.

Zaharia, M., Chowdhury, M., Franklin, M. J., Shenker, S., and Stoica, I. (2010). Spark: cluster computing with working sets. In *Proceedings of the 2nd USENIX conference on Hot topics in cloud computing*, volume 10, page 10.

Zaytar, M. A. and El Amrani, C. (2016). Sequence to sequence weather forecasting with long short-term memory recurrent neural networks. *International Journal of Computer Applications*, 143(11).

Zervas, G., Proserpio, D., and Byers, J. W. (2017). The rise of the sharing economy: Estimating the impact of airbnb on the hotel industry. *Journal of Marketing Research*, 54(5):687–705.

Zhai, S. and Jiang, T. (2015). A new sense-through-foliage target recognition method based on hybrid differential evolution and self-adaptive particle swarm optimization-based support vector machine. *Neurocomputing*, 149:573–584.

Zhang, K. and Teo, K. L. (2015). A penalty-based method from reconstructing smooth local volatility surface from american options. *J. Ind. Manag. Optim*, 11:631–644.

Zhao, Z.-Q., Zheng, P., Xu, S.-t., and Wu, X. (2019). Object detection with deep learning: A review. *IEEE transactions on neural networks and learning systems*.

Zhou, S., Chen, Q., and Wang, X. (2013). Active deep learning method for semi-supervised sentiment classification. *Neurocomputing*, 120:536–546.

Appendices

A
Scattered Feature Guided Data Imputation

Following are represented the cumulative error bar plot of the four imputation methods considered in Section 3.3 for the Contraceptive, Yeast, Car, Titanic, Abalone, White Wine, Page Block, Ring, Two Norm, Pen Based, Nursery, and Magic04 datasets. For each dataset, the x-axis discrete values represent the attributes of the dataset, the y-axis represents a % error cumulative to 1 (a smaller segment means smaller RMSE). Each segment shows different imputation method, ordered from the shortest (bottom) to the highest (top). For each attribute, the bottom segment is the one which performed best. The values in the segments are rounded to the second significant digit for readability purpose, while the height of segments has not been rounded.

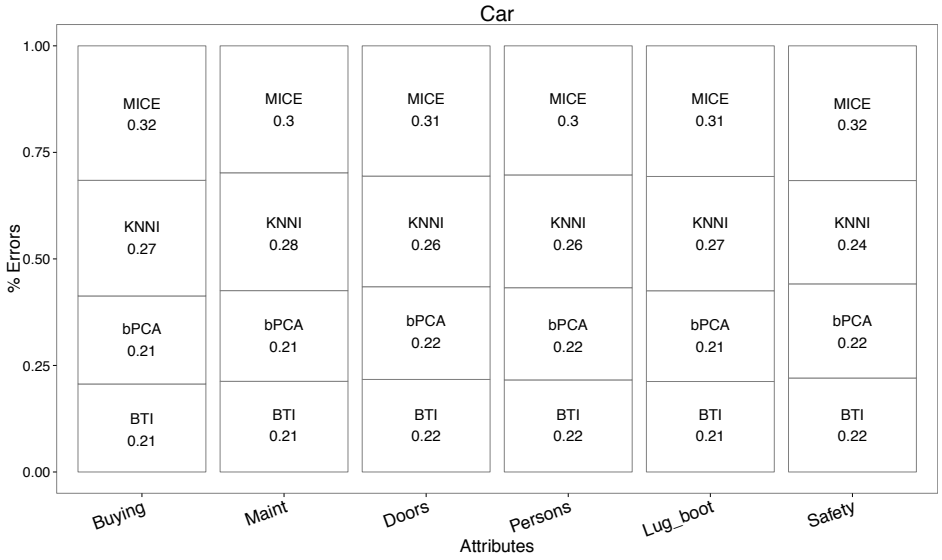
Car
% Errors
1.00
0.75
0.50
0.25
0.00
MICE 0.32
KNNI 0.27
bPCA 0.21
BTI 0.21
MICE 0.3
KNNI 0.28
bPCA 0.21
BTI 0.21
MICE 0.31
KNNI 0.26
bPCA 0.22
BTI 0.22
MICE 0.3
KNNI 0.26
bPCA 0.22
BTI 0.22
MICE 0.31
KNNI 0.27
bPCA 0.21
BTI 0.21
MICE 0.32
KNNI 0.24
bPCA 0.22
BTI 0.22
Buying
Maint
Doors
Persons
Lug_boot
Safety
Attributes

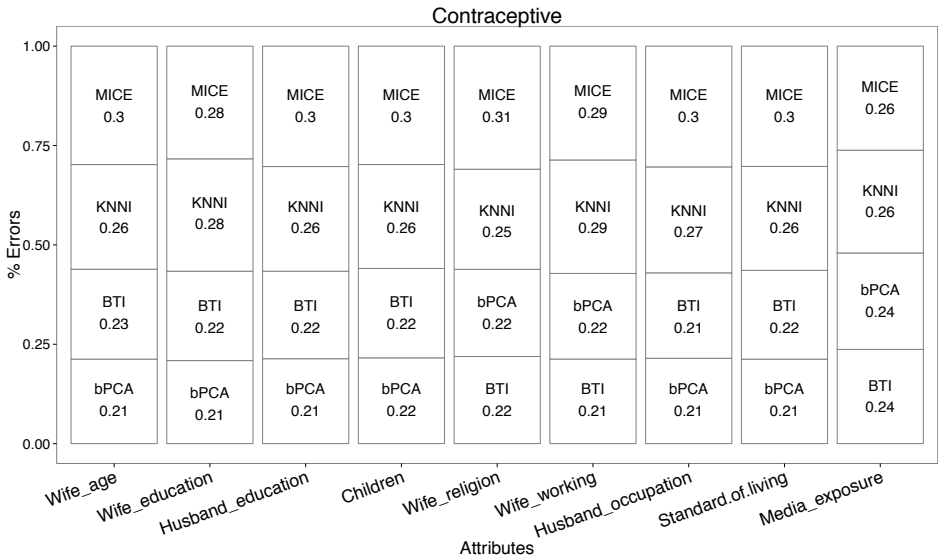
Contraceptive
% Errors
1.00
0.75
0.50
0.25
0.00
MICE 0.3
KNNI 0.26
BTI 0.23
bPCA 0.21
MICE 0.28
KNNI 0.28
BTI 0.22
bPCA 0.21
MICE 0.3
KNNI 0.26
BTI 0.22
bPCA 0.21
MICE 0.3
KNNI 0.26
BTI 0.22
bPCA 0.22
MICE 0.31
KNNI 0.25
bPCA 0.22
BTI 0.22
MICE 0.29
KNNI 0.29
bPCA 0.22
BTI 0.21
MICE 0.3
KNNI 0.27
BTI 0.21
bPCA 0.21
MICE 0.3
KNNI 0.26
BTI 0.22
bPCA 0.21
MICE 0.26
KNNI 0.26
bPCA 0.24
BTI 0.24
Wife_age
Wife_education
Husband_education
Children
Wife_religion
Wife_working
Husband_occupation
Standard.of.living
Media_exposure
Attributes

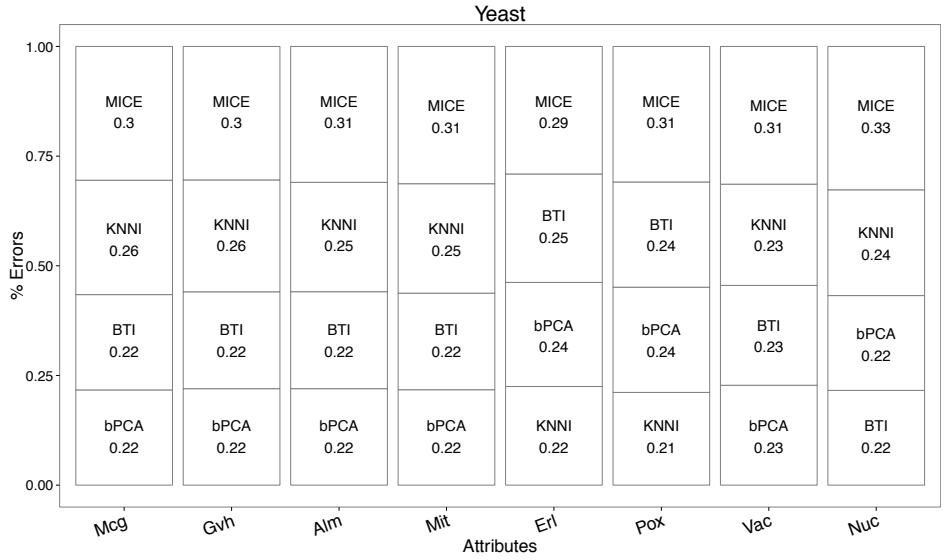
Yeast
% Errors
1.00
0.75
0.50
0.25
0.00
MICE 0.3
KNNI 0.26
BTI 0.22
bPCA 0.22
MICE 0.3
KNNI 0.26
BTI 0.22
bPCA 0.22
MICE 0.31
KNNI 0.25
BTI 0.22
bPCA 0.22
MICE 0.31
KNNI 0.25
BTI 0.22
bPCA 0.22
MICE 0.29
BTI 0.25
bPCA 0.24
KNNI 0.22
MICE 0.31
BTI 0.24
bPCA 0.24
KNNI 0.21
MICE 0.31
KNNI 0.23
BTI 0.23
bPCA 0.23
MICE 0.33
KNNI 0.24
bPCA 0.22
BTI 0.22
Mcg
Gvh
Alm
Mit
Erl
Pox
Vac
Nuc
Attributes

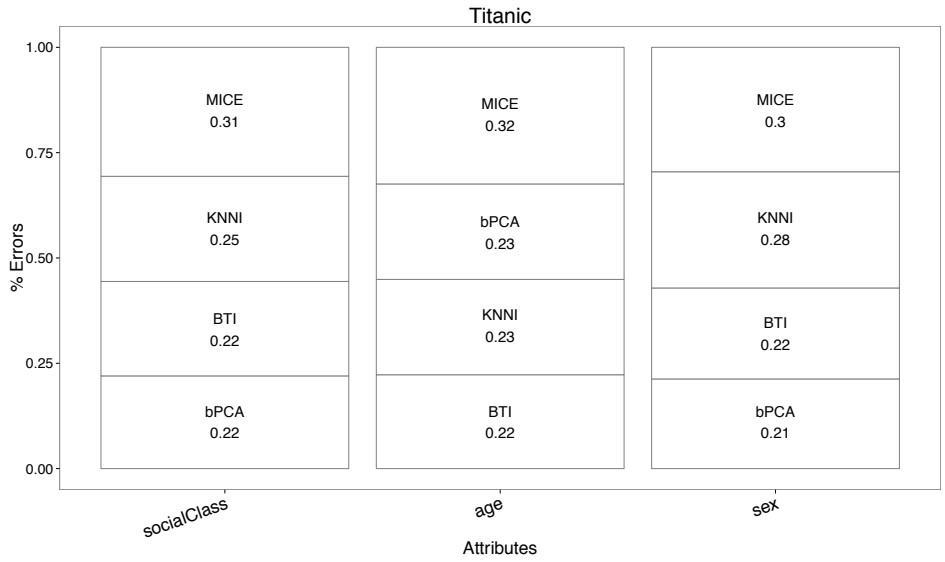
Titanic
% Errors
1.00
0.75
0.50
0.25
0.00
MICE 0.31
KNNI 0.25
BTI 0.22
bPCA 0.22
MICE 0.32
bPCA 0.23
KNNI 0.23
BTI 0.22
MICE 0.3
KNNI 0.28
BTI 0.22
bPCA 0.21
socialClass
age
sex
Attributes

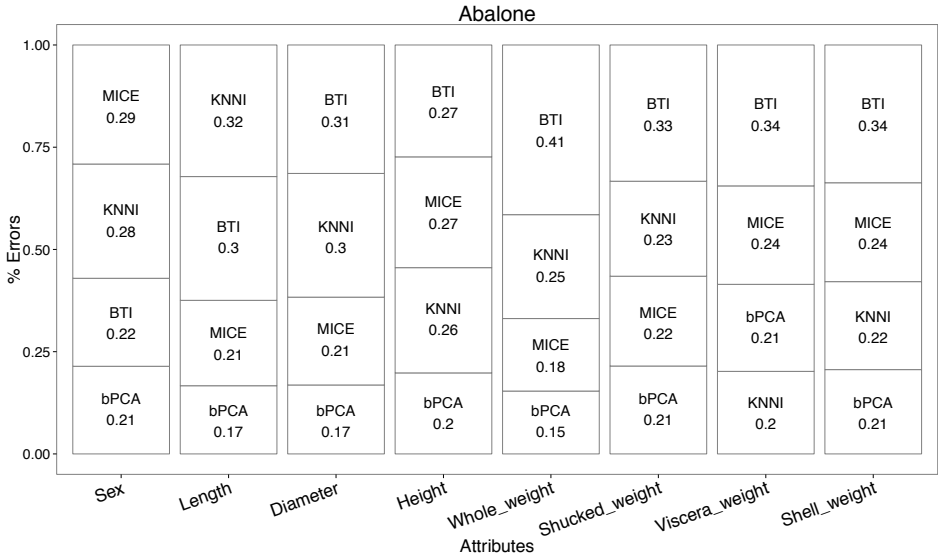
Abalone
% Errors
1.00
0.75
0.50
0.25
0.00
MICE 0.29
KNNI 0.28
BTI 0.22
bPCA 0.21
KNNI 0.32
BTI 0.3
MICE 0.21
bPCA 0.17
BTI 0.31
KNNI 0.3
MICE 0.21
bPCA 0.17
BTI 0.27
MICE 0.27
KNNI 0.26
bPCA 0.2
BTI 0.41
KNNI 0.25
MICE 0.18
bPCA 0.15
BTI 0.33
KNNI 0.23
MICE 0.22
bPCA 0.21
BTI 0.34
MICE 0.24
bPCA 0.21
KNNI 0.2
BTI 0.34
MICE 0.24
KNNI 0.22
bPCA 0.21
Sex
Length
Diameter
Height
Whole_weight
Shucked_weight
Viscera_weight
Shell_weight
Attributes

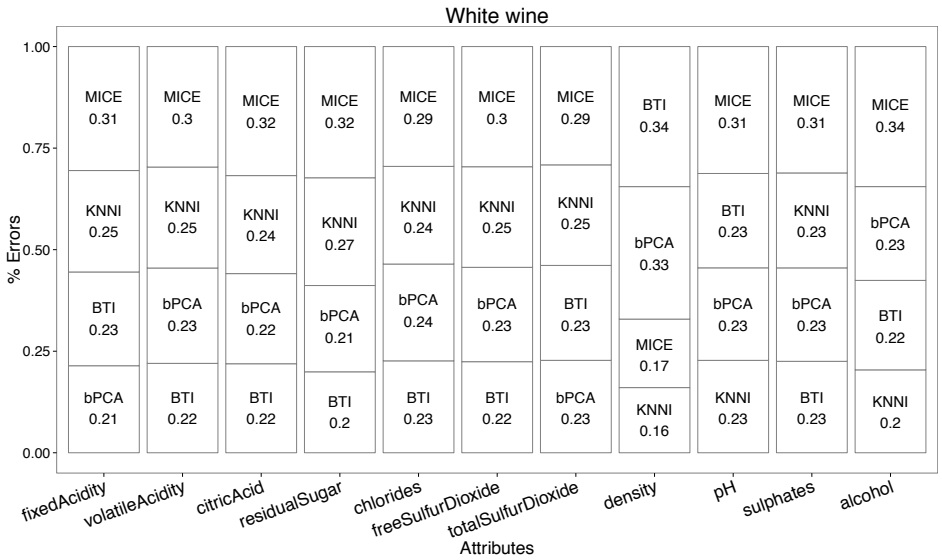
White wine
% Errors
1.00
0.75
0.50
0.25
0.00
MICE 0.31
KNNI 0.25
BTI 0.23
bPCA 0.21
MICE 0.3
KNNI 0.25
bPCA 0.23
BTI 0.22
MICE 0.32
KNNI 0.24
bPCA 0.22
BTI 0.22
MICE 0.32
KNNI 0.27
bPCA 0.21
BTI 0.2
MICE 0.29
KNNI 0.24
bPCA 0.24
BTI 0.23
MICE 0.3
KNNI 0.25
bPCA 0.23
BTI 0.22
MICE 0.29
KNNI 0.25
BTI 0.23
bPCA 0.23
BTI 0.34
bPCA 0.33
MICE 0.17
KNNI 0.16
MICE 0.31
BTI 0.23
bPCA 0.23
KNNI 0.23
MICE 0.31
KNNI 0.23
bPCA 0.23
BTI 0.23
MICE 0.34
bPCA 0.23
BTI 0.22
KNNI 0.2
fixedAcidity
volatileAcidity
citricAcid
residualSugar
chlorides
freeSulfurDioxide
totalSulfurDioxide
density
pH
sulphates
alcohol
Attributes

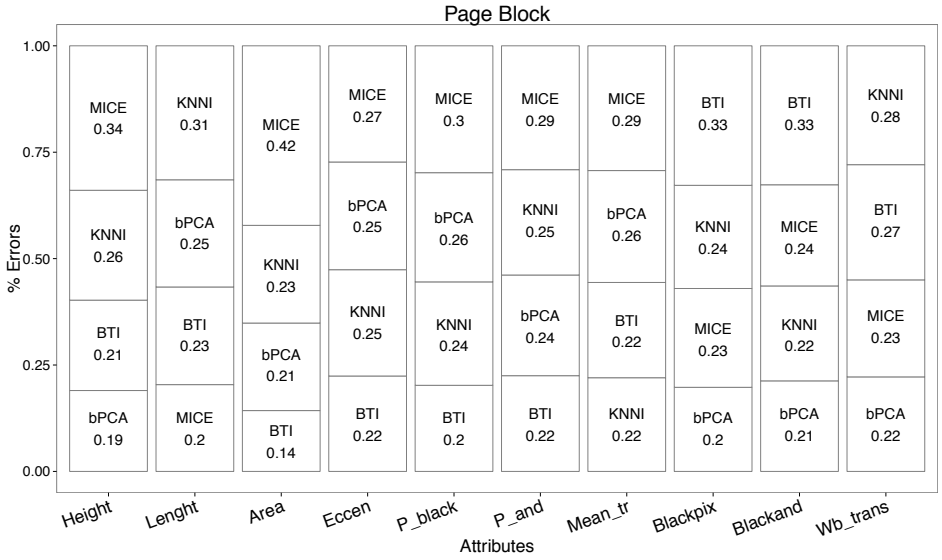
Page Block
% Errors
1.00
0.75
0.50
0.25
0.00
MICE 0.34
KNNI 0.26
BTI 0.21
bPCA 0.19
KNNI 0.31
bPCA 0.25
BTI 0.23
MICE 0.2
MICE 0.42
KNNI 0.23
bPCA 0.21
BTI 0.14
MICE 0.27
bPCA 0.25
KNNI 0.25
BTI 0.22
MICE 0.3
bPCA 0.26
KNNI 0.24
BTI 0.2
MICE 0.29
KNNI 0.25
bPCA 0.24
BTI 0.22
MICE 0.29
bPCA 0.26
BTI 0.22
KNNI 0.22
BTI 0.33
KNNI 0.24
MICE 0.23
bPCA 0.2
BTI 0.33
MICE 0.24
KNNI 0.22
bPCA 0.21
KNNI 0.28
BTI 0.27
MICE 0.23
bPCA 0.22
Height
Lenght
Area
Eccen
P_black
P_and
Mean_tr
Blackpix
Blackand
Wb_trans
Attributes

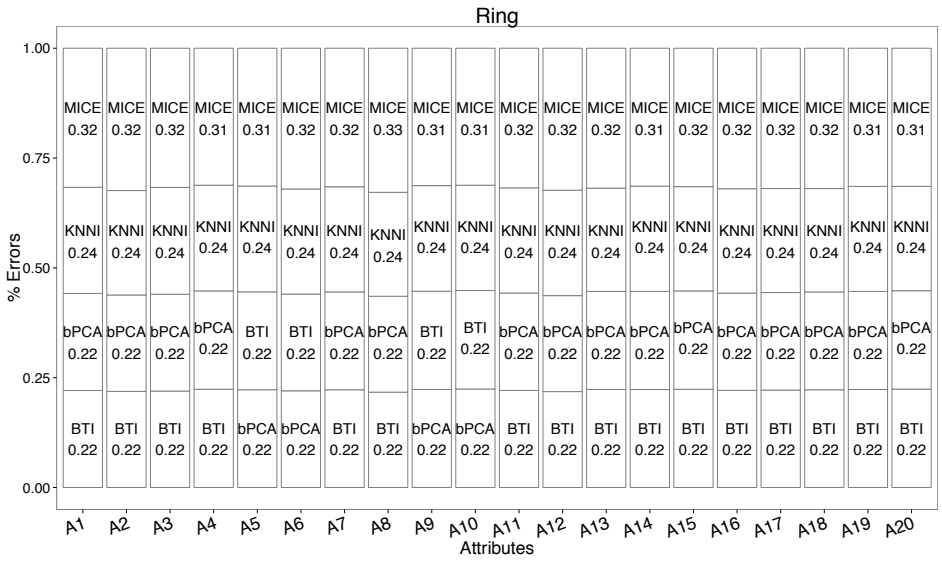
Ring
% Errors
1.00
0.75
0.50
0.25
0.00
MICE 0.32
KNNI 0.24
bPCA 0.22
BTI 0.22
MICE 0.32
KNNI 0.24
bPCA 0.22
BTI 0.22
MICE 0.32
KNNI 0.24
bPCA 0.22
BTI 0.22
MICE 0.31
KNNI 0.24
bPCA 0.22
BTI 0.22
MICE 0.31
KNNI 0.24
BTI 0.22
bPCA 0.22
MICE 0.32
KNNI 0.24
bPCA 0.22
BTI 0.22
MICE 0.32
KNNI 0.24
BTI 0.22
bPCA 0.22
MICE 0.33
KNNI 0.24
bPCA 0.22
BTI 0.22
MICE 0.31
KNNI 0.24
BTI 0.22
bPCA 0.22
MICE 0.31
KNNI 0.24
BTI 0.22
bPCA 0.22
MICE 0.32
KNNI 0.24
bPCA 0.22
BTI 0.22
MICE 0.32
KNNI 0.24
bPCA 0.22
BTI 0.22
MICE 0.32
KNNI 0.24
bPCA 0.22
BTI 0.22
MICE 0.31
KNNI 0.24
bPCA 0.22
BTI 0.22
MICE 0.32
KNNI 0.24
bPCA 0.22
BTI 0.22
MICE 0.31
KNNI 0.24
bPCA 0.22
BTI 0.22
MICE 0.31
KNNI 0.24
bPCA 0.22
BTI 0.22
MICE 0.32
KNNI 0.24
bPCA 0.22
BTI 0.22
MICE 0.32
KNNI 0.24
bPCA 0.22
BTI 0.22
MICE 0.32
KNNI 0.24
bPCA 0.22
BTI 0.22
MICE 0.32
KNNI 0.24
bPCA 0.22
BTI 0.22
MICE 0.31
KNNI 0.24
bPCA 0.22
BTI 0.22
MICE 0.31
KNNI 0.24
bPCA 0.22
BTI 0.22
A1
A2
A3
A4
A5
A6
A7
A8
A9
A10
A11
A12
A13
A14
A15
A16
A17
A18
A19
A20
Attributes

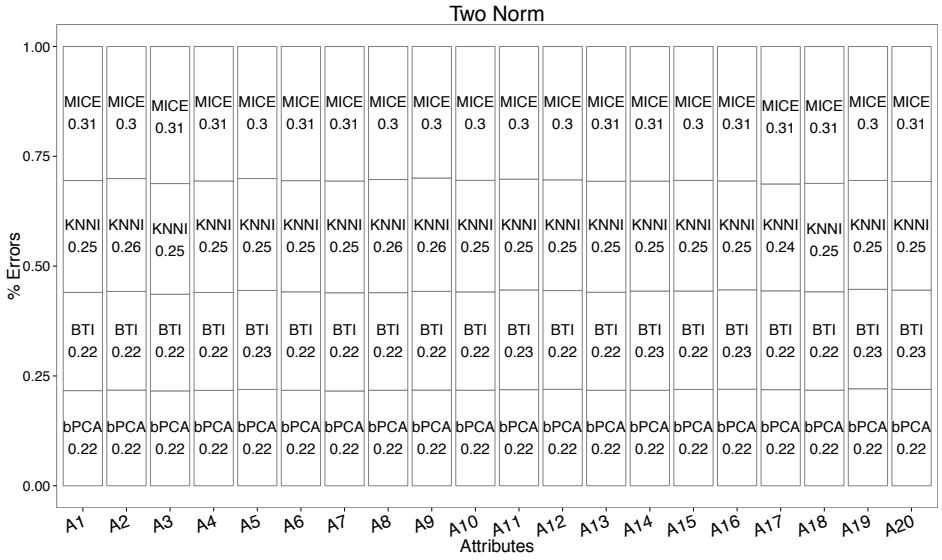
Two Norm
% Errors
1.00
0.75
0.50
0.25
0.00
A1 A2 A3 A4 A5 A6 A7 A8 A9 A10 A11 A12 A13 A14 A15 A16 A17 A18 A19 A20
Attributes
MICE 0.31 MICE 0.3 MICE 0.31 MICE 0.31 MICE 0.3 MICE 0.31 MICE 0.31 MICE 0.3 MICE 0.3 MICE 0.3 MICE 0.3 MICE 0.3 MICE 0.31 MICE 0.31 MICE 0.3 MICE 0.31 MICE 0.31 MICE 0.31 MICE 0.3 MICE 0.31
KNNI 0.25 KNNI 0.26 KNNI 0.25 KNNI 0.25 KNNI 0.25 KNNI 0.25 KNNI 0.25 KNNI 0.26 KNNI 0.26 KNNI 0.25 KNNI 0.25 KNNI 0.25 KNNI 0.25 KNNI 0.25 KNNI 0.25 KNNI 0.25 KNNI 0.24 KNNI 0.25 KNNI 0.25 KNNI 0.25
BTI 0.22 BTI 0.22 BTI 0.22 BTI 0.22 BTI 0.23 BTI 0.22 BTI 0.22 BTI 0.22 BTI 0.22 BTI 0.22 BTI 0.23 BTI 0.22 BTI 0.22 BTI 0.23 BTI 0.22 BTI 0.23 BTI 0.22 BTI 0.22 BTI 0.23 BTI 0.23
bPCA 0.22 bPCA 0.22 bPCA 0.22 bPCA 0.22 bPCA 0.22 bPCA 0.22 bPCA 0.22 bPCA 0.22 bPCA 0.22 bPCA 0.22 bPCA 0.22 bPCA 0.22 bPCA 0.22 bPCA 0.22 bPCA 0.22 bPCA 0.22 bPCA 0.22 bPCA 0.22 bPCA 0.22 bPCA 0.22

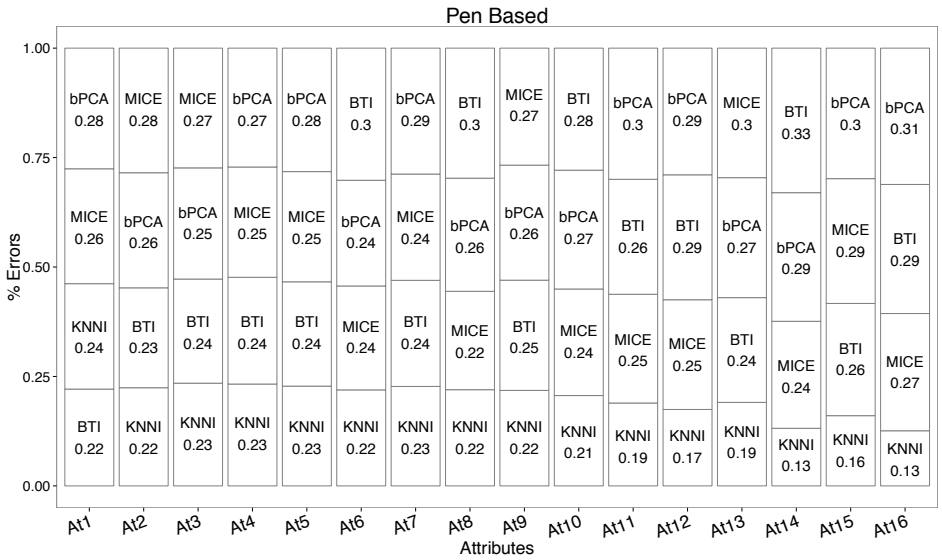
Pen Based
% Errors
1.00
0.75
0.50
0.25
0.00
At1 At2 At3 At4 At5 At6 At7 At8 At9 At10 At11 At12 At13 At14 At15 At16
Attributes
bPCA 0.28 MICE 0.28 MICE 0.27 bPCA 0.27 bPCA 0.28 BTI 0.3 bPCA 0.29 BTI 0.3 MICE 0.27 BTI 0.28 bPCA 0.3 bPCA 0.29 MICE 0.3 BTI 0.33 bPCA 0.3 bPCA 0.31
MICE 0.26 bPCA 0.26 bPCA 0.25 MICE 0.25 MICE 0.25 bPCA 0.24 MICE 0.24 bPCA 0.26 bPCA 0.26 bPCA 0.27 BTI 0.26 BTI 0.29 bPCA 0.27 bPCA 0.29 MICE 0.29 BTI 0.29
KNNI 0.24 BTI 0.23 BTI 0.24 BTI 0.24 BTI 0.24 MICE 0.24 BTI 0.24 MICE 0.22 BTI 0.25 MICE 0.24 MICE 0.25 MICE 0.25 BTI 0.24 MICE 0.24 BTI 0.26 MICE 0.27
BTI 0.22 KNNI 0.22 KNNI 0.23 KNNI 0.23 KNNI 0.23 KNNI 0.22 KNNI 0.23 KNNI 0.22 KNNI 0.22 KNNI 0.21 KNNI 0.19 KNNI 0.17 KNNI 0.19 KNNI 0.13 KNNI 0.16 KNNI 0.13

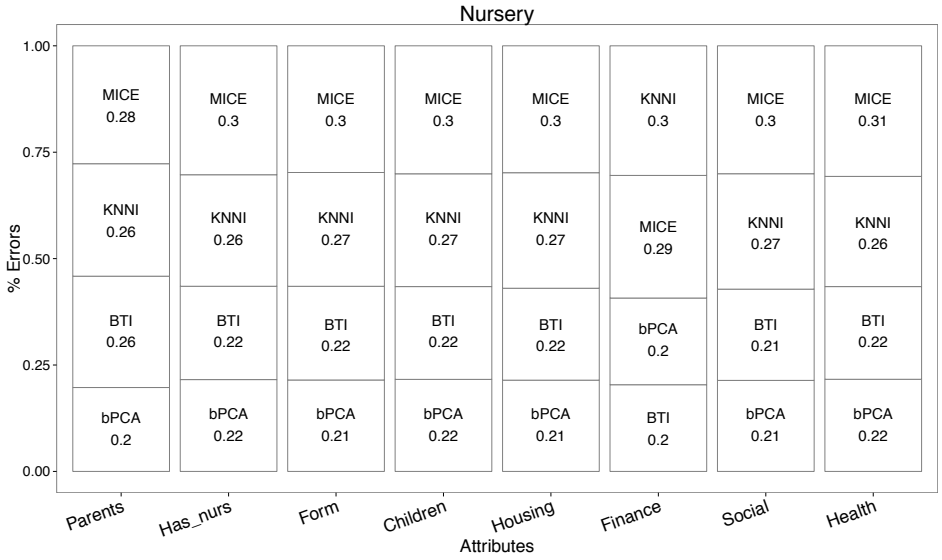
Nursery
% Errors
1.00
0.75
0.50
0.25
0.00
MICE 0.28
KNNI 0.26
BTI 0.26
bPCA 0.2
MICE 0.3
KNNI 0.26
BTI 0.22
bPCA 0.22
MICE 0.3
KNNI 0.27
BTI 0.22
bPCA 0.21
MICE 0.3
KNNI 0.27
BTI 0.22
bPCA 0.22
MICE 0.3
KNNI 0.27
BTI 0.22
bPCA 0.21
KNNI 0.3
MICE 0.29
bPCA 0.2
BTI 0.2
MICE 0.3
KNNI 0.27
BTI 0.21
bPCA 0.21
MICE 0.31
KNNI 0.26
BTI 0.22
bPCA 0.22
Parents
Has_nurs
Form
Children
Housing
Finance
Social
Health
Attributes

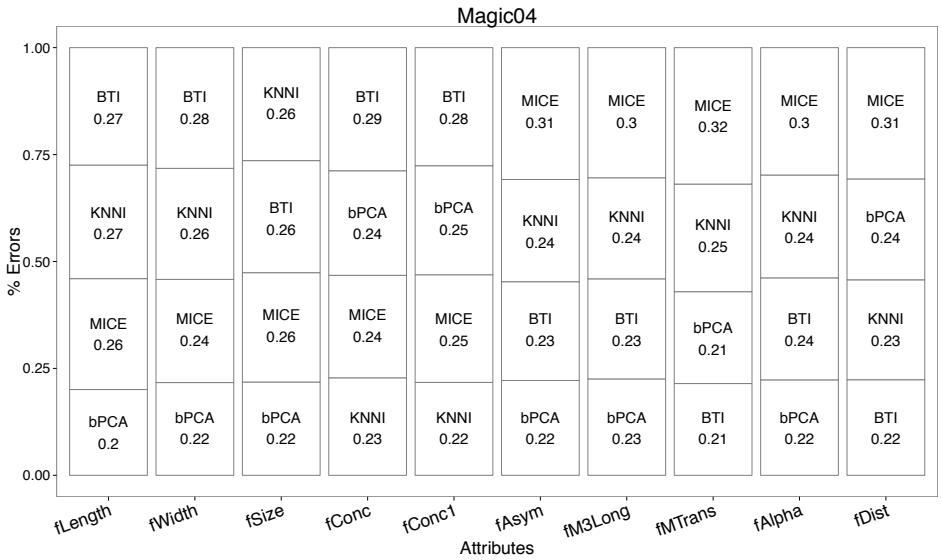
Magic04
% Errors
1.00
0.75
0.50
0.25
0.00
BTI 0.27
KNNI 0.27
MICE 0.26
bPCA 0.2
BTI 0.28
KNNI 0.26
MICE 0.24
bPCA 0.22
KNNI 0.26
BTI 0.26
MICE 0.26
bPCA 0.22
BTI 0.29
bPCA 0.24
MICE 0.24
KNNI 0.23
BTI 0.28
bPCA 0.25
MICE 0.25
KNNI 0.22
MICE 0.31
KNNI 0.24
BTI 0.23
bPCA 0.22
MICE 0.3
KNNI 0.24
BTI 0.23
bPCA 0.23
MICE 0.32
KNNI 0.25
bPCA 0.21
BTI 0.21
MICE 0.3
KNNI 0.24
BTI 0.24
bPCA 0.22
MICE 0.31
bPCA 0.24
KNNI 0.23
BTI 0.22
fLength
fWidth
fSize
fConc
fConc1
fAsym
fM3Long
fMTrans
fAlpha
fDist
Attributes

B

Online Traveling Recommender System with Missing Values

```
//function to assign a membership function (for each point) to each cluster

import org.apache.spark.ml.linalg.{Vectors=>MLVs,Vector=>MLV}

val clusterSim = udf((landmarks1km:Double, landmarks5km:Double, top10:Double, metrohalfkm:Double, metro1km:Double, trainhalfkm:Double, train1km:Double,
closestAirport:Double) => {
  val centers = model.clusterCenters // hardcoded
  val c = MLVs.dense(landmarks1km,landmarks5km,top10,metrohalfkm,metro1km,trainhalfkm,train1km, closestAirport)
  val errors = centers.map( centerVector=>  MLVs.sqdist(centerVector,c) )
  val sum = errors.sum
  val finalErrors = errors.map(value => value/sum)
  finalErrors
})
```

```
import org.apache.spark.ml.linalg.{Vectors=>MLVs, Vector=>MLV}
clusterSim: org.apache.spark.sql.expressions.UserDefinedFunction = UserDefinedFunction(<function8>,ArrayType(DoubleType,false),Some(List(DoubleType, DoubleType, Double
Type, DoubleType, DoubleType, DoubleType, DoubleType, DoubleType)))
```

Figure B.1: Code snippet for cluster similarity prediction based on geographical features.

```
// calculate the jaccard similarity measure
val  jaccard = udf((x:Seq[Any], y:Seq[Any]) => {

  val unionSet = x.toSet.union(y.toSet).size
  val intersectionSet = x.toSet.intersect(y.toSet).size

  if(x.toSet.isEmpty && y.toSet.isEmpty){
    1
  }else{
    intersectionSet / unionSet.toDouble
  }
})

import scala.collection.mutable.ArrayBuffer
val  hammingWeighted = udf((ids:Seq[Int], weights:Seq[Double], len:Integer) => {

  val m = ids zip weights toMap
  val k = m.keySet

var x = new ArrayBuffer[Double]()
for(i <- 1 to len){
  if(k contains i)
    x+= m(i)
  else
    x+= 0
}
  x
})
```

Figure B.2: Code snippet for Jaccard and weighted hamming similarity measures in scala.

C

Deep Learning for fetal monitoring in labour

```
model_fhr = Sequential([
    BatchNormalization(axis=-1, momentum=momentum, epsilon=0.001, center=True, scale=True, beta_initializer='zeros', gamma_initializer='ones', moving_mean_in
    keras.layers.GaussianNoise(0.1),
    Conv1D(filters=nb_filter_1, filter_length=filter_length_1, activation=activation, kernel_initializer=initializer, name="layer_1_fhr_CNN"),
    MaxPooling1D(name="layer_1_fhr_MP"),     # Downsample the output of convolution by 2X.
    Dropout(percDropout, name="layer_1_fhr_DO"),
    BatchNormalization(axis=-1, momentum=momentum, epsilon=0.001, center=True, scale=True, beta_initializer='zeros', gamma_initializer='ones', moving_mean_in
  #Conv1D(filters=nb_filter, kernel_size=filter_length, activation='relu', kernel_initializer=initializer),
    Conv1D(filters=nb_filter_2, filter_length=filter_length_2, activation=activation, kernel_initializer=initializer, name="layer_2_fhr_CNN"),
    MaxPooling1D(name="layer_2_fhr_MP"),
    Dropout(percDropout, name="layer_2_fhr_DO"),
    BatchNormalization(axis=-1, momentum=momentum, epsilon=0.001, center=True, scale=True, beta_initializer='zeros', gamma_initializer='ones', moving_mean_in
    #Conv1D(filters=nb_filter, kernel_size=filter_length, activation='relu', kernel_initializer=initializer),
    Conv1D(filters=nb_filter_3, filter_length=filter_length_3, activation=activation, kernel_initializer=initializer, name="layer_3_fhr_CNN"),
    MaxPooling1D(name="layer_3_fhr_MP"),
    Dropout(percDropout, name="layer_3_fhr_DO"),
    BatchNormalization(axis=-1, momentum=momentum, epsilon=0.001, center=True, scale=True, beta_initializer='zeros', gamma_initializer='ones', moving_mean_in
    #Conv1D(filters=nb_filter, kernel_size=filter_length, activation='relu', kernel_initializer=initializer),
    Conv1D(filters=nb_filter_4, filter_length=filter_length_4, activation=activation, kernel_initializer=initializer, name="layer_4_fhr_CNN"),
    MaxPooling1D(name="layer_4_fhr_MP"),
    Dropout(percDropout, name="layer_4_fhr_DO"),
    BatchNormalization(axis=-1, momentum=momentum, epsilon=0.001, center=True, scale=True, beta_initializer='zeros', gamma_initializer='ones', moving_mean_in
    #Conv1D(filters=nb_filter, kernel_size=filter_length, activation='relu', kernel_initializer=initializer),
    Conv1D(filters=nb_filter_5, filter_length=filter_length_5, activation="sigmoid", kernel_initializer=initializer, name="layer_5_fhr_CNN"),
    MaxPooling1D(name="layer_5_fhr_MP"),
    Dropout(percDropout, name="layer_5_fhr_DO"),
    BatchNormalization(axis=-1, momentum=momentum, epsilon=0.001, center=True, scale=True, beta_initializer='zeros', gamma_initializer='ones', moving_mean_in
    Flatten(name="layer_5_fhr_FLAT"),
    Dense(10, name="layer_5_fhr_DENSE10")
])
```

Figure C.1: Convolutional Neural Network python definition for FHR.

D

Deep Learning for stock market volatility forecasting

Table D.1: Evaluation Metrics for the NASDAQ 100 dataset: The MSE, QLIKE and Pearson measures are reported for each asset and for each compared model.

Asset	LSTM-1			LSTM-29			R-GARCH			GJR-MEM		
	MSE	QLIKE	Pearson	MSE	QLIKE	Pearson	MSE	QLIKE	Pearson	MSE	QLIKE	Pearson
AAPL	5.27	0.81	0.17	5.37	1.17	0.13	5.58	0.90	0.08	5.22	0.74	0.18
ADBE	4.36	0.97	0.29	4.74	1.21	0.16	4.76	1.00	0.18	4.75	0.91	0.21
ADI	4.68	1.15	0.29	4.73	1.40	0.24	4.99	1.07	0.07	4.80	0.99	0.20
ADP	7.20	0.25	0.34	7.50	0.69	0.17	8.42	327.54	0.28	9.62	0.33	0.20
ADSK	9.42	1.74	0.30	9.86	1.63	0.23	11.20	1.40	0.15	9.39	1.30	0.29
AKAM	16.65	1.28	0.23	17.13	1.55	0.20	18.50	141.45	-0.00	20.66	1.24	0.19
ALGN	16.09	1.53	0.18	16.01	1.72	0.16	16.39	1.58	0.01	16.68	1.46	0.10
ALXN	13.66	1.77	0.33	14.24	2.08	0.23	14.43	1.89	0.15	13.86	1.79	0.30
AMAT	4.59	1.44	0.29	5.06	1.59	0.17	4.84	1.29	0.14	4.72	1.27	0.22
AMGN	2.78	2.45	0.37	3.03	1.19	0.25	3.04	1.03	0.30	2.80	0.95	0.32
AMZN	14.15	1.25	0.21	14.64	1.51	0.13	14.76	1.29	0.07	14.75	1.21	0.13
ATVI	12.42	2.67	0.27	13.44	1.77	0.12	13.48	1.46	0.12	12.42	1.40	0.25
AVGO	10.12	1.53	0.35	10.99	1.94	0.22	12.63	125.69	0.22	10.26	1.50	0.29
BIDU	113.24	10.93	0.07	113.21	2.60	0.07	119.20	24709.19	0.03	183.97	1.71	0.04
BIIB	10.70	1.58	0.26	11.20	1.95	0.19	11.44	1.60	0.13	11.08	1.52	0.24
CA	2.14	1.36	0.27	2.36	0.97	0.12	2.66	0.72	0.08	2.23	0.52	0.19
CELG	21.25	1.55	0.22	22.41	2.00	0.13	25.88	80.25	0.12	23.10	1.55	0.12
CERN	2.47	0.99	0.34	2.77	1.26	0.18	2.97	0.99	0.16	2.55	0.91	0.29
CHKP	5.51	6.44	0.13	5.66	1.24	0.07	6.55	0.77	0.10	5.67	0.81	0.06
CHTR	4.98	1.21	0.41	5.94	1.63	0.20	5.89	1.31	0.10	5.21	1.19	0.34
CMCSA	1.30	14.94	0.28	1.41	0.81	0.19	1.54	0.68	0.16	1.32	0.60	0.22
COST	2.84	0.28	0.47	3.37	0.85	0.10	3.50	0.46	0.07	3.42	0.31	0.14
CSCO	2.22	9.53	0.24	2.29	0.85	0.19	2.42	0.68	0.07	2.26	0.56	0.19
CTAS	1.96	0.57	0.26	2.11	0.95	0.12	2.51	0.50	0.13	2.02	0.42	0.18
CTRP	64.41	2.07	0.28	66.95	2.28	0.21	66.67	1994.53	0.18	65.07	2.04	0.24
CTSH	4.72	1.04	0.27	4.92	1.29	0.21	4.98	1.03	0.12	4.52	0.91	0.34
CTXS	4.92	1.09	0.31	5.36	1.45	0.19	5.75	1.16	0.13	5.52	1.08	0.18
DISCA	5.26	1.68	0.38	5.83	1.64	0.25	5.85	568.75	0.17	5.22	1.31	0.35
DISCK	3.96	1.42	0.40	4.48	1.59	0.27	4.52	1.34	0.19	4.09	1.25	0.34
DISH	5.54	1.51	0.37	6.12	1.54	0.25	6.47	1.36	0.09	5.34	1.21	0.39
DLTR	5.12	1.27	0.29	5.51	1.46	0.19	5.55	1.16	0.16	5.51	1.15	0.16
EA	11.81	1.36	0.24	12.68	1.79	0.11	12.84	1.63	0.05	11.81	1.33	0.23
EBAY	4.38	1.25	0.26	4.62	1.25	0.18	4.68	1.05	0.10	4.45	0.99	0.21
ESRX	8.41	1.12	0.21	8.74	1.21	0.10	9.48	1.01	0.06	8.55	0.88	0.16
EXPE	10.49	1.50	0.29	10.71	1.80	0.27	11.82	1.51	0.04	11.15	1.42	0.18
FAST	3.47	1.09	0.36	3.75	1.14	0.23	3.95	0.99	0.15	3.52	0.83	0.33
FB	9.48	1.14	0.25	9.87	1.53	0.18	10.75	1.28	0.14	9.96	1.10	0.20
FISV	0.61	0.35	0.41	0.68	0.47	0.29	0.83	0.42	0.21	0.59	0.20	0.42
FOXA	8.15	2.27	0.24	8.37	1.53	0.21	8.56	1.09	0.12	7.69	1.03	0.33
FOX	7.20	9.03	0.23	7.39	1.38	0.19	7.38	1.02	0.13	6.70	0.92	0.33
GILD	13.92	1.20	0.16	12.12	1.62	0.17	13.87	1.24	0.13	11.80	1.21	0.21
GOOGL	4.71	1.12	0.23	4.91	0.93	0.15	5.09	0.81	0.07	6.10	0.65	0.11
HAS	9.63	5.92	0.19	9.95	1.33	0.12	9.93	1.03	0.06	10.55	0.91	0.11
HOLX	2.92	1.40	0.26	3.09	1.33	0.20	3.27	0.95	0.17	3.04	0.89	0.22
HSIC	1.36	0.73	0.28	1.41	0.76	0.21	1.55	0.53	0.20	1.34	0.41	0.28
IDXX	7.29	1.22	0.30	7.69	1.30	0.22	8.05	1.11	0.16	7.53	1.03	0.31
ILMN	33.51	1.94	0.25	35.14	2.48	0.17	35.82	1.90	0.15	40.41	1.88	0.12

Asset	LSTM-1			LSTM-29			R-GARCH			GJR-MEM		
	MSE	QLIKE	Pearson	MSE	QLIKE	Pearson	MSE	QLIKE	Pearson	MSE	QLIKE	Pearson
INCY	41.34	2.52	0.47	49.49	2.55	0.32	60.61	1378.67	0.28	42.65	2.32	0.44
INTC	2.50	1.44	0.28	2.56	0.97	0.23	2.87	0.88	0.17	2.45	0.71	0.27
INTU	2.40	0.73	0.27	2.50	1.10	0.22	2.80	0.75	0.15	2.53	0.65	0.23
ISRG	6.79	0.93	0.23	7.04	1.17	0.16	7.24	1.03	0.04	7.20	0.86	0.28
JBHT	1.18	1.11	0.42	1.40	1.05	0.22	1.67	0.82	0.14	1.25	0.64	0.33
KLAC	16.97	1.06	0.18	17.39	1.27	0.09	17.56	1.12	0.02	33.65	0.93	0.04
LBTYA	6.45	6.09	0.26	6.22	1.44	0.33	7.43	1.30	0.17	6.03	1.21	0.34
LBTYK	4.46	1.15	0.44	4.86	1.42	0.34	5.65	1.22	0.15	4.63	1.13	0.36
LRCX	5.42	1.49	0.33	6.26	1.67	0.13	6.27	1.33	0.11	5.61	1.25	0.26
LVNTA	4.32	1.52	0.38	4.71	1.63	0.27	5.24	1.23	0.22	4.44	1.16	0.33
MCHP	4.05	1.19	0.22	4.23	1.34	0.17	4.13	1.04	0.15	4.12	0.98	0.22
MDLZ	1.91	0.65	0.36	2.17	1.01	0.18	2.18	0.69	0.15	2.08	0.64	0.20
MELI	30.82	1.84	0.21	31.94	2.07	0.14	32.45	123.43	0.03	35.65	1.80	0.14
MNST	36.40	1.37	0.23	37.65	1.76	0.06	37.84	1.82	0.01	42.45	1.40	0.02
MSFT	2.88	4.43	0.30	3.12	1.14	0.15	3.20	0.79	0.09	3.10	0.68	0.19
MU	23.94	2.20	0.29	24.50	2.31	0.28	30.71	12.19	0.19	24.12	2.08	0.25
MXIM	6.57	1.35	0.29	6.99	1.39	0.18	7.30	1.16	0.01	6.53	0.99	0.28
MYL	27.51	2.61	0.24	28.48	2.41	0.20	30.09	1.94	0.09	28.60	1.82	0.24
NFLX	42.50	3.66	0.28	45.43	2.32	0.16	46.40	494.89	0.08	47.72	1.87	0.25
NTES	20.94	2.03	0.36	22.73	2.21	0.24	24.78	2.60	0.08	21.67	1.89	0.30
NVDA	34.16	1.84	0.27	34.99	2.05	0.22	35.20	1.75	0.14	33.77	1.69	0.25
ORLY	3.25	1.68	0.32	3.50	1.01	0.24	3.65	0.90	0.18	3.66	0.77	0.26
PAYX	0.68	0.26	0.53	0.84	0.52	0.27	1.08	0.48	0.13	0.78	0.24	0.35
PCAR	2.18	0.84	0.44	2.40	1.11	0.32	2.76	0.96	0.23	2.23	0.80	0.37
PCLN	4.09	1.00	0.35	4.27	1.48	0.31	4.47	1.02	0.23	4.66	0.92	0.23
QCOM	9.80	6.79	0.30	9.44	1.27	0.39	7.17	396.55	0.59	7.41	0.76	0.55
QVCA	7.18	1.36	0.32	7.42	1.36	0.24	11.24	1.21	0.22	6.71	1.11	0.35
ROST	3.25	5.52	0.25	3.42	1.04	0.17	3.45	0.90	0.13	3.61	0.82	0.13
SBUX	11.57	0.51	0.21	12.09	1.12	0.07	21.81	0.80	0.07	12.03	0.72	0.08
SHPG	14.19	3.01	0.17	14.51	1.88	0.14	13.84	1.41	0.30	15.76	1.27	0.23
SIRI	2.03	0.66	0.26	2.03	1.22	0.18	2.52	0.81	0.14	1.90	0.74	0.26
STX	28.43	1.85	0.23	28.66	2.09	0.22	32.28	202.89	0.19	32.80	1.74	0.14
SWKS	14.11	1.68	0.39	16.39	1.94	0.18	18.19	1420.19	0.18	14.38	1.69	0.36
SYMC	4.94	0.98	0.34	5.56	1.41	0.14	5.41	1.08	0.13	6.38	0.96	0.20
TSCO	7.59	7.38	0.19	7.79	1.44	0.15	8.00	1.17	0.06	8.89	1.14	0.09
TSLA	22.80	2.20	0.37	24.99	2.32	0.21	33.94	8162.71	0.28	23.02	2.00	0.30
TXN	1.93	0.72	0.31	2.00	0.95	0.28	2.14	0.78	0.24	1.92	0.64	0.30
ULTA	45.69	3.35	0.10	46.38	1.93	0.04	47.07	454.42	0.05	46.06	-	0.02
VIAB	23.25	2.56	0.27	22.31	1.84	0.32	29.69	7751.06	0.24	21.04	1.36	0.36
VOD	1.96	3.15	0.26	2.06	0.84	0.16	2.35	0.59	0.08	2.05	0.36	0.13
VRSK	1.66	0.49	0.28	1.80	0.78	0.16	1.99	0.52	0.11	1.62	0.37	0.31
WDC	13.70	1.75	0.33	14.46	1.83	0.27	17.23	1.70	0.22	16.40	1.62	0.25
WYNN	43.73	2.72	0.27	42.82	2.59	0.31	51.81	99924.84	0.28	37.19	1.92	0.44
XLNX	5.46	1.14	0.26	5.78	1.29	0.17	6.01	1.13	-0.03	6.00	0.90	0.23
XRAY	1.45	0.50	0.41	1.68	0.79	0.22	1.85	0.71	0.16	1.48	0.53	0.37

E

Deep Learning for threat detection in luggage from x-ray images

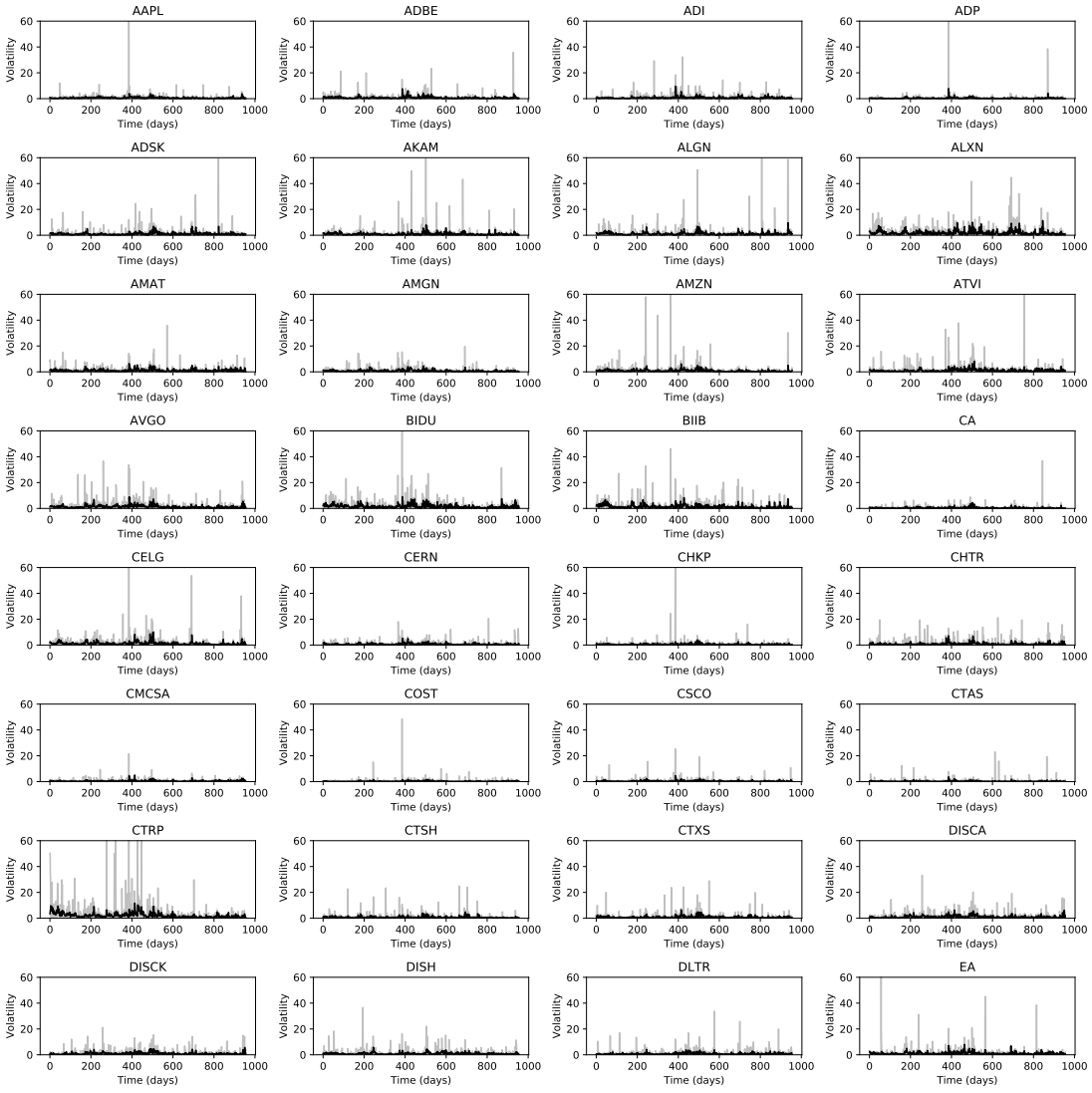

Figure D.1: LSTM-92 one step ahead predictions for the NASDAQ 100 dataset (APPL to EA assets). The observed time series are given in gray and the predicted volatility values in black.

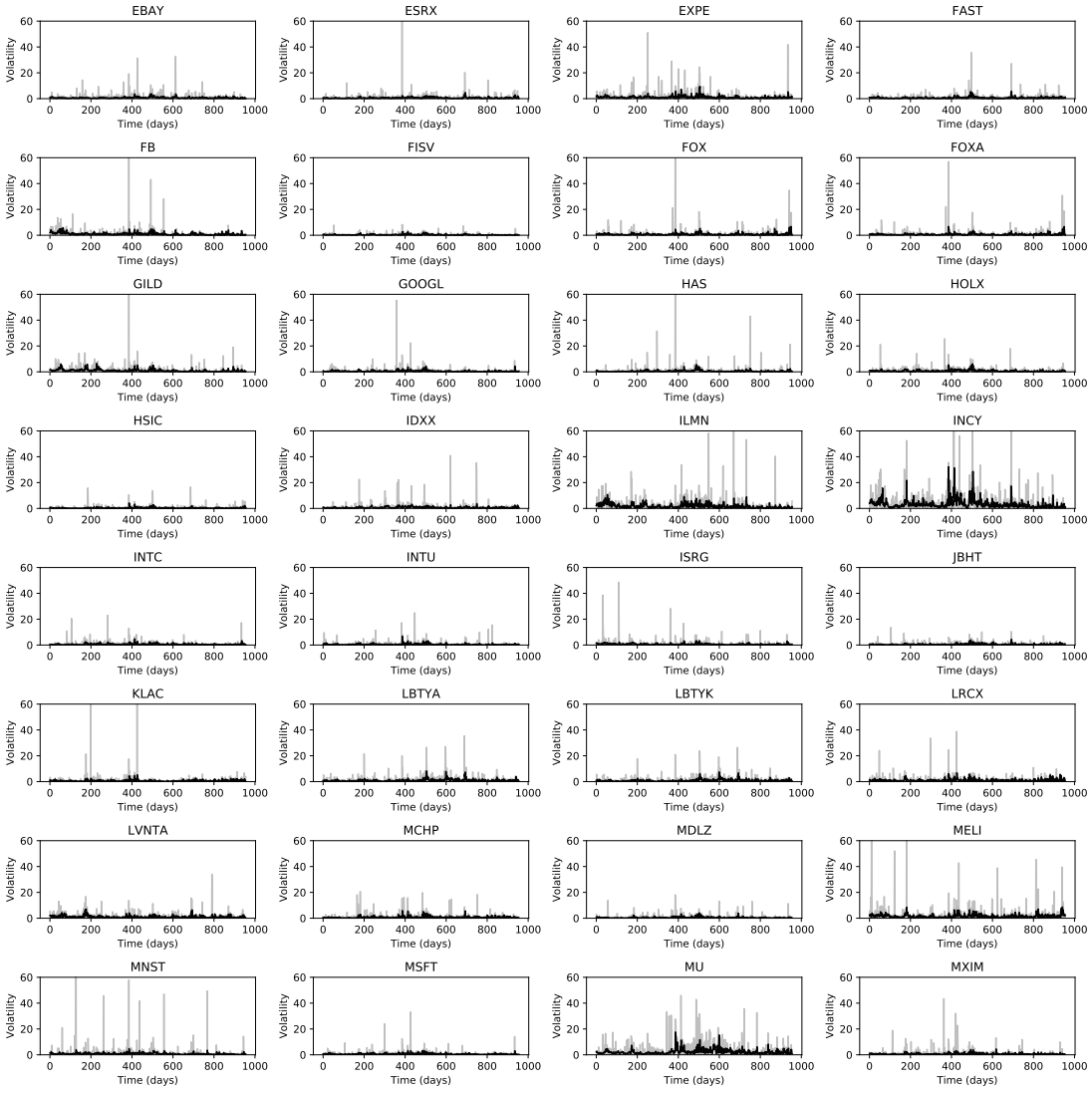

Figure D.2: LSTM-92 one step ahead predictions for the NASDAQ 100 dataset (EBAY to MXIM assets). The observed time series are given in gray and the predicted volatility values in black.

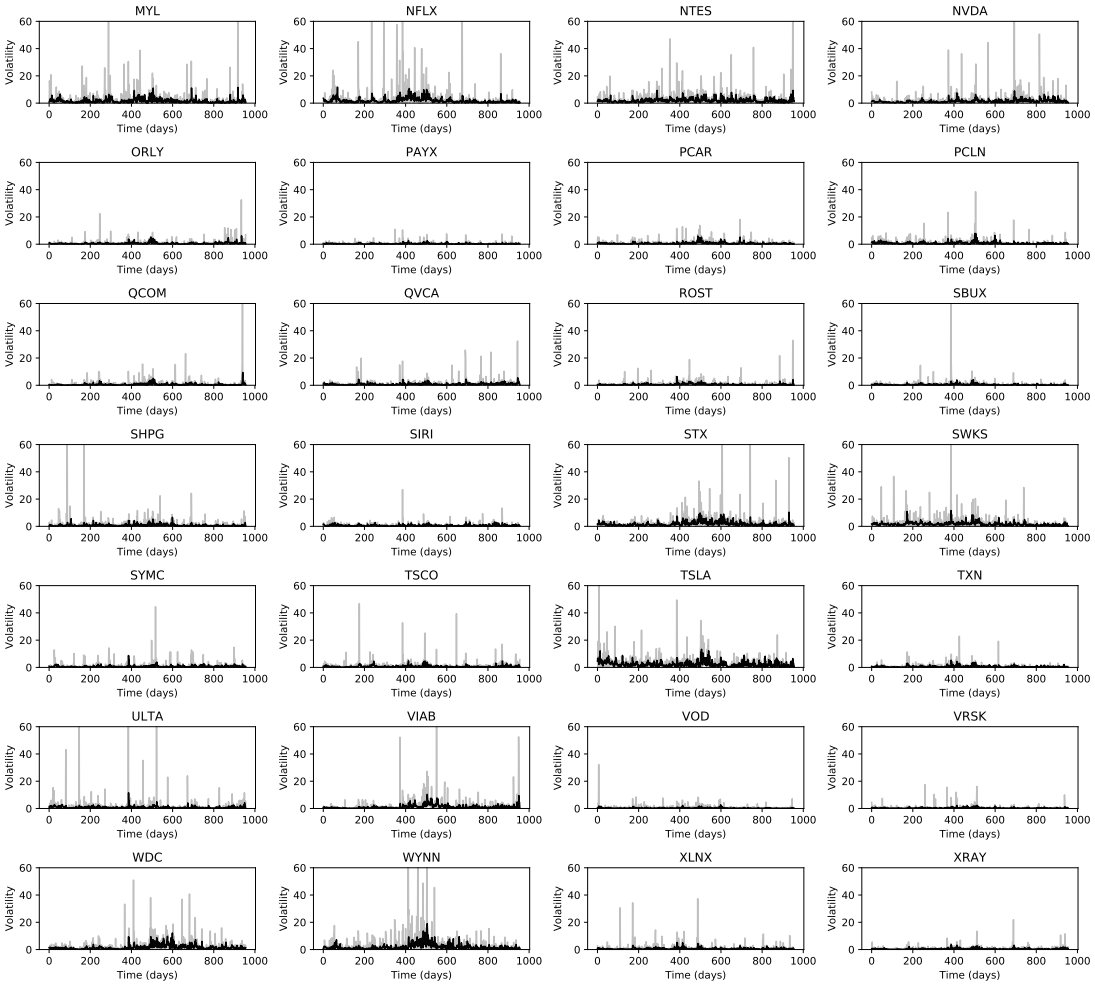

Figure D.3: LSTM-92 one step ahead predictions for the NASDAQ 100 dataset (MYL to XRAY assets). The observed time series are given in gray and the predicted volatility values in black.

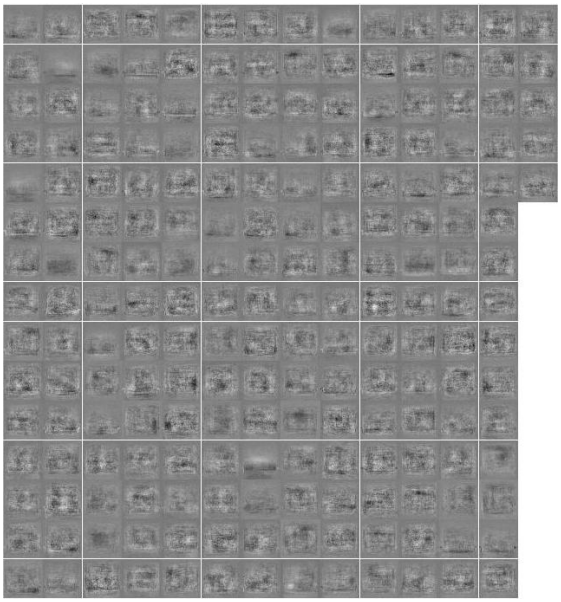

Figure E.1: Weights learned from the first autoencoder for threats and benign detection.

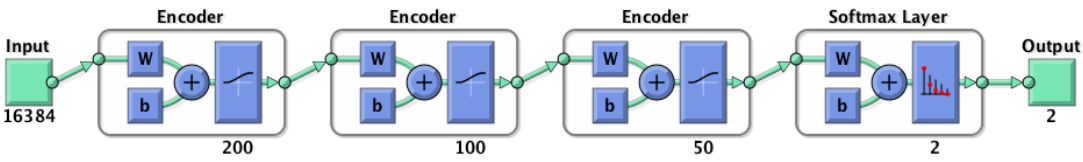

Figure E.2: Autoencoder topology.